GNA AS A SCAFFOLD FOR CHROMOPHORES AGGREGATES AND DESIGN OF SILICON-BASED DNA BINDERS

A DISSERTATION

in

Chemistry

Presented to the Faculties of Philipps-Universität Marburg in Partial Fulfillment

of the Requirements for the Degree of Doctor of Science

(Dr. rer. nat.)

Yonggang Xiang

Wuhan, Hubei, P. R. China

Marburg/Lahn

Department of Chemistry of Philipps-Universität Marburg, accepted as a dissertation on

Supervisors: Prof. Dr. Lilu Zhang
Prof. Dr. Eric Meggers

Date of submission:

Date of defense

This thesis is dedicated to my beloved family...

Acknowledgements

The entire work embodied in this thesis is the result of investigation carried out from July 2009 to April 2013 at the department of chemistry of Philipps-Universität Marburg under the supervision of Prof. Dr. Lilu Zhang and Prof. Eric L. Meggers. The past four years has been very challenging, exciting and unforgettable. I would like to express my deepest gratitude to my supervisors for giving me this opportunity to finish my research work in Marburg University. With their help, I have learned how to do research in the right way and grow as a research scholar. I wish them and their family all the best.

In addition, I would also like to express my sincere gratitude to my master research advisors Prof. Dr. Peiqiang Huang and Prof. Dr. Xiao Zheng in Xiamen University, China. They led me into the field of chemistry and their passion of science has great influence on me, and I express my best wishes for them.

During the past several years, a lot of people offered so much generous help. Particularly, our secretary Ina Pinnschmidt, lab technician Katjia Kräling, and my colleague Dr. Hui Zhou. I also would like to express my gratitude to Dr. Xiulan Xie of the NMR facility, Dr.Uwe Linne of MS facility and Dr. Klaus Harms of the X-ray crystallography facility. I am also indebted to all of the group members of Meggers group, especially to Dr. Lei Gong, Zhijie Lin, Chen Fu, Xiaodong Shen, Haohua Huo, Wei Zuo, Dr. Pijus Sasmal, Dr. Alexander Wilbuer, Dr. Sandra Dieckmann, Dr. Sebastian Blanck, Dr. Stefan Mollin, Dr. Gabriella Benedek, Dr. Nathan Kilah, Matthias Bischof, Tom Breiding, Peter Göbel, Manuel Streib, Kathrin Wähler, Elisabeth Martin, Marianne Wenzel, Rajathees Rajaratnam, Cornelia Ritter, Anja Kastl, Jens Henker, Melanie Helms, Markus Dörr and Yu Su for sharing their knowledge and friendship.

I feel so lucky that I have met so many kind people in Marburg: Prof. Zhien Lin, Prof. Min Chen, Dr. Yumei Lin, Zhiliang You, Dr. Jie Hou, Dr. Fei Chen, Min Chen,

Qian Zhang, Yuting Ye and some others. We shared so much happy memory together. I greatly cherish the friendship with them.

Most importantly, everything becomes so great with the love and patience of my family. The constant concern, support and encouragement from my family always keep me going bravely all these years. I would like to express my heart-felt gratitude and dedicate the dissertation to them. I wish my endeavor will bring them a lot of happiness.

Part of this work has already been published:

Hydrolytically stable octahedral silicon complexes as bioactive scaffolds: application to the design of DNA intercalators (Front Cover)

Y. G. Xiang, C. Fu, T. Breiding, P. K. Sasmal, H. D. Liu, Q. Shen, K. Harms, L. L. Zhang, E. Meggers, *Chem. Commun.* **2012**, *48*, 7131-7133.

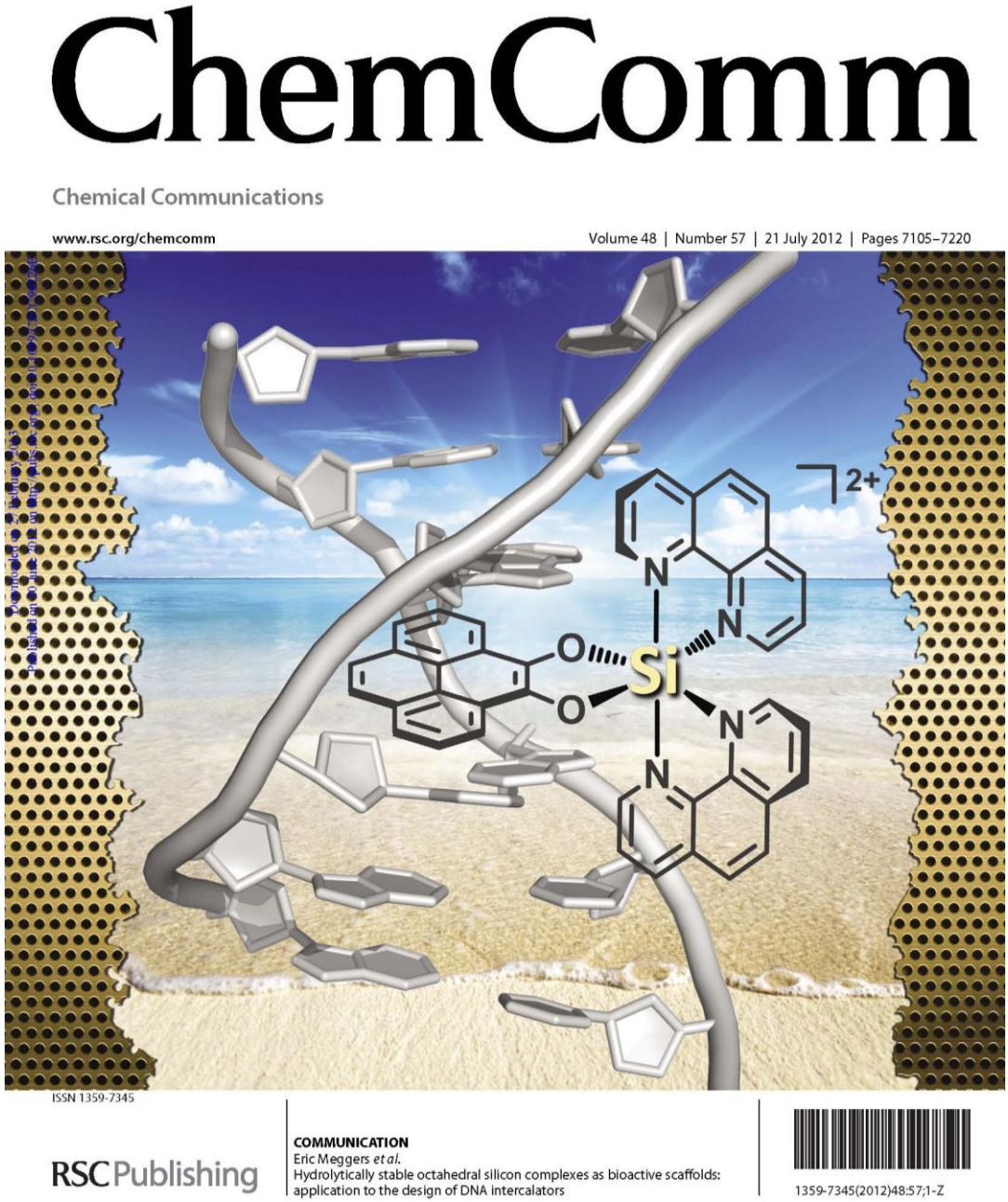

Abstract

My work mainly includes two parts, one is GNA as a scaffold for molecular aggregates of chromophores, and the other one is the design of octahedral silicon complexes as DNA binders.

In the first part of the thesis, simplified glycol nucleic acid (GNA) was used as the template for the helical assembly of covalently bound homochromophores and heterochromophores: perylene bisimide (**B**), phthalocyanine (**Y**), and porphyrin (**P**), and different numbers of chromophores could be stacking inside a duplex which led to functional artificial double-helical structures

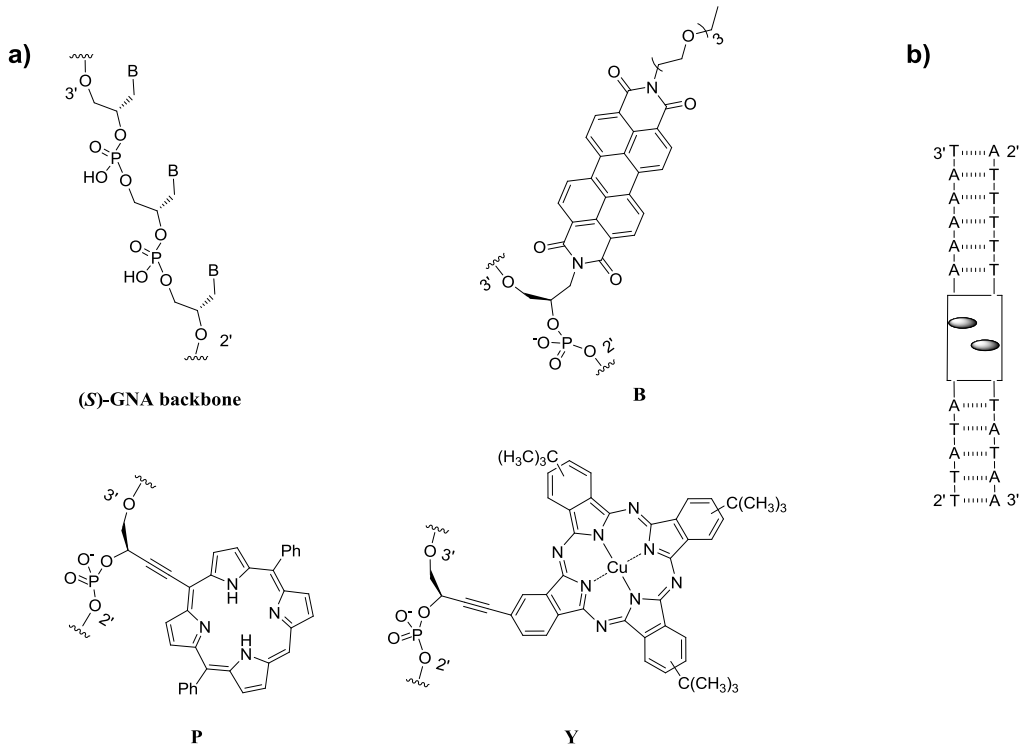

Figure I (a) Constitution of the (*S*)-GNA and structure of the artificial bases. (b) Sequence of the duplexes

In the second part of the thesis, the first examples of biologically active complexes based on octahedral silicon were designed, and silicon complexes with simple arenediol ligands and phenazinediol ligands were successfully synthesized. These kinds of silicon

complexes could be used to intercalate with DNA duplexes, detect mismatched DNA base pairs, and stabilize the formation of the G-quadruplex.

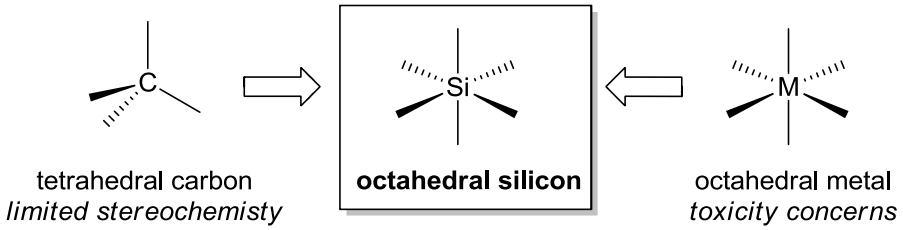

Figure II Octahedral silicon as a non-classical structural template

Abstract auf Deutsch

Meine Arbeit umfasst hauptsächlich zwei Teile, eines ist GNA als Gerüst für molekülare Aggregaten von Chromophoren, das andere ist das Design der oktaedrischen Silicium-Komplexe als DNA Bindemitteln.

Im ersten Teil meiner Arbeit wurde die vereinfachte Glykol Nukleinsäure (GNA) als Template für die spiralförmige Anordnung von kovalent gebundenen homochromophoren und heterochromophoren (Perylenbisimide (**B**), Phthalocyanine (**Y**) und Porphyrine (**P**)) verwendet. Unterschiedliche Anzahlen von Chromophoren konnten sich innerhalb des Duplexes stapeln, und daduch die künstliche Doppelhelix-Strukturen mit modifizierten Funktionen zu schaffen.

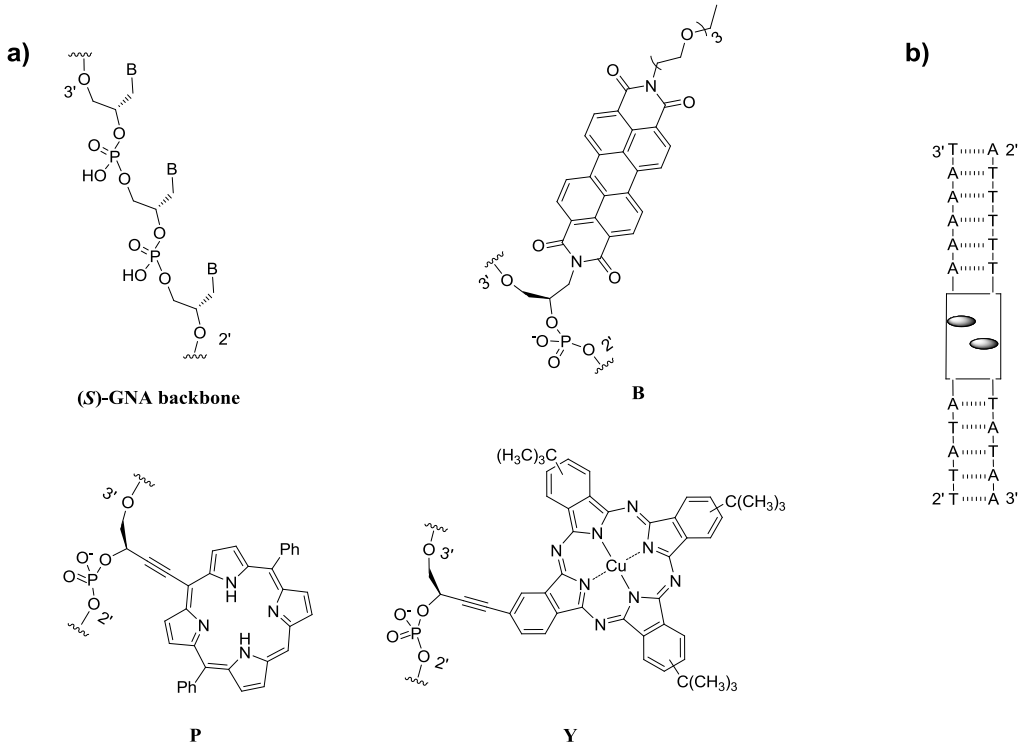

Figur I (a) Konstitution des (S)-GNAs und Strukturen der künstlichen Basen: **B**, **P** und **Y**. (b) Darstellung der mit künstlichen Basen modifizierten Duplexen.

Im zweiten Teil der Arbeit wurden die ersten Beispiele für biologisch aktive Komplexe, basierend auf oktaedrisch coordiniertem Silizium mit arenediol und phenazinediol Liganden, entwickelt.

Figur II Oktaedrisch coordinierte Silizium-Kompexe als nichtklassische strukturelle Templaten

Solche Silicium-Komplexe können verwendet werden, um mit DNA-Duplexe zu interkalieren, falsch eingeordnete DNA-Basenpaare zu erkennen, und die Bildung des G-Quadruplexs zu stabilisieren.

Table of Contents

List of Schemes I
List of Tables II
List of Figures III
Chapter 1 Theoretical part 1
1.1 Nucleic Acid-Assisted Multichromophore Assemblies 1
1.1.1 Properties of multichromophores 1
1.1.2 DNA-templated multichromophore systems 2
1.1.3 GNA-templated multichromophore systems 8
1.2 Metal Complexes as Nucleic Acid Binders 12
1.2.1 DNA duplex binders 12
1.2.2 G-quadruplex DNA/ligand interactions 17
1.2.3 Methods to investigate ligand interactions 22
1.2.4 Hypervalent silicon complexes 25
Chapter 2 Aim of work 29
Chapter 3 Results and Discussion 32
3.1 GNA as Scaffold for Chromophore Aggregates 32
3.1.1 Synthesis of GNA building blocks 32
3.1.2 PBI as an artificial GNA surrogate 37
3.1.3 Phthalocyanine as an artificial GNA surrogate 51
3.1.4 Interstrand stacking of heterochromophores as an artificial GNA surrogate 57
3.1.5 Interstrand stacking of PBI-porphyrin 57
3.1.6 Interstrand stacking of phthalocyanine-porphyrin 65
3.1.7 Interstrand stacking of phthalocyanine-PBI 72
3.2 Design of Octahedral Silicon Complexes as DNA Binders 80
3.2.1 Synthesis of silicon complexes 80
3.2.2 Silicon complexes as DNA intercalators or groove binders 87
3.2.3 Silicon complexes as DNA-insertors 99

3.2.4 Silicon complexes interaction with DNA G-quadruplex 105
Chapter 4 Summary and Outlook 110
Chapter 5 Experimental part 115
5.1 Materials and Methods 115
5.2 GNA as Scaffold for Molecular Aggregates of Chromophores 118
5.3 Octahedral Silicon Complexes as DNA Binders 133
5.3.1 Synthesis of Octahedral Silicon Complexes 133
5.3.2 Evaluation of Hydrolytic Stabilities of Octahedral Silicon Complexes 155
Chapter 6 References 159
6.1 Literature 159
6.2 List of synthesized compounds 168
6.3 Abbreviations and Symbols 176
6.4 Appendix 179
Curriculum Vitae 185

List of Schemes

Scheme 1 General synthesis of dimethoxytritylated glycol nucleoside phosphoramidites of adenine (A), thymine (T), uracil (U), guanine (G), and cytosine (C) for the synthesis of GNA oligonucleotide (**B** represents a natural base or artificial base) 9

Scheme 2 Diamine coordinates with halogenosilanes to afford hexa-coordinated silicon complexes 27

Scheme 3 Hexa-coordinated silicon complexes from **1a** and **2** 27

Scheme 4 Procedure of synthesis of **12**.....28

Scheme 5 Examples of synthesis of silicon complexes with substitution in a tetrafunctional silane 28

Scheme 6 Structures of enterobactin-Si(IV) and salmochelin-Si(IV) 28

Scheme 7 Synthesis of amine derivative **21** and **25**.....33

Scheme 8 Synthesis of GNA building block **16** (DIPEA = *N*,*N*-Diisopropylethylamine) 35

Scheme 9 Synthesis of GNA building block **17** 36

Scheme 10 Synthesis of octahedral silicon complexes containing arenediolate ligands 81

Scheme 11 Structure and synthesis of *ortho*-dihydroxyarenes. Compound **56** and **57** were synthesized by Chen Fu from Meggers Group.....82

Scheme 12 Structure and synthesis of diamine silicon complexes **72** and **74** 85

Scheme 13 Synthesis of octahedral silicon complexes harboring phenazinediolate ligand. (In this step, all the starting material **72** or **74** has been consumed; the yield is difficult to be calculated, about 20% in two steps, **75** and **76** were synthesized by Chen Fu from Meggers Group).....86

Scheme 14 Structure of $[Rh(bpy)_2(chrysi)]Cl_3$ (**87**) and $[Rh(bpy)_2(phzi)](Cl)_3$ (**88**)...99

Scheme 15 Sequences of **PBI**-containing 16mer GNA duplexes together with Watson–Crick reference duplex 111

Scheme 16 Sequences of phthalocyanine-containing 16mer GNA duplexes together with Watson–Crick reference duplex 112

Scheme 17 Sequences of heterochromophores-containing 16mer GNA duplexes together with Watson–Crick reference duplex.....113

Scheme 18 Structures of octahedral silicon complexes 114

Scheme 19 Synthetic cycle for preparation of oligonucleotides by phosphoramidite method 132

List of Tables

Table 1 Thermal stabilities of **PBI**-containing 16mer GNA duplexes together with Watson–Crick reference duplexes [a] 39

Table 2 Thermal stabilities of phthalocyanine-containing 16mer GNA duplexes together with Watson–Crick reference duplexes [a] 52

Table 3 Thermal stabilities of **PBI**-porphyrin 16mer GNA duplexes together with Watson–Crick reference duplexes [a] 58

Table 4 Thermal stabilities of **PBI**-Phthalocyanine 16mer GNA duplexes together with Watson–Crick reference duplexes [a].....65

Table 5 Thermal stabilities of **PBI**-Phthalocyanine 16mer GNA duplexes together with Watson–Crick reference duplexes [a].....73

Table 6 UV-melting temperature of 2 μM DNA duplex in Tris-HCl (5 mM, pH 7.4) with NaCl (50 mM) in the presence of or in the absence of 4.0 equiv silicon complexes 89

Table 7 UV-melting temperature of 2 μM DNA duplex in Tris-HCl (5 mM, pH 7.4) with NaCl (50 mM) in the presence of or in the absence of 4.0 equiv silicon complexes 96

Table 8 UV-melting temperature of 2 μM matched and mismatched DNA duplex in Tris-HCl (5 mM, pH 7.4) with NaCl (50 mM) in the presence of or in the absence of 1.0 equiv silicon complexes.....101

Table 9 MALDI-TOF MS data of used oligonucleotides [a].....130

List of Figures

Figure 1 Examples of DNA terminal modification with chromophores 4

Figure 2 Structures for the base-paired hairpin oligonucleotides 5

Figure 3 (A) Examples of DNA base replacements with chromophores. (B) Schematic representation of zipper-like interstrand stacking within the DNA duplex..... 6

Figure 4 DNA natural base modification with chromophores..... 7

Figure 5 Side and top view of the force-field minimized structures of the duplexes... 7

Figure 6 Constitutions of DNA, RNA, and *S*- and *R*-enantiomers of GNA 8

Figure 7 Metallo-base pairs investigated in GNA containing hydroxypyridone (**H**) and pyridylpurine (**P**) homo- and heterobase.....10

Figure 8 Constitution of (*S*)-GNA and the base pairs modified with hydroxypyridone and pyrene.....11

Figure 9 The three binding modes of metal complexes with B-DNA: (A) groove binding. (B) intercalation, and (C) insertion. (This figure from Chem. Commun. 2007, 4565-4579)[34].....13

Figure 10 Square-planar platinum intercalator: terpy = terpyridine; phen= 1,10-phenanthroline; bipy = 2,2´-bipyridine; HET = 2-hydroxyethanethiolate; en= ethanediamine 14

Figure 11 Metallo-intercalators containing 2,2´-bipyridine, 1,10-phenantroline, PHETA, HAT and dppz [38-40].....14

Figure 12 Structure of two common metallo-intercalators.....15

Figure 13 Octahedral metal complexes for DNA groove binding. TMP = 3,4,7,8-tetramethyl phenanthroline; DIP = 4,7-diphenyl-1,10-phenanthroline 16

Figure 14 Chemical structure of mismatch-specific metallo-insertors. (chrysi = 5,6-chrysene quinone diimine; phzi = benzo[*a*]phenazine-5,6-quinone diimine) 17

Figure 15 Four guanines can hydrogen bond in a square arrangement to form a G-quartet. There are two hydrogen bonds on each side of the square 18

Figure 16 Structure and topology of G-quadruplexes: (A) tetramolecular with parallel strands. (B) bimolecular antiparallel. (C) unimolecular antiparallel structure with alternating parallel strands. (D) unimolecular parallel structure with three double-chain reversal loops. (E) unimolecular antiparallel structure with adjacent parallel strands and a diagonal loop. (F) unimolecular mixed structure with three parallel and one antiparallel strands 18

Figure 17 G-quadruplex π-stacking ligands.....20

Figure 18 (A) structure of distamycin A. (B) Side view representation of the 4:1 complex Dist-A/[d(TGGGGT)]$_4$. Intermolecular head to tail drug-drug NOE contacts are indicated with green dashed lines (*J. Am. Chem. Soc.* **2007**, *129*, 16048-16056)[60] 21

Figure 19 Dinuclear groove binder.....21

Figure 20 Central channel binding ligands 22

Figure 21 FRET for detecting DNA hybridization with fluorescence 23

Figure 22 Equation for measurement of binding constant.....25

Figure 23 (a) Constitution of the (*S*)-GNA and structure of the artificial bases. (b) Sequence of the duplexes.....30

Figure 24 Octahedral silicon as a non-classical structural template.....31

Figure 25 Structure of phosphoramidite building block **16** and **17**.....32

Figure 26 Constitution of the (*S*)-GNA and structure of the artificial bases 36

Figure 27 Structure of perylene bisimide phosphoramidite **16** and constitution of the (*S*)-GNA backbone. **B**:**H** base pair used in this study.....37

Figure 28 UV-melting curves of duplexes (from **GNA1** to **GNA8**). Changes in absorbance upon heating as monitored at 260 nm. Conditions: 10 mM sodium phosphate, 100 mM NaCl, pH 7.0, and 2 μM of each strand 40

Figure 29 UV-melting curves of duplexes (from **GNA9** to **GNA16**). Changes in absorbance upon heating as monitored at 260 nm. Conditions: 10 mM sodium phosphate, 100 mM NaCl, pH 7.0, and 2 μM of each strand 41

Figure 30 UV/Vis-absorption spectra of GNA duplexes and their corresponding single strands. Conditions: 10 mM sodium phosphate, 100 mM NaCl, pH 7.0, and 2 μM of each strand. (A) **ON6**:**ON7**, **ON6** and **ON7** at 20 ^{o}C. (B) **ON8**:**ON9**, **ON8** and **ON9** at 20 ^{o}C 42

Figure 31 UV/Vis-absorption spectra of GNA duplexes and their corresponding single strands at 20 ^{o}C (**ON10**:**ON11**, **ON10** and **ON11**). Conditions: 10 mM sodium phosphate, 100 mM NaCl 42

Figure 32 UV/Vis-absorption spectra of GNA duplexes and their corresponding single strands. Conditions: 10 mM sodium phosphate, 100 mM NaCl, pH 7.0, and 2 μM of each strand. (A) **ON13**:**ON14**, **ON13** and **ON14** at 20 ^{o}C. (B) **GNA9** temperature-dependent 43

Figure 33 UV/Vis-absorption spectra of GNA duplexes and their corresponding single strands at 20 ^{o}C. Conditions: 10 mM sodium phosphate, 100 mM NaCl, pH 7.0, and 2 μM of each strand. (A) **ON17**:**ON18**, **ON17** and **ON18**. (B) **ON19:ON20**, **ON19** and **ON20** 44

Figure 34 Temperature-dependent UV/Vis-absorption spectra of GNA duplexes. Conditions: 10 mM sodium phosphate, 100 mM NaCl, pH 7.0, and 2 μM of each strand. (A) **GNA13**. (B) **GNA14**. (C) **GNA15**. (D) **GNA16** 45

Figure 35 CD spectra of modified GNA duplexes and their corresponding single strands at 20 ^{o}C. Conditions: 10 mM sodium phosphate, 100 mM NaCl, pH 7.0, and 8 μM of each strand. **ON3**, **ON4** and **ON3:ON4** 46

Figure 36 CD spectra of modified GNA duplexes and their corresponding single strands at 20 ^{o}C. Conditions: 10 mM sodium phosphate, 100 mM NaCl, pH 7.0, and 8 μM of each strand. (A) **ON6**, **ON7** and **ON6:ON7** at 20 ^{o}C. (B) **ON8**, **ON9** and **ON8:ON9** 48

Figure 37 CD spectra of modified GNA duplexes and their corresponding single strands at 20 ^{o}C. Conditions: 10 mM sodium phosphate, 100 mM NaCl, pH 7.0, and 8 μM of each strand. (A) **ON13**, **ON14** and **ON13:ON14**. (B) **ON15**, **ON16** and **ON15:ON16** 48

Figure 38 Temperature-dependent CD spectra of modified GNA duplexes and their corresponding single strands. Conditions: 10 mM sodium phosphate, 100 mM NaCl, pH 7.0, and 8 μM of each strand. (A) **GNA13**. (B) **GNA14**. (C) **GNA15**. (D) **GNA16** 49

Figure 39 Structure of phthalocyanine phosphoramidite **17** and constitution of the (*S*)-GNA backbone. **Y**:**H** base pair used in this study.....51

Figure 40 UV-melting curves of duplexes (from **GNA17 to GNA23**). Changes in absorbance upon heating as monitored at 260 nm. Conditions: 10 mM sodium phosphate, 100 mM NaCl, pH 7.0, and 2 mM of each strand 53

Figure 41 UV/Vis-absorption spectra of GNA duplexes and their corresponding single strands. Conditions: 10 mM sodium phosphate, 100 mM NaCl, pH 7.0, and 2 μM of each strand. (A) **ON26**:**ON27**, **ON26** and **ON27** at 20 ^{o}C. (B) **GNA18** temperature-dependent. (C) **ON28**:**ON29**, **ON28** and **ON29** at 20 ^{o}C. (D) **GNA19** temperature-dependent 54

Figure 42 UV/Vis-absorption spectra of **GNA23**. Conditions: 10 mM sodium phosphate, pH 7.0, and 2 μM of each strand. (A) temperature dependence without salt. (B) temperature dependence in 10mM NaCl. (C) temperature dependence in 100mM NaCl. (D) NaCl concentration dependence at 20 ^{o}C.....55

Figure 43 UV/Vis-absorption spectra of **GNA23**. Conditions: 10 mM sodium phosphate, pH 7.0, and 1 μM of each strand. (A) temperature dependence without salt. (B) NaCl concentration dependence at 20 ^{o}C 56

Figure 44 UV-melting curves of duplexes (from **GNA24** to **GNA31**). Changes in absorbance upon heating as monitored at 260 nm. Conditions: 10 mM sodium phosphate, 100 mM NaCl, pH 7.0, and 2 μM of each strand 59

Figure 45 UV/Vis-absorption spectra of GNA duplexes and their corresponding single strands. Conditions: 10 mM sodium phosphate, 100 mM NaCl, pH 7.0, and 2 μM of each strand. (A) **ON37**, **ON04** and **ON37**:**ON04** at 20 ^{o}C. (B) **GNA24** temperature-dependent 60

Figure 46 UV/Vis-absorption spectra of GNA duplexes and their corresponding single strands. Conditions: 10 mM sodium phosphate, 100 mM NaCl, pH 7.0, and 2 μM of each strand. (A) **ON13**, **ON41** and **ON13**:**ON41** at 20 ^{o}C. (B) **GNA28** temperature-dependent. (C) **ON42**, **ON14** and **ON42**:**ON14** at 20 ^{o}C. (D) **GNA29** temperature-dependent 61

Figure 47 UV/Vis-absorption spectra of GNA duplexes and their corresponding single strands. Conditions: 10 mM sodium phosphate, 100 mM NaCl, pH 7.0, and 2 μM of each strand. (A) **ON43**, **ON16** and **ON43**:**ON16** at 20 °C. (B) **GNA46** temperature-dependent 62

Figure 48 CD spectra of modified GNA duplexes and their corresponding single strands. Conditions: 10 mM sodium phosphate, 100 mM NaCl, pH 7.0, and 12 μM of each strand at 20 °C. (A) **ON37**, **ON07** and **ON37:ON07**. (B) **ON06**, **ON38** and **ON06:ON38**. (C) **ON39**, **ON09** and **ON39:ON09**. (D) **ON08**, **ON40** and **ON08:ON40** 63

Figure 49 CD spectra of modified GNA duplexes and their corresponding single strands. Conditions: 10 mM sodium phosphate, 100 mM NaCl, pH 7.0, and 12 μM of each strand at 20 °C. (A) **ON13**, **ON41** and **ON13:ON41**. (B) **ON42**, **ON14** and **ON42:ON14**. (C) **ON43**, **ON16** and **ON43:ON16**. (D) **ON15**, **ON44** and **ON15:ON44** 64

Figure 50 UV-melting curves of duplexes (from **GNA32 to GNA39** (see Table 4 for the sequences)). Changes in absorbance upon heating as monitored at 260 nm. Conditions: 10 mM sodium phosphate, 100 mM NaCl, pH 7.0, and 2 μM of each strand 66

Figure 51 UV/Vis-absorption spectra of GNA duplexes and their corresponding single strands at 20 °C. Conditions: 10 mM sodium phosphate, 100 mM NaCl, pH 7.0, and 2 μM of each strand. (A) **ON36**, **ON27** and **ON36**:**ON27**. (B) **ON26**, **ON38** and **ON26**:**ON38** (C) **ON39**, **ON29** and **ON39**:**ON29** (D) **ON28**, **ON40** and **ON28**:**ON40** 68

Figure 52 UV/Vis-absorption spectra of GNA duplexes and their corresponding single strands. Conditions: 10 mM sodium phosphate, 100 mM NaCl, pH 7.0, and 2 μM of each strand. (A) **ON31**, **ON41** and **ON31**:**ON41** at 20 °C. (B) **GNA36** temperature-dependent. (C) **ON42**, **ON32** and **ON42**:**ON32** at 20 °C. (D) **GNA37** temperature-dependent. (E) **ON43**, **ON34** and **ON43**:**ON34** at 20 °C. (F) **GNA38** temperature-dependent. (G) **ON33**, **ON44** and **ON33**:**ON44** at 20 °C. (H) **GNA39** temperature-dependent 69

Figure 53 CD spectra of GNA duplexes and their corresponding single strands at 20 °C. Conditions: 10 mM sodium phosphate, 100 mM NaCl, pH 7.0, and 2 μM of each strand. (A) **ON36**, **ON27** and **ON36**:**ON27**. (B) **ON26**, **ON38** and **ON26**:**ON38**. (C) **ON39**, **ON29** and **ON39**:**ON29** (d) **ON28**, **ON40** and **ON28**:**ON40** 71

Figure 54 CD spectra of GNA duplexes and their corresponding single strands. Conditions: 10 mM sodium phosphate, 100 mM NaCl, pH 7.0, and 2 μM of each strand. (A) **ON31**, **ON41** and **ON31**:**ON41** at 20 °C. (B) **GNA36** temperature-dependent 71

Figure 55 UV-melting curves of duplexes (from **GNA24 to GNA31** (see Table 3 for the sequences)). Changes in absorbance upon heating as monitored at 260 nm. Conditions: 10 mM sodium phosphate, 100 mM NaCl, pH 7.0, and 2 mM of each strand 73

Figure 56 UV/Vis-absorption spectra of GNA duplexes and their corresponding single strands. Conditions: 10 mM sodium phosphate, 100 mM NaCl, pH 7.0, and 2 μM of each strand. (A) **ON06**, **ON27** and **ON06**:**ON27** at 20 °C. (B) **GNA40** temperature-dependent. (C) **ON26**, **ON07** and **ON26**:**ON07** at 20 °C. (D) **GNA41** temperature-dependent. (E) **ON08**, **ON29** and **ON08**:**ON29** at 20 °C. (F) **GNA42** temperature-dependent. (G) **ON28**, **ON09** and **ON28**:**ON09** at 20 °C. (H) **GNA43** temperature-dependent 76

Figure 57 UV/Vis-absorption spectra of GNA duplexes and their corresponding single strands. Conditions: 10 mM sodium phosphate, 100 mM NaCl, pH 7.0, and 2 μM of each strand. (A) **ON31**, **ON14** and **ON31**:**ON14** at 20 °C. (B) **GNA44** temperature-dependent. (C) **ON13**, **ON32** and **ON13**:**ON32** at 20 °C. (D) **GNA45** temperature-dependent. (E) **ON15**, **ON34** and **ON15**:**ON34** at 20 °C. (F) **GNA46** temperature-dependent. (G) **ON33**, **ON16** and **ON28**:**ON09** at 20 °C. (H) **GNA47** temperature-dependent 77

Figure 58 CD spectra of modified GNA duplexes and their corresponding single strands at 20 °C. Conditions: 10 mM sodium phosphate, 100 mM NaCl, pH 7.0, and 12 μM of each strand. (A) **ON06**, **ON27** and **ON06**:**ON27** at 20 °C. (B) **GNA24** temperature-dependent 78

Figure 59 CD spectra of modified GNA duplexes and their corresponding single strands. Conditions: 10 mM sodium phosphate, 100 mM NaCl, pH 7.0, and 12 μM of each strand. (A) **ON31**, **ON14** and **ON31**:**ON14** at 20 °C. (B) **GNA44** temperature-dependent. (C) **ON13**, **ON32** and **ON13**:**ON32** at 20 °C. (D) **ON31**, **ON14** and **ON31**:**ON14** at 20 °C. (E) **ON33**, **ON16** and **ON33**:**ON16** at 20 °C.....79

Figure 60 Crystal structure of the silicon 9, 10-phenanthrenediolate complex **48**. ORTEP representation with 50% thermal ellipsoids. Counterions and solvent molecules are omitted for clarity. Selected bond distances (Å) and angles (°): N1-Si1

1.956(2), N4-Si1 1.926(2), N15-Si1 1.947(2), N18-Si1 1.923(2), O1-Si1 1.7081(19), O2-Si1 1.7172(19); O1-Si1-N18 93.28(9), O1-Si1-N4 92.98(9), O1-Si1-N15 175.42(10), O1-Si1-N1 88.55(9), N15-Si1-N1 89.13(9).....83

Figure 61 Hydrolytic stability of complex **48** at room temperature in CD_3CN/D_2O 5:1 84

Figure 62 UV-melting curves of duplex DNA 5′-AGTGCCAAGCTTGCA-3′/3′ -TCACGGTT CGAACGT-5′. Changes in absorbance upon heating as monitored at 260 nm. Conditions: 5 mM Tris-HCl, 50 mM NaCl, pH 7.4, and 2 μM of each strand in the presence of different concentration of 9, 10-phenanthrenediolate **48** 88

Figure 63 UV-melting curves of duplex DNA 5′-AGTGCCAAGCTTGCA-3′/3′ -TCACGGTT CGAACGT-5′. Changes in absorbance upon heating as monitored at 260 nm. Conditions: 5 mM Tris-HCl, 50 mM NaCl, pH 7.4, and 2 μM of each strand in the presence of 8 μM $[Si(Phen)_2(arenediolate)]^{2+}$ (**46**–**51**).....88

Figure 64 UV-melting curves of duplex DNA 5′-AGTGCCAAGCTTGCA-3′/3′ -TCACGGTT CGAACGT-5′. Changes in absorbance upon heating as monitored at 260 nm. Conditions: 5 mM Tris-HCl, 50 mM NaCl, pH 7.4, and 2 μM of each strand in the presence of 8 μM $[Si(Phen)_2(arenediolate)]^{2+}$ (A) Complex **42** and complex **48**. (B) Complex **43** and complex **49** 89

Figure 65 CD spectra of duplex DNA 5′-AGTGCCAAGCTTGCA-3′/3′-TCACGGTTCGAACGT-5′ titrated with increasing amounts of complexes. Conditions: 5 mM Tris-HCl, 50 mM NaCl, pH 7.4 and 20 μM duplex. (A) 9, 10-phenanthrenediolate **48** (0–120 μM). (B) 4, 5-pyrenediolate complex **51** (0–180 μM) 91

Figure 66 HPLC trace for racemic silicon complex **48** (Measurement carried out by Chen Fu from Meggers group).....91

Figure 67 HPLC trace for enantiomer A of complex **48**. Integration of peak areas: 94.8:5.2 e.r.; **B**) HPLC trace for enantiomer B of complex **48**. Integration of peak areas: 5.8:94.2 e.r. (Measurement carried out by Chen Fu from Meggers Group).....91

Figure 68 CD spectra of the two enantiomers of **48**. Conditions: 5 mM Tris-HCl, 50 mM NaCl, pH 7.4 and 20 μM enantiomer. Based on these CD spectra, enantiomer A is assigned the absolute configuration Λ and enantiomer B is assigned as Δ[91] 92

Figure 69 CD spectra of the racemic **48** and the two enantiomers of **48** in the presence of DNA. Conditions: 5 mM Tris-HCl, 50 mM NaCl, pH 7.4, 20 μM duplex and 40 μM racemic **48** or enantiomers of **48**. The CD spectra of the duplex DNA (5′-AGTGCCAAGCTTGCA-3′/3′-TCACGGTTCGAACGT-5′) alone and the sum of the CD spectra of the individual enantiomers in the presence of DNA are given for comparison 92

Figure 70 UV/Vis-absorption spectra of 4, 5-pyrenediolate complex **51** titrated with increasing amounts of calf thymus DNA (0-200 μM). Conditions: 5 mM Tris-HCl, 20 mM NaCl, pH 7.5 and 20 μM complex. Insert: Plot of $(\varepsilon_a-\varepsilon_f)/(\varepsilon_b-\varepsilon_f)$ *versus* increasing DNA concentration, with ε_a = extinction coefficient of the complex at a given DNA concentration, ε_b = extinction coefficient when fully bound to DNA, and ε_f = extinction coefficient of the complex in the absence of DNA. (Measurement carried out by Dr. Pijus Sasmal from Meggers Group) 93

Figure 71 UV-melting curves of duplex DNA 5′-AGTGCCAAGCTTGCA-3′/3′ -TCACGGTT CGAACGT-5′. Changes in absorbance upon heating as monitored at 260 nm. Conditions: 5 mM Tris-HCl, 50 mM NaCl, pH 7.4, and 2 μM of each strand in the presence of 8 μM $[Si(Phen)_2(arenediolate)]^{2+}$ (**77**-**86**).....96

Figure 72 UV/Vis-absorption spectra of phenazinediolate complexes titrated with increasing amounts of calf thymus DNA. Conditions: 5 mM Tris-HCl, 20 mM NaCl, pH 7.5 and 20 μM complexes. (A) Complex **77**. (B) Complex **78**. (C) Complex **80**. (D) Complex **81** 97

Figure 73 UV/Vis-absorption spectra of Benzo[*a*]quinoxalino[2,3-*c*]phenazinediolate complex **79** titrated with increasing amounts of calf thymus DNA (0-200 μM). Conditions: 5 mM Tris-HCl, 20 mM NaCl, pH 7.5 and 20 μM complexes. Insert: Plot of $(\varepsilon_a-\varepsilon_f)/(\varepsilon_b-\varepsilon_f)$ *versus* increasing DNA concentration, with ε_a = extinction coefficient of the complex at a given DNA concentration, ε_b = extinction coefficient when fully bound to DNA, and ε_f = coefficient of the complex in the absence of DNA 98

Figure 74 CD spectra of matched and C-C mismatched DNA duplexes titrated with increasing amounts of rhodium complexes. Conditions: 5 mM Tris-HCl, 50 mM NaCl, pH 7.4 and 20 μM duplex. (A) Matched DNA with complex **87** (0–80 μM). (B) C-C

mismatched DNA with complex **87** (0–80 μM) (C) Matched DNA with complex **88** (0–80 μM). (D) C-C mismatched DNA with complex **88** (0–80 μM) 101

Figure 75 CD spectra of matched and C-C mismatched DNA duplexes titrated with increasing amounts of silicon complexes. Conditions: 5 mM Tris-HCl, 50 mM NaCl, pH 7.4 and 20 μM duplex. (A) Matched DNA with complex **42** (0–80 μM). (B) C-C mismatched DNA with complex **42** (0–80 μM) (C) Matched DNA with complex **44** (0–80 μM). (D) C-C mismatched DNA with Complex **44** (0–80 μM) 102

Figure 76 CD spectra of C-C mismatched DNA duplex titrated with increasing amounts of silicon complexes. Conditions: 5 mM Tris-HCl, 50 mM NaCl, pH 7.4 and 20 μM duplex. (A) C-C matched DNA with Complex **49** (0–80 μM). (B) C-C mismatched DNA with racemic complex **48** (0–80 μM) (C) C-C matched DNA with enantiomer complex **48-A** (0–80 μM). (D) C-C mismatched DNA with enantiomer complex **48-B** (0–80 μM) 103

Figure 77 CD spectra of the G-quadruplex $(T_2AG_3)_4$ titrated with increasing amounts of complexes $[Si(bpy)_2(phenazinediolte)]^{2+}$. Conditions: 5 mM Tris-HCl. 12.5 μM G-quadruplex and *r* values from 0 to 4. (*r* = [silicon complex]/$[(T_2AG_3)_4]$). (A) Complex **77**. (B) Complex **78.** (C) Complex **79**. (D) Complex **80**. (E) Complex **81** 105

Figure 78 CD spectra of the G-quadruplex $(T_2AG_3)_4$ titrated with increasing amounts of complexes $[Si(bpy)_2(phenazinediolte)]^{2+}$. Conditions: 5 mM Tris-HCl. 12.5 μM G-quadruplex and *r* values from 0 to 4. (*r* = [silicon complex]/$[(T_2AG_3)_4]$). (A) Complex **82**. (B) Complex **83**. (C) Complex **84**. (D) Complex **85**. (E) Complex **86** 107

Figure 79 UV/Vis-absorption spectra of Silicon complexes titrated with increasing amounts of G-quadruplex. Conditions: 5 mM Tris-HCl, 20 mM NaCl, pH 7.5 and 20 μM complexes. (**A**) Complex **78**. (**B**) Complex **79**. (**C**) Complex **80**. (**D**) Complex **81**. Insert: Plot of $(\varepsilon_a-\varepsilon_f)/(\varepsilon_b-\varepsilon_f)$ *versus* increasing DNA concentration, with ε_a = extinction coefficient of the complex at a given DNA concentration, ε_b = extinction coefficient when fully bound to DNA, and ε_f = extinction coefficient of the complex in the absence of DNA 109

Figure 80 CD melting curves of DNA oligonucleotides $(T_2AG_3)_4$. Changes in cotton effect upon heating as monitored at 295 nm. Conditions: 10 mM Tris–HCl, 100 mM NaCl, pH 7.4, 12.5 μM DNA, and concentration ratio of complex/DNA (*r*) is 5:1 ..109

Figure 81 ABI 392 Solid Phase Synthesizer 131

Figure 82 Hydrolytic stability of complex **42** at room temperature in CD_3CN/D_2O 5:1 156

Figure 83 Hydrolytic stability of complex **46** at room temperature in CD_3CN/D_2O 5:1 156

Figure 84 Hydrolytic stability of complex **46** at room temperature in 1:1 DMSO/buffer (10 mM sodium phosphate, 20 mM NaCl, pH 7.0) 157

Figure 85 Hydrolytic stability of complex **46** at room temperature in in 1:1 $DMSO/D_2O$ with 5 mM β-mercaptoethanol.....157

Figure 86 Hydrolytic stability of complex **46** at 40 ^oC in CD_3CN/D_2O 1:1 158

Figure 87 Hydrolytic stability of complex **47** at room temperature in CD_3CN/D_2O 5:1 158

Figure 88 Crystal structure of silicon complex **42**. ORTEP representation with 50% thermal ellipsoids. Two hexafluorophosphate counterions and three acetonitrile solvent molecules are omitted for clarity.....179

Figure 89 Crystal structure of silicon complex **48**. ORTEP representation with 50% thermal ellipsoids. Two hexafluorophosphate counterions and three acetonitrile solvent molecules are omitted for clarity.....182

Chapter 1 Theoretical part

1.1 Nucleic Acid-Assisted Multichromophore Assemblies

1.1.1 Properties of multichromophores

Chromophores play important roles as imaging tools in the life sciences and as components of industrial dyes and pigments.[1] The field of multichromophoric systems has attracted more and more interest.[2] Compared to the monochromophore, multichromophores arrayed in close proximity will result in many advantageous properties. First, the collective absorption is higher, and this is very useful in the application of light harvesting in solar cells.[3] Second, photophysical properties are also different from the monochromophore. Dimer and exciplexes form as a result of the interaction between chromophores in the ground state and the excited state.[1a] Third, different geometric and directional control of the assembly will lead to diverse and useful properties of multiple chromophoric systems.[4]

There are two methods to assemble multichromophore arrays. One is covalent assembly through a synthetic approach; however, this method is not easily applied. The other is self-assembly through intrinsic non-covalent interactions: van der waals forces, dipole interactions, and hydrophobic interactions. These kinds of interactions make the formation of large numbers of chromophoric arrays feasible. However, arranging them in the desired way is also very challenging.

Würthner *et al*. have made many investigations into self-assembled π-stacks of functional dyes in solutions.[5] They compared the binding strength of different classes of functional π-conjugated systems: benzene, triphenylenes, hexabenzocoronenes, heteroaromatic porphyrins, phthalocyanines, quadrupolar naphthalene, perylene bisimides, zwitterionic merocyanines, and squaraines. In addition to the main factors of electrostatic interactions, the size and geometry of the dyes that determine the binding strength, as well as the solution have a great impact on the binding strength.

They found out that the highest binding constants in the following order: merocyanine (8.0×10^8 M^{-1} in dioxane) ≈ perylene bisimide > phthalocyanine (10^6 M^{-1}) > phenylacetylene macrocycles (PAMs, (10^4 M^{-1})) ≈ hexabenzocoronenes (HBCs) > naphthalene bisimide (10^2 M^{-1}) > porphyrin ≈ naphthalene > benzene.

1.1.2 DNA-templated multichromophore systems

For the past several decades, scientists have been searching for methods to assemble molecules and materials with nanometer scale precision. There are two basic types of nanotechnological construction: "top-down" often uses traditional workshop or microfabrication methods to fashion elegant patterns with small numbers of atoms or molecules, while the "bottom-up" approach uses the chemical properties of single molecules to cause self-assembly in parallel steps. Natural systems have developed their own "bottom-up" way to organize complex architectures with sophisticated functions. DNA is a fascinating example of self-assembly, and has emerged as a promising scaffold for generating functional materials in the bottom-up approach because of its inherent merits. 1) self-assembly: canonical Watson-Crick base pairing into duplex; 2) the structure of B-DNA is a predictable topology, its diameter and helical repeat is 2.0 nm and 3.4 nm, respectively, making it ideal for the hydrophobic and photophysical interaction of chromophores; 3) modern development of automated oligonucleotide chemistry makes it possible to realize the modifications and the functionalization of DNA.

Supramolecular chemistry is an important and mature research area that has significantly contributed to the bottom-up construction. It mainly consists of synthetic organic and inorganic molecules that assemble into remarkably diverse architectures.[6] All functional components of molecules still possess intrinsic special properties, such as redox, photophysical, magnetic, and catalytic characteristics, which allow for the rational design of complicated functions into the assemblies. If some functional organic or inorganic molecules are incorporated into DNA, it will bear completely

new structural motifs and impart functional properties. By adding the DNA to its toolbox, the field of supramolecular chemistry will assemble complicated new structures in a programmable pattern. Many achievements have been made regarding DNA with synthetic insertions, such as using synthetic vertices to bring a higher order to the DNA structure and boosting its complexity with branched junctions.[7]

Based on the properties of DNA and organic chromophores, our main focus here is on the DNA-multichromophore systems. These kinds of systems have gained more and more attention. They can harness the DNA phosphodiester backbone as a scaffold for arraying chromophores, and be utilized in the fields of fluorescent nucleic acid probes, nonenzymatic fluorophore systems, molecular beacons, DNA microarrays, DNA nanotechnology, photonic wires, and DNA sensor device.[2, 8]

Generally, there are three methods to functionalize DNA: modifications of the inter-nucleoside phosphate residue, the nucleoside unit, or the DNA terminus. Based on these strategies, chromophores could be incorporated into DNA at precise sites by following three main aspects: (A) DNA terminal modification; (B) DNA internal modification; (C) DNA external modification.

i. DNA terminal modification

Chromophores could be covalently linked to the DNA terminus through direct oligonucleotide synthesis, post-DNA synthesis, or combined approaches. For example, porphyrin and perylene bisimide (**PBI**) have been successfully incorporated into the 5′-terminal of the DNA via direct reaction of a phosphitylated modifier with the 5′-position of the ribose moiety (Figure 1A and Figure 1B).[9] On the other hand, anthracene could be introduced into the 5′-terminal of DNA through post-DNA synthesis (Figure 1C and Figure 1D).[10]

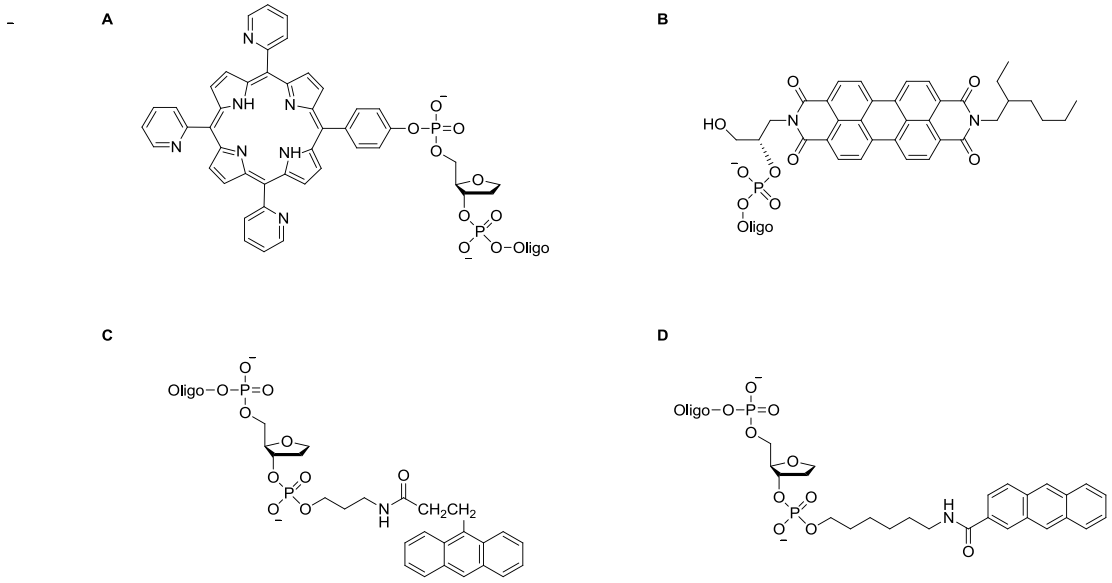

Figure 1 Examples of DNA terminal modification with chromophores

The terminal modification of DNA with chromophores may be used as promising material in the field of nanotechnology. Lewis et al. studied the structure and properties of hairpin-forming bis(oligonucleotide) conjugates possessing perylene bisimide (**PBI**). However, these conjugates predominantly exist as monomers at room temperature in the absence of NaCl; when the concentration of NaCl reaches 50 mM, the head-to-head dimer becomes dominant (Figure 2A). The monomer-dimer equilibrium is found to be dependent upon temperature and the concentration of NaCl.[11] They then continued to design novel DNA dumbbell conjugates containing hydrophobic **PBI** separated by eight-base pairs. In an aqueous buffer containing 100 mM NaCl, self-assembly of 10-30 dumbbell monomers will conjugate into supramolecular polymers and larger branched aggregates (Figure 2B).[12] A recent study by Wagenknecht et al. shows that **PBI** could be incorporated as caps onto a Y-shaped DNA triple strand. Triangular DNA assembles spontaneously through the stacking interaction of **PBI**. The aggregates will be destroyed by thermal dehybridization of the DNA scaffold and assemble back by reannealing of the DNA.[13]

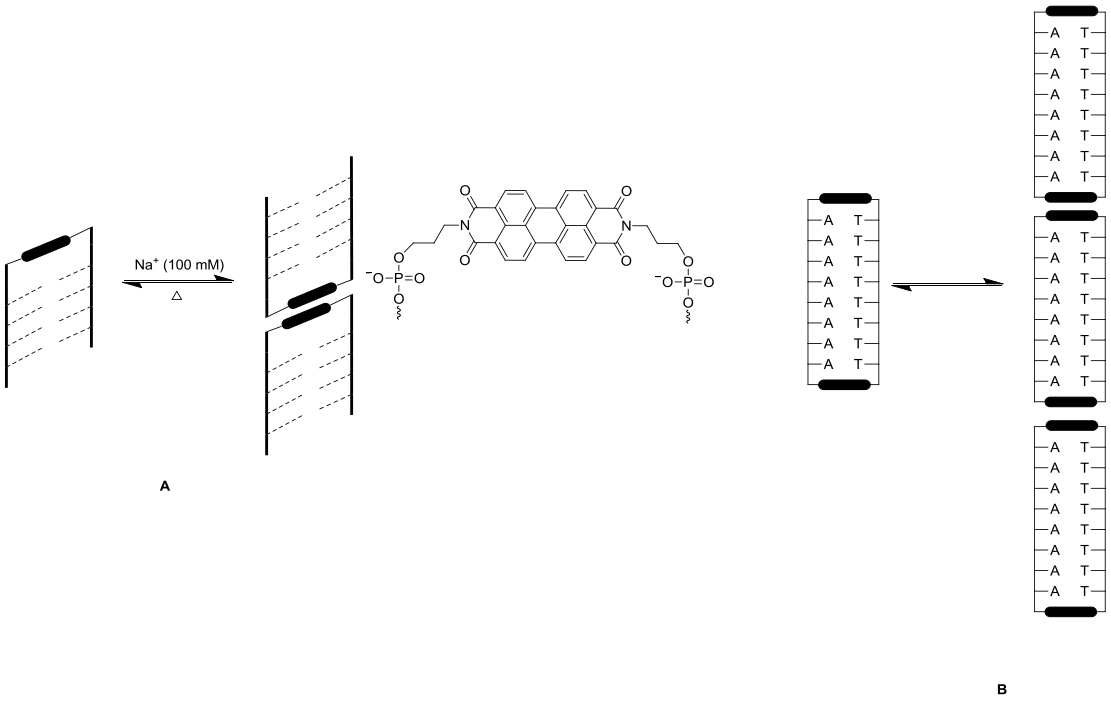

Figure 2 Structures for the base-paired hairpin oligonucleotides

In addition, terminal modification could be employed to design sensitive electronic sensors of analytes[14] and monitor DNA structural changes.[15]

ii. DNA internal modification (backbone modification)

The chromophores could also be introduced into the internal sites of DNA covalently with four natural nucleobases replaced or modified by chromophores.

A number of deoxyribonucleosides based on C-nucleosides have been synthesized and successfully introduced into the internal site of DNA, such as Kool introduced naphthalene, anthracene, pyrene, and porphyrin into DNA (Figure 3A), where the natural nucleobases are replaced by chromophores.[16]

The aromatic nature of chromophores is crucial in forming a stable duplex via π-π stacking. Therefore, chromophores can be designed as artificial nucleobases to stack on one another in a zipper-like fashion (Figure 3B). Wagenknecht et al. synthetically incorporated **PBI** into oligonucleotides by using automated DNA building-block chemistry. The 2′-deoxyribofuranoside was replaced by (*S*)-aminopropan- 2, 3-diol as an acyclic linker, which was tethered to the **PBI** chromophores. Up to six **PBI** were incorporated in the middle of 18-mer DNA

duplexes in the form of zipper-like interstrand stacking; however, only the duplex bearing interstrand dimer inside the duplex revealed a slight stabilization relative to fully unmodified DNA. One or more than two **PBI** in the duplex will destabilize the DNA.[9c, 17]

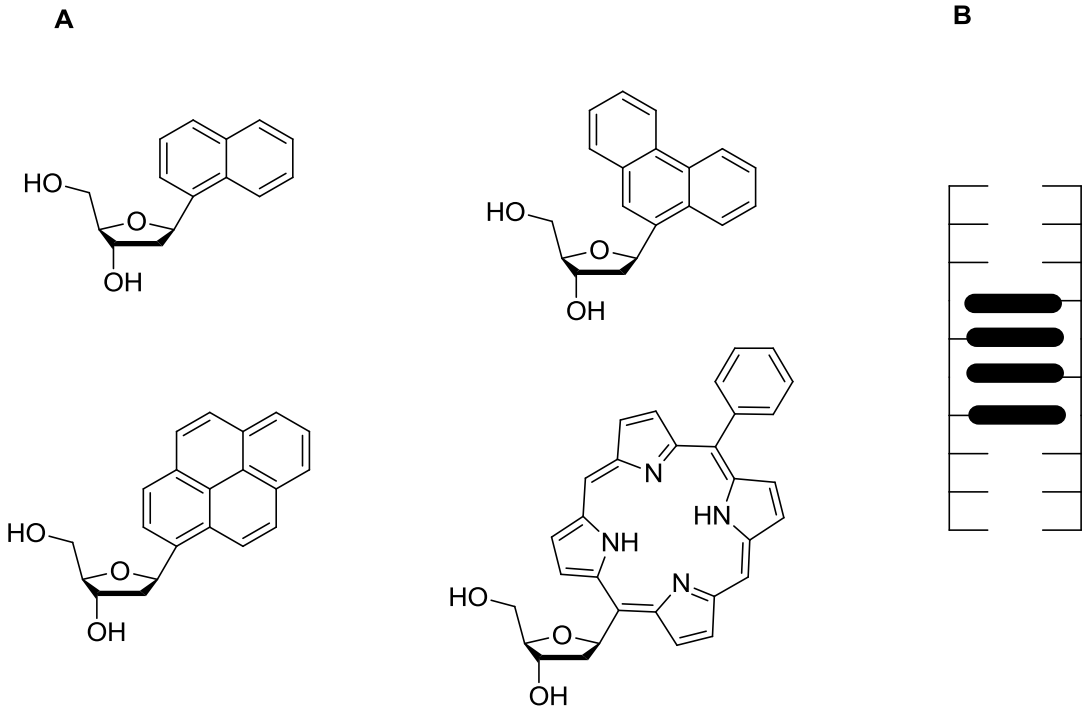

Figure 3 (A) Examples of DNA base replacements with chromophores. (B) Schematic representation of zipper-like interstrand stacking within the DNA duplex

iii. DNA external modification

DNA provides an ideal scaffold for introducing chromophores to the outer rim of the DNA and forms a helical array upon duplex hybridization. The incorporation of the chromophores in the grooves of the DNA helix is referred to as external modification.[18] Modification at the 5′-position of pyrimidine (Figure 4A) and replacement purine with 7′-deazapurines (Figure 4B) are typical methods to incorporate chromophores into DNA. The advantage of external modification with chromophores along the DNA helix is that the canonical Watson-Crick base-pairing property will not change significantly.

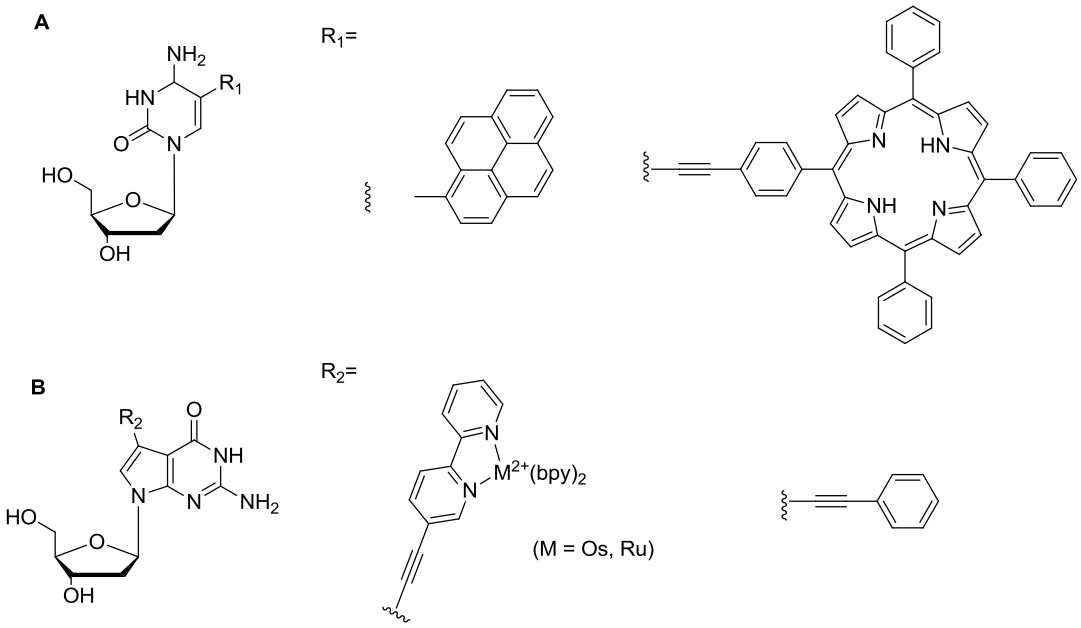

Figure 4 DNA natural base modification with chromophores

Up to 11 tetraphenyl porphyrin-modified deoxyuridine were incorporated into DNA by Stulz to form discrete multiporphyrin arrays via site specific incorporation. It also seems that there is no limitation in the amount of the chromophores, and scale of the porphyrin arrays could reach about 10 nm (Figure 5).[19]

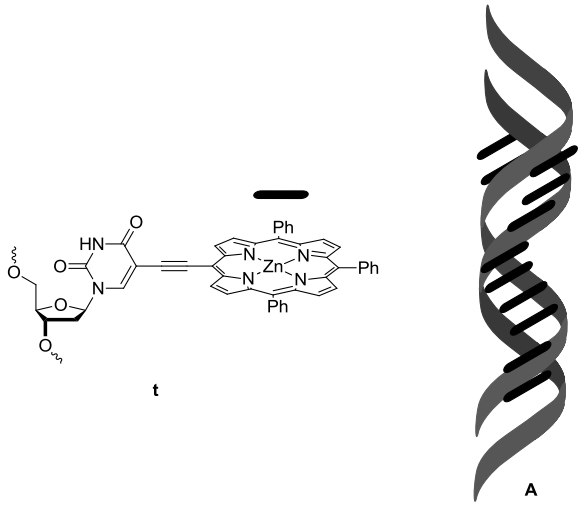

Figure 5 Side and top view of the force-field minimized structures of the duplexes

Overall, covalent modification of DNA with chromophores at the desired sites could be achieved in three strategies, and the incorporation of chromophores will functionalize DNA with novel properties.

1.1.3 GNA-templated multichromophore systems

Chemical synthesis of oligonucleotides from nucleoside phosphoramidites and non-nucleoside phosphoramidites are carried out by automated solid phase synthesis. However, due to the stereocenters in the deoxyribose moiety, and especially the anomeric C1′-stereocenter, the chemical synthesis of the modified nucleotide building blocks is often tedious and lengthy, and includes the chromatographic separation of diastereomers, and therefore proves challenging to scale-up. Consequently, the chemical synthesis of modified nucleotides is a critical bottleneck for progress in this and related areas of research.

As a result, Meggers et al. developed glycol nucleic acid (GNA) consisting of a simplified acyclic propylene glycol phosphodiester backbone. GNA can also form stable antiparallel duplexes in a Watson-Crick fashion.[20] Moreover, it combines atomic economy, structural simplicity, and high duplex stability (Figure 6).

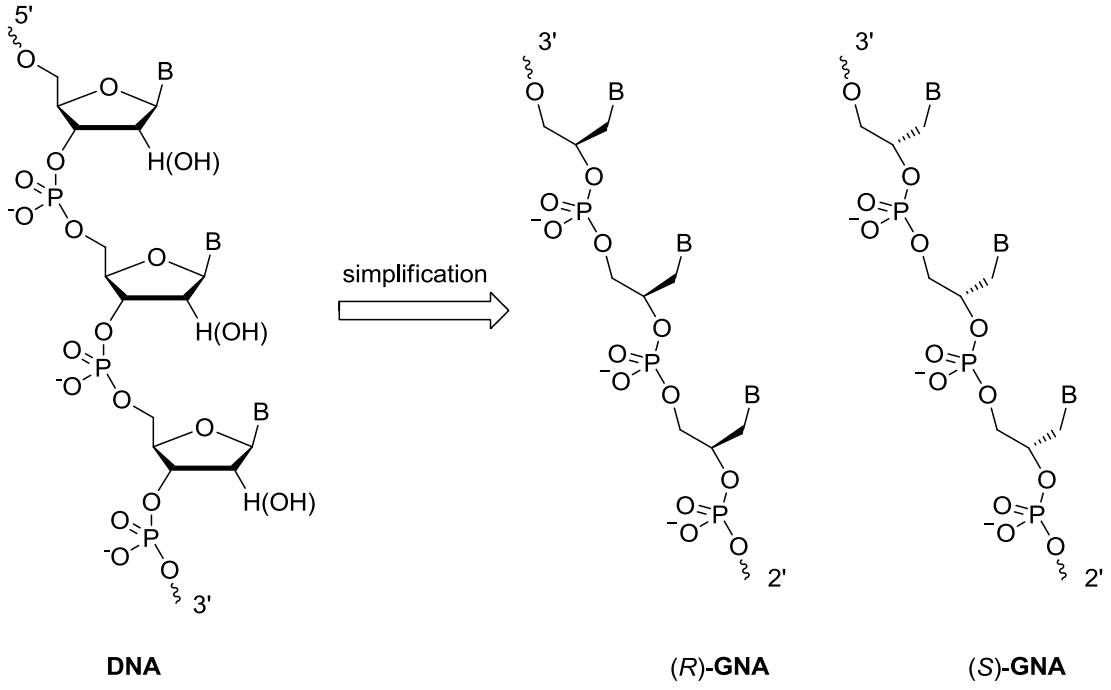

Figure 6 Constitutions of DNA, RNA, and *S*- and *R*-enantiomers of GNA

Similar to DNA and RNA, the homoduplex formation of GNA relies on Watson-Crick base pairing, with antiparallel strand complementarity and a 1:1 strand

stoichiometry. (*R*)-GNA and (*S*)-GNA do not significantly cross-pair with each other, either in a parallel or antiparallel manner.[20b, 21] Compared to corresponding DNA and RNA, GNA displayed higher thermal stability. For example, T_m of the GNA sequence 3′-TAAAATTTATATTATTAA-2′/2′-ATTTTAAATATAATAATT-3′ is 63.0 ℃, while T_M of analogous DNA and RNA is 40.5 ℃ and 42.5 ℃, respectively.

In addition to the high thermal stability, the chemical synthesis of glycol nucleoside phosphoramidites starting from glycidol is rather easy, and the synthesis route of dimethoxytritylated glycol nucleoside phosphoramidites of adenine (A), thymine (T), uracil (U), guanine (G), and cytosine (C) are simply described in scheme 1; all these nucleoside phosphoramidites could be obtained in several steps with an easy purification process.[22]

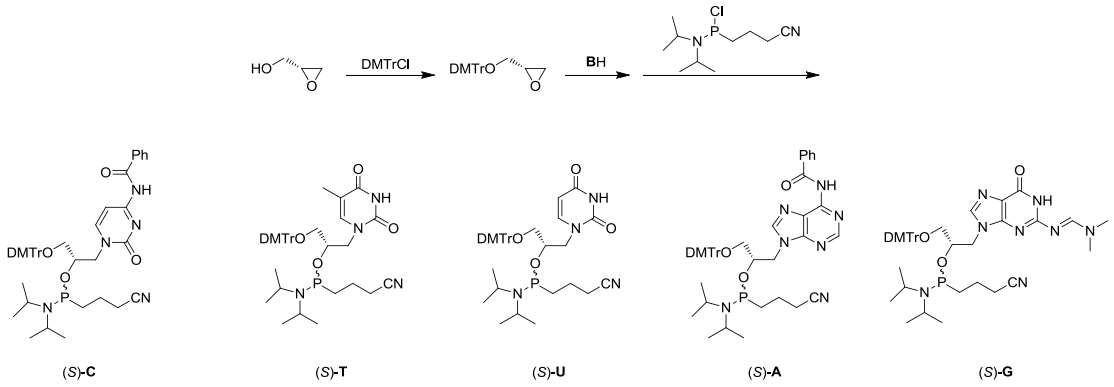

Scheme 1 General synthesis of dimethoxytritylated glycol nucleoside phosphoramidites of adenine (A), thymine (T), uracil (U), guanine (G), and cytosine (C) for the synthesis of GNA oligonucleotide (**B** represents a natural base or artificial base)

The atomic resolution structure of the self-complementary (*S*)-GNA strand 3′-G^{Br}CGCGC-2′ demonstrates that the GNA helix possesses only one large groove, whereas the canonical major groove is a convex surface. Hence, the double helix of GNA is significantly different from canonical A- and B- form nucleic acids, and may be best described as a helical ribbon loosely wrapped around the helix axis.[21]

The advantage of the high stability and easy synthesis makes GNA a potential scaffold for functional nucleic acid based nanostructures. Meggers et al. have investigated the functionalization of GNA by incorporating artificial nucleotides into

GNA oligonucleotides. A copper(II)-mediated hydroxypyridone homobase pair (**M**-Cu-**M**) and a nickel(II)-mediated pyridylpurine homobase pair (**P**-Ni-**P**), which were developed in DNA, were successfully incorporated into GNA (Figure 7).[23]

The study of metal ion-dependent duplex stabilities reveals that the pyridylpurine base pair displays a preference for Ni^{2+} ions (ΔT_m = +17.9 ℃ with two equivalents of $NiCl_2$), and the hydroxypyridone base pair is stabilized most strongly with Cu^{2+} ions (ΔT_m = +33.2 ℃ with two equivalents of $CuSO_4$).[23c] The crystal structure of an (*S*)-GNA duplex from the self-complementary strand 3′-CG**M**AT**M**CG-2′ in the presence of copper ions has been obtained. [24] Moreover, the metal-mediated cross-pairing of the hydroxypyridone and pyridylpurine chelates was also investigated in GNA duplexes, and the addition of two equivalents of $CuSO_4$ resulted in an increase of the T_m value of the GNA duplex by 37.1 °C. This indicates that metal-ion-mediated base pairing is well-accommodated in the GNA duplex.

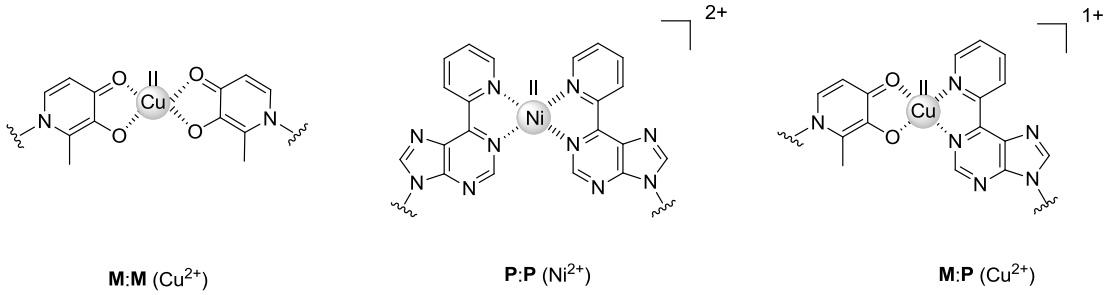

Figure 7 Metallo-base pairs investigated in GNA containing hydroxypyridone (**H**) and pyridylpurine (**P**) homo- and heterobase

In our group, chromophores have been successfully introduced into GNA as artificial bases.[25] We found that the interstrand pyrene acetylide excimer formation could be used to monitor GNA duplex formation, and applied to the design of a copper(II)-selective "turn-on" fluorescence sensor. In the absence of the copper ion, the GNA duplex 3'-TATAPyr'HTAA**M**TAAA-2'/2'-ATATHPyr'ATT**M**ATTT-3' is strongly destabilized and doesn't show any cooperative melting behavior, and regular emission of fluorescence exclusively at approximately 400 nm is observed. After one equivalent of copper ion is added, the duplex will show a melting point at 50 °C and

the excimer emission of fluorescence appears at approximately 500 nm. However, other metal ions, such as Ni^{2+}, Co^{2+}, Zn^{2+}, Cd^{2+}, Mn^{2+} or $Fe^{2/3+}$, do not show any effect (Figure 8).[25b]

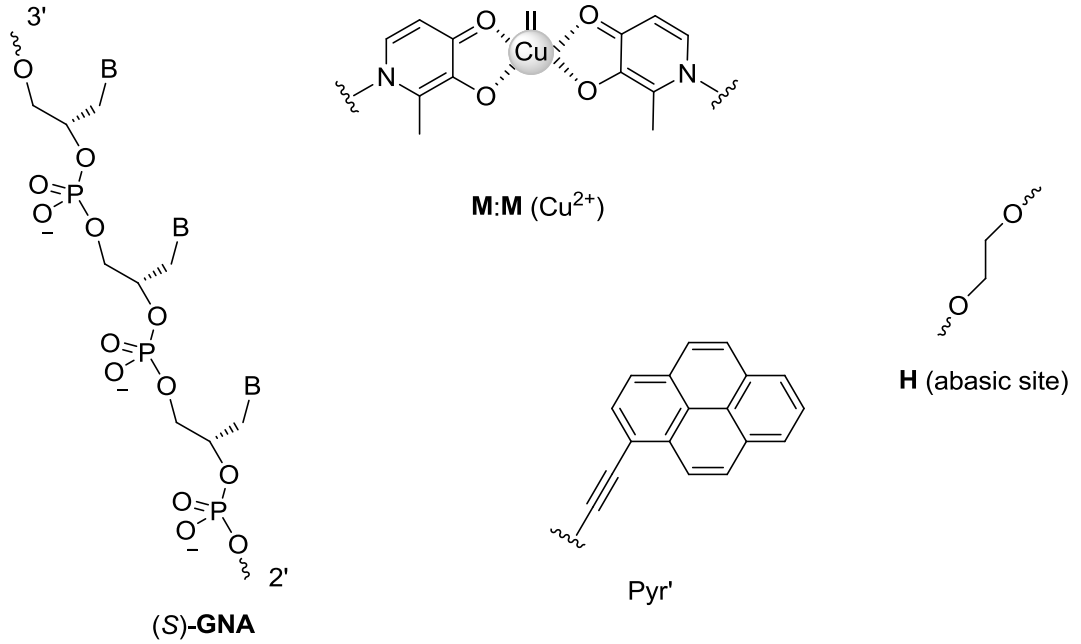

Figure 8 Constitution of (*S*)-GNA and the base pairs modified with hydroxypyridone and pyrene

The GNA duplex could also be a suitable scaffold for bringing two porphyrin chromophores into close contact and to enable the interaction of porphyrins. The duplex displays lower thermal stability, and the situation will change in the presence of a metal ion. Incorporation of Zn^{2+} will further destabilize the duplex, and Ni^{2+} will stabilize it relative to the uncomplexed porphyrin. The properties of these kinds of GNA duplexes modified with chromophores make it possible for the design of photoelectronic devices.[26]

Based on these fascinating features of GNA and chromophores, functional GNA architectures with chromophores are expected to be applied in nanotechnology.

1.2 Metal Complexes as Nucleic Acid Binders

1.2.1 DNA duplex binders

The dogma of molecular biology was introduced about 55 years ago.[27] Along with RNA and proteins, DNA is one of the three macromolecules that play a crucial role in life forms. DNA sequencing encodes information that could be read through the genetic code, and then transcribed and translated into the synthesis of proteins. Concomitant with our increasing knowledge of the structure and biological role of nucleic acids, developing small molecules that can regulate DNA and RNA functioning have attracted enormous attention. According to the traditional method, significant effort has been devoted to synthesizing organic molecules that can target specific DNA and RNA sequences.[28] However, Dwyer[29], Lippard[30], Nordén[31] and Barton[32] found that transition metal complexes could also be used as nucleic acid binding agents. Compared to the traditional small molecules, transitional metal complexes possess two advantages. First, the metal center acts like an anchor and three-dimensional scaffold of ligands that can bear recognition elements. Second, many transition complexes bear rich photophysical and electrochemical properties. As a result, these characteristics can be widely utilized, such as for fluorescence and electrochemical probes.[33] Accordingly, the study of transition metal complexes binding to DNA has been a burgeoning field.

Before we discuss the DNA binding, the different forms of DNA should be reviewed. The anti-parallel right-handed double helix B-DNA is the most common, and the right-handed A-DNA and left-handed Z-DNA are less common. It comprises two helical chains, each coiled round the same axis with the 3.4 Å rise base pair, with ten base pairs per helical turn. The polyanionic sugar-phosphate backbone forms two different grooves; one is called the major groove, and the other is regarded as the minor groove. Non-covalent metal complexes can bind DNA in three different types: groove binding, intercalation, and insertion (Figure 9).[34] Groove binding means that

the metal complex approaches within van der waals contact and resides in the DNA groove. The intercalation involves the insertion of a planar-fused aromatic ring between the DNA base pairs, and metallo-insertors bearing the aromatic ligands that perform like replacements of the DNA base stake can eject a single base pair.

Figure 9 The three binding modes of metal complexes with B-DNA: (A) groove binding. (B) intercalation, and (C) insertion. (This figure from Chem. Commun. 2007, 4565-4579)[34]

Metallo-intercalators

Two main classes of metal complexes that can intercalate into DNA are relatively inert square-planar Pt(II) complexes and octahedral metal complexes with aromatic ligands.

In 1973, Lippard first observed that $[(terpy)Pt(HET)]^{+}$ (terpy = 2,2 ΄6 ΄2 ΄΄-terpyridine, HET = 2-hydroxyethanethiolate) could bind strongly to DNA, indicating that the square-planar platinum complexes completely inhibited the binding of the intercalating dye, ethidium bromide, to calf thymus DNA by using fluorescence spectroscopy. The complex increased the melting point and exhibited induced CD of the DNA.[30] He continued to report that the platinum complexes with other heterocyclic aromatic ligands, such as quaterpyridine, 1,10-phenantroline, and 2,2 ΄-bipyridine, also bound to DNA duplexes through intercalating between the base pairs (Figure 10),[35] and the crystal structure of DNA in the presence of $[Pt(terpy)(HET)]^{+}$ confirmed that the flat metal cation intercalated symmetrically between two Watson-Crick GC base pairs.[36]

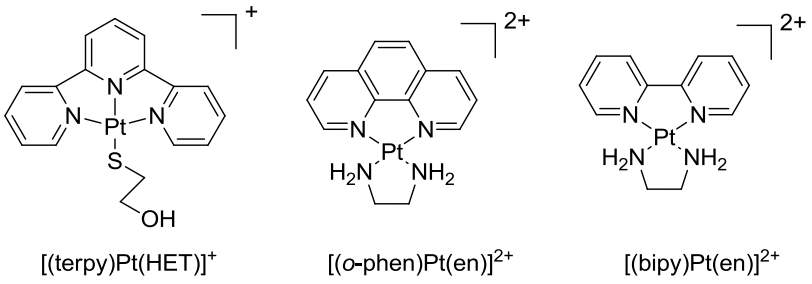

Figure 10 Square-planar platinum intercalator: terpy = terpyridine; phen= 1,10-phenanthroline; bipy = 2,2 ´-bipyridine; HET = 2-hydroxyethanethiolate; en= ethanediamine

Three-dimensional octahedral metallo-intercalators were then introduced by Barton and others, and included octahedral Rh, Ru, Co, Ni, or Os complexes harboring multi-heterocyclic aromatic ligands.[34, 37] 2,2 ´-bipyridine and 1,10-phenantroline complexes of ruthenium containing dipyrido[3,2-a:2',3'-c]phenazine (dppz) could intercalate into B-form DNA,[38] and analogous ruthenium, osmium, nickel and cobalt complexes with 1,10-phenanthrolino[5,6-*b*]1,4,5,8,12-hexaazaphenylene (PHETA), 1,4,5,8,12-hexaazaphenylene (HAT), dppz could also interact with DNA (Figure 11).[39]

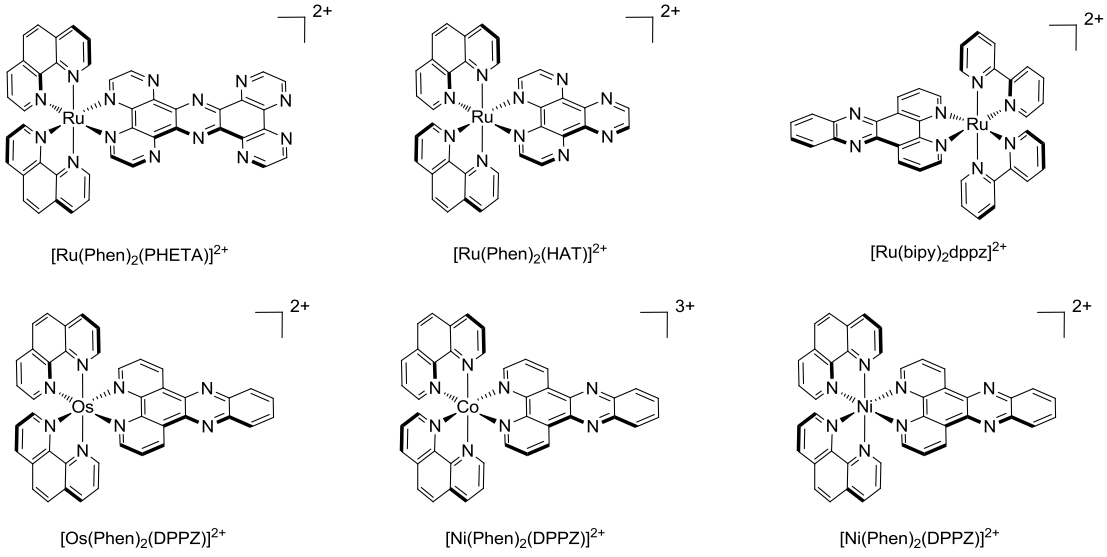

Figure 11 Metallo-intercalators containing 2,2 ´-bipyridine, 1,10-phenantroline, PHETA, HAT and dppz [38-40]

Two other typical examples of this type of metallo-intercalator are Δ-$[Rh(phen)_2(Phi)]^{3+}$ (Phi = 9,10-phenanthrenequinone diimine), and Δ-$[Ru(bipy)_2(dppz)]^{2+}$.[41] Both of these are stereoselective and the Δ-enantiomers are preferred (Figure 12). They demonstrate that the metallo-intercalators enter the double helix via the major groove, and the ligands act like a new base pair through physical studies[42] and extensive NMR measurement.[43] No base pairs will be ejected from the duplexes. A high resolution crystal structure is also a very effective method to illuminate the intercalation mode. The crystal structure reveals that Λ-$[Ru(Phen)_2dppz]^{2+}$ perform two different modes to interact with the oligonucleotides d(CCGG**TA**CCGG)$_2$ and d(CCGG**AT**CCGG)$_2$: The dppz ligand intercalates symmetrically and perpendicularly from the minor groove of the first duplex at the central TA/TA step, but not at the central AT/AT step of the second duplex.[44]

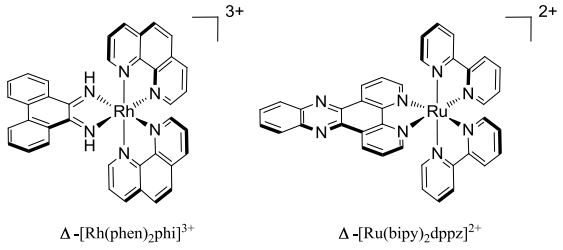

Figure 12 Structure of two common metallo-intercalators

Groove binding

Metal complexes that bind DNA *via* major or minor grooves have also attracted a lot of attention. More than 30 years ago, Sigman et al. found that $[Cu(Phen)]^{2+}$ could bind DNA in the minor groove and cleave the DNA in the presence of H_2O_2.[45] tris(phen) complexes of zinc, cobalt, nickel, and ruthenium are the earliest octahedral metal complexes utilized to investigate DNA groove binding (Figure 13).[43, 46] However, tris(phen) metal complexes bind DNA two ways: (i) hydrophobic binding in the minor groove; (ii) partial intercalation into DNA bases from the major groove. For example, Λ-$[Ru(phen)_3]^{2+}$ shows preferential binding in the minor groove and

Δ-$[Ru(Phen)_3]^{2+}$ is preferred in intercalation. If the phenantroline is replaced by more steric 4,7-diphenyl-1,10-phenanthroline (DIP), $[Ru(DIP)_3]^{2+}$ becomes specific for chiral discrimination, with the Λ-enantiomer only binding the left-handed Z-DNA, and Δ-enantiomer binding the right-handed B-DNA, specifically.[47] Geometric and steric factors also play a role for $[Ru(TMP)_3]^{2+}$ (TMP = 3,4,7,8-tetramethyl phenanthroline), where the methyl group hinders the intercalation.[48] However, the metal complex through groove binding is quite sophisticated and needs more investigation.

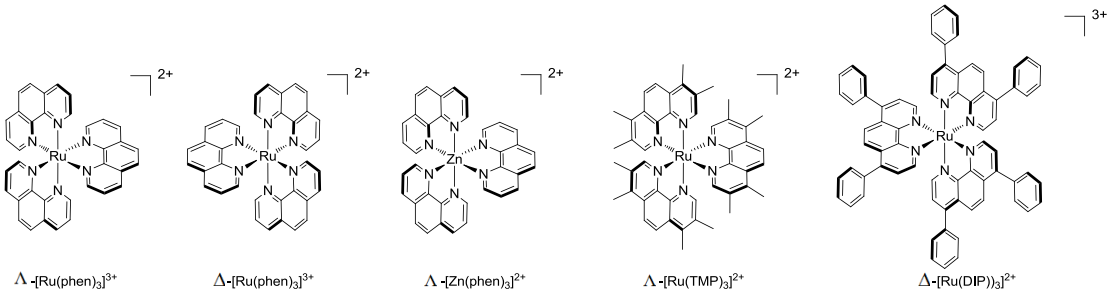

Figure 13 Octahedral metal complexes for DNA groove binding. TMP = 3,4,7,8-tetramethyl phenanthroline; DIP = 4,7-diphenyl-1,10-phenanthroline

Metallo-insertors

Another very important mode of interaction is metallo-insertors. Until Barton et al. discovered a series of rhodium complex DNA-insertors, no one had ever reported that organic molecules or metal complexes could be used as DNA-insertors.[34] Similar to metallo-intercalators, the metallo-insertors also contain a planar aromatic ligand which can interact with base pairs. However, unlike the intercalators, which insert into the center of the two intact base pairs, the metallo-insertors will displace the base-pair out of the π-stack. DNA base mismatches will result in errors during replication or exposure to genotoxic agents. If these kinds of mismatches are not repaired, it will ultimately lead to single nucleotide polymorphism (SNPs). The cell has developed a complex mismatch repair (MMR) machinery to locate and repair these. Designing a kind of agent that can recognize the mismatch site of the DNA is very important. The research on metallo-insertors offers a very promising tool for the

detection of mismatch-specific DNA. The most classic of the metallo-insertors are Δ-$[Rh(bpy)_2(chrysi)]^{3+}$ (chrysi = 5,6-chrysene quinone diimine) and Δ-$[Ru(bipy)_2(phzi)]^{3+}$ (phzi = benzo[a]phenazine-5,6-quinone diimine), which show a strong preference for DNA mismatch sequences (Figure 14).[49] Recently, Barton et al. reported the high-resolution crystal structure of Δ-$[Ru(bipy)_2dppz]^{2+}$ bound to both mismatched and matched sites in the oligonucleotide 5′-$d(CGGAAATTACCG)_2$-3′.

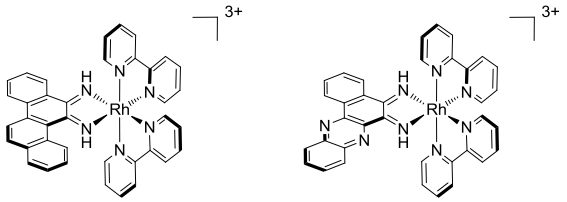

Δ-$[Rh(bpy)_2Chrysl]^{3+}$ Δ-$[Ru(bipy)_2Phzi]^{3+}$

Figure 14 Chemical structure of mismatch-specific metallo-insertors. (chrysi = 5,6-chrysene quinone diimine; phzi = benzo[*a*]phenazine-5,6-quinone diimine)

1.2.2 G-quadruplex DNA/ligand interactions

DNA structure is not only limited to the double helix, and can adopt a wide variety of topologies. The G-quadruplex DNA structure is a classic one. This kind of structure consists of nucleic acid sequences that are rich in guanine and comprise four strands of stacked guanine-tetrads (G-quarter motif), and four guanine bases that can associate through Hoogsteen hydrogen bonding to form a square planar structure (Figure 15). The G-quarter motif results in the formation of four grooves.[50] G-quadruplex structures present a large π-surface and carry a high negative charge. Quadruplex-specific stabilization by cations has an order of preference of K^+ > NH_4^+ >Na^+ >Li^+. K^+ ions, shown to be separated by approximately 3.3Å in the crystal structure of the human telomeric quadruplex[51]. All four strands may be four parallel, three parallel and one antiparallel, or two in one direction and two in the other, either with the parallel pairs adjacent to each other (Figure 16).

In 2013, a breakthrough on the G-quadruplex was made by Balasubramanian et al. from Cambridge University; they reported that the G-quadruplex structures in human cells could be quantitatively visualized by employing the generation and application of an engineered, structure-specific antibody. Although there has been enough indirect evidence to suggest that these structures play an important role inside the cell, this is the first direct evidence of G-quadruplex existence *in vivo*.[52]

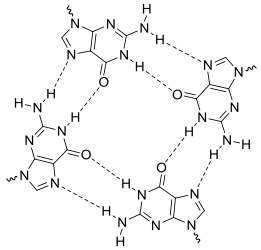

Figure 15 Four guanines can hydrogen bond in a square arrangement to form a G-quartet. There are two hydrogen bonds on each side of the square

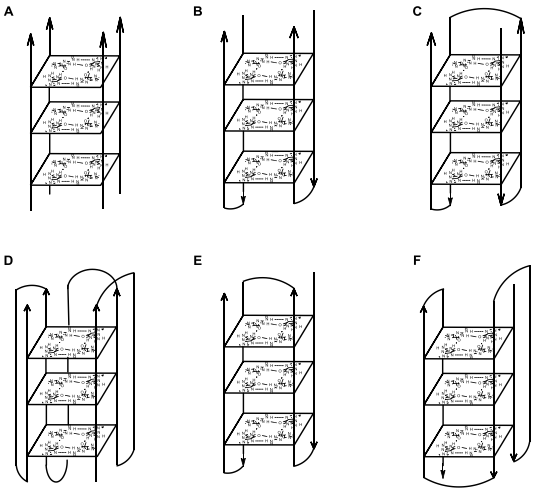

Figure 16 Structure and topology of G-quadruplexes: (A) tetramolecular with parallel strands. (B) bimolecular antiparallel. (C) unimolecular antiparallel structure with alternating parallel strands. (D) unimolecular parallel structure with three double-chain reversal loops. (E) unimolecular antiparallel structure with adjacent parallel strands and a diagonal loop. (F) unimolecular mixed structure with three parallel and one antiparallel strands

G-quadruplex structures have been evoked in the control of the expression of certain genes.[53] The telomers of human cells consist of tandem repeats of the sequence 5´-TTAGGG-3´ with 3´-overhang of the G-strand extending hundreds of

bases beyond the C-strand.[54] Telomeric repeats can be extended by telomerase. As telomerase is overexpressed in most tumor cells and not in normal cells, it is a good target for us to design antitumor drugs with high selectivity.[55] Moreover, single-stranded overhang of telomeric DNA can be coiled into intramolecular G-quadruplex structures, which will hinder the reaction of telomerase.[56] Accordingly, the development of a ligand to stabilize the G-quadruplex has a potential application as a telomerase inhibitor. There are normally three types of interactions between G-quadruplex with ligands: π-stacking, groove/loop binding, and central channel binding.

π-stacking ligands

The π-stacking interaction between the ligand with G-quadruplex is mainly controlled by hydrophobic and van der waals forces. As previously discussed, ligands could insert between stacked DNA duplex base pairs. However, the situation is completely different for the G-quadruplex; ligands interact with quadruplexes by stacking onto the ends of the G-quartets, moreover, ligands must exhibit reasonable water solubility.[50c, 57]

Aromatic molecules based on acridine derivatives substituted at the 3- and 6-positions with 3-pyrrolidinopropionamide (**BSU6039**, Figure 17) have been developed by Haider, and the G-quadruplex crystal structure from the telomeric DNA sequence d(GGGGTTTTGGGG) in the presence of **BSU6039** revealed that acridine bound at one end of the G-quartets, within one of the thymine loops.[57] The widely used (tetra(*N*-methyl-4-pyridyl)porphyrin) (**TMPyP4**, Figure 17) selectively bound G-quadruplexes over duplexes.[58] While the metals Mg, Mn, Fe, Co, Ni, Cu, and Zn are incorporated into the TMPyP4, the resulting complexes are also over the central channel to improve electrostatic stabilization. The natural product, telomestatin, and a non-polycyclic aromatic ligand, such as bis-triazole derivative, could also be used for quadruplex stabilization (Figure 17).[59]

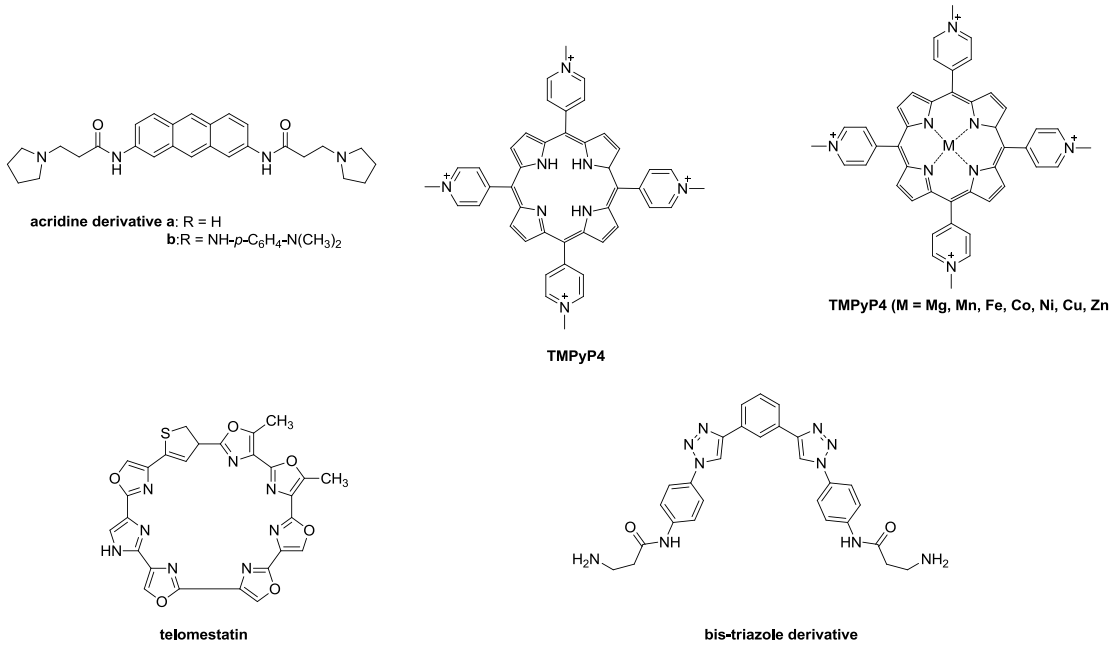

Figure 17 G-quadruplex π-stacking ligands

Groove/loop binding ligands

As chemical and conformational differences between quadruplex and duplex grooves are significant, designing ligands that discriminate between the G-quadruplex and DNA duplex becomes possible.

Randazzo reported that the three-dimensional structure of a groove binder molecule, distamycin A, complexed to a parallel quadruplex $[d(TGGGGT)]_4$. This is also the only compound for which a pure groove binding has been proven. NMR and isothermal titration calorimetry (ITC) investigation revealed that the ratio of [istamycin A]/$[d(TGGGGT)]_4$ is 4:1 with two antiparallel distamycin dimers that bind simultaneously two opposite grooves of the quadruplex (Figure 18).[60]

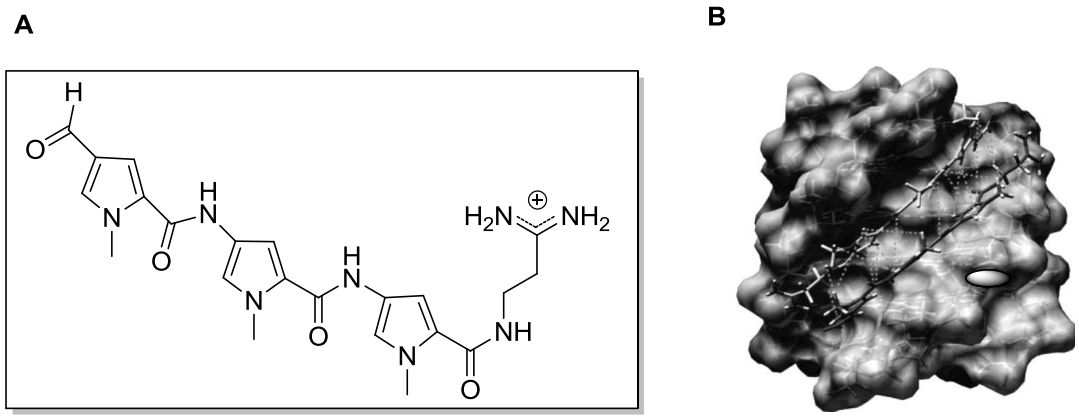

Figure 18 (A) structure of distamycin A. (B) Side view representation of the 4:1 complex Dist-A/[d(TGGGGT)]$_4$. Intermolecular head to tail drug-drug NOE contacts are indicated with green dashed lines (*J. Am. Chem. Soc.* **2007**, *129*, 16048-16056)[60]

Octahedral metal complexes could also be used as G-quadruplex groove binders, and ligands have the capability to stack on G-tetrads; the charged molecule as a whole interacts with grooves/loops.[61] Thomas et al. found that dinuclear Ru(II) complexes containing ditopic ligands, tetrapyrido[3,2-*a*:2 ′,3 ′-*c*:3 ′′,2 ′′-*h*:2 ′′′,3 ′′′-*j*]phenazine (TPPZ) and tetraazatetrapyrido[3,2-*a*:2 3 ′-*c*:3 ′′,2 ′′-l:2 ′′′,3 ′′′-*n*]pentacene (TATPP) not only bound to duplex DNA with high affinities in the way of intercalation, but also bound to 22-mer d ($AG_3[T_2AG_3]_3$) [G3] human telomeric sequence with high affinity (Figure 19). Moreover, G-quadruplex binding was accompanied by a distinctive blue-shifted "light-switch" effect, and emission enhancements were 2.5 times higher than those observed in the analogous duplex effect.

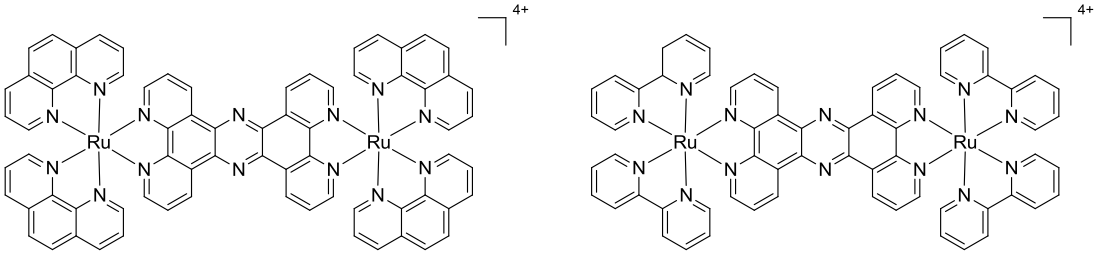

Figure 19 Dinuclear groove binder

Central channel binding ligands

As we mentioned, potassium cation could stabilize the structure of the G-quadruplex. To mimic this kind of function, Balasubramanian et al. synthesized the anthracene derivative (Figure 20), based on the hypothesis that anthracene moiety would stack onto guanines and ammonium would induce the formation of the single, parallel, quadruplex conformation. CD spectroscopy revealed that this ligand could selectively induce a parallel quadruplex formation from unfolded DNA in the absence of added cations; this situation may be caused by threading and stacking modes of interaction.[62]

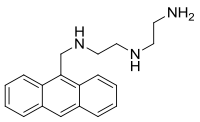

Figure 20 Central channel binding ligands

1.2.3 Methods to investigate ligand interactions

Before the discussion of our study on octahedral silicon complexes begins, we first give a brief introduction of the normal detection methods of the interaction.

Melting temperature (T_m) measurement

Hypochromicity is the increase of absorbance of a material, and the hyperchromic effect is the striking increase in absorbance of DNA upon denaturation. Nucleic acids show strong absorbance around 260 nm, and hyperchromicity can be used to track the condition of DNA as the temperature changes. The melting temperature (T_m) is when the UV absorbance is 50% between the maximum and minimum. A change of melting temperature is an effective tool to detect the interaction between the complexes with DNA. Similarly, the melting temperature of the G-quadruplex could be measured at 295 nm. The melting temperature could also

be measured by circular dichroism; upon denaturation, the signal of the DNA duplex at 260 nm and the G-quadruplex at 295 nm will be reduced.

However, the UV and CD melting curves have limitations because of the low intensity and signal change. Fluorescence resonance energy transfer (FRET) is a powerful tool to track the status of DNA hybridization. For example, fluorescence of the acceptor dye and donor dye show a mild signal in the DNA duplex; after denaturation, the fluorescence of the acceptor dye disappears and the fluorescence of the donor dye intensifies.[63] While oligonucleotides are labeled at 3′ and 5′ using a fluorophore and quencher, the formation of a quadruplex will result in the quench of the fluorescence; after denaturation, the fluorescence will be restored (Figure 21).[64]

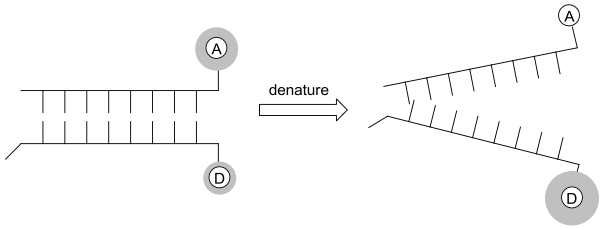

Figure 21 FRET for detecting DNA hybridization with fluorescence

Circular dichroism (CD)

CD spectroscopy is based on the different absorption of left and right circularly polarized light; it could be utilized to analyze the DNA conformation. If molecules interact with DNA, CD spectroscopy is recorded to analyze the change of the cotton effect. For example, the interaction of the tricyclic tetrahydroanthracene ligand on Ru^{II} (Ru-tha) with calf thymus DNA results in the appearance of a CD band centered around 370-380 nm.[64]

Fluorescence measurements

Although the intrinsic fluorescence of most nucleic acids is very low, the polynucleotide structure could be measured by incorporation of a fluorescence group. The most typical example is $[Ru(Phen)_2(dppz)]^{2+}$, which shows solvatochromic

luminescence in organic solvents. However, no luminescence will be detected because water deactivates the excited state through hydrogen-bonding with the endocyclic nitrogen atoms of the intercalating ligand. When the complex intercalates with DNA, the luminescence appears, as DNA creates a region of organic "solvent" in which the complex avoids the hydrogen-bonding formation.[42b]

NMR spectroscopy

NMR allows for the structural determination of a complex at an atomic level. Intercalation of DNA with complexes often results in the change of NMR, including ^{1}H-NMR shifts, NOE cross-peaks, and interruption or weakening of NOE connection between sequential DNA nucleotides. The one- and two-dimensional NMR data for $d(TGGCCA)_2$ in the presence of $[Rh(NH_3)_4(Phi)]^{3+}$ is consistent with the rhodium complex intercalated into the G_3C_4 site from the major groove with the Phi ligand fully inserted and stacked in the column of base pairs.[65] Fedoroff also investigated the interaction of *N*,*N*′-bis-(2-(dimethylamino)ethyl)-3,4,9,10-perylenetetracarboxylic acid diimide (PIPER) with tetramolecular quadruplex $d[TTAGGGT]_4$ through NMR. The results indicate that the ligand is sandwiched between terminal G4 planes.[66]

X-ray crystallography

A lot of DNA crystals in the presence of complexes have been reported, including metallo-intercalators[67] and metallo-inserters.[44] This is a very powerful method to analyze the interaction. As previously mentioned, the crystal structure from the telomeric DNA sequence d(GGGGTTTTGGGG) in the presence of **BSU6039** revealed that acridine bound at one end of the G-quartets.[57]

Isothermal titration calorimetry (ITC)

ITC is a physical technique employed to obtain the thermodynamic parameters of interactions in a solution, and it has been applied to investigate small molecules binding to the DNA duplex [68]and the G-quadruplex.

Binding constants measurement

Binding constants are usually measured to demonstrate the strength of the interaction between ligands and DNA, and the value K_b could be obtained in the following equation (Figure 22). d is the concentration of DNA, K_b is the intrinsic binding constant, s is the binding site size, ε_a is the extinction coefficient observed for the metal-to-ligand ($\pi_M \rightarrow \pi_L$) charge transfer (MLCT) absorption band at a given DNA concentration, ε_f is the extinction coefficient of the complex free in solution, and ε_b is the extinction coefficient of the complex when fully bound to DNA K_b.

$$\frac{\varepsilon_a-\varepsilon_f}{\varepsilon_b-\varepsilon_f}=\frac{b-\sqrt{b^2-\frac{2\times K_b{}^2\times 0.00003\times d}{s}}}{2\times K_b\times 0.00003} \qquad (b=1+K_b\times 0.00003+\frac{K_b\times d}{2s})$$

Figure 22 Equation for measurement of binding constant

There are still some other methods to detect the interaction between the DNA and complexes, such as linear dichroism (LD), and viscosity.

1.2.4 Hypervalent silicon complexes

Silicon complexes with more than four coordination numbers date back to the beginning of the 19th century with the discovery of $[SiF_6]^{2-}$ and $Si(NH_3)_2F_4$. These kinds of hypervalent silicon complexes have attracted a lot of attention as they may have a potential application in the field of nucleophilic activation and catalysis. The preparation of these types of compounds has been extensively studied.[69] The general procedures to synthesize penta- and hexa-coordinated silicon compounds are similar.

Here, we mainly give some typical examples for synthesizing the hexa-coordinated silicon complexes.

Through fluoride donation to a halogenosilane, Kumada et al successfully obtained the organopentafluorosilicates by reaction of excessive KF in H_2O with $RSiCl_3$.[70] Another very useful method is the intermolecular coordination to an organosilane. Hexa-coordinated complexes $Me_2SiX_2 \cdot 2Py$, $MeSiX_3 \cdot 2Py$ and $SiX_4 \cdot 2Py$,[71] and $SiX_4 \cdot 2PMe_3$[72] could be obtained very easily. 2,2'-bipyridine and 1,10-phenanthroline react with halogenosilanes to afford a neutral compound **1a**[73], or cationic compounds **2**[74], **3a**[75] and **4**[76] (Scheme 2). If **1a** was used as the starting material, it can react with one equivalent or two equivalents of Li_2bipyridine to afford the new neutral complex **5** or **6**. Then **5** would further react with ROH (R = CH_3, H) or Cl_2 to give the cationic silicon(IV) complex **7** or **8**, respectively. In addition, **6** could be oxidized by I_2 to afford the new cationic tris(2,2´-bipyridine)silicon(IV) complex **9**. Moreover, compound **2** is a very good intermediate, which can react with two equivalents of MeOH and H_2O to give the product **10** (Scheme 3).[74] Another special example is that the neutral silicon complex **11** coordinated with 1,10-phenantroline to afford **12** (Scheme 4).

Hexa-coordinated silicon complexes could also be obtained by the use of a substitution in a tetrafunctional silane by a bidentate ligand. Some complexes have been reported. β-diketones as ligands reacted with $SiCl_4$ to afford a cationic complex **13**[77] while the neutral product **14**[78] will be obtained from the starting compound $Si(OAc)_4$ (Scheme 5).

Albeit, many hypervalent silicon complexes exist. Rare reports on hypervalent silicon in biological systems have been reported. Recently, Suessmuth et al. obtained the first examples of a six-coordinate silicon complex of natural products enterobactin-Si(IV) (**15a**) and salmochelin-Si(IV) (**15b**) (Scheme 6). Both of these complexes are stable under normal physiological conditions. Compared to other silicon complexes, enterobactin and salmochelin cause significant bacterial growth.[79]

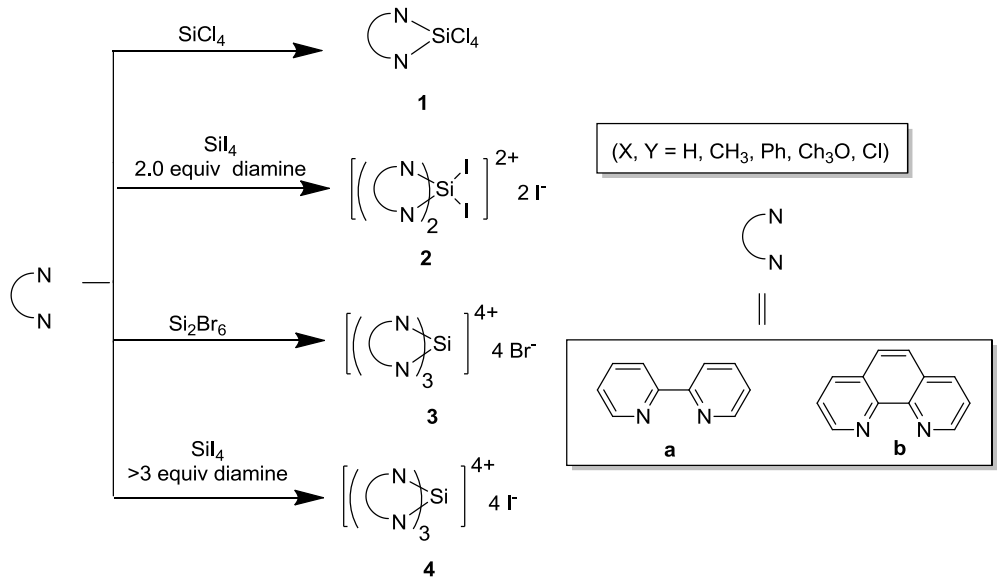

Scheme 2 Diamine coordinates with halogenosilanes to afford hexa-coordinated silicon complexes

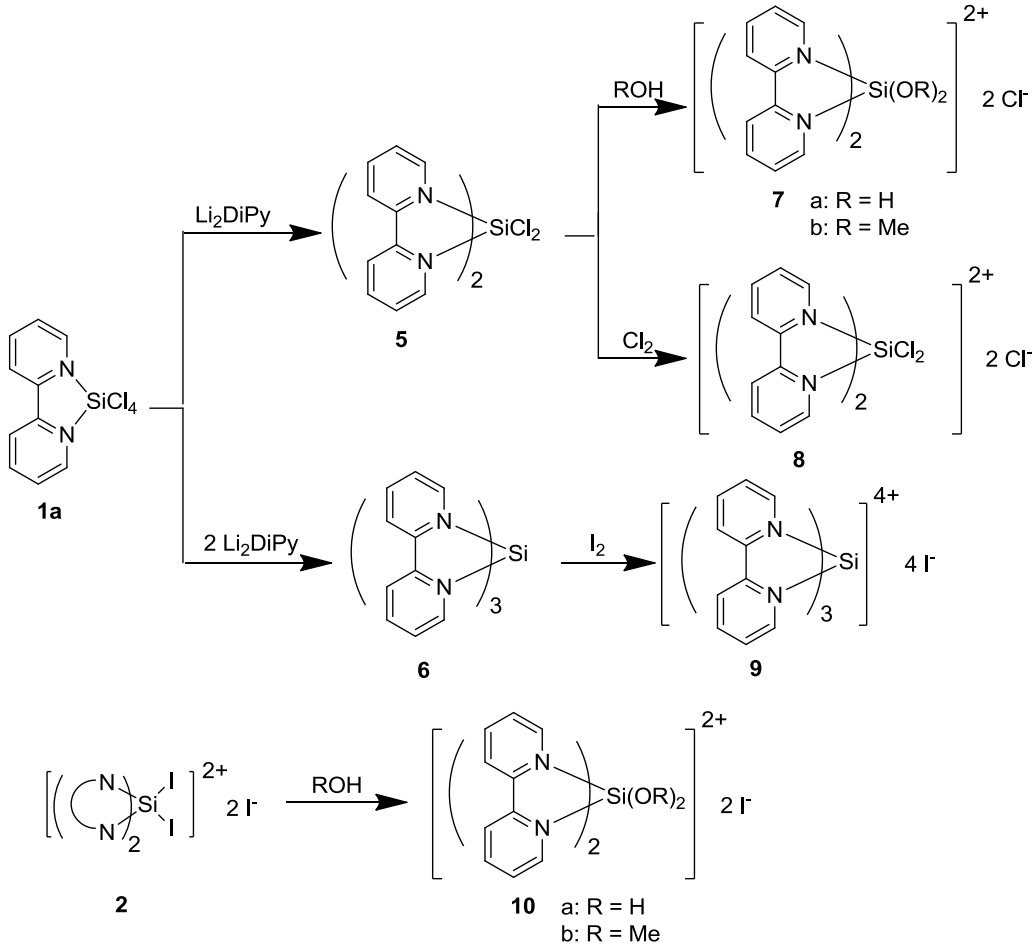

Scheme 3 Hexa-coordinated silicon complexes from **1a** and **2**

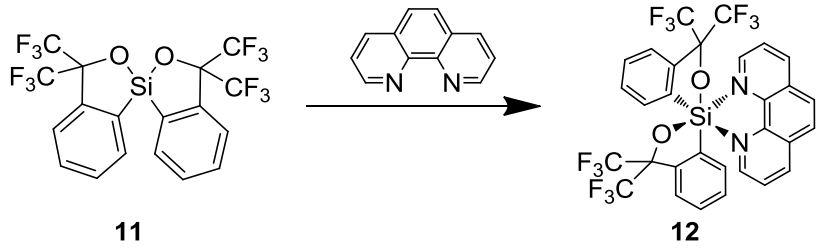

11 **12**

Scheme 4 Procedure of synthesis of **12**

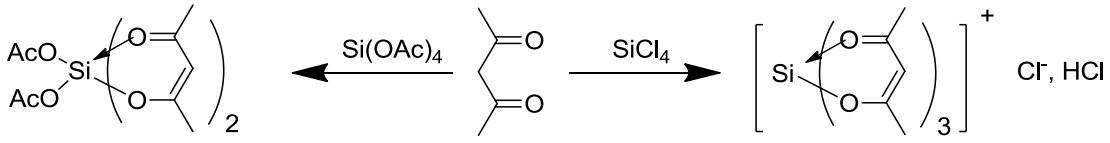

14 **13**

Scheme 5 Examples of synthesis of silicon complexes with substitution in a tetrafunctional silane

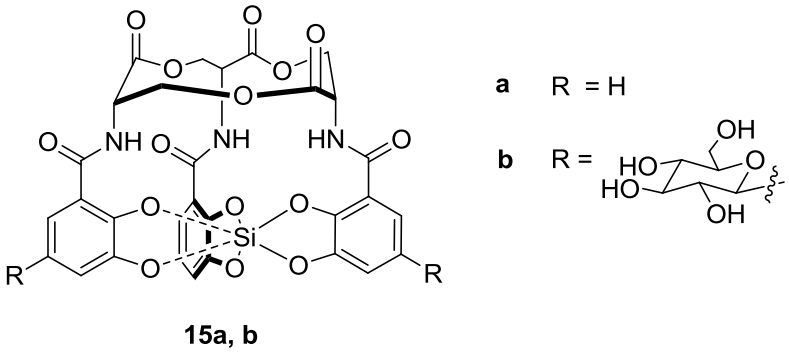

15a, b

Scheme 6 Structures of enterobactin-Si(IV) and salmochelin-Si(IV)

Chapter 2 Aim of work

My work mainly includes two parts, one is GNA as a scaffold for molecular aggregates of chromophores, and the other one is the design of octahedral silicon complexes as DNA binders.

GNA as a scaffold for chromophore aggregates

π Arrays and clusters of chromophores have been used as imaging tools in life sciences and as components of industrial dyes and pigments because of their different properties between momomeric state and stacking states.[1a]

Over the past few decades, DNA plays more and more significant role for the design and construction of nanostructures and functional π systems.[80] DNA itself lacks remarkable functionality; therefore, applications of DNA based on material rely on the controlled modification of DNA in order to introduce the required functionality. Modified nucleic acids are nowadays readily accessible through standard automated solid phase synthesis using nucleoside phosphoramidites as building blocks, enabling the synthesis of oligonucleotides greater than 100 bases. Unfortunately, in particular due to the stereocenters in the deoxyribose moiety and especially the anomeric C1′-stereocenter, the chemical synthesis of modified nucleotide building blocks for automated nucleic acid synthesis is often tedious and lengthy, includes the chromatographic separation of diastereomers.

Due to the straightforward synthetic accessibility of GNA nucleotide building blocks in combination with high duplex stabilities, GNA comprises an appealing scaffold for future nucleic acid base functional nanostructures.[20c]

Our work mainly focuses on design of functional architectures, control stacking and assembly of functional building block by using GNA backbone; in particular we pursue the control of stacking and assembly of chromophores (π-conjugated molecules) within a GNA duplex scaffold. Chromophores which have extended

hydrophobic moieties such as: perylene bisimide, phthalocyanine and porphyrin (Figure 23), can be readily incorporated into single strands with a DNA synthesizer and upon hybrization of another single strands, different numbers of chromophores can be stacking inside a duplex which lead to functional artificial double-helical structures.

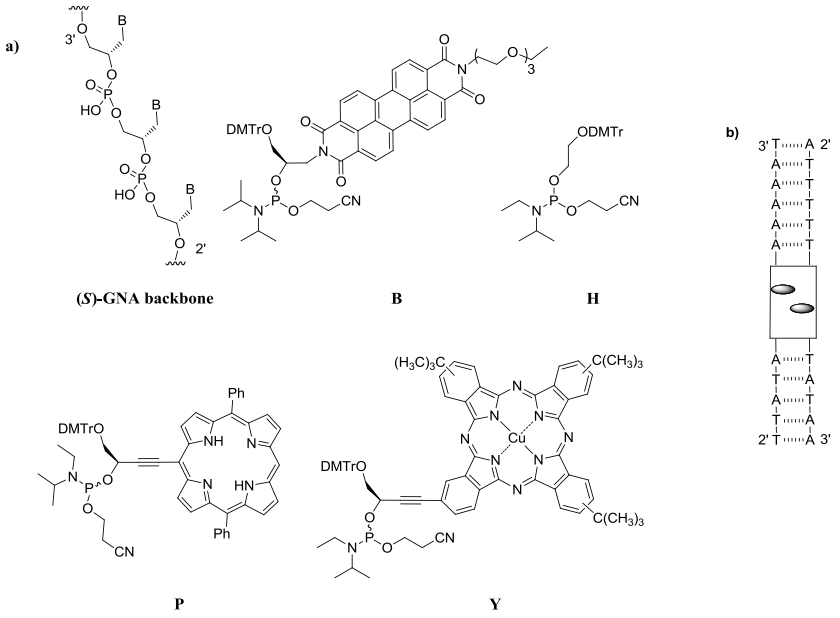

Figure 23 (a) Constitution of the (*S*)-GNA and structure of the artificial bases. (b) Sequence of the duplexes

Design of octahedral silicon complexes as DNA binders

DNA is one of the three major macromolecules (along with RNA and protein) that are essential for all known forms of life. Since the elucidation of the structure of double helical DNA, there is growing interest in developing the small organic molecules and metal complexes that can bind specific site of DNA for promising diagnostic probe.

Carbon of small moleculars is limited to coordination numbers ≤ 4 which make it a significant handicap for the efficient construction of defined globular three-dimensional structures. Over the past several decades, octahedral transition metal complexes are a burgeoning class of DNA-binders, they have been

extentensively applied in DNA groove bining, intercalation and insertion.[34, 41] These kinds of octahedral metal complexes have their own advantages, such as the ability of the structural center to organize substituents in the three dimensional space and create novel globular structures increase substantially as manifested by the difference of possible stereoisomers of 2 for an asymmetric tetrahedral center versus up to 30 for an octahedral center.[81] Moreover, Meggers group have designed a family of octahedral highly potent and selective octahedral metal-based inhibitors of protein kinases.[82] Unfortunately, metal-based toxicities currently is the general concern for wider application of octahedral metal complexes in the life sciences. Accordingly, designing the low toxic octahedral non-metal DNA binders is very promising and challenging.

In contrast to low coordination carbon and toxic transition metal, silicon is the next higher congener of carbon, this element has available empty 3d orbitals, and it has the tendency to form penta- and hexa-coordinated complexes and might therefore constitute an interesting candidate to serve as a stable structural substitute for a lacking hypervalent carbon; moreover, the synthesis of the penta- and hexa-coordinated silicon complexes has been extensively studied.[69, 79, 83]. We envisage that designing of the hydrolytically stable and at the same time structurally diverse hypervalent silicon compound scaffolds is a very promising choice for DNA binder instead of small organic molecules and the toxic octahedral transition metal complexes (Figure 24). To reach this goal, the progress into this direction with the design of a class of hydrolytically stable, high affinity DNA binders based on octahedral silicon will be discussed in the subsequent parts.

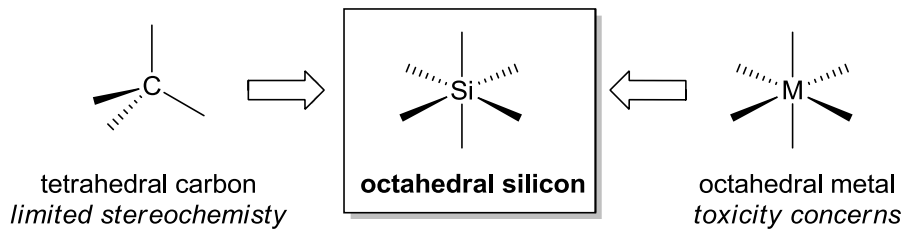

Figure 24 Octahedral silicon as a non-classical structural template

Chapter 3 Results and Discussion

3.1 GNA as Scaffold for Chromophore Aggregates

3.1.1 Synthesis of GNA building blocks

We designed the asymmetric, amphiphilic phosphoramidite building block **16** based on two criteria: the large planar and hydrophobic perylene bisimides (**PBI**) molecule can stack well in GNA duplexes opposite an ethylene glycol spacer as shown in Figure 25, and long hydrophilic oligoethylene glycol side chain improves the solubility of **PBI** moiety, while modified **PBI** planarity and distinguished physical properties are kept at the same time. Due to the low solubility and strong π-π stacking interaction of **PBI** derivatives in a variety of organic solvents, synthesis and purification of the designed building block are quite challenging. Another very interesting chromophore phthalocyanine phosphoramidite, building block **17**, was also designed, and the main problem is still the separation of the product from the mixture because of the strong π-π stacking interaction (Figure 25).

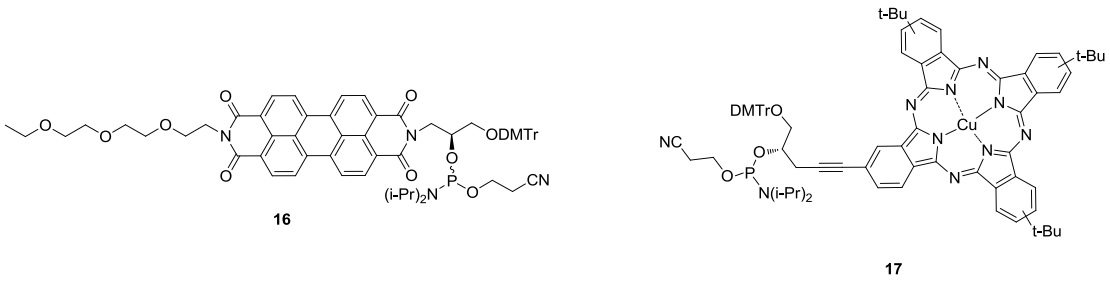

Figure 25 Structure of phosphoramidite building block **16** and **17**

In order to obtain the unsymmetrical **PBI**, the monoanhydride monoimide should be synthesized first. Although the simple *N*-alkyl-3,4:9,10-perylenetetracarboxylic monoanhydride monoimide (alkyl = H, methyl, ethyl, propyl, butyl, etc.) can be obtained by condensation of 3,4:9,10-perylenetetracarboxylic dianhydride with alkylamine easily,[84] this method did not work when the amine was not the alkyl amine. Scheme 7 depicts the synthesis of two starting amine derivatives **21** and **25**.

2-(2-(2-ethoxyethoxy)ethoxy)-ethanamine **21** was synthesized in three steps. 2-(2-(2-ethoxyethoxy)ethoxy)ethyl *p*-tosylate **19** was easily obtained from the triglycol monoethyl ether **18** in the presence of TsCl. Then, **19** further reacted with sodium azide to afford the compound 2-(2-(2-ethoxyethoxy)ethoxy)ethyl azide **20**, and 2-(2-(2-ethoxyethoxy)ethoxy)-ethanamine **21** was obtained from **20** in the presence of PPh_3. The enantiomerically pure compound (*S*)-3-(dimethoxytrityloxy)-2-hydroxylpropanamine **25** was also synthesized in three steps. The starting material, (*S*)-3-amino-1,2-propanediol **22**, was first acylated to give the 3-trifluoroacetamido-1,2-propanediol **23**, which was easily converted to the corresponding dimethoxytrityl compound **24**. After being deprotected, the final (*S*)-3-(dimethoxytrityloxy)-2-hydroxylpropanamine was obtained.[85]

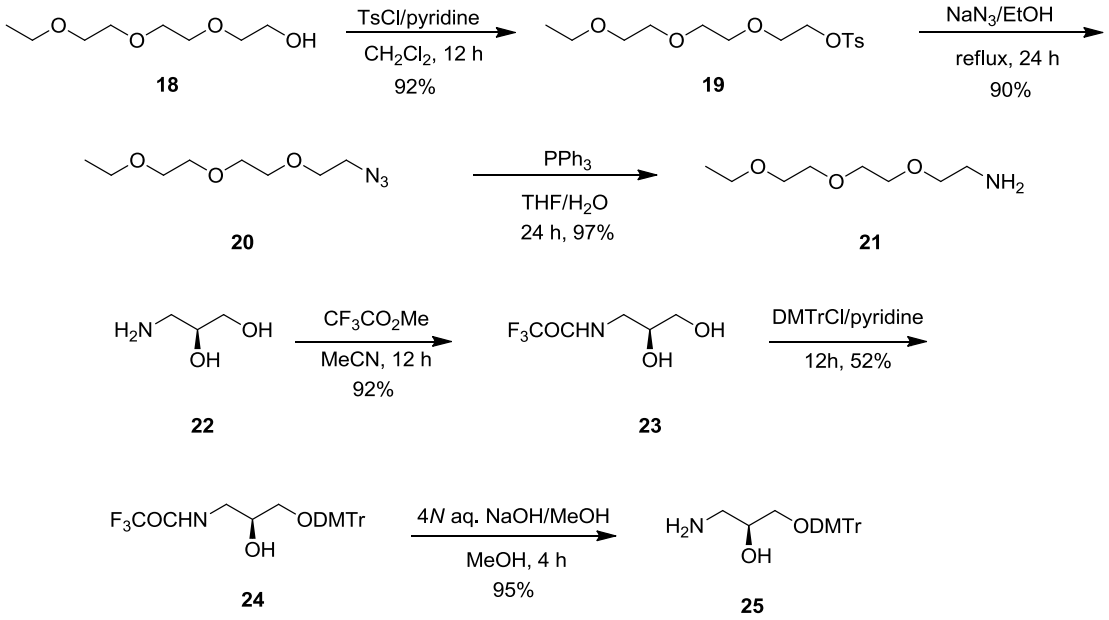

Scheme 7 Synthesis of amine derivative **21** and **25**

With **21** and **25** in hand, the GNA building block **PBI** derivative **16** was synthesized (Scheme 8). According to the procedure in the literature,[84] 3,4:9,10-perylenetetracarboxylic acid monopotassium **27** can easily be prepared from perylenetetracarboxylic dianhydride. However, condensation of **27** with amine **21** did not afford the desired monoanhydride monoimide product. After many attempts, the

best condition for carrying out this step was discovered. The reaction was first stirred at room temperature for four hours, and then heated at 90 ℃ for another two hours in 1:1 H_2O-PrOH (v/v). The resulting mixture was acidified with 1*N* HCl. The precipitate was filtered and rinsed with water to remove residual amine. The solid was stirred in hot 10% potassium hydroxide, then the mixture was filtered to remove the unreacted **21**, and the filtrate was acidified with 1*N* HCl to precipitate the product. The final suspension was filtered, and the solid was rinsed with water and dried at 100 ^oC overnight to afford monoimide **28**. Unfortunately, monoimide **PBI** was not dissolve in any organic solvent; however, monoimide **28** was dissolved in $CHCl_3$ when CF_3COOH was added (about 1/20 v/v). ^{1}H-NMR spectrum of **28** could be measured in $CF_3COOD/CDCl_3$ (1/20 v/v), and the spectrum looked very good. However, ^{13}C-NMR spectrum of **28** showed double the estimated peaks number, the reason for which is still unclear. Compound **28** was precipitated again after methanol was added, and the precipitate was used for the further reactions. Monoimide **28** reacted with an excess of amine **25** in pyridine in the presence of $Zn(OAc)_2$ to give the unsymmetrical perylene bisimide **29**, and the final phosphoramidite, building block **30**, was obtained after unsymmetrical perylene bisimide **29** reacted with 2-cyanoethyl-*N*, *N*- diisopropylchlorophosphoramidite in the presence of DIPEA. This product can be readily purified by using silica gel chromatography. It has good solubility in CH_3CN, which made it very suitable for further GNA synthesis.

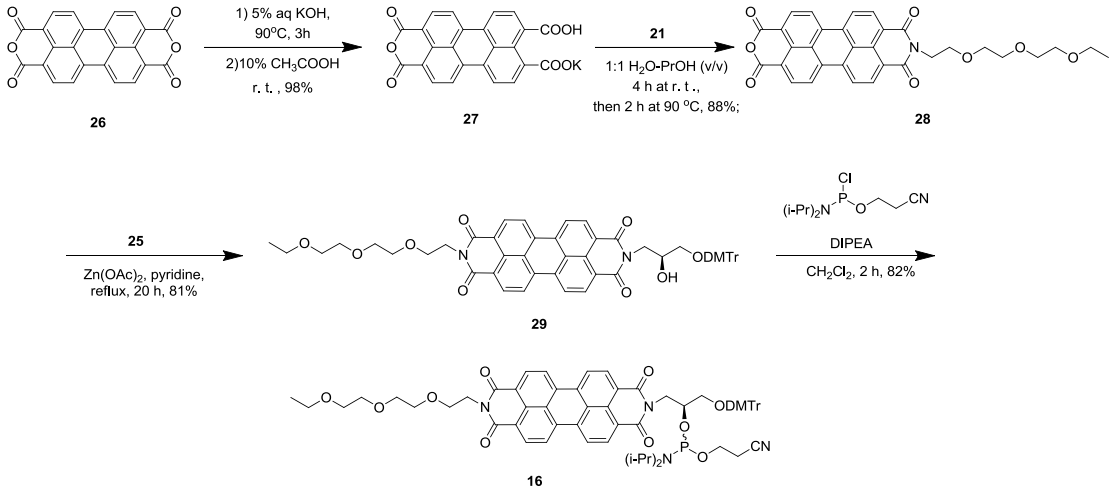

Scheme 8 Synthesis of GNA building block **16** (DIPEA = *N*,*N*-Diisopropylethylamine)

Next, we continued with the synthesis of another chromophore phthalocyanine phosphoramidite, building block **17**. Scheme 9 displays the route of synthesis. Nitration of phthalimide afforded the 4-nitrophthalamide **31**, which further reacted with aq NH_4OH to give the 4-nitrophthalamide **32**. Dehydration of **32** with trifluoacetic anhydride resulted in the formation of the product 4-nitrophthalonitrile **33**. Then the reduction product was obtained from **33** by 10 wt. % Pd/C. The amino group was converted to iodido group with $NaNO_2$ and KI in 25% H_2SO_4. With 4-iodophthalonitrile and 4-*tert*-butylphthalonitrile in hand, tri-*tert*-butyliodophthalocyaninatocopper **37** was synthesized at 15% yield, then coupling of **37** and **38** afforded the compound **39**, which reacted with 2-cyanoethyl-*N*, *N*-diisopropylchlorophosphoramidite to furnish phosphoramidite building block **17** (Scheme 9).

Together with the porphyrin GNA building block that was synthesized in our lab, there were three GNA building blocks in hand (Figure 26).

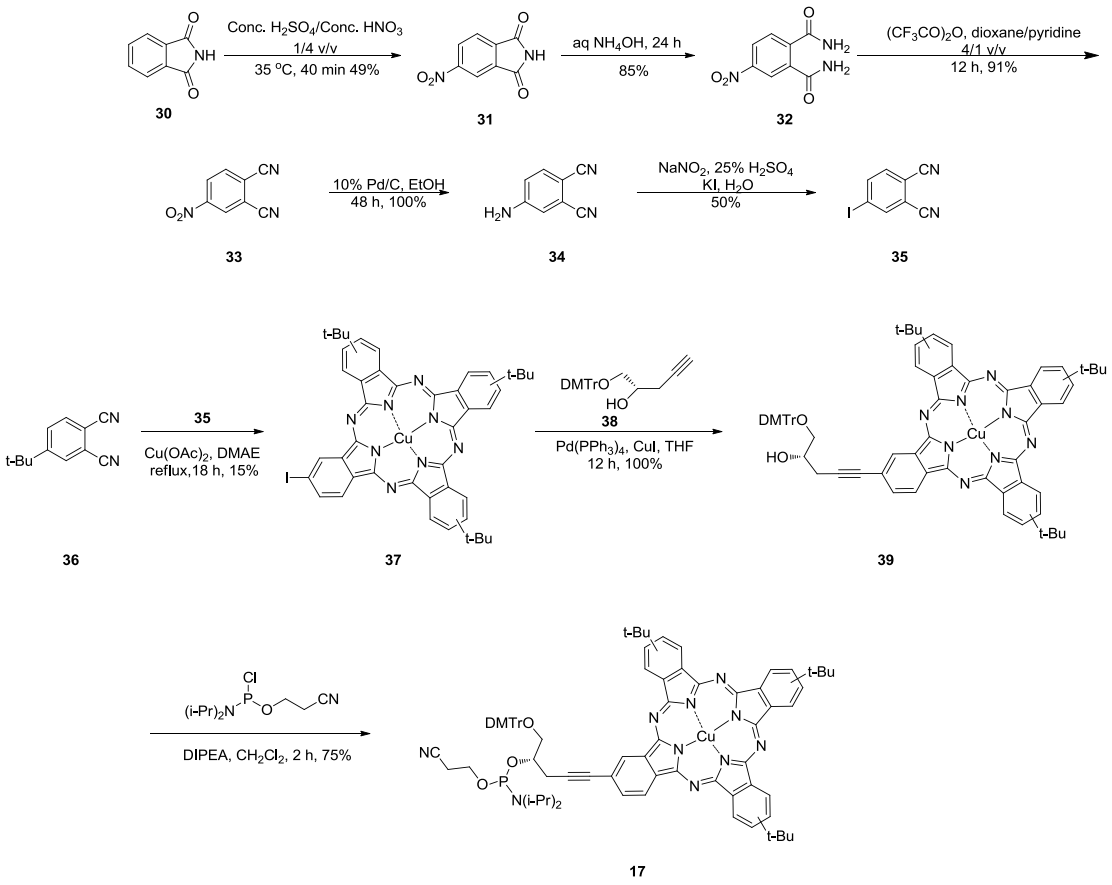

Scheme 9 Synthesis of GNA building block **17**

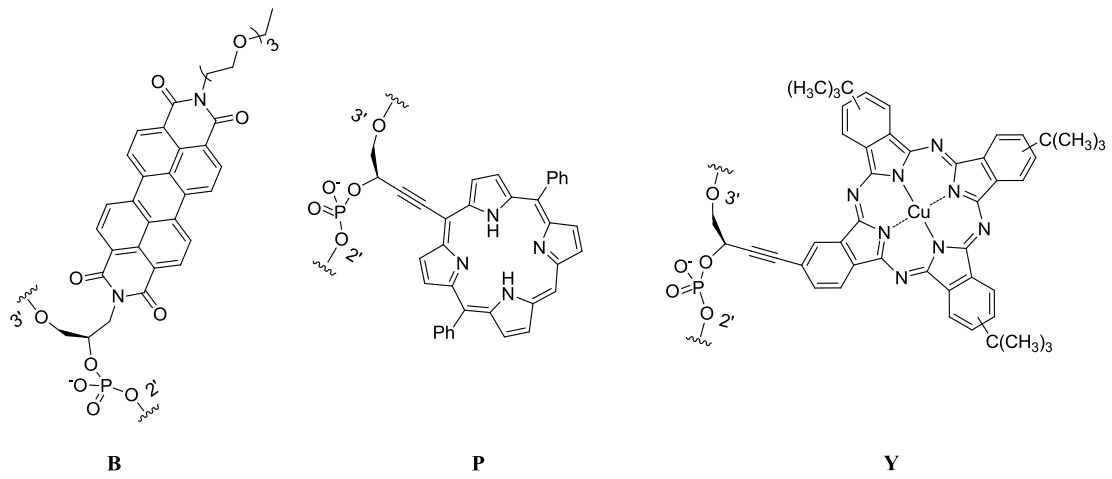

Figure 26 Constitution of the (*S*)-GNA and structure of the artificial bases

3.1.2 PBI as an artificial GNA surrogate

3.1.2.1 Synthesis of PBI-modified GNA oligonucleotides

Now we had obtained the propane-1, 2-diol-modified **PBI** building block that has a unique combination of properties: (i) the building block is capable of stacking in GNA duplexes opposite an ethylene glycol **H** spacer, as shown in Figure 27; (ii) the phosphoramidite building block is easily synthesized, and this building block was then incorporated into GNA oligonucleotides (**B**, Figure 27).

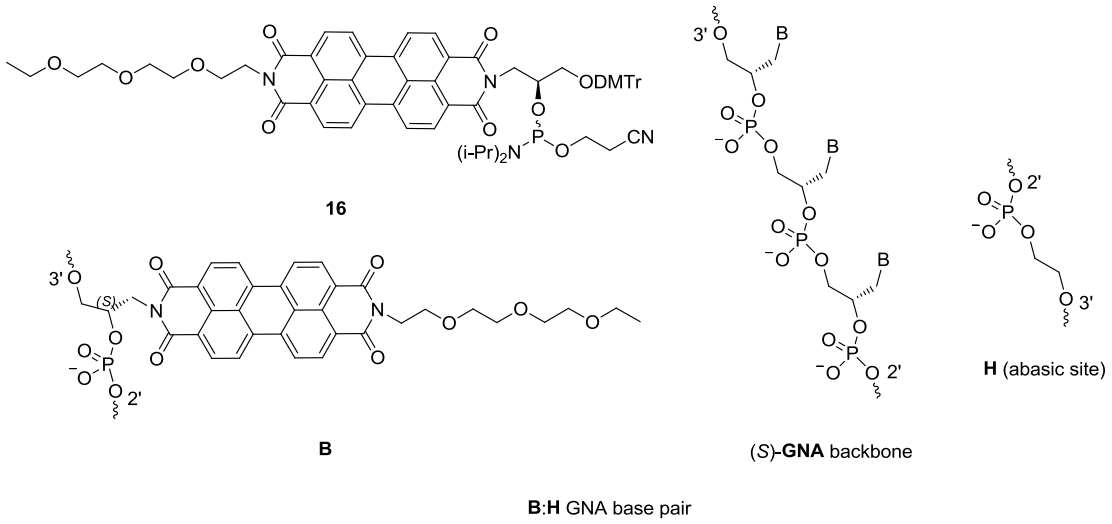

Figure 27 Structure of perylene bisimide phosphoramidite **16** and constitution of the (*S*)-GNA backbone. **B**:**H** base pair used in this study

The **PBI**-contained GNA oligonucleotides were synthesized by using a DNA synthesizer. **PBI** phosphoramidite **16** was dissolved in CH_3CN for use in the DNA synthesizer and the coupling time was three minutes. The synthesis and detritylation of GNA strands was followed by an additional purification step with a reversed-phase HPLC column, and the **PBI**-containing GNA oligonucleotides were obtained in high purities. The modified oligonucleotides were identified by MALDI spectrometry.

3.1.2.2 Thermal stability

Thermal stability of DNA duplexes was usually measured as a main tool for investigating the effects of modification on DNA. In order to investigate how the **PBI** surrogate will influence the GNA duplexes, the melting point (T_m) of the modified duplexes should be measured first.

The stability of GNA duplexes containing a single **PBI** (**B**) was first investigated. Table 1 shows the UV-melting data of duplexes with **B** in the middle of 16mer duplexes and two reference duplexes. It is noteworthy that all GNA duplexes investigated in this work contained only A and T nucleotides, in order to keep the GNA scaffold as simple as possible. Pairing **B** with the ethylene glycol abasic site **H** afforded a duplex with a melting point of 49 ^{o}C (**GNA2**, Table 1), compared to 54 ^{o}C for an A:T base pair at the same position (**GNA1**, Table 1). Replacing the abasic site **H** of the **B**:**H** base pair in **ON3**:**ON4** (**GNA2**, Table 1) for the natural nucleobases T or A, both resulting in **B**:T and **B**:A base pairs, reduced the stability by an additional 6 ^{o}C (**GNA3** and **GNA4**, Table 1). Apparently, these larger natural nucleobases could not be accommodated well opposite the space-consuming nucleobase **B**, suggesting that the **PBI** nucleobase was accommodated within the π-π stacking of the GNA duplex (Figure 28A).

We also investigated duplexes that contained two adjacent **PBI** base pairs. Incorporation of a second adjacent **B**:**H** base pair positioning the **PBI** on opposite strands (**GNA5** and **GNA6**, Table 1) increased the duplex melting temperature (T_m = 65 ^{o}C and 61 ^{o}C, respectively), by 11 ^{o}C and 7 ^{o}C, respectively, upon the melting temperatures of the reference Watson–Crick duplexes (**GNA1**, Table 1, T_m = 54 ^{o}C). Replacing the abasic site **H** of the **B**:**H** base pair with the natural nucleobase T (**GNA8**, Table 1) improved stability by an additional 6 ^{o}C. However, when the two **PBI** dyes were sited in one same oligonucleotide, the stability of the duplex **GNA7** was reduced by 12 ^{o}C (Figure 28A).

.

Table 1 Thermal stabilities of **PBI**-containing 16mer GNA duplexes together with Watson–Crick reference duplexes [a]

Entry	Sequence		T_m (°C)
GNA1	3′-TAAAAATAATAATATT-2′	(**ON01**)	54
	2′-ATTTTTATTATTATAA-3′	(**ON02**)	
GNA2	3′-TAAAAATHATAATATT-2′	(**ON03**)	49
	2′-ATT TTTABTATTATAA-3′	(**ON04**)	
GNA3	3′-TAA AAATAATAA TATT-2′	(**ON01**)	48
	2′-ATT TTTABTATTATAA-3′	(**ON04**)	
GNA4	3′-TAA AAATTATAATATT-2′	(**ON05**)	48
	2′-ATTTTTABTATTATAA-3′	(**ON04**)	
GNA5	3′-TAA AAATHBTAATATT-2′	(**ON06**)	65
	2′-ATT TTTABHATTATAA-3′	(**ON07**)	
GNA6	3′-TAAAAATBHTAATATT-2′	(**ON08**)	61
	2′-ATTTTTAHBATTATAA-3′	(**ON09**)	
GNA7	3′-TAAAAATBBTAATATT-2′	(**ON10**)	42
	2′-ATTTTTAHHATTATAA-3′	(**ON11**)	
GNA8	3′-TAAAAATTBTAATATT-2′	(**ON12**)	60
	2′-ATTTTTABTATTATAA-3′	(**ON04**)	
GNA9	3′-TAAAAAHBHTAATATT-2′	(**ON13**)	50
	2′-ATTTTTBHBATTATAA-3′	(**ON14**)	
GNA10	3′-TAAAAAHBHBAATATT-2′	(**ON15**)	50
	2′-ATTTTTBHBHTTATAA-3′	(**ON16**)	
GNA11	3′-TAAAAHBAAHBATATT-2′	(**ON17**)	68
	2′-ATTTTBHTTBHTATAA-3′	(**ON18**)	
GNA12	3′-TAAAHBTAATHBTATT-2′	(**ON19**)	58
	2′-ATTTBHATTABHATAA-3′	(**ON20**)	
GNA13	3′-TAAAAABTHTAATATT-2′	(**ON21**)	46
	2′-ATTTTTHTBATTATAA-3′	(**ON22**)	
GNA14	3′-TAAAAABAHTAATATT-2′	(**ON23**)	42
	2′-ATTTTTHABATTATAA-3′	(**ON24**)	
GNA15	3′-TAAAAABTHTAATATT-2′	(**ON21**)	52
	2′-ATTTTTHABATTATAA-3′	(**ON24**)	
GNA16	3′-TAAAAABAHTAATATT-2′	(**ON23**)	53
	2′-ATTTTTHTBATTATAA-3′	(**ON22**)	

[a] Conditions: 10 mM sodium phosphate, 100 mM NaCl, and 2 μM individual strands

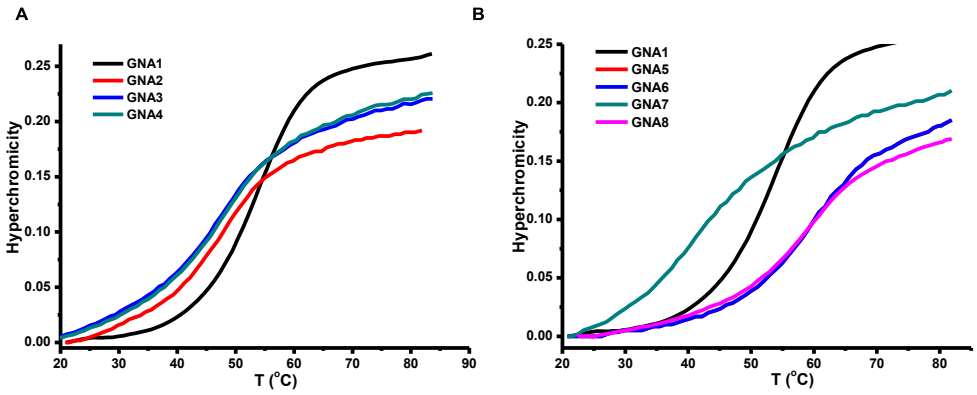

Figure 28 UV-melting curves of duplexes (from **GNA1** to **GNA8**). Changes in absorbance upon heating as monitored at 260 nm. Conditions: 10 mM sodium phosphate, 100 mM NaCl, pH 7.0, and 2 μM of each strand

The results encouraged us to incorporate more than two **PBI**s into the GNA duplexes, thus the duplexes **GNA9** and **GNA10** were synthesized. **GNA9** contained three **PBI** dyes in the form of the interstrand **BHB**/**HBH** with the opposite abasic site **H**. However, the result was quite disappointing; the stability of the duplex **GNA9** was reduced by 4 ^{o}C. As the number of **PBI** dyes in the GNA duplex increased to four in the form of zipper-like **BHBH**/**HBHB**, the T_m of duplex **GNA10** was about 50 ^{o}C. It seemed only the duplexes bearing one **PBI** interstrand dimer **BH**/**HB** increased thermal stability. We also synthesized the duplexes **GNA11** and **GNA12**, and both of them contained two pairs of **PBI** interstrand dimers. For **GNA11**, the two **PBI** dimers were separated by two natural base pairs A/T, while the **PBI** dimers of **GNA12** were separated by four natural base pairs A/T. Both of the duplexes were stabilized by 14 ^{o}C and 4 ^{o}C, respectively.

PBI in the dimeric form might have a potential application as a probe for mismatched GNA base pair detection. **GNA13**, **GNA14**, **GNA15** and **GNA16** were synthesized and studied; they contained an interstrand **PBI** dimer that was separated by one intervening base pair A/T, T/T or A/A with the counterbase **H**. Figure 29B displays the melting curves of these duplexes. When the separated base pair was mismatched with base pair T/T or A/A, T_m of **GNA13** and **GNA14** was 46 ^{o}C and 42 ^{o}C, respectively. This indicated that the duplexes were highly destabilized. However,

when the intervening separated base pair was matched base pair A/T, the melting temperatures of **GNA15** and **GNA16** were 52 °C and 53 °C, respectively; they showed similar stability to the reference duplex **GNA1**. Compared to **GNA2** with only one pair of **B**:**H** in the middle of duplex, which destabilized the duplex by 6 °C, it seemed that the **PBI** dyes in **GNA15** and **GNA16** had a minor influence on the stability of the GNA duplexes (Figure 29).

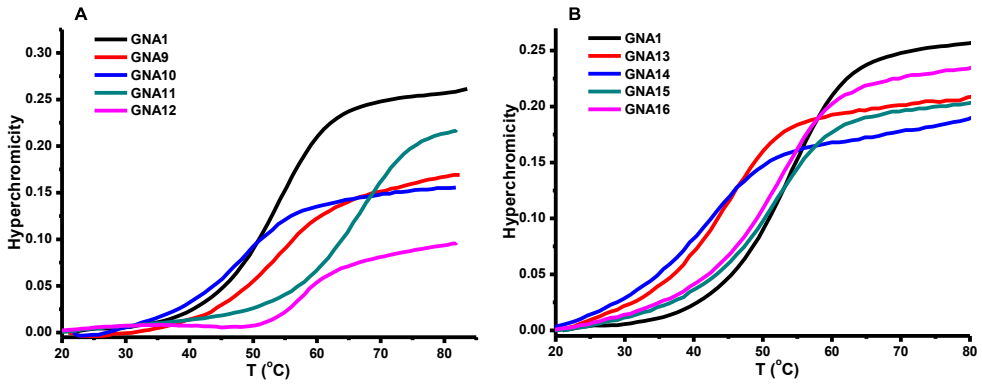

Figure 29 UV-melting curves of duplexes (from **GNA9** to **GNA16**). Changes in absorbance upon heating as monitored at 260 nm. Conditions: 10 mM sodium phosphate, 100 mM NaCl, pH 7.0, and 2 μM of each strand

3.1.2.3 UV/Vis-absorption spectroscopy

UV/Vis-absorption is a very important tool for understanding the relative conformation of closely located molecules. Hence, UV/Vis-absorption of **PBI**-modified GNA should be measured.

Figure 30 shows that the UV/Vis-absorption spectra of duplex **GNA5**, **GNA6** and their corresponding single strands **ON6**, **ON7**, **ON8** and **ON9** at room temperature. Both the absorption bands shifted bathochromically and the relative ratios of the absorption bands at 505 and 545 nm were significantly changed in duplexes compared to the relative ratio of the 0→1 and 0→0 vibronic transitions of the **PBI** monomer in single strands. This showed that there were π-π excitonic interactions of the two **PBI** dyes inside **GNA5** and **GNA6** at room temperature.

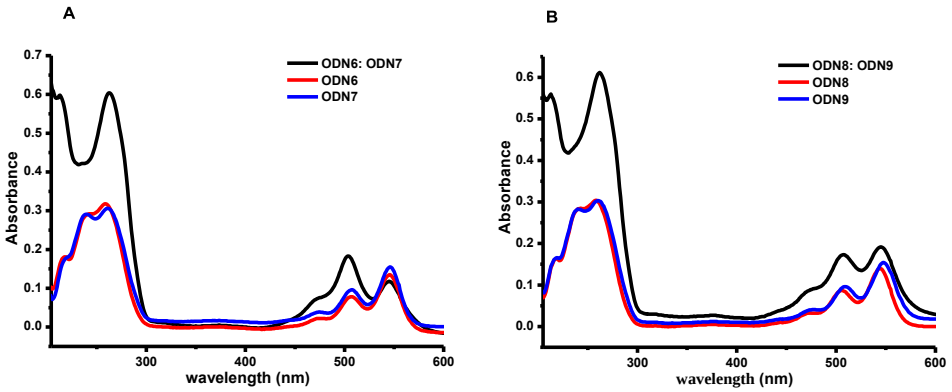

Figure 30 UV/Vis-absorption spectra of GNA duplexes and their corresponding single strands. Conditions: 10 mM sodium phosphate, 100 mM NaCl, pH 7.0, and 2 μM of each strand. (A) **ON6**:**ON7**, **ON6** and **ON7** at 20 °C. (B) **ON8**:**ON9**, **ON8** and **ON9** at 20 °C

As expected, absorption of the **PBI** in the duplex **GNA7** was the same as that in the single strand **ON10**, while the two **PBI** chromophores existed in the same single strand **ON10** in the form of **BB** with the couterbases **HH** (Figure 31).

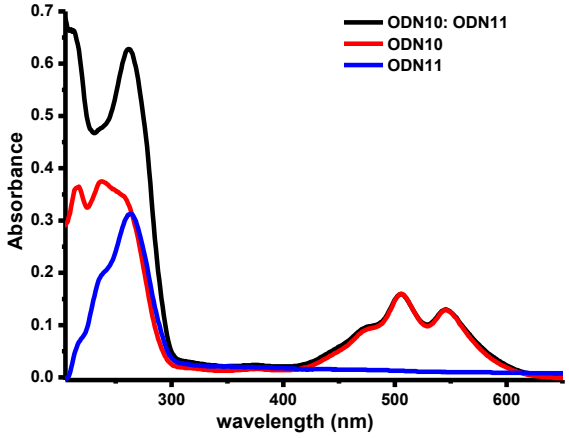

Figure 31 UV/Vis-absorption spectra of GNA duplexes and their corresponding single strands at 20 °C (**ON10**:**ON11**, **ON10** and **ON11**). Conditions: 10 mM sodium phosphate, 100 mM NaCl

GNA9 contained three **PBI** dyes in the form of the interstrand **BHB**/**HBH** with the opposite abasic site **H**. Figure 32A shows that the UV/Vis-absorption spectrum of **GNA9** at low temperatures was different from the corresponding spectra of the **PBI** monomer and dimer in oligonucleotides. As the obvious change of peak ratio occurred between 50 °C and 60 °C, the range of the melting temperatures of the duplexes (T_m =

50 °C). However, if there were four interstrand **PBI** chromophores in the duplex, the situation was definitely different. The UV/Vis-absorption spectrum of **GNA10** showed similar absorption of **PBI** dimer in the duplex; as the temperature increased, the change of band absorption was not very obvious even though the duplex completely denatured. This was caused by the π-π excitonic interactions between **PBI** inside the oligonucleotides.

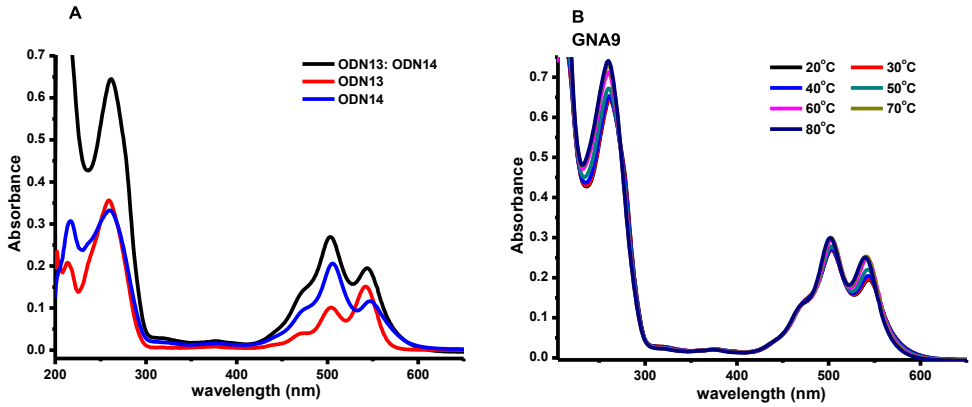

Figure 32 UV/Vis-absorption spectra of GNA duplexes and their corresponding single strands. Conditions: 10 mM sodium phosphate, 100 mM NaCl, pH 7.0, and 2 μM of each strand. (A) **ON13**:**ON14**, **ON13** and **ON14** at 20 °C. (B) **GNA9** temperature-dependent

As we know, more than two **PBI** chromophores in the form of interstrand would result in the destabilization of the duplexes. On the other hand, if the two **PBI** dyes in one single strand were separated by intervening matched GNA natural bases, the duplexes would be stabilized (**GNA11** and **GNA12**). The UV/Vis-absorption spectra of **GNA11** and **GNA12** were very similar to that of **GNA10**. At 20 °C, both the single strands (**ON17**, **ON18**, **ON19** and **ON20**) and double strands (**GNA11** and **GNA12**) showed that there were strong π-π excitonic interactions of the two **PBI** dyes. Even as the temperature increased to 80 °C, at which the duplexes had been completely dehybridized, there were still strong π-π excitonic interactions of the two **PBI** dyes (Figure 33).

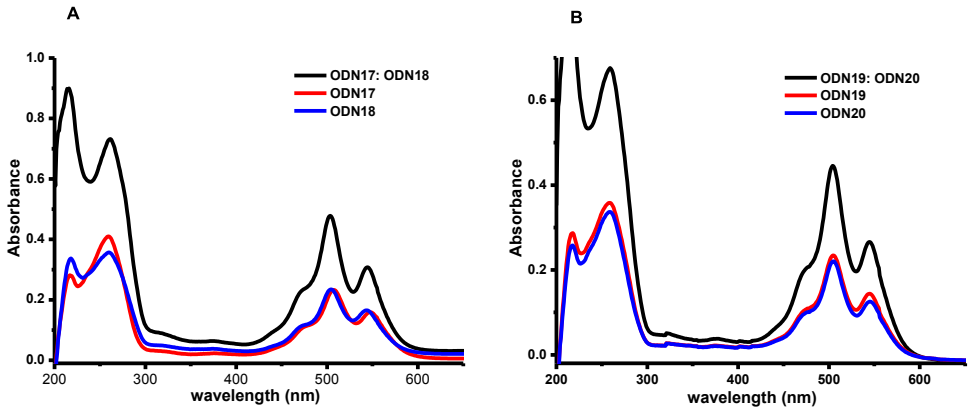

Figure 33 UV/Vis-absorption spectra of GNA duplexes and their corresponding single strands at 20 °C. Conditions: 10 mM sodium phosphate, 100 mM NaCl, pH 7.0, and 2 μM of each strand. (A) **ON17**:**ON18**, **ON17** and **ON18**. (B) **ON19:ON20**, **ON19** and **ON20**

We have mentioned that **PBI** dye might be used as a tool for the detection of mismatched GNA base pairs. The temperature-dependent UV/Vis-absorption of these kinds of duplexes was measured. **GNA13** had two **PBI** chromophores, which had been separated by the intervening mismatched natural **T**:**T** base pair; as the temperature increased, the absorption of the **PBI** had no obvious change, and always showed the corresponding spectra of the **PBI** monomer in oligonucleotides (Figure 34A). However, the situation was completely different for **GNA14** in which the two chromophores were separated by the mismatched **A**:**A** base pair. At 20 °C, we found that the **PBI** chromophores could interact with each other. As the temperature increased to 80 °C, only the corresponding spectrum of the **PBI** monomer in oligonucleotides was observed (Figure 34B). For **GNA15** and **GNA16** in which two **PBI** chromophores were separated by the matched **A**:**T** base pair, no matter how the temperature changed, only the **PBI** monomer band absorption was observed.

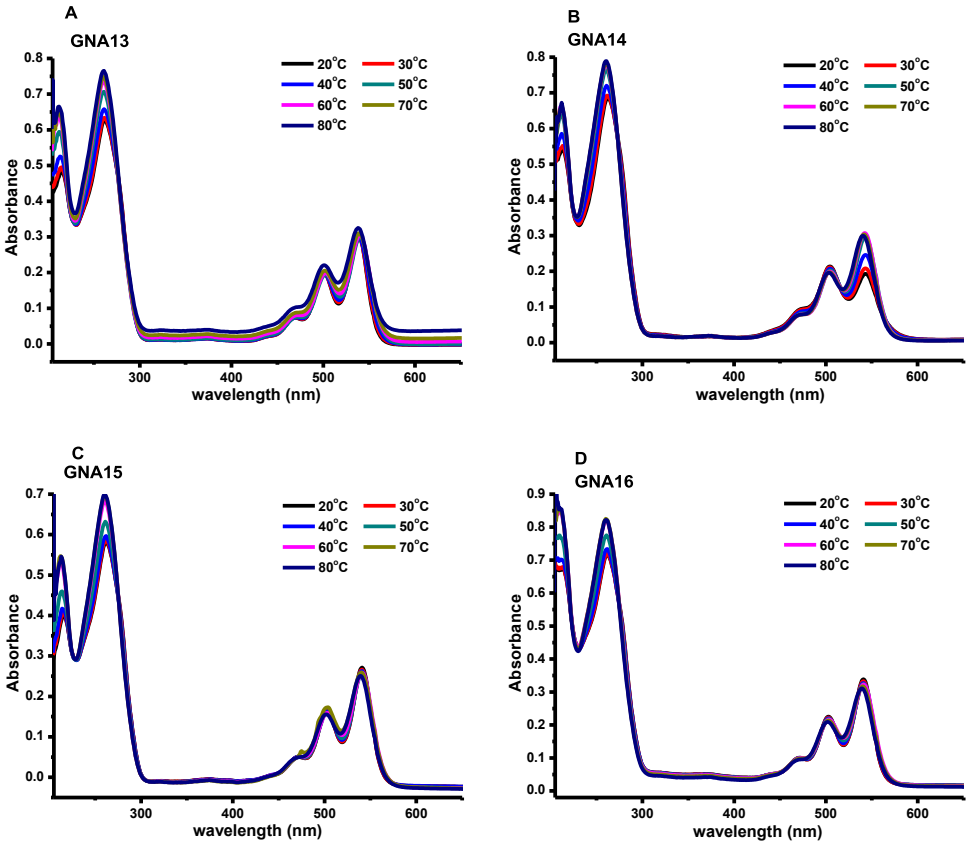

Figure 34 Temperature-dependent UV/Vis-absorption spectra of GNA duplexes. Conditions: 10 mM sodium phosphate, 100 mM NaCl, pH 7.0, and 2 µM of each strand. (A) **GNA13**. (B) **GNA14**. (C) **GNA15**. (D) **GNA16**

3.1.2.4 CD spectroscopy

In order to learn more about the conformation of **PBI** in GNA duplexes, CD spectroscopy was applied to gain more insight into the excitonic interaction of the **PBI** dyes inside GNA duplexes.

Figure 35 shows the CD spectrum of **GNA2** that contained only one **PBI** chromophore with **H** or **T** as the opposite abasic site. The CD signals in the GNA absorption region were almost identical to those of the native GNA duplex. No long-wavelength CD bands of exciton coupling (EC-CD) between the two **PBI** chromophores were observed.

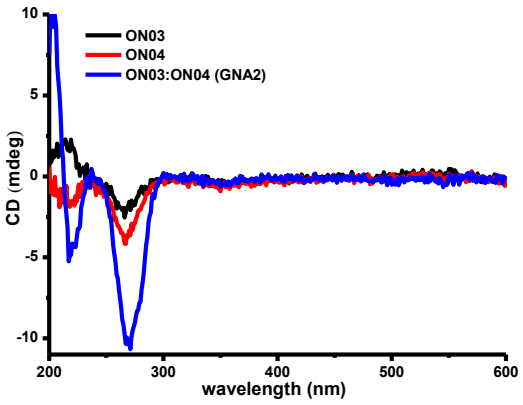

Figure 35 CD spectra of modified GNA duplexes and their corresponding single strands at 20 °C. Conditions: 10 mM sodium phosphate, 100 mM NaCl, pH 7.0, and 8 μM of each strand. **ON3**, **ON4** and **ON3:ON4**

As shown in Figure 36A, CD spectra of the duplexes **GNA5**, **GNA6** and **GNA7** were investigated. **GNA5** and **GNA6** contained the interstrand **PBI** dimer in the duplexes, while two **PBIs** of **GNA7** sat in the same single strand. For **GNA5**, in addition to the CD spectrum of the duplex poly[d(A)]:poly[d(T)] in the base-pair region (200–300 nm), the CD spectrum of duplex **GNA5** also displayed a strong negative band at 565 nm and a positive band at 505 nm. These long-wavelength CD bands were attributed to the exciton-coupling CD between the two **PBI** chromophores.[86] Remarkably, the long-wavelength bands of **GNA6** were different

from **GNA5**, and the CD spectrum showed a mirror image; there was a strong positive band at 565 nm and a negative band at 505 nm (Figure 36B). The difference between **GNA5** and **GNA6** was in accordance with a similar observation reported by Lewis and co-workers.[87] The intensity of the positive and negative bands of the exciton-coupling CD spectra for two identical parallel chromophores can be described with the following equation:

$$\Delta\varepsilon \approx \pm\frac{\pi}{4\lambda}\mu_a\mu_d R_{da}^{-2}\sin(2\theta)$$

Where μ_a and μ_d are the electronic transition dipole moments of the two chromophores, μ_{da} is their center-to-center distance, and θ is the angle between their transition dipoles. The intensity is sin(2θ) dependent. When θ = 0°, 90°, or 180°, the intensity is zero. The maximum intensity is obtained when θ = 45° or 135°. However, the exact value is very difficult to obtain. Comparing **GNA5** and **GNA6**, the alignment directions of two same **PBI** chromophores were opposite, so the mirror long-wavelength bands in the region of 500–600 nm were reasonable. The CD spectrum of **GNA7** were also investigated; almost no long-wavelength bands in the region of 500 nm to 600 nm for the single strand **ON10** were observed at 20 °C

The CD spectra of **GNA9** (three **PBI** chromophores interstrand) and **GNA10** (four **PBI** chromophores interstrand) were also measured. Because there were strong exciton-coupling CD spectra for the single strands **ON14**, **ON15** and **ON16**, the situation was more complicated. At 20 °C, there was a strong negative band at 575 nm and a positive band at 505 nm for **ON14**, and a strong positive band at 570 nm and a negative band at 505 nm for **ON16** (Figures 37A and 37B). On the other hand, the CD spectrum of duplex **GNA9** at 20 °C displayed strong negative bands at 575 nm and 490 nm and a strong positive band at 550 nm. There was a strong negative band at 575 nm and a positive band at 510 nm in the CD spectrum of duplex **GNA10** (Figures 37A and 37B).

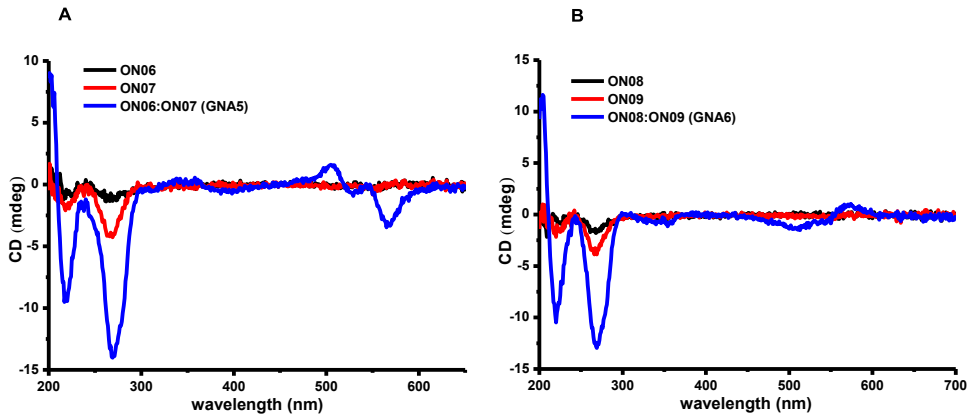

Figure 36 CD spectra of modified GNA duplexes and their corresponding single strands at 20 °C. Conditions: 10 mM sodium phosphate, 100 mM NaCl, pH 7.0, and 8 μM of each strand. (A) **ON06**, **ON07** and **ON06:ON07**. (B) **ON08**, **ON09** and **ON08:ON09**

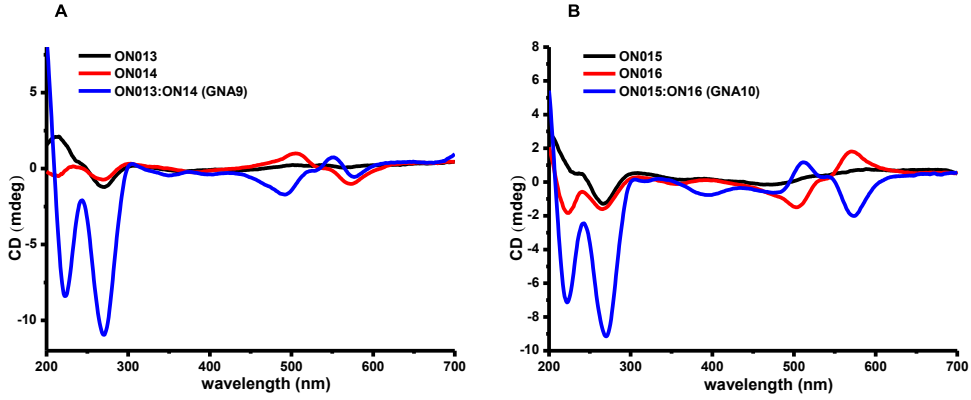

Figure 37 CD spectra of modified GNA duplexes and their corresponding single strands at 20 °C. Conditions: 10 mM sodium phosphate, 100 mM NaCl, pH 7.0, and 8 μM of each strand. (A) **ON13**, **ON14** and **ON13:ON14**. (B) **ON15**, **ON16** and **ON15:ON16**

UV/Vis-absorption spectra of **GNA13**, **GNA14**, **GNA15** and **GNA16** in which two **PBI** chromophores were separated by one matched base pair **A**:**T** or one mismatched base pair **T**:**T** or **A**:**A** were also measured. Only the UV/Vis-absorption spectrum of **GNA14** was different from the other three. As shown in Figure 38, **GNA13**, **GNA15** and **GNA16** displayed a strong negative band at 550 nm in the long-wavelength region, which might be induced by the exciton-coupling between **PBI** chromophores with nature base pairs. However, the CD spectrum of **GNA14** displayed a strong positive band at 570 nm and a strong negative band at 505 nm, which were the typical exciton-coupling CDs of two same **PBI** chromophores. These

CD result were consistent with the UV/Vis-absorption spectra and gave us more confidence to use **PBI** as a potential mismatched-base pair detector.

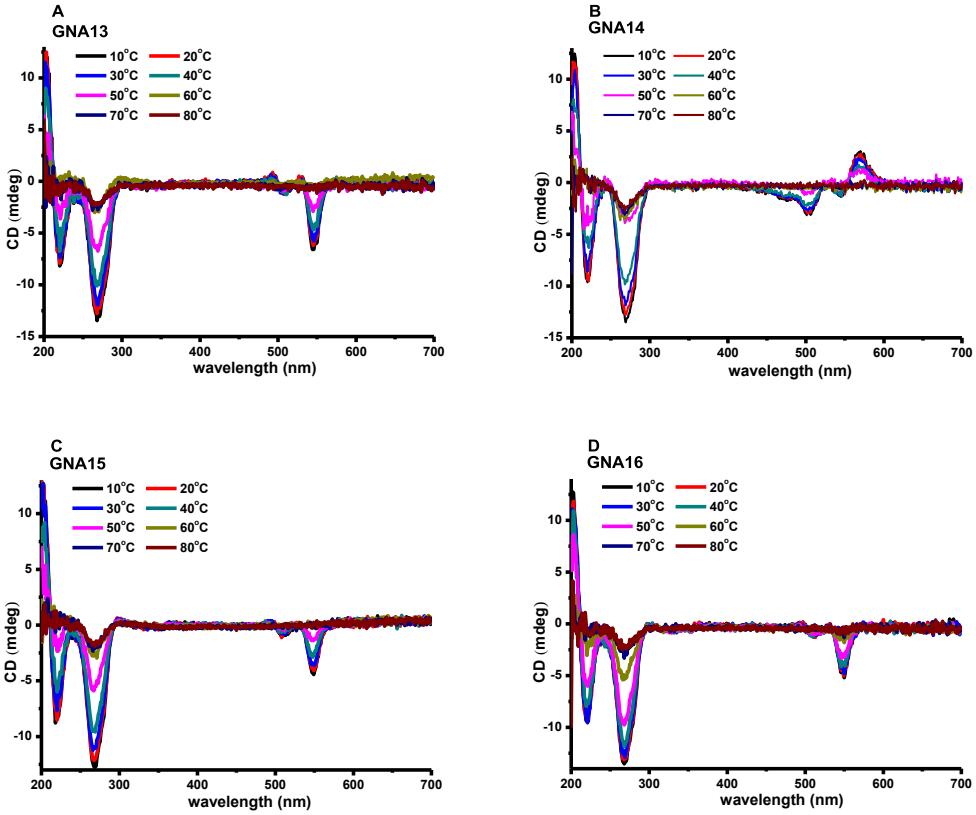

Figure 38 Temperature-dependent CD spectra of modified GNA duplexes and their corresponding single strands. Conditions: 10 mM sodium phosphate, 100 mM NaCl, pH 7.0, and 8 μM of each strand. (A) **GNA13**. (B) **GNA14**. (C) **GNA15**. (D) **GNA16**

3.2.1.5 Fluorescence spectroscopy

PBI and its derivatives have been applied as fluorescent dyes in organic materials owing to their outstanding photochemical stability as well as the high fluorescence quantum yields.[88] Based on these, **PBI** may be used as a potential probe for fluorescent DNA/RNA analytics and functionalized DNA-based architectures. It is disappointing that the fluorescence is strongly quenched as a result of the π-π stacking between **PBI** chromophores and the adjacent DNA bases in our case.

3.1.3 Phthalocyanine as an artificial GNA surrogate

3.1.3.1 Synthesis of phthalocyanine-modified GNA oligonucleotides

With the phthalocyanine phosphoramidite building block **17** in hand, the phthalocyanine-modified oligonucleotides were prepared (Figure 39). To avoid precipitation of the phthalocyanine **17** during the automated DNA synthesis, a building block solution was prepared in THF, and the coupling time for **17** was extended from 1.6 min (standard) to 10 min. The other processes were the same as synthesis of **PBI** modified oligonucleotides.

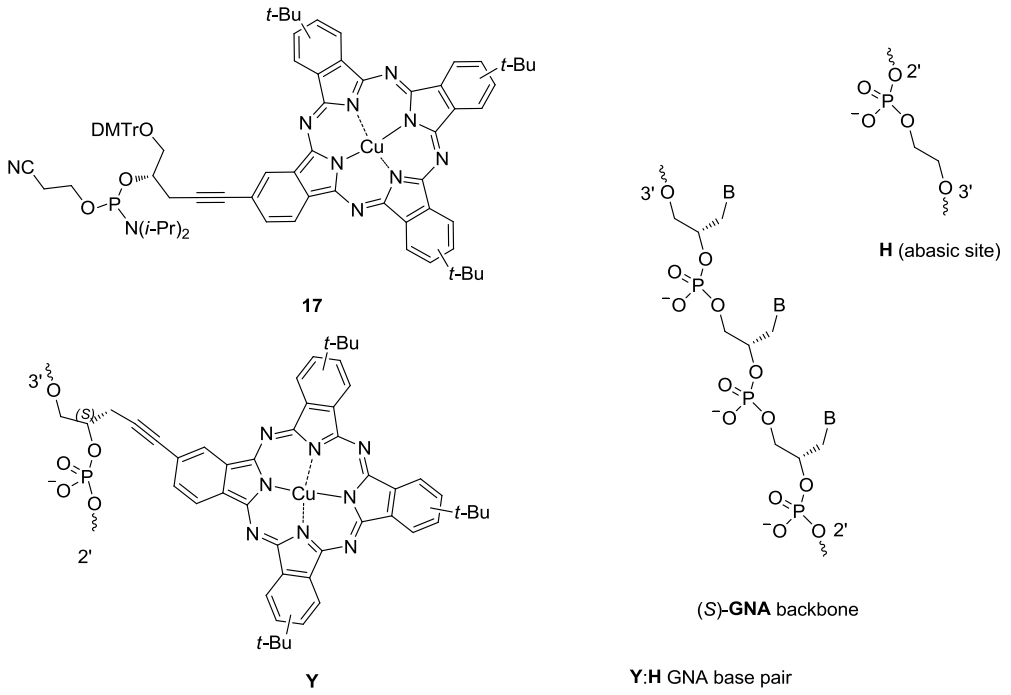

Figure 39 Structure of phthalocyanine phosphoramidite **17** and constitution of the (*S*)-GNA backbone. **Y**:**H** base pair used in this study

3.1.3.2 Thermal stability

Table 2 shows the 16mer GNA duplexes with phthalocyanine surrogate in the middle and two reference duplexes. In comparison to the reference **GNA1**, pairing

phthalocyanine with the ethylene glycol abasic site **H** was strongly destabilized (**GNA17**, Table 2); the duplex could not form a stable structure at 20 °C. This result was unexpected. However, incorporation of a second adjacent **Y**:**H** base pair positioning the phthalocyanine on opposite strands (**GNA18** and **GNA19**, Table 2) could form stable duplexes. The T_m values of **GNA18** and **GNA19** were 54 °C and 62 °C, respectively. In contrast, the stability of **GNA18** was very close to the reference **GNA1**, and the interstrand dimer inside the duplex **GNA19** stabilized the duplex by 8 °C. When the two phthalocyanine chromophores existed in the same single strand **ON30**, the duplex GNA again became very unstable. When more than two interstrand phthalocyanine chromophores were incorporated into the duplexes **GNA21** and **GNA22**, they could not form Watson-Crick structures at 20 °C. We tried to synthesize the oligonucleotides containing more than two phthalocyanine chromophores; however, it was impossible to purify them by the general HPLC method as the content of acetonitrile of the mixed eluents reached almost 100%.

Table 2 Thermal stabilities of phthalocyanine-containing 16mer GNA duplexes together with Watson–Crick reference duplexes [a]

Entry	Sequence		T_m (°C)
GNA17	3′-TAA AAA THA TAA TATT-2′	(**ON03**)	-
	2′-ATT TTT AYT ATT ATAA-3′	(**ON25**)	
GNA18	3′-TAA AAATHYTAATATT-2′	(**ON26**)	54
	2′-ATT TTTAYHATTATAA-3′	(**ON27**)	
GNA19	3′-TAAAAATYHTAATATT-2′	(**ON28**)	62
	2′-ATTTTTAHYATTATAA-3′	(**ON29**)	
GNA20	3′-TAAAAATYYTAATATT-2′	(**ON30**)	-
	2′-ATTTTTAHHATTATAA-3′	(**ON11**)	
GNA21	3′-TAAAAAHYHTAATATT-2′	(**ON31**)	-
	2′-ATTTTTYHYATTATAA-3′	(**ON32**)	
GNA22	3′-TAAAAAHYHYAATATT-2′	(**ON33**)	-
	2′-ATTTTTYHYHTTATAA-3′	(**ON34**)	
GNA23	3′-Y TAA AAA TTA TAA TATT-2′	(**ON35**)	65
	2′-ATT TTT AAT ATT ATAA Y-3′	(**ON36**)	

[a] Conditions: 10 mM sodium phosphate, 100 mM NaCl, and 2 μM individual strands

GNA23 bears the phthalocyanine moiety (**Y**) attached to the 3′-terminus of the

two oligonucleotides. With caps on the end, the duplex **GNA23** was stabilized by 11 ^{o}C (Figure 40). It is noteworthy that this kind of aggregation may be applied to supramolecular material.

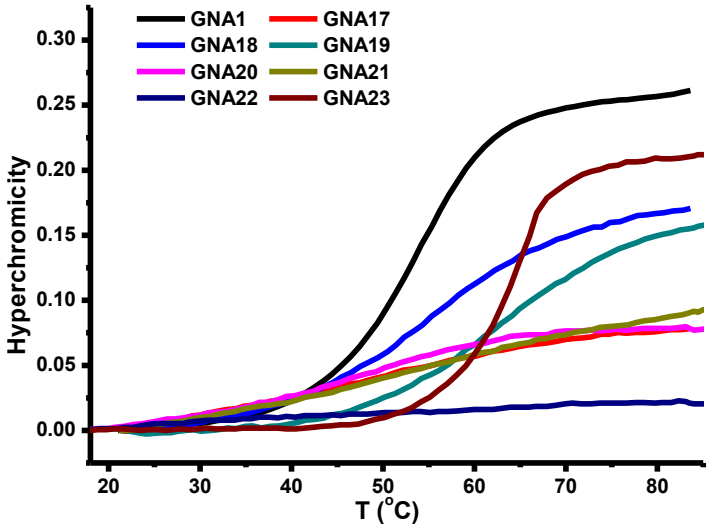

Figure 40 UV-melting curves of duplexes (from **GNA17 to GNA23**). Changes in absorbance upon heating as monitored at 260 nm. Conditions: 10 mM sodium phosphate, 100 mM NaCl, pH 7.0, and 2 mM of each strand

3.1.3.3 UV/Vis-absorption spectroscopy

Because we know that only the duplexes **GNA19**, **GNA20** and **GNA23** could form stable duplexes at 20 ^{o}C, herein we discuss the UV/Vis-absorption spectra of only these three GNA duplexes and their corresponding single strands in detail.

The UV/Vis-absorption spectra of **GNA18** and **GNA19** (Figure 41) at low temperatures were different from the corresponding spectra of single strands with one phthalocyanine. Both the absorption bands shifted bathochromically from 694 nm to 684 nm, and the relative ratios of the absorption bands at 642 nm and 694 nm were significantly changed compared to the relative ratio of the 0→1 and 0→0 vibronic transitions of the phthalocyanine monomer in single strands. This suggested that there was π-π excitonic interaction of the two phthalocyanine dyes inside **GNA18** and

GNA19 at room temperature. At high temperature, the absorption maxima shifted to those that are typical for a monomer phthalocyanine modification in single strands.

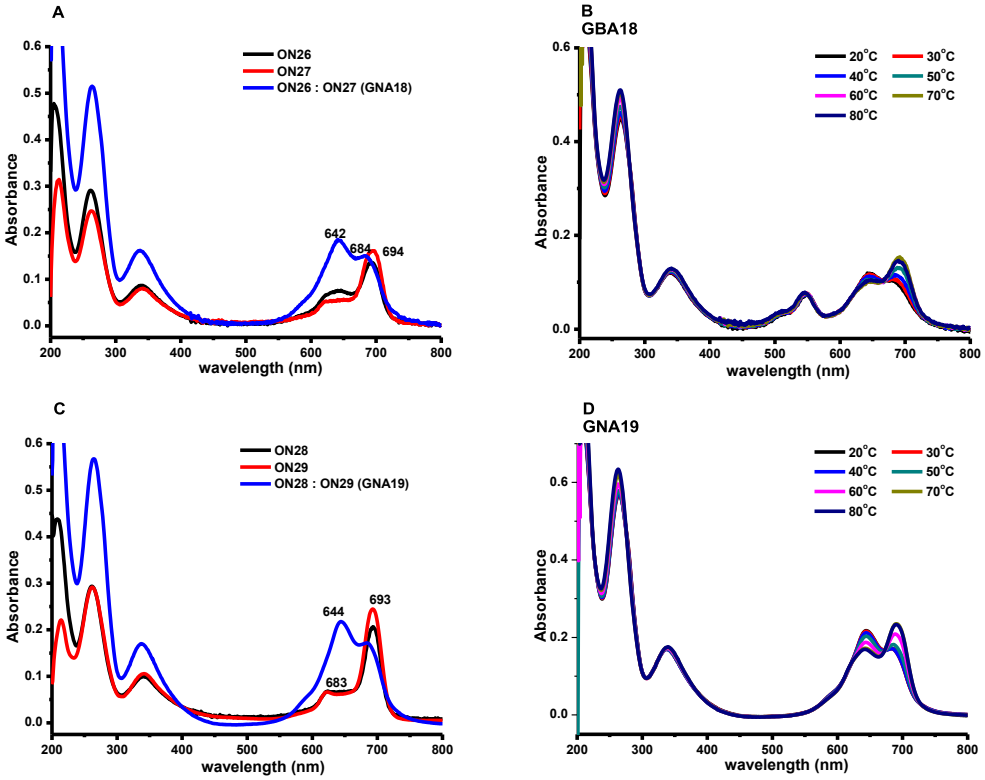

Figure 41 UV/Vis-absorption spectra of GNA duplexes and their corresponding single strands. Conditions: 10 mM sodium phosphate, 100 mM NaCl, pH 7.0, and 2 µM of each strand. (A) **ON26**:**ON27**, **ON26** and **ON27** at 20 °C. (B) **GNA18** temperature-dependent. (C) **ON28**:**ON29**, **ON28** and **ON29** at 20 °C. (D) **GNA19** temperature-dependent

3.1.3.4 Self-Assembly of a Phthalocyanine-Linked GNA Dumbbell into Supramolecular Polymers

In contrast to the duplexes **GNA18** and **GNA19**, the situation was completely different; the UV/Vis-absorption spectrum of **GNA23** was measured in the normal conditions (10 mM sodium phosphate, 100 mM NaCl, pH 7.0, and 2 µM duplex) at 20 °C. No typical absorption for a single phthalocyanine modification in oligonucleotides was observed. The two phthalocyanine dyes between two independent duplexes strongly interacted with each other. As the temperature increased, the

long-wavelength absorption region of phthalocyanine barely varied. This indicated that the phthalocyanine could still interact even after complete denaturation of the GNA duplex (Figure 42C). Next, we continued to investigate the monomer-dimer equilibrium for **GNA23**, which is dependent upon salt concentration and temperature, as well as the concentration of the duplex. This phthalocyanine existed predominantly as a monomeric state at 20 ^{o}C in aqueous buffer in the absence of added salt. As the temperature increased, the phthalocyanines seemed to interact with each other again (Figure 42A). However, when the concentration of salt NaCl was increased to 10 mM, the aggregation of the duplex **GNA23** became dominant at 20 ^{o}C (Figure 42B). We also measured the UV/Vis-absorption spectra of **GNA23** in 30 mM and 60 mM NaCl at 20 ^{o}C, and it indicated aggregation among this kind of duplex would be intensified as the salt concentration increased (Figure 42D).

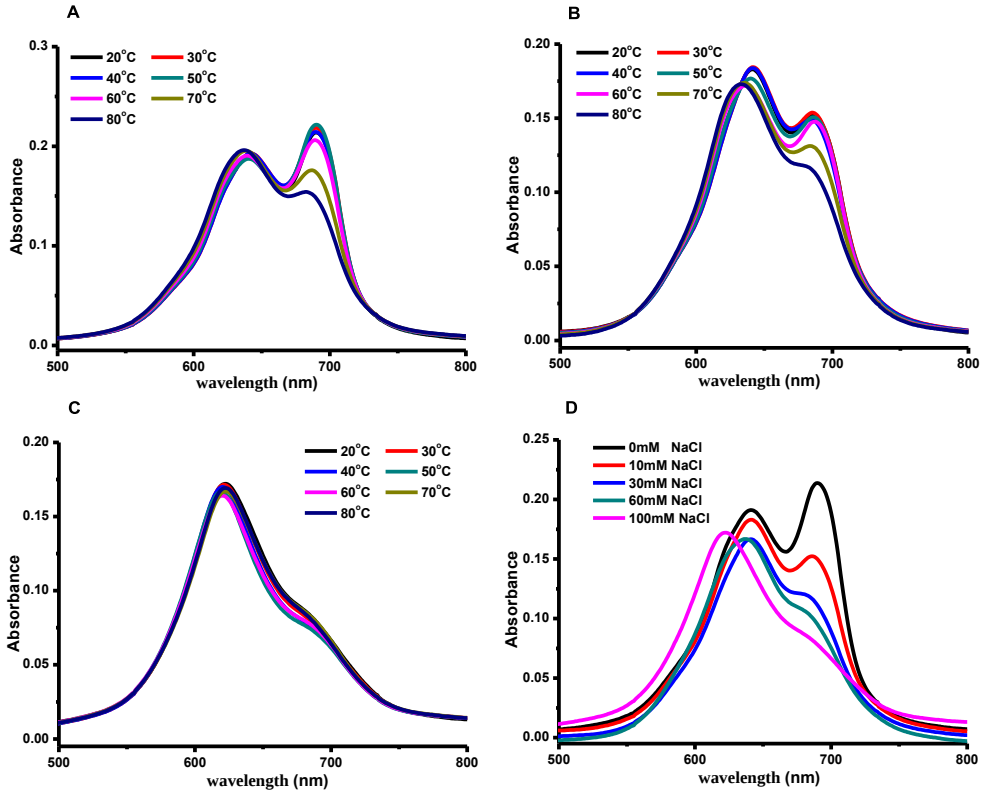

Figure 42 UV/Vis-absorption spectra of **GNA23**. Conditions: 10 mM sodium phosphate, pH 7.0, and 2 μM of each strand. (A) temperature dependence without salt. (B) temperature dependence in 10mM NaCl. (C) temperature dependence in 100mM NaCl. (D) NaCl concentration dependence at 20 ^{o}C

The UV/Vis-absorption spectrum of **GNA23** was also measured in 1 μM. In contrast to the spectra in 2 μM, the ratio of monomeric phthalocyanine was much higher in the same buffer and salt conditions. Moreover, the trend of aggregation was similar as the salt concentration increased (Figure 43).

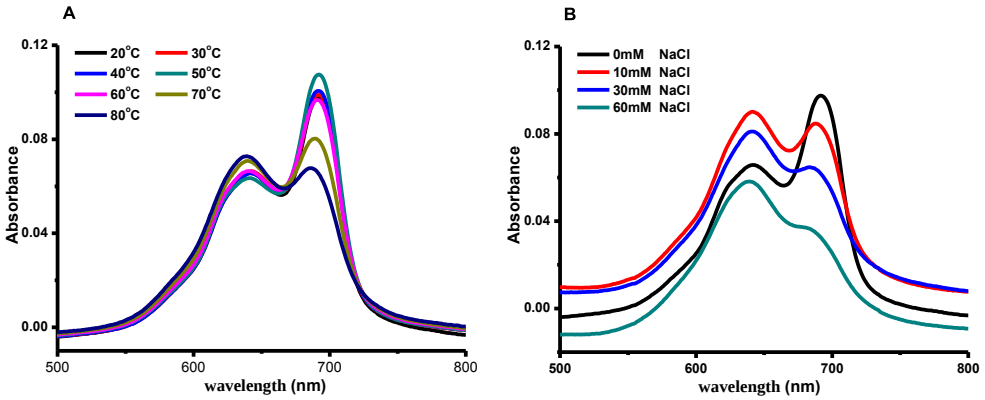

Figure 43 UV/Vis-absorption spectra of **GNA23**. Conditions: 10 mM sodium phosphate, pH 7.0, and 1 μM of each strand. (A) temperature dependence without salt. (B) NaCl concentration dependence at 20 ^{o}C

In addition, the CD spectra of the phthalocyanine-modified GNA duplexes were also measured to investigate the conformation. However, no long-wavelength CD bands of exciton coupling between the two phthalocyanine chromophores were found.

3.1.4 Interstrand stacking of heterochromophores as an artificial GNA surrogate

Our group successfully incorporated porphyrin into GNA as an artificial surrogate.[26] Even GNA bearing one interstrand porphyrins dimer inside the duplex was destabilized. So it is unrealistic to incorporate more porphyrins into GNA duplexes. Next, a series of oligonucleotides with three different chromophore surrogate (Porphyrin/**P**, Phthalocyanine/**Y**, Perylene bisimide/**B**, Figure 26) modifications in the middle were synthesized. This triggered our great interest in investigating heterochromophore interaction in GNA duplexes. Although there are no reports about heterochromophore interaction inside DNA scaffolds, we envisioned that this might give us some interesting results.

3.1.5 Interstrand stacking of PBI-porphyrin

3.1.5.1 Thermal stability

The influence of **PBI** and porphyrin on the stability of the duplexes was evaluated by thermal denaturation studies. I worked together with Hui Zhou from our group, and some of results were also described in his thesis.[25a] Table 3 displays the experimental T_m values of the duplexes that contained **PBI** and porphyrins, as well as of the reference duplex.

Table 3 Thermal stabilities of **PBI**-porphyrin 16mer GNA duplexes together with Watson–Crick reference duplexes [a]

Entry	Sequence		T_m (°C)
GNA1	3′-TAAAAATAATAATATT-2′	(**ON01**)	54
	2′-ATTTTTATTATTATAA-3′	(**ON02**)	
GNA24	3′-TAAAAATHPTAATATT-2′	(**ON37**)	64
	2′-ATTTTTABHATTATAA-3′	(**ON07**)	
GNA25	3′-TAAAAATHBTAATATT-2′	(**ON06**)	68
	2′-ATTTTTAPHATTATAA-3′	(**ON38**)	
GNA26	3′-TAAAAATPHTAATATT-2′	(**ON39**)	63
	2′-ATTTTTAHBATTATAA-3′	(**ON09**)	
GNA27	3′-TAAAAATBHTAATATT-2′	(**ON08**)	64
	2′-ATTTTTAHPATTATAA-3′	(**ON40**)	
GNA28	3′-TAAAAAHBHTAATATT-2′	(**ON13**)	78
	2′-ATTTTTPHPATTATAA-3′	(**ON41**)	
GNA29	3′-TAAAAAHPHTAATATT-2′	(**ON42**)	57
	2′-ATTTTTBHBATTATAA-3′	(**ON14**)	
GNA30	3′-TAAAAAHPHPAATATT-2′	(**ON43**)	70
	2′-ATTTTTBHBHTTATAA-3′	(**ON16**)	
GNA31	3′-TAAAAAHBHBAATATT-2′	(**ON15**)	66
	2′-ATTTTTPHPHTTATAA-3′	(**ON44**)	

[a] Conditions: 10 mM sodium phosphate, 100 mM NaCl, and 2 mM individual strands

As described in Table 3, **GNA24**, **GNA25**, **GNA26** and **GNA27** all contained the interstrand heterochromophores **PBI**-porphyrin dimer. In contrast to the T_m (54 ℃) of **GNA1** with two A:T base pairs at the same position, the four modified duplexes showed T_m at 64 ℃, 68 ℃, 63 ℃ and 64 ℃, respectively, demonstrating that the incorporation of a **PBI**-porphyrin pair had a stabilizing effect on the duplexes (ΔT_m = 10 ℃ for **GNA24**, ΔT_m = 14 ℃ for **GNA25**, ΔT_m = 9 ℃ for **GNA26** and ΔT_m = 10 ℃ for **GNA27**). When more than two heterochromophores were incorporated into GNA duplexes, duplex **GNA28** containing three chromophores in the form of sandwich-type **P-B-P** exhibited a melting point (T_m) of 78 ℃, and the duplex was stabilized by an additional 24 ℃. On the other hand, duplex **GNA29** was only stabilized by 3 ℃ in which the three heterochromophores arrayed in the form of

sandwich-type **B-P-B**. The melting points of **GNA30** and **GNA31** containing four heterochromophores (**B-P-B-P** and **P-B-P-B**) were 70 ℃ and 66 ℃, respectively. Figure 44 displays the UV-melting curves of the duplexes. As a result, it was revealed that **PBI**-porphyrin aggregation had remarkably positive effects on the stabilization of GNA duplexes.

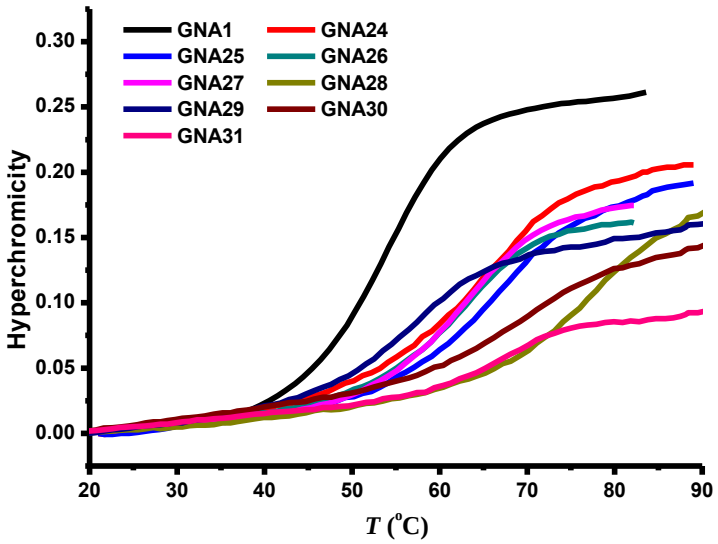

Figure 44 UV-melting curves of duplexes (from **GNA24** to **GNA31**). Changes in absorbance upon heating as monitored at 260 nm. Conditions: 10 mM sodium phosphate, 100 mM NaCl, pH 7.0, and 2 μM of each strand

3.1.5.2 UV/Vis-absorption spectroscopy

A J-aggregate is a type of dye with an absorption band that shows bathochromic shift of wavelength with increasing sharpness when it aggregates under the influence of a solvent or additive or concentration as a result of supramolecular self-organisation.[89] J-aggregate dyes are found with polymethine dyes in general, with cyanines, merocyanines, squaraine and perylene bisimides. One the other hand, H-aggregates displays hypsochromic shift of wavelength with low or no fluorescence. Almost all these kinds of aggregation are investigated among identical dyes. The heteroaggregation is seldom studied. To acquire information about the interaction

between **PBI** and porphyrin in the GNA duplexes, in the present study, the modified duplexes and their corresponding single strands are investigated by UV/Vis-absorption spectra.

The modified duplexes **GNA24**, **GNA25**, **GNA26** and **GNA27** all contained **B-P** dimer**.** Here we only gave the detailed analysis of **GNA24** as an example. Figure 45 shows UV absorption of **GNA24** and the corresponding single strands **ON0**4 and **ON37**; the soret band for porphyrin shifted bathochromically from 427 to 431 nm, whereas the **PBI** absorption band also had a small bathochromic shift from 508 to 514 nm and 546 to 550 nm, respectively. Moreover, the relative ratios of peak heights of porphyrin and **PBI** also changed. Together with T_m, we could clearly infer that there was interaction of the **PBI** and porphyrin in **GNA24**.

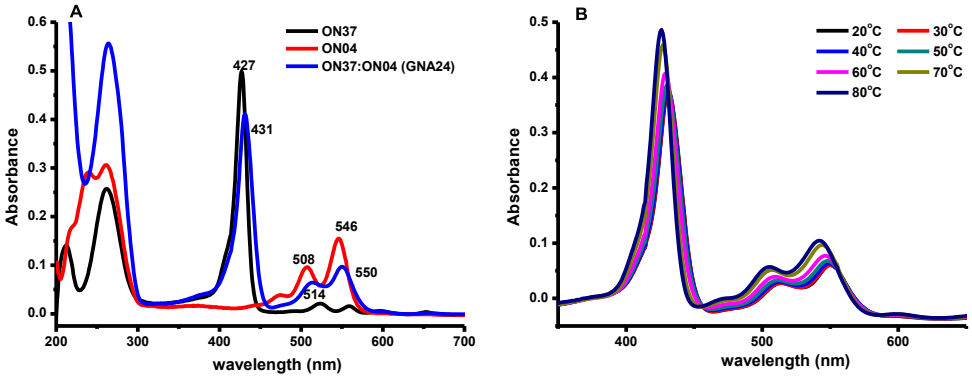

Figure 45 UV/Vis-absorption spectra of GNA duplexes and their corresponding single strands. Conditions: 10 mM sodium phosphate, 100 mM NaCl, pH 7.0, and 2 μM of each strand. (A) **ON37**, **ON04** and **ON37**:**ON04** at 20 °C. (B) **GNA24** temperature-dependent

As described in Figures 46A and 46B, the absorption spectrum of the duplex **GNA28** containing three chromophores in the form of sandwich-type **P-B-P** was investigated. Remarkably, the absorption properties of the duplex were different from the single strands. The absorption band for the porphyrin in single strands **ON41** showed a bathochromic shift from 409 nm to 426 nm, on the other hand, there were two absorption bands at 504 nm and 542 nm for **PBI** in single strand **ON13**. However, the broad absorption band appeared at 542 nm for **PBI** in the duplex **GNA28**. As the temperature increased from 20 ℃ to 90 ℃, the gradual dissociation of the duplex

GNA28 was observed, and the interaction of chromophores in the single strands in **ON15** and **ON34** was weakened. Moreover, Figures 46C and 46D show the absorption spectra of the duplex **GNA29**; there was an obvious bathochromic shift for the porphyrin from 424 nm to 433 nm upon the formation of the duplex **GNA29**. There was no absorption band shift for **PBI** observed, whereas the ratio of the absorption intensity at 510 nm and 548 nm changed.

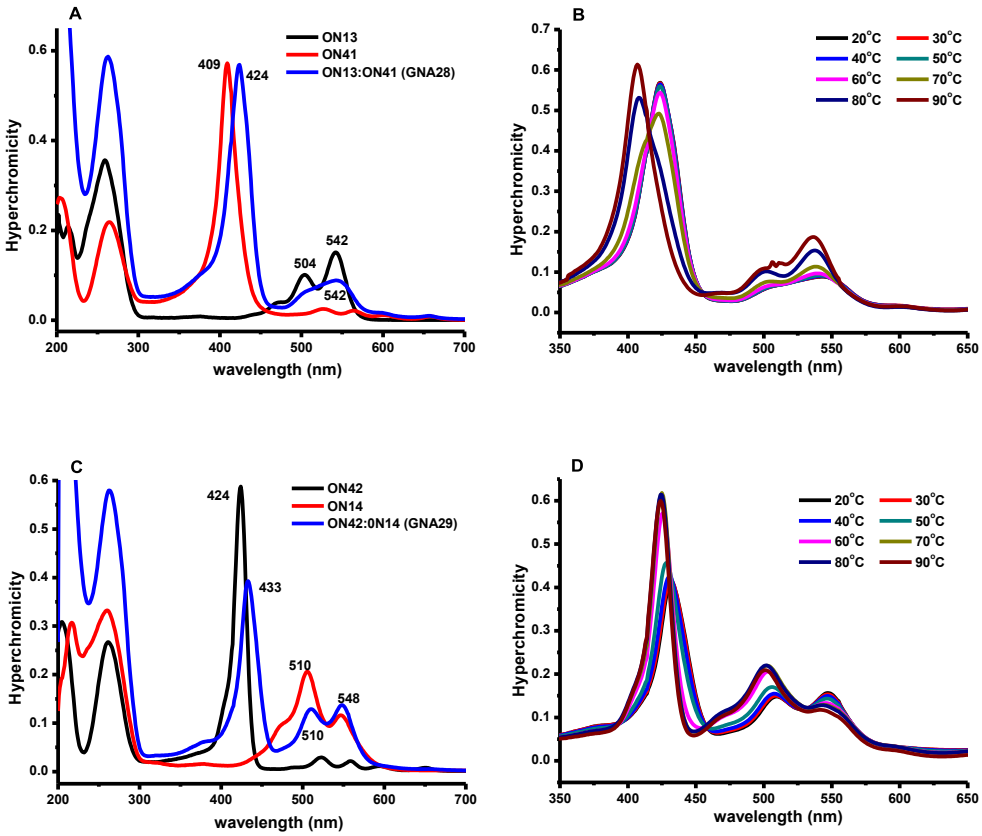

Figure 46 UV/Vis-absorption spectra of GNA duplexes and their corresponding single strands. Conditions: 10 mM sodium phosphate, 100 mM NaCl, pH 7.0, and 2 μM of each strand. (A) **ON13**, **ON41** and **ON13**:**ON41** at 20 °C. (B) **GNA28** temperature-dependent. (C) **ON42**, **ON14** and **ON42**:**ON14** at 20 °C. (D) **GNA29** temperature-dependent

Figure 47 shows the UV absorption of **GNA30** and corresponding single strands **ON43** and **ON16**. The absorption band of **GNA30** containing **B-P-B-P** showed that there was an 18 nm bathochromic shift in the range of the porphyrin soret band and a 4 nm bathochromic shift in the range of the **PBI** band, respectively

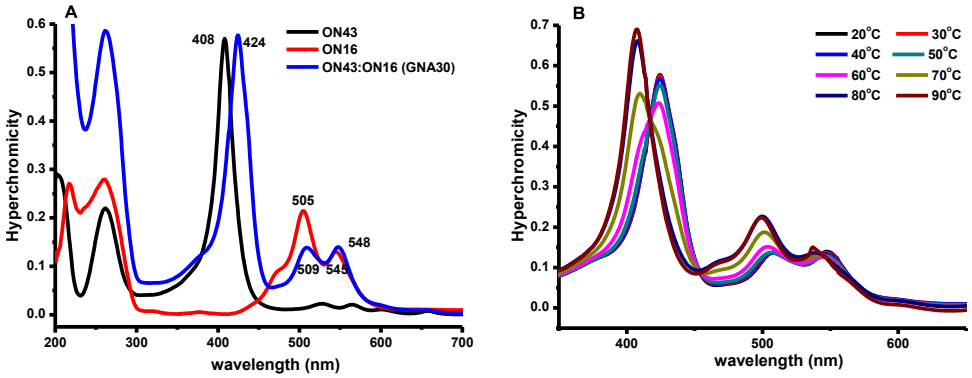

Figure 47 UV/Vis-absorption spectra of GNA duplexes and their corresponding single strands. Conditions: 10 mM sodium phosphate, 100 mM NaCl, pH 7.0, and 2 μM of each strand. (A) **ON43**, **ON16** and **ON43**:**ON16** at 20 °C. (B) **GNA46** temperature-dependent

3.1.5.3 CD spectroscopy

As shown in Figure 48, the CD spectra of duplexes **GNA24**, **GNA25**, **GNA26** and **GNA27** that contain **B** and **P** dimer were investigated first. The CD spectra resembled that of the native duplex in the GNA absorption region (200–300 nm). A negative CD signal was observed at 428 nm, which attributed to the porphyrin in duplex **GNA24** (Figure 48A). There was also a very weak negative signal at 425 nm in duplex **GAN25** (Figure 48B). However, the situation was a little different for **GNA26** and **GNA27** in comparison to **GNA24** and **GNA25**. The CD spectrum of **GNA26** displayed a strong negative peak at 428 nm and a positive peak at 441 nm, which were both in the porphyrin soret band; however, there was very weak cotton effect of the **PBI** observed (Figure 48C). A similar phenomenon was also observed for duplex **GNA27**.

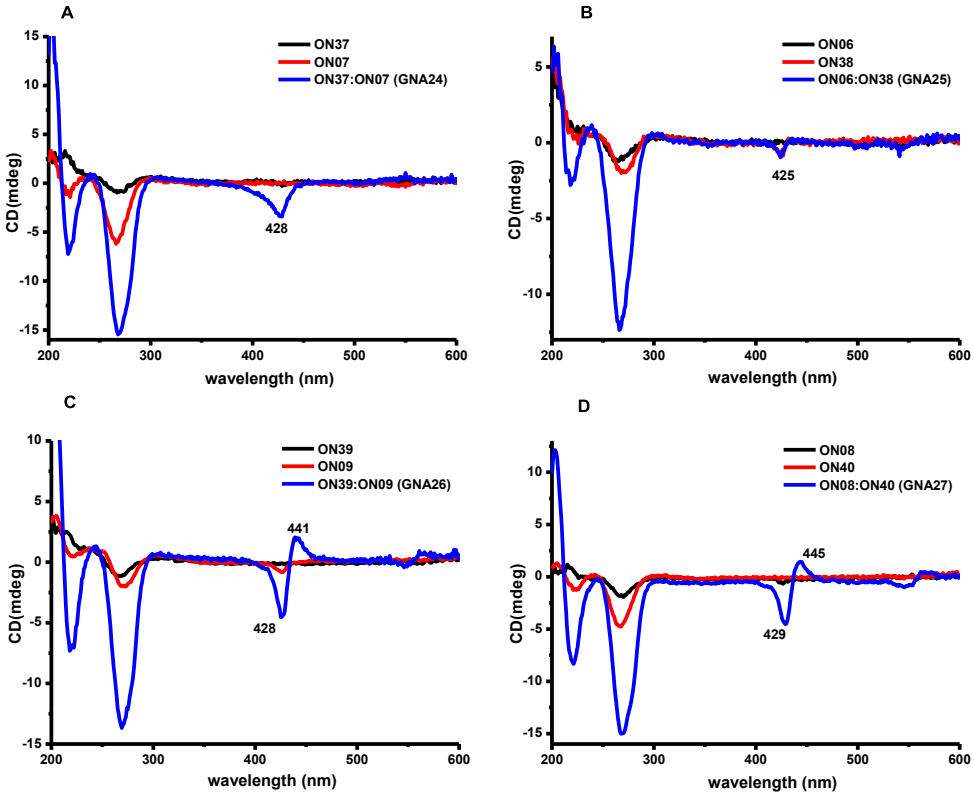

Figure 48 CD spectra of modified GNA duplexes and their corresponding single strands. Conditions: 10 mM sodium phosphate, 100 mM NaCl, pH 7.0, and 12 μM of each strand at 20 °C. (A) **ON37**, **ON07** and **ON37:ON07**. (B) **ON06**, **ON38** and **ON06:ON38**. (C) **ON39**, **ON09** and **ON39:ON09**. (D) **ON08**, **ON40** and **ON08:ON40**

Figure 49 shows the CD spectrum of GNA duplexes modified by more than two heterochromophores. A strong negative CD signal at 421 nm and a positive CD signal at 436 nm were observed, and both of these two absorption bands attributed to the porphyrin in duplex **GNA28**; however, no obvious cotton effect of **PBI** was found (Figure 49A). On the other hand, soret bands of porphyrin in duplex **GNA29** displayed a strong negative signal at 431 nm and a relatively weak positive signal at 448 nm; moreover, the CD signal at 505 nm and 570 nm attributed to **PBI** could also be observed. As we know, both **GNA30** and **GNA31** contained four heterochromophores, but the CD spectrum showed little difference. For **GNA30**, a strong positive signal at 422 nm and a strong negative signal at 437 nm attributing to porphyrin were observed, while a negative signal at 502 nm and a positive signal at

565 nm attributing to **PBI** were also detected (Figure 49C). The soret bands of porphyrin observed in **GNA31** were similar to that of **GNA30**; however, the cotton effect of **PBI** was nearly unobservable.

Accordingly, together with T_m and UV-spectroscopy measurement, more than two interstrand heterochromophores incorporated into GNA duplexes were possible to increase the stability.

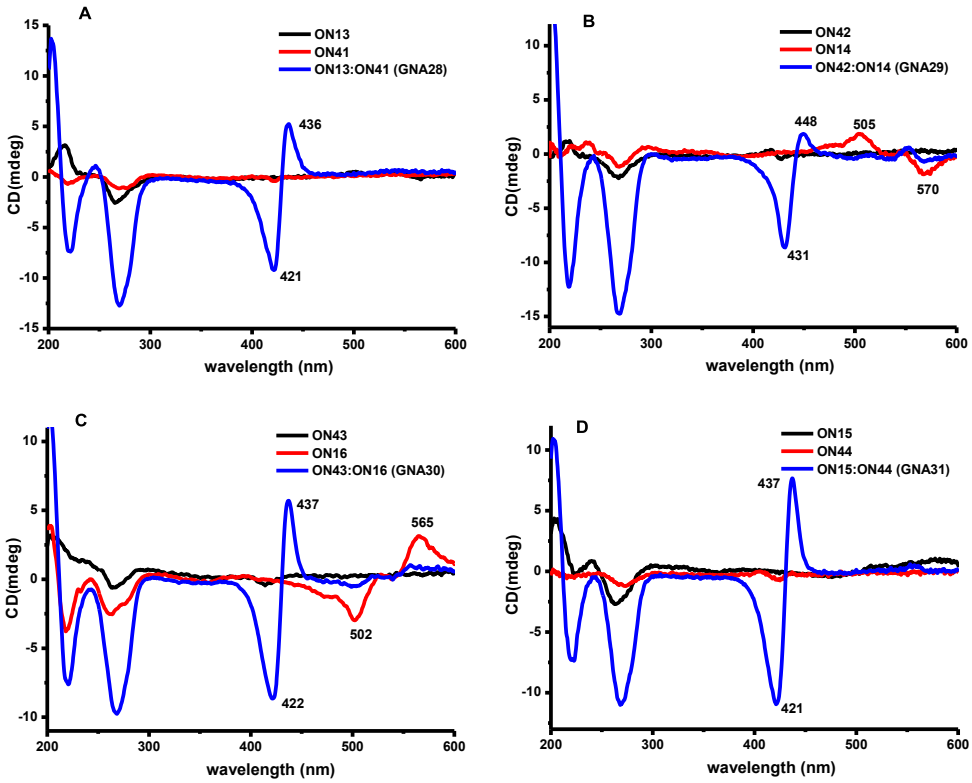

Figure 49 CD spectra of modified GNA duplexes and their corresponding single strands. Conditions: 10 mM sodium phosphate, 100 mM NaCl, pH 7.0, and 12 μM of each strand at 20 °C. (A) **ON13**, **ON41** and **ON13:ON41**. (B) **ON42**, **ON14** and **ON42:ON14**. (C) **ON43**, **ON16** and **ON43:ON16**. (D) **ON15**, **ON44** and **ON15:ON44**

3.1.6 Interstrand stacking of phthalocyanine-porphyrin

3.1.6.1 Thermal stability

Encouraged by the results of interstrand stacking of **PBI**-porphyrin, we continued to investigate the interstrand stacking of phthalocyanine-porphyrin.

Table 4 Thermal stabilities of **PBI**-Phthalocyanine 16mer GNA duplexes together with Watson–Crick reference duplexes [a]

Entry	Sequence		T_m(°C)
GNA1	3′-TAAAAATAATAATATT-2′	(**ON01**)	54
	2′-ATTTTTATTATTATAA-3′	(**ON02**)	
GNA32	3′-TAAAAATHPTAATATT-2′	(**ON37**)	53
	2′-ATTTTTAYHATTATAA-3′	(**ON27**)	
GNA33	3′-TAAAAATHYTAATATT-2′	(**ON26**)	60
	2′-ATTTTTAPHATTATAA-3′	(**ON38**)	
GNA34	3′-TAAAAATPHTAATATT-2′	(**ON39**)	66
	2′-ATTTTTAHYATTATAA-3′	(**ON29**)	
GNA35	3′-TAAAAATYHTAATATT-2′	(**ON28**)	62
	2′-ATTTTTAHPATTATAA-3′	(**ON40**)	
GNA36	3′-TAAAAAHYHTAATATT-2′	(**ON31**)	74
	2′-ATTTTTPHPATTATAA-3′	(**ON41**)	
GNA37	3′-TAAAAAHPHTAATATT-2′	(**ON42**)	low
	2′-ATTTTTYHYATTATAA-3′	(**ON32**)	
GNA38	3′-TAAAAAHPHPAATATT-2′	(**ON43**)	low
	2′-ATTTTTYHYHTTATAA-3′	(**ON34**)	
GNA39	3′-TAAAAAHYHYAATATT-2′	(**ON33**)	low
	2′-ATTTTTPHPHTTATAA-3′	(**ON44**)	

[a] Conditions: 10 mM sodium phosphate, 100 mM NaCl, and 2 μM individual strands.

As shown in Table 4, **GNA32**, **GNA33**, **GNA34** and **GNA35** contain all possible permutations of the interstrand heterochromophore porphyrin-phthalocyanine dimer. In contrast to the T_m (54 ℃) of GNA with two A:T base pairs at the same position, the four modified duplexes showed T_m at 53 ℃, 60 ℃, 66 ℃ and 62 ℃, respectively, demonstrating that the incorporation of a porphyrin-phthalocyanine pair had a

stabilizing effect on the GNA duplexes. (ΔT_m = -1 ℃ for **GNA32**, ΔT_m = 6 ℃ for **GNA33**, ΔT_m = 12 ℃ for **GNA34** and ΔT_m = 8 ℃ for **GNA35**).

When more than two heterochromophores were incorporated into GNA duplexes, the situation became more complicated. The duplex **GNA36** containing three chromophores in the form of sandwich-type **P-Y-P** exhibited a melting point (T_m) of 74 ℃, and it improved the duplex stability by an additional 20 ℃. However, duplexes **GNA37**, **GNA38** and **GNA39**, in which the heterochromophores arrayed in the form of **Y-P-Y** or **P-Y-P-Y** or **Y-P-Y-P**, were even unstable at 20 ^{o}C; no T_m value was obtained (Figure 50).

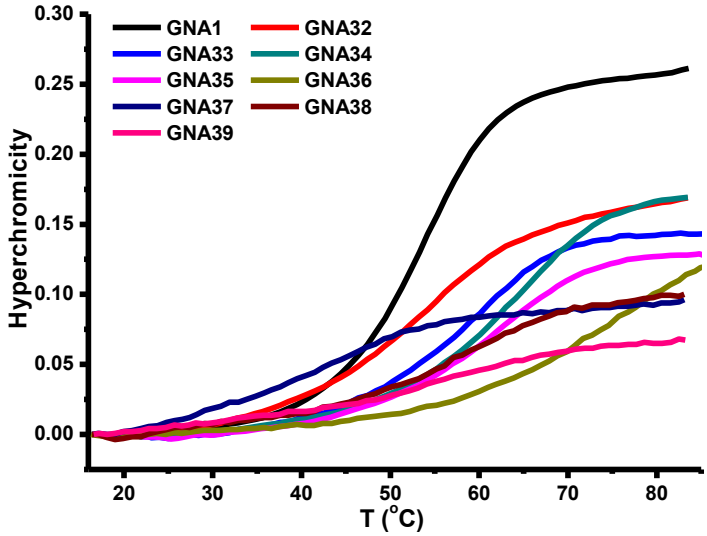

Figure 50 UV-melting curves of duplexes (from **GNA32 to GNA39** (see Table 4 for the sequences)). Changes in absorbance upon heating as monitored at 260 nm. Conditions: 10 mM sodium phosphate, 100 mM NaCl, pH 7.0, and 2 μM of each strand

3.1.6.2 UV/Vis-absorption spectroscopy

First, the modified duplexes **GNA32**, **GNA33**, **GNA34** and **GNA35** that contain **P** and **Y** dimer were studied in detail. The UV/Vis-absorption spectrum of **GNA32** displayed that the absorption bands shifted bathochromically from 695 nm to 705 nm for phthalocyanine, and had a small bathochromic shift from 427 nm to 430 nm for

porphyrin (Figure 51A). In addition, we observed that the intensity of the absorption also had a pronounced change (Figure 51A). As shown in Figure 51, similar results were obtained for the other three duplexes (**GNA33**, **GNA34** and **GNA35**).

The UV/Vis-absorption spectra of duplexes that have more than two chromophores were also measured. Remarkably, the UV/Vis-absorption properties of duplex **GNA36** containing three chromophores in the form of sandwich-type **P-Y-P** were significantly different from the single strands. The absorption band for the porphyrin in single strand **ON41** showed a small bathochromic shift from 419 nm to 426 nm; on the other hand, there were two absorption bands at 643 nm and 687 nm for the phthalocyanine in single strand **ON31**. The absorption band mainly appeared at 717 nm for phthalocyanine in duplex **GNA36** (Figure 52A). All these results indicated that a strong interaction of porphyrin and phthalocyanine existed in this kind of arrangement in the GNA duplexes (Figure 52A). The influence of temperature on the UV/Vis-absorption spectrum of the duplexes was analyzed. As shown in Figure 52B, a temperature increase from 20 ℃ to 90 ℃ resulted in the gradual change of the absorption band. After complete denaturation of the duplex, there was no interaction of the heterochromophores.

Although we could not determine the melting points of duplexes **GNA37**, **GNA38** and **GNA39** with UV-dependent thermal stability, temperature-dependent UV/Vis-absorption spectra showed that interaction between two chromophores was temperature dependent. As shown in Figures 52C and 52D, the UV/Vis-absorption spectrum of **GNA37** showed that there was a bathochromic shift from 424 nm to 427 nm for the porphyrin surrogate; the intensity of the absorption band at 639 nm for the phthalocyanine surrogate also changed. As the temperature increased, the trend of the absorption change in the long-wavelength still did not give us enough information about the stability of the duplex (Figure 52D). For **GNA38** and **GNA39**, both of the absorption bands shifted bathochromically from 408 nm to 425 nm, and the absorption bands in the region 500–800 nm showed pronounced changes at 20 ^{o}C (Figures 52E and 52F).

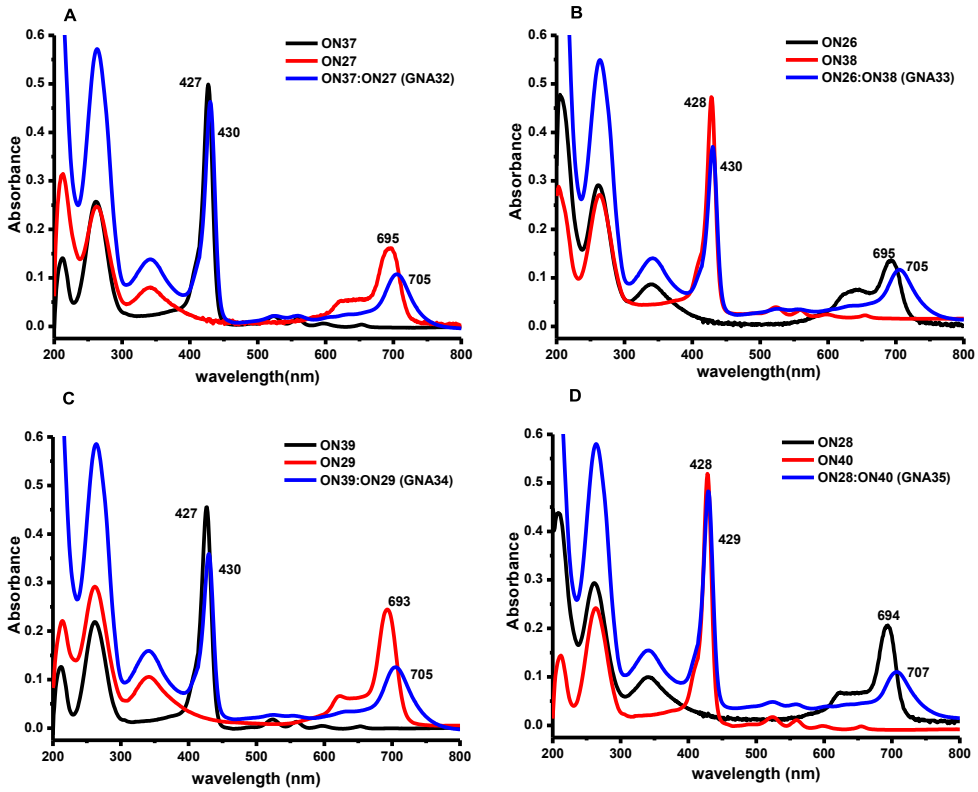

Figure 51 UV/Vis-absorption spectra of GNA duplexes and their corresponding single strands at 20 °C. Conditions: 10 mM sodium phosphate, 100 mM NaCl, pH 7.0, and 2 µM of each strand. (A) **ON36**, **ON27** and **ON36**:**ON27**. (B) **ON26**, **ON38** and **ON26**:**ON38** (C) **ON39**, **ON29** and **ON39**:**ON29** (D) **ON28**, **ON40** and **ON28**:**ON40**

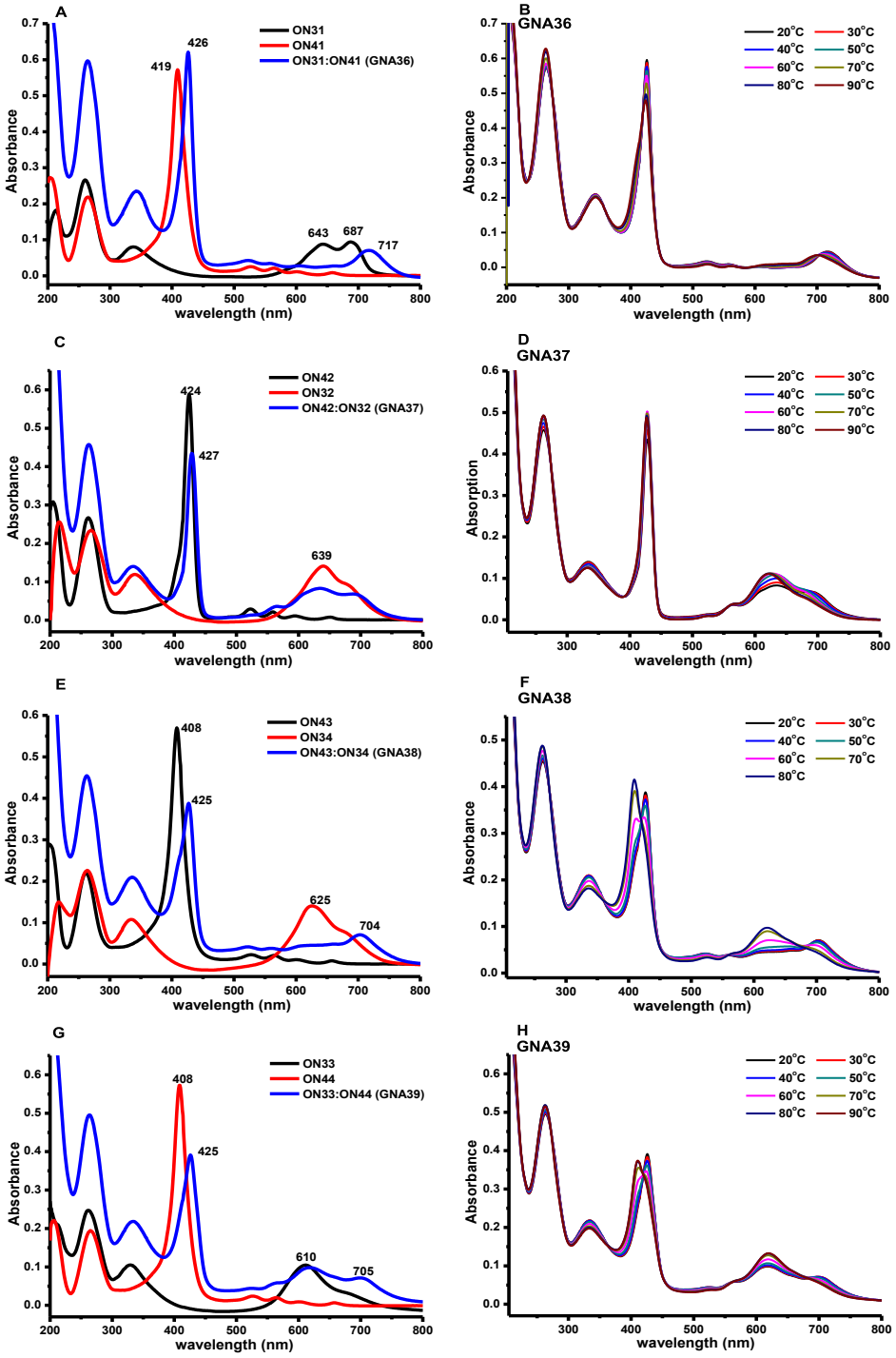

Figure 52 UV/Vis-absorption spectra of GNA duplexes and their corresponding single strands. Conditions: 10 mM sodium phosphate, 100 mM NaCl, pH 7.0, and 2 µM of each strand. (A) **ON31**, **ON41** and **ON31**:**ON41** at 20 °C. (B) **GNA36** temperature-dependent. (C) **ON42**, **ON32** and **ON42**:**ON32** at 20 °C. (D) **GNA37** temperature-dependent. (E) **ON43**, **ON34** and **ON43**:**ON34** at 20 °C. (F) **GNA38** temperature-dependent. (G) **ON33**, **ON44** and **ON33**:**ON44** at 20 °C. (H) **GNA39** temperature-dependent

3.1.6.3 CD spectroscopy

First, the CD spectra of duplexes **GNA32**, **GNA33**, **GNA34** and **GNA35** containing one pair of interstrand heterochromophore phthalocyanine and porphyrin were investigated. The CD signal of the modified GNA duplexes in the GNA region resembled that of the native GNA duplex. Only a very weak negative CD signal was observed at 428 nm, which attributed to porphyrin surrogate. No signal was observed in the corresponding region for the phthalocyanine. In addition, CD melting profiles also provided values of T_m similar to those obtained from the UV data (Figure 53).

As we have mentioned, the duplex **GNA36** containing three chromophores in the form of **P-Y-P** was highly stabilized. Remarkably, it was noted that the CD signal of porphyrin in **GNA36** was completely different from that in **ON41** in the long-wavelength region. CD spectrum of **GNA36** had an obvious positive signal at around 432 nm and a strong negative signal at around 420 nm, in contrast to that of **ON41** in the same regions (Figure 54A). Together with these results, it was demonstrated that the phthalocyanine and porphyrin interacted in GNA. Since the CD spectra of **GNA37**, **GNA38** and **GNA39** in the base-pair region (200–300 nm) were very weak at 20 ^{o}C, it indicated that such modification somehow distorted the overall GNA duplex conformation.

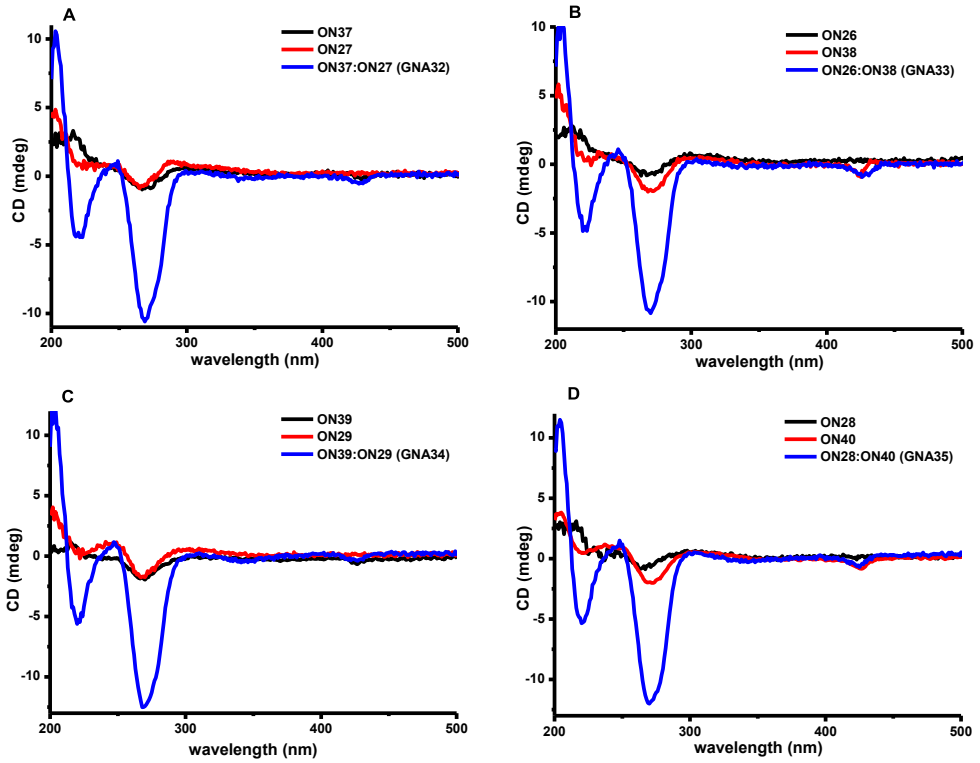

Figure 53 CD spectra of GNA duplexes and their corresponding single strands at 20 °C. Conditions: 10 mM sodium phosphate, 100 mM NaCl, pH 7.0, and 2 μM of each strand. (A) **ON36**, **ON27** and **ON36**:**ON27**. (B) **ON26**, **ON38** and **ON26**:**ON38**. (C) **ON39**, **ON29** and **ON39**:**ON29** (d) **ON28**, **ON40** and **ON28**:**ON40**

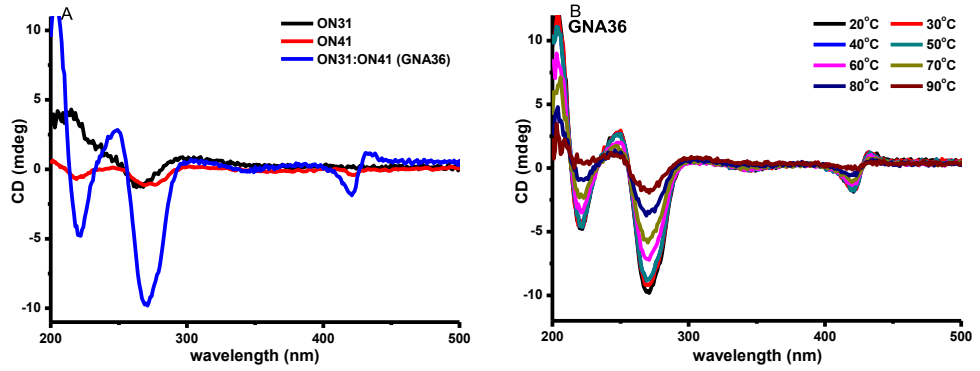

Figure 54 CD spectra of GNA duplexes and their corresponding single strands. Conditions: 10 mM sodium phosphate, 100 mM NaCl, pH 7.0, and 2 μM of each strand. (A) **ON31**, **ON41** and **ON31**:**ON41** at 20 °C. (B) **GNA36** temperature-dependent

3.1.7 Interstrand stacking of phthalocyanine-PBI

3.1.7.1 Thermal stability

As described in Table 5, **GNA40**, **GNA41**, **GNA42** and **GNA43** had four different permutations of adjacent **PBI**-phthalocyanine heterochromophores. In contrast to the T_m (54 ℃) of the GNA with two A:T base pairs at the same position, the four modified duplexes showed T_m at 56 ℃, 55 ℃, 60 ℃ and 58 ℃, respectively (Table 5 and Figure 55), demonstrating that the incorporation of a **PBI**-phthalocyanine pair had little stabilizing effect (ΔT_m = 2 ℃ for **GNA40**, ΔT_m = 1 ℃ for **GNA41**, ΔT_m = 6 ℃ for **GNA42** and ΔT_m = 4 ℃ for **GNA43**).

When more than two heterochromophores were incorporated into GNA duplexes, the situation was more complicated. Duplex **GNA44** containing three chromophores in the form of sandwich-type **B**-**Y**-**B** exhibited a melting point (T_m) of 69 ℃. It improved the duplex stability by an additional 15 ℃. However, if the sandwich-type was **Y**-**B**-**Y**, the duplex **GNA45** was highly destabilized and only displayed a T_m of 43 ℃. Melting temperature of **GNA46** only showed 42 ^{o}C, and **GNA47** was also very unstable even at 20 ^{o}C. Both of them contained four interstrand heterochromophores in the form of **B**-**Y**-**B**-**Y** (Figure 55).

Table 5 Thermal stabilities of **PBI**-Phthalocyanine 16mer GNA duplexes together with Watson–Crick reference duplexes [a]

Entry	Sequence		T_m(°C)
GNA1	3′-TAAAAATAATAATATT-2′	(**ON01**)	54
	2′-ATTTTTATTATTATAA-3′	(**ON02**)	
GNA40	3′-TAAAAATHBTAATATT-2′	(**ON06**)	56
	2′-ATTTTTAYHATTATAA-3′	(**ON27**)	
GNA41	3′-TAAAAATHYTAATATT-2′	(**ON26**)	55
	2′-ATTTTTABHATTATAA-3′	(**ON07**)	
GNA42	3′-TAAAAATBHTAATATT-2′	(**ON08**)	60
	2′-ATTTTTAHYATTATAA-3′	(**ON29**)	
GNA43	3′-TAAAAATYHTAATATT-2′	(**ON28**)	58
	2′-ATTTTTAHBATTATAA-3′	(**ON09**)	
GNA44	3′-TAAAAAHYHTAATATT-2′	(**ON31**)	69
	2′-ATTTTTBHBATTATAA-3′	(**ON14**)	
GNA45	3′-TAAAAAHBHTAATATT-2′	(**ON13**)	43
	2′-ATTTTTYHYATTATAA-3′	(**ON32**)	
GNA46	3′-TAAAAAHBHBAATATT-2′	(**ON15**)	42
	2′-ATTTTTYHYHTTATAA-3′	(**ON34**)	
GNA47	3′-TAAAAAHYHYAATATT-2′	(**ON33**)	-
	2′-ATTTTTBHBHTTATAA-3′	(**ON16**)	

[a] Conditions: 10 mM sodium phosphate, 100 mM NaCl, and 2 mM individual strands.

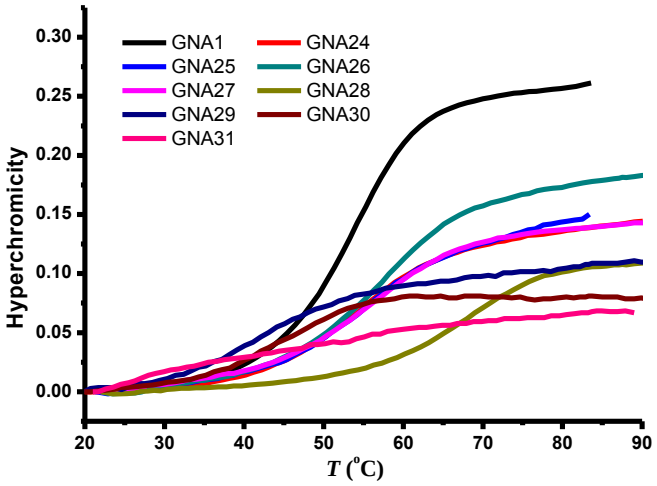

Figure 55 UV-melting curves of duplexes (from **GNA24 to GNA31** (see Table 3 for the sequences)). Changes in absorbance upon heating as monitored at 260 nm. Conditions: 10 mM sodium phosphate, 100 mM NaCl, pH 7.0, and 2 mM of each strand

3.1.7.2 UV/Vis-absorption spectroscopy

First, duplexes **GNA40**, **GNA41**, **GNA42** and **GNA43** that contain **PBI** and phthalocyanine dimer were studied. The UV/Vis-absorption spectrum of **GNA40** mainly displayed the band absorption at 694 nm for phthalocyanine, 545 nm and 508 nm for **PBI** in the long-wavelength region at 20 ^{o}C. In comparison to the single strands **ON06** and **ON27**, no band shift was observed, but the ratio of the absorption bands for **PBI** at 508 nm and 545 nm changed; in addition, the intensity of band absorption at 694 nm for phthalocyanine also changed. Similar results were also observed for the UV/Vis-absorption spectra of **GNA25**, **GNA26** and **GNA27** (Figure 56). This initial measurement indicated that there was some kind of interaction between phthalocyanine and the **PBI** inside GNA duplexes.

Figure 57 shows the UV/Vis-absorption spectra of duplexes in which more than two heterochromophores were incorporated. Remarkably, the UV/Vis-absorption properties of duplex **GNA44** containing three chromophores in the form of sandwich-type **B-Y-B** were significantly different from the single strands. The absorption band for the **PBI** shifted bathochromically from 542 nm to 547 nm, and for the phthalocyanine, there was a small bathochromic shift from 687 nm to 693 nm. It was noted that the absorption band at 643 nm almost disappeared. The relative ratio of the absorption bands for **PBI** at 506 nm and about 545 nm had a pronounced change. All these results gave us clear information that the strong interaction of **PBI** and phthalocyanine would occur in this kind of arrangement in the GNA duplexes (Figure 57A). The influence of temperature on the UV/Vis-absorption spectrum of the duplexes was analyzed. As shown in Figure 57B, a temperature increase from 20 ℃ to 90 ℃ resulted in the gradual change of the absorption band, which can be explained by the dissociation of the duplexes into their corresponding single strands (phthalocyanine and **PBI** moieties), leading to no interaction. Although duplexes **GNA45**, **GNA46** and **GNA47** had been strongly destabilized by the heterochromophore aggregation, the UV/Vis-absorption spectra indicated that three

types of arrangement, **B-Y-B**, **B-Y-B-Y** and **Y-B-Y-B**, still interacted with each other (Figure 57). The most apparent one was **GNA30** with **B-Y-B-Y** type; the UV/Vis-absorption spectrum of single strand **ON34** indicated that the interaction was very strong between two phthalocyanine dyes because the main peak showed at around 642 nm. However, the UV/Vis-absorption spectrum of **GNA46** was definitely different; the interaction between phthalocyanine and **PBI** resulted in a change of the ratio of peaks at 693 nm and 642 nm. As the temperature increased, the duplex **GNA46** denatured; only interaction of chromophores in the single strands in **ON15** and **ON34** existed.

Accordingly, we found that the UV/Vis-absorption spectra of heterochromophore aggregation were more complicated than those of homochromophore aggregation. These initial results inspired us to make an extensive study in the future.

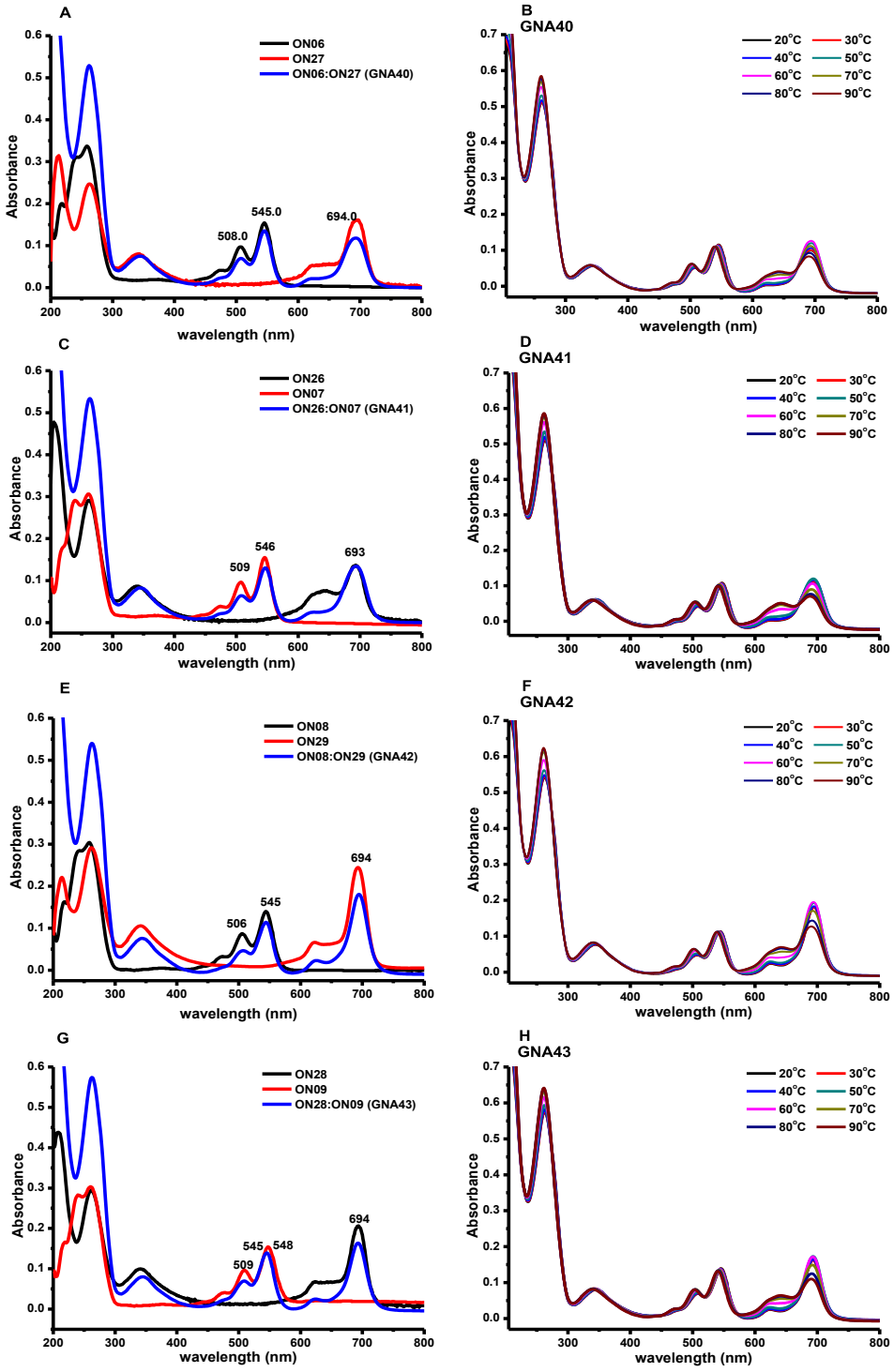

Figure 56 UV/Vis-absorption spectra of GNA duplexes and their corresponding single strands. Conditions: 10 mM sodium phosphate, 100 mM NaCl, pH 7.0, and 2 µM of each strand. (A) **ON06**, **ON27** and **ON06**:**ON27** at 20 °C. (B) **GNA40** temperature-dependent. (C) **ON26**, **ON07** and **ON26**:**ON07** at 20 °C. (D) **GNA41** temperature-dependent. (E) **ON08**, **ON29** and **ON08**:**ON29** at 20 °C. (F) **GNA42** temperature-dependent. (G) **ON28**, **ON09** and **ON28**:**ON09** at 20 °C. (H) **GNA43** temperature-dependent

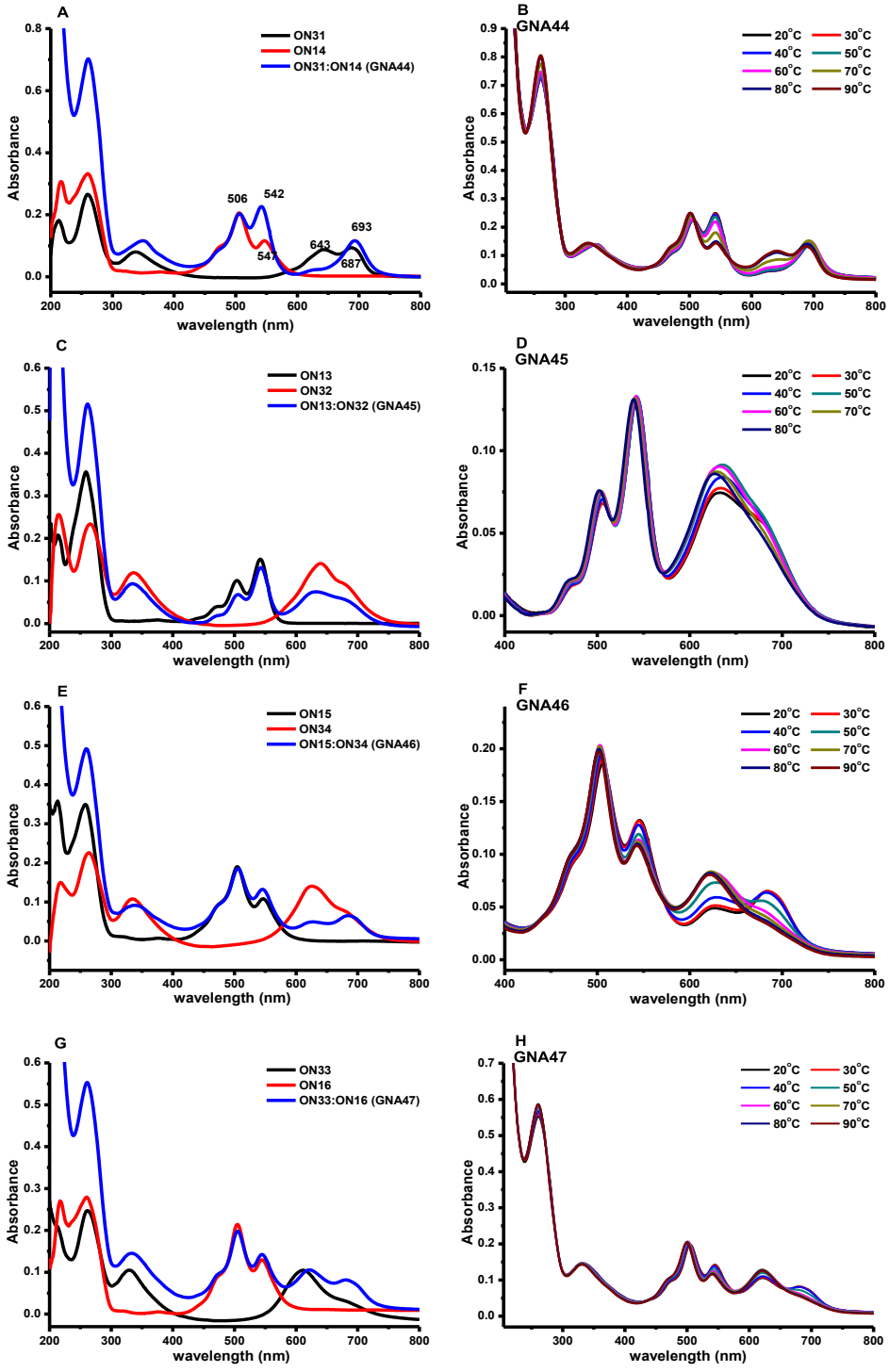

Figure 57 UV/Vis-absorption spectra of GNA duplexes and their corresponding single strands. Conditions: 10 mM sodium phosphate, 100 mM NaCl, pH 7.0, and 2 µM of each strand. (A) **ON31**, **ON14** and **ON31**:**ON14** at 20 °C. (B) **GNA44** temperature-dependent. (C) **ON13**, **ON32** and **ON13**:**ON32** at 20 °C. (D) **GNA45** temperature-dependent. (E) **ON15**, **ON34** and **ON15**:**ON34** at 20 °C. (F) **GNA46** temperature-dependent. (G) **ON33**, **ON16** and **ON28**:**ON09** at 20 °C. (H) **GNA47** temperature-dependent

3.1.7.3 CD spectroscopy

First, the CD spectra of modified duplexes **GNA40**, **GNA41**, **GNA42** and **GNA43** were investigated. The CD signals of those modified duplexes in the GNA absorption region were almost identical to those of the native GNA duplex. A very weak negative CD signal at 545 nm which attributed to **PBI** was observed. No signal appeared in the corresponding region of the phthalocyanine (Figure 58). In addition, CD melting profiles also provided values of T_m similar to those obtained from the UV data.

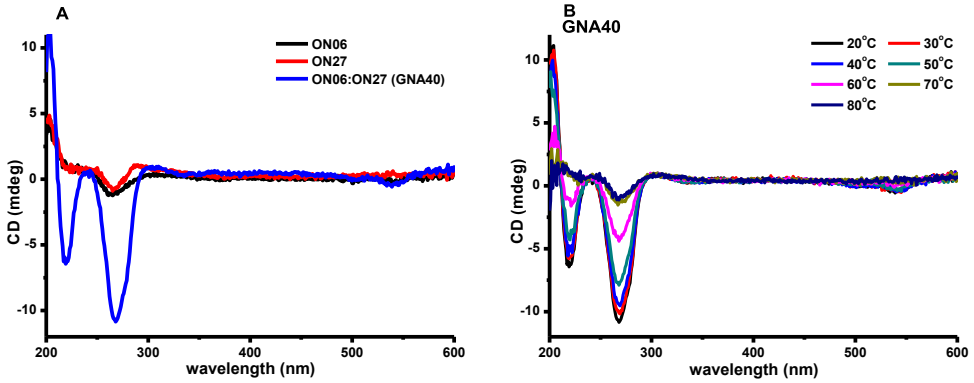

Figure 58 CD spectra of modified GNA duplexes and their corresponding single strands at 20 °C. Conditions: 10 mM sodium phosphate, 100 mM NaCl, pH 7.0, and 12 μM of each strand. (A) **ON06**, **ON27** and **ON06**:**ON27** at 20 °C. (B) **GNA24** temperature-dependent

It is noteworthy that the absorption band of **PBI** in **GNA44** was completely different from that in **ON14**. The CD spectrum of **GNA44** had a strong positive signal at 550 nm and a strong negative signal at 529 nm and 486 nm, but the CD spectrum of single strand **ON14** displayed a strong negative signal at around 570 nm and a strong positive signal at 505 nm (Figure 59). Together with these results, it demonstrated that **PBI** and phthalocyanine interacted in this kind of special arrangement in GNA. The situation for **GNA45**, **GNA46** and **GNA47** that were strongly destabilized was definitely different (Figure 59).

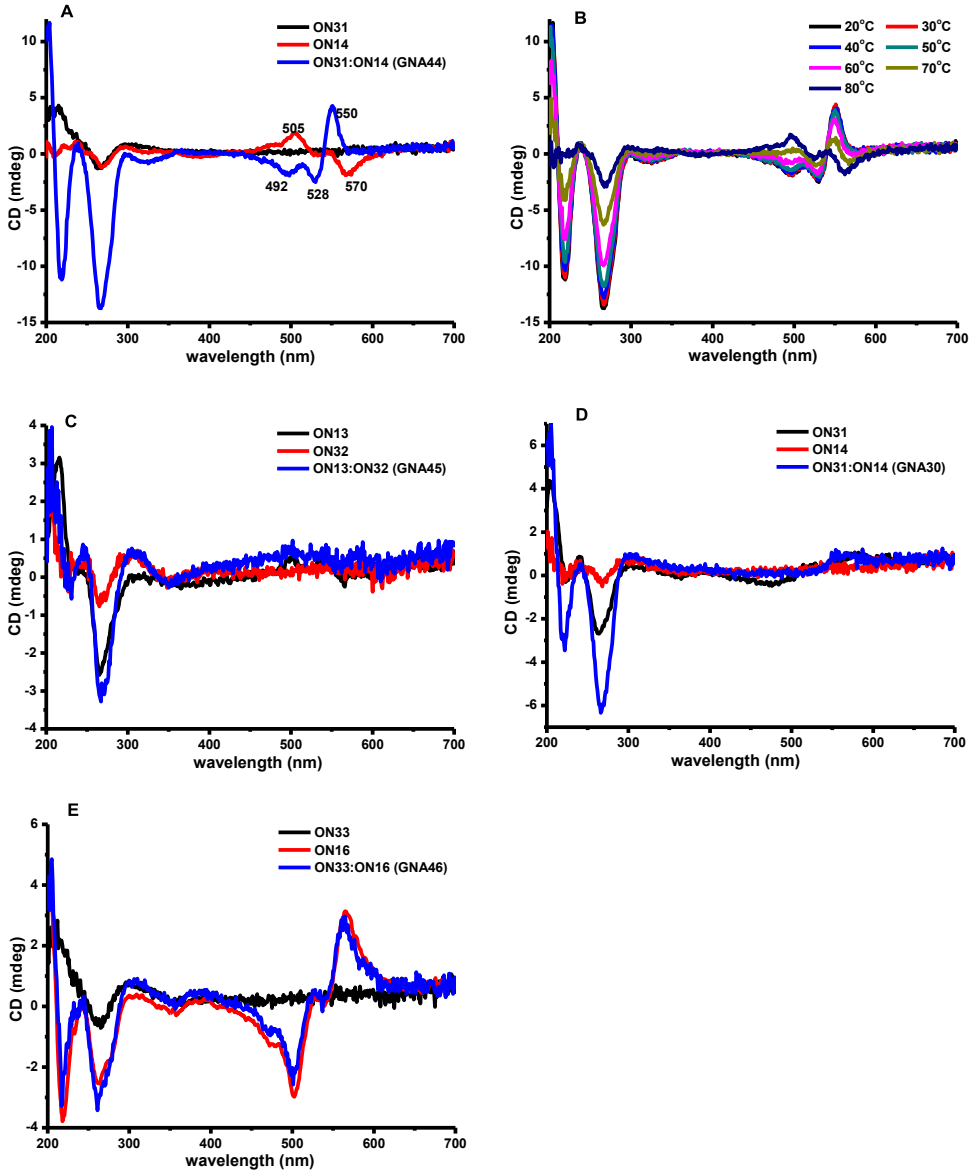

Figure 59 CD spectra of modified GNA duplexes and their corresponding single strands. Conditions: 10 mM sodium phosphate, 100 mM NaCl, pH 7.0, and 12 μM of each strand. (A) **ON31**, **ON14** and **ON31**:**ON14** at 20 °C. (B) **GNA44** temperature-dependent. (C) **ON13**, **ON32** and **ON13**:**ON32** at 20 °C. (D) **ON31**, **ON14** and **ON31**:**ON14** at 20 °C. (E) **ON33**, **ON16** and **ON33**:**ON16** at 20 °C

3.2 Design of Octahedral Silicon Complexes as DNA Binders

3.2.1 Synthesis of silicon complexes

The synthesis of octahedral silicon complexes was divided into two parts: the first was the direct synthesis of silicon complexes harboring arenediolate ligands from arenendiol, and the second was synthesis of silicon complexes harboring phenazinediolate from the octahedral silicon complexes that were obtained in part one.

3.2.1.1 Octahedral silicon complexes containing arenediolate ligands

According to the literature,[74] SiI_4 reacts with 2,2′-bipyridine and 1,10-phenantroline to afford *cis*-$[Si(bpy)_2I_2]I_2$ **40** and *cis*-$[Si(phen)_2I_2]I_2$ **41**, respectively, at room temperature (Scheme 10). However, the desired products were never obtained in this condition. When the reaction was carried out at 55 ^oC, the desired products could be obtained in high yield, and the products were highly stable at -20 ^oC.

Seven *ortho*-dihydroxyarenes (catechol **52**, 2,3-dihydroxynaphthalene **53**, phenanthrene-9,10-diol **54**, benz[*a*]anthracene-5,6-diol **55**, 5,6-chrysenediol **56**, 4,5-pyrenediol **57** and benzo[*a*]phenazine-5,6-diol **58**) were chosen (Scheme 11). Compounds **52** and **53** are commercially available. 10 wt. % Pd/C catalyzed hydrogenation of 9, 10-phenanthrenedione **59** affords phenanthrene-9, 10-diol **54**, which is not stable and can be oxidized by air very fast; hence it should be used immediately after it is synthesized. Compound **55** can be synthesized from **60** and **61** in five steps. Compound α-bromotolunitrile **60** reacts with benzenesulfinic acid sodium salt dehydrate **61** to afford *ortho*-(Phenylsulfonylmethyl)benzonitrile **62**, which is further reduced to the *ortho*-(Phenylsulfonylmethyl)benzaldehyde **63**, and compound 1,1-dimethoxynaphthalen-2(1*H*)-one **65** is obtained from β-naphthol in one

step in the presence of $PhI(OAc)_2$. Then, **63** and **65** react to give the Benz[*a*]anthracene-5, 6-dione **66** in the presence of *t*-BuOLi.[90] The final compound, Benz[*a*]anthracene-5,6-diol **55**, can be obtained by direct reduction of **66** in the presence of H_2 with 10 wt. % Pd/C as catalyst. Similar to **54**, compound **55** is not stable, and it should be used directly. In order to compare with the complex $[Rh(bpy)_2(phzi)](Cl)_3$,[49c] we also attempted to get compound benzo[*a*]phenazine-5,6-diol **58**. The compound benzo[*a*]phenazine-5, 6-dione **69** can be synthesized from **67** in two steps in high yield. However, when **69** is reduced, it affords a purple solid which has little solubility in normal solvent. It could not be used for the next step even though we screened a lot of conditions.

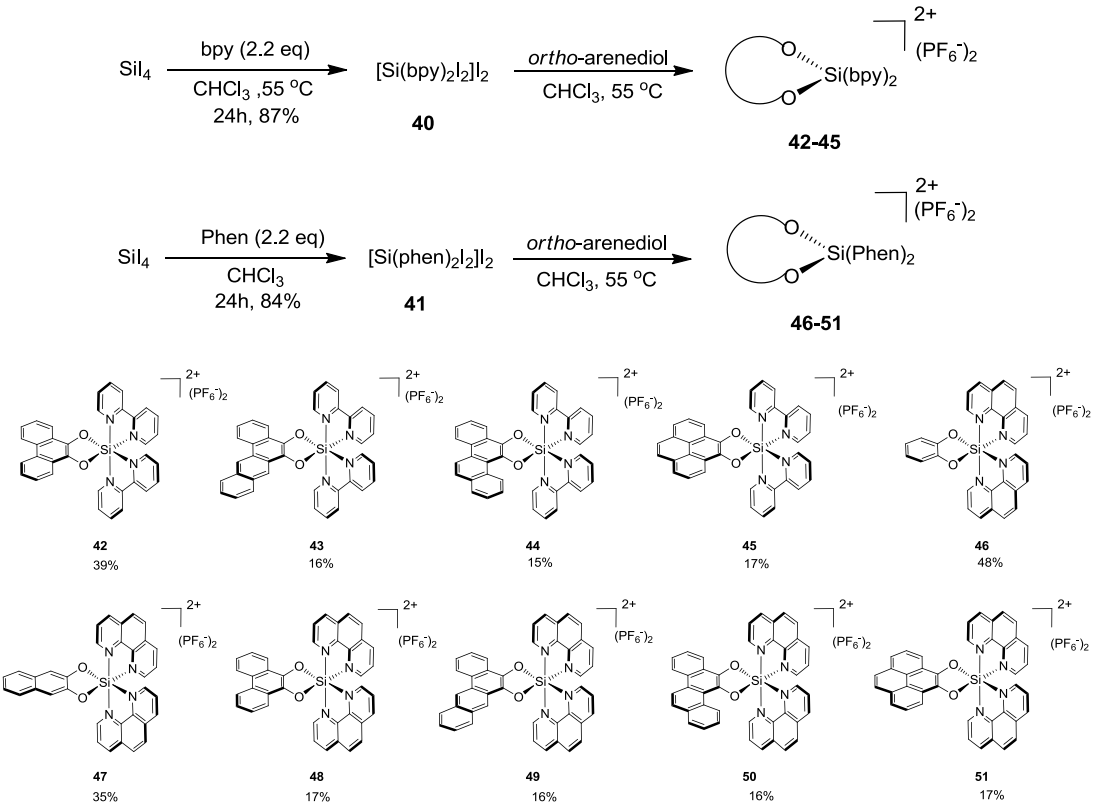

Scheme 10 Synthesis of octahedral silicon complexes containing arenediolate ligands

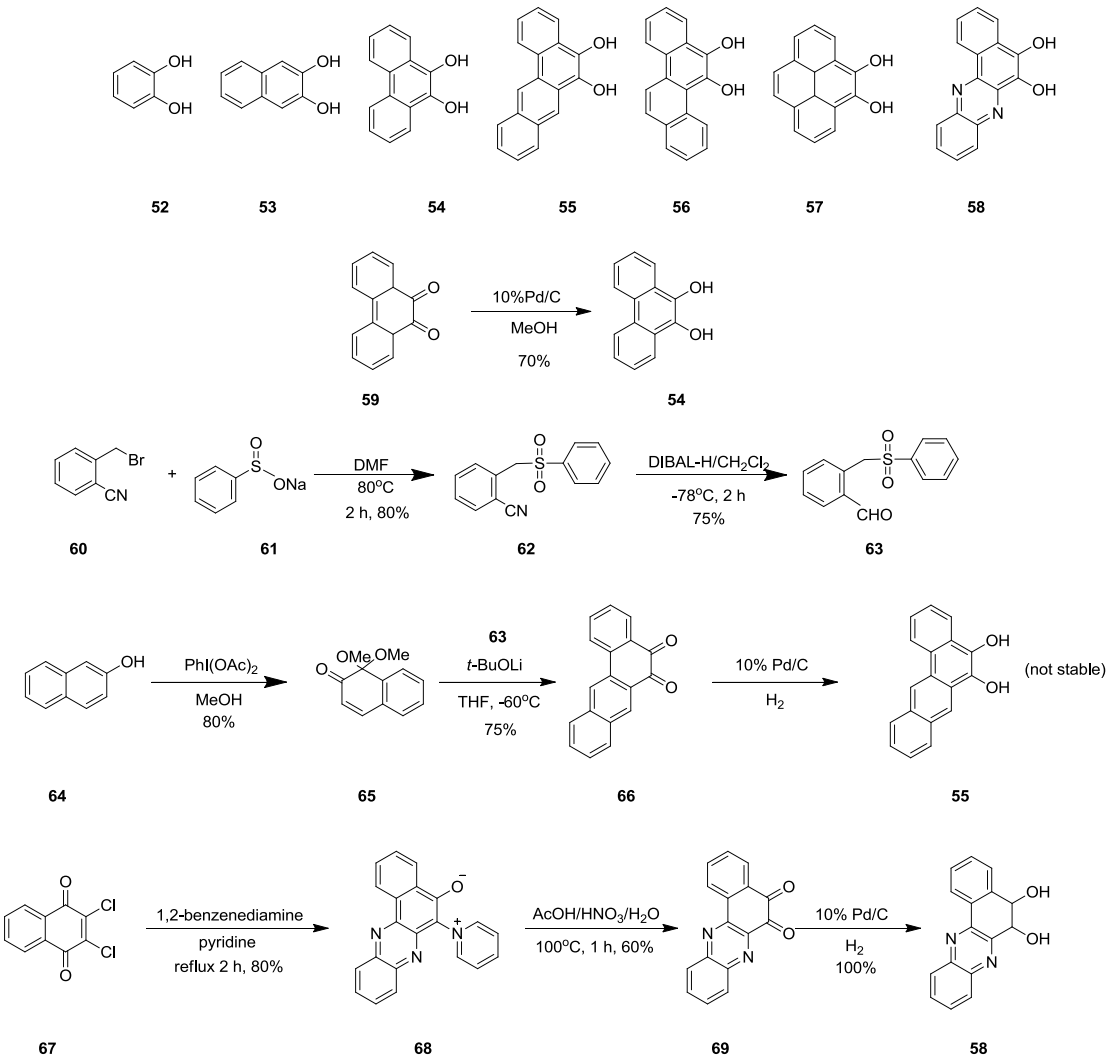

Scheme 11 Structure and synthesis of *ortho*-dihydroxyarenes. Compound **56** and **57** were synthesized by Chen Fu from Meggers Group

Having all the *ortho*-dihydroxyarenes precursor synthesized, we tried to synthesize the octahedral silicon complexes from $[Si(bpy)_2I_2]I_2$ **40** and $[Si(phen)_2I_2]I_2$ **41**. A series of solvents were screened, such as DMF, DMSO, CH_3CN, CH_2Cl_2, toluene, chlorobenzene and chloroform. Only chloroform, toluene and chlorobenzene were suitable for the reaction, and maybe DMF, DMSO and CH_3CN can coordinate with $[Si(bpy)_2I_2]I_2$ and $[Si(phen)_2I_2]I_2$. Complexes **40** and **41** reacted with a number of different *ortho*-dihydroxyarenes to afford the novel silicon complexes **42**–**51** harboring arenediolate ligands with varying aromatic π-systems (Scheme 10).

As shown in Figure 60, the silicon complex cation **48** was structurally characterized by single-crystal X-ray diffraction. The central atom in silicon complex **48** ligated by four nitrogen atoms and two oxygen atoms in slightly distorted octahedral coordination geometry. N1 and O2 occupied two sites of axis (the angle of N1-Si1-O2 is 173.5 (8)^{o}). Four atoms, O1, N4, N15 and N18 can be considered to occupy equatorial positions with the sum of the bond angles around the silicon atom (O1-Si1-N4, N4-Si1-N15, N18-Si1-N15 and O1-Si1-N18) of 359.68 (9) ^{o}. X-ray crystal structure confirmed the octahedral coordination mode around silicon.

The hydrolytic stability of several silicon complexes was evaluated by ^{1}H-NMR in CD_3CN/D_2O 5:1. No signs of decomposition were observed after one week at room temperature. Figure 61 shows that **48** was hydrolytically stable in 5:1 CD_3CN/D_2O. The stability of **48** in 1:1 DMSO/buffer (10 mM sodium phosphate and 20 mM NaCl pH = 7.0) and 1:1 DMSO/H_2O in the presence of 5 mM mercaptoethanol was also studied, and no signs of decomposition were observed. It is also worth noting that this remarkable kinetic inertness is complemented with a high configurational stability as determined with the resolved individual enantiomers of **48**.

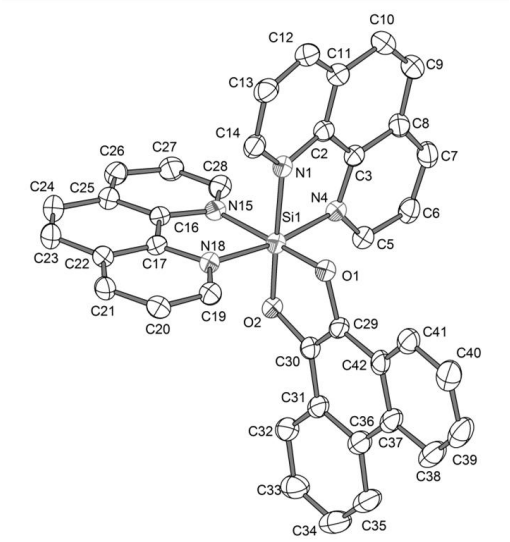

Figure 60 Crystal structure of the silicon 9, 10-phenanthrenediolate complex **48**. ORTEP representation with 50% thermal ellipsoids. Counterions and solvent molecules are omitted for clarity. Selected bond distances (Å) and angles (°): N1-Si1 1.956(2), N4-Si1 1.926(2), N15-Si1 1.947(2), N18-Si1 1.923(2), O1-Si1 1.7081(19), O2-Si1 1.7172(19); O1-Si1-N18 93.28(9), O1-Si1-N4 92.98(9), O1-Si1-N15 175.42(10), O1-Si1-N1 88.55(9), N15-Si1-N1 89.13(9)

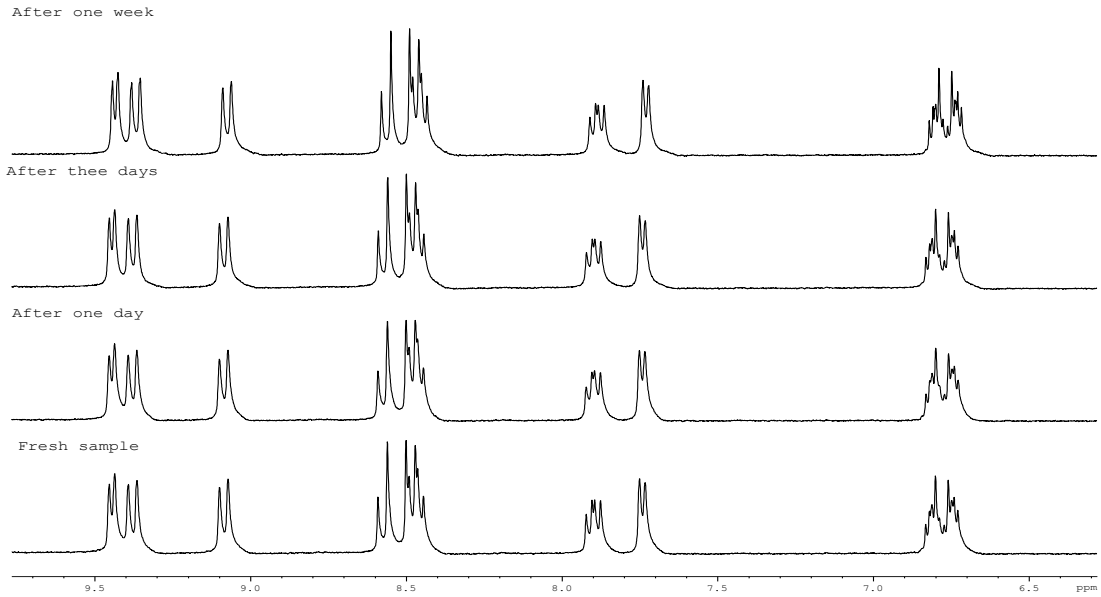

Figure 61 Hydrolytic stability of complex **48** at room temperature in CD_3CN/D_2O 5:1

3.2.1.2 Octahedral silicon complexes containing phenazinediolate ligands

It became very difficult when we strived to get more complicated silicon complexes because of the low solubility and inert reactivity of *ortho*-dihydroxyarenes. Since metallo-complexes with dppz ligand have been reported having strong interaction with DNA, we also wanted to introduce this ligand to the silicon complexes; however, the low yield makes synthesis meaningless. Some other ligands, such as phenantroline-9, 10-dione and other phenantroline derivatives, which have functional groups for further reaction, were used to replace the 2,2′-bipyridine and 1,10-phenantroline; it seems that this method is almost impossible.

As silicon complexes are stable in acid conditions, we envisaged that it might be possible to modify the current octahedral silicon complexes. Silicon protection group is very useful in organic synthesis, and it inspired us to consider that the $Si(Phen)_2$ part of **46** could be regarded as protection of the catechol. The reactivity of catechol will not change very much. On the other hand, the catechol could be converted to 3,

4-dinitro catechol or 4, 5-dihydroxycyclohexa-3, 5-diene-1, 2-dione in acidic condition easily. Fortunately, the dinitiro complexes **71** and **73** were obtained in quantitative yield from **70** and **46** in the presence of fume nitric acid and concentrated sulfuric acid, respectively. **71** and **73** were then further reduced to the diamine silicon complexes **72** and **74** (Scheme 12). However, **72** and **74** oxidized very fast and even decomposed at -20 ^{o}C. It was impossible for us to purify them using normal chromatography. After the reduction step, the diamine product should be used immediately.

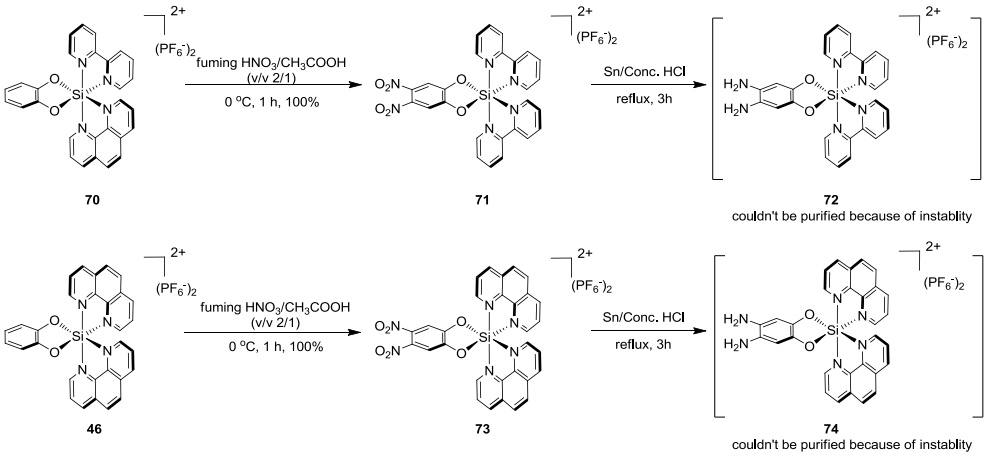

Scheme 12 Structure and synthesis of diamine silicon complexes **72** and **74**

These two diamine silicon complexes, **72** and **74**, condensed with a series of *ortho*-arenediones in CH_3CN at room temperature, affording the silicon complexes **77**-**86** harboring phenazinediolate ligands (Scheme 13). Fluorescence properties of all these silicon complexes in DMSO and CH_3CN were measured, and the excitation wavelength started from 350 to 500 nm; at interval 10 nm, unfortunately, no fluorescence signal was observed. Compared to silicon complexes **42**-**51**, silicon complexes **77**-**86** contain phenazine part which may increase the possibility of forming hydrogen bond between ligands and DNA bases.

In conclusion, we have successfully synthesized a series of octahedral silicon complexes which may be used for biological activity investigation.

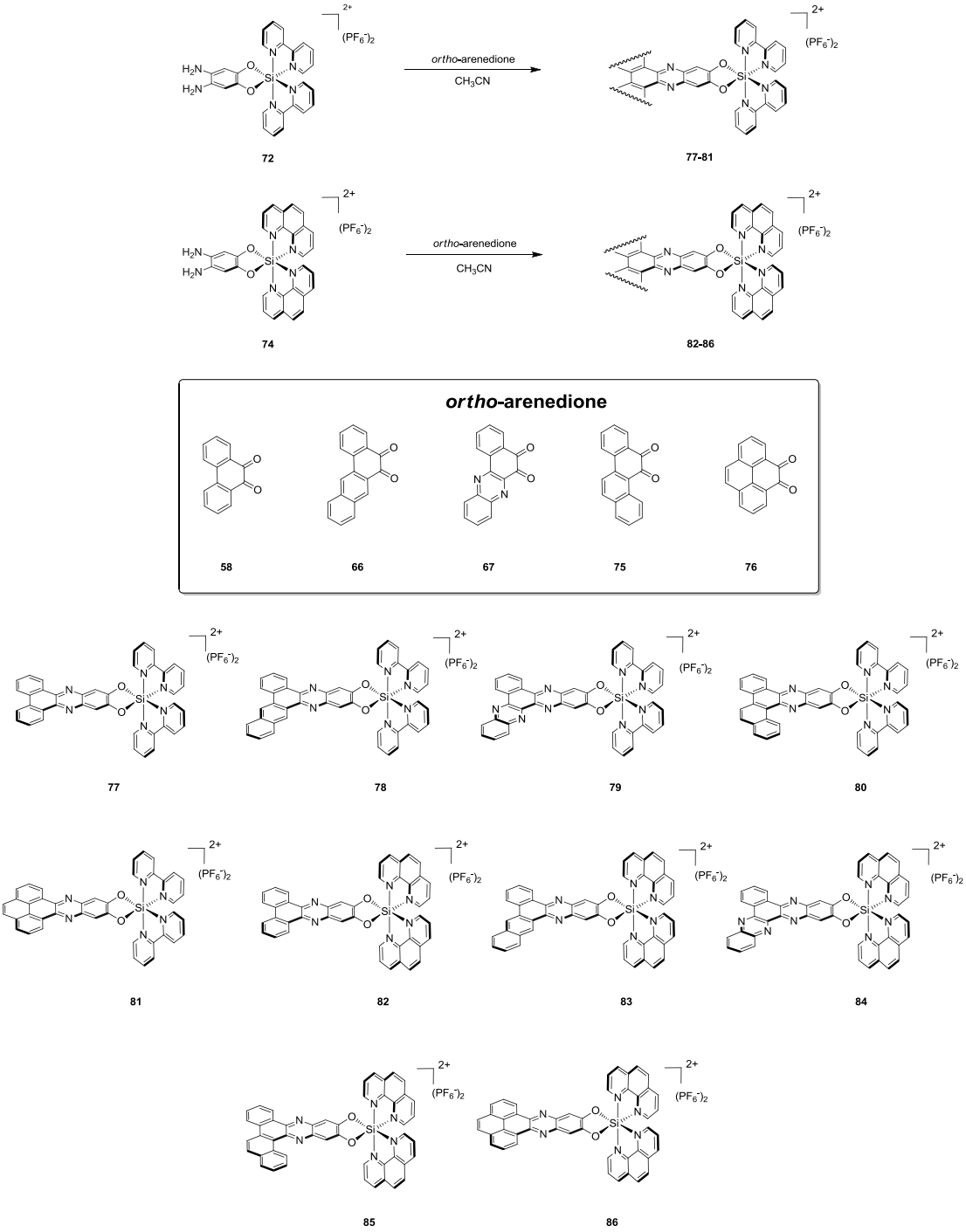

Scheme 13 Synthesis of octahedral silicon complexes harboring phenazinediolate ligand. (In this step, all the starting material **72** or **74** has been consumed; the yield is difficult to be calculated, about 20% in two steps, **75** and **76** were synthesized by Chen Fu from Meggers Group)

3.2.2 Silicon complexes as DNA intercalators or groove binders

3.2.2.1 Silicon complexes with simple arenediolate ligands

Having these stable octahedral silicon complexes (**46**-**51**) in hand, the influence of octahedral silicon complexes on the thermal stability of duplex DNA was firstly investigated, and the 15mer oligonucleotides duplex 5′-AGTGCCAAGCTTGCA-3′/3′-TCACGGTTCGAACGT-5′ was chosen for the measurement. The melting temperature of a mixed-sequence 15mer duplex DNA (2 μM) in the presence of complexes was monitored by temperature-dependent UV spectroscopy at 260 nm. Figure 62 displays melting curves of the duplex. In the presence of different concentrations of 9, 10-phenanthrenediolate **48**, the melting temperatures of the DNA duplex increased as the concentration of **48** was increased gradually, and the final relative concentration of silicon complex to DNA duplex was fixed at 4. From this result, we inferred that the octahedral silicon complexes might be used as DNA intercalators. Next, we continued to investigate the impact of different ligands of the $[Si(Phen)_2(arenediolate)]^{2+}$ on the stability of DNA duplexes. The melting temperature of 15mer duplex DNA (2 μM) in the presence of complexes **46**-**51** (8 μM) was determined by temperature-dependent UV spectroscopy at 260 nm. As displayed in Figure 63, whereas the complexes **46**, **47**, and **50** did not significantly alter the melting point of the DNA duplex, the 1,10-phenanthrolinediolate complex **48**, benz[*a*]anthracene-5, 6-diolate complex **49**, particularly the 4, 5-pyrenediolate complex **51**, led to a remarkably strong stabilization of the duplex DNA. Table 6 shows the change of the melting point in the presence of silicon complexes.

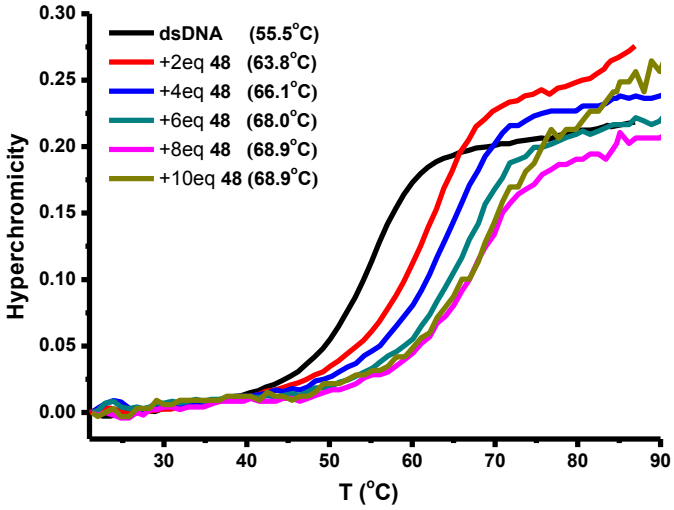

Figure 62 UV-melting curves of duplex DNA 5′-AGTGCCAAGCTTGCA-3′/3′-TCACGGTT CGAACGT-5′. Changes in absorbance upon heating as monitored at 260 nm. Conditions: 5 mM Tris-HCl, 50 mM NaCl, pH 7.4, and 2 μM of each strand in the presence of different concentration of 9, 10-phenanthrenediolate **48**

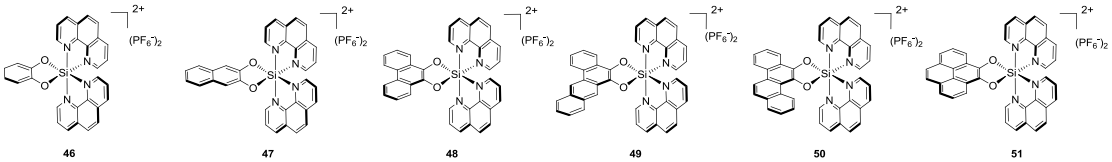

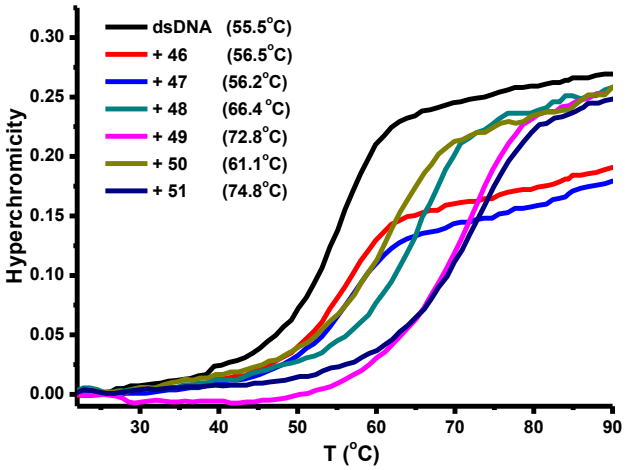

Figure 63 UV-melting curves of duplex DNA 5′-AGTGCCAAGCTTGCA-3′/3′-TCACGGTT CGAACGT-5′. Changes in absorbance upon heating as monitored at 260 nm. Conditions: 5 mM Tris-HCl, 50 mM NaCl, pH 7.4, and 2 μM of each strand in the presence of 8 μM $[Si(Phen)_2(arenediolate)]^{2+}$ (**46**–**51**)

Table 6 UV-melting temperature of 2 μM DNA duplex in Tris-HCl (5 mM, pH 7.4) with NaCl (50 mM) in the presence of or in the absence of 4.0 equiv silicon complexes

complex	T_m	ΔT_m
-	55.5	-
46	56.5	1.0
47	56.2	0.8
48	66.4	10.9
49	72.8	17.3
50	61.1	5.6
51	74.8	19.3

We also compared $[Si(Phen)_2(arenediolate)]^{2+}$ with $[Si(bpy)_2(arenediolate)]^{2+}$ to investigate the different influence of 2,2′-bipyridine and 1,10-phenantroline on the stability of the DNA duplexes. As shown in Figure 64, compared to complex **48**, which led to a strong stabilization of the duplex DNA by 11.1 ^oC, the melting temperature of the duplex was only increased by 4.5 ^oC in the presence of **42**. Similar results were obtained for other corresponding silicon complexes. All the $[Si(Phen)_2(arenediolate)]^{2+}$ (**48**, **49**, **50** and **51**) intensified the stability more than the corresponding $[Si(bpy)_2(arenediolate)]^{2+}$ (**42**, **43**, **44** and **45**) in the same condition. This indicated that $[Si(Phen)_2(arenediolate)]^{2+}$ is a better DNA-intercalator than $[Si(bpy)_2(arenediolate)]^{2+}$. Next, we mainly focused on the properties of $[Si(Phen)_2(arenediolate)]^{2+}$ (**48**, **49**, **50** and **51**).

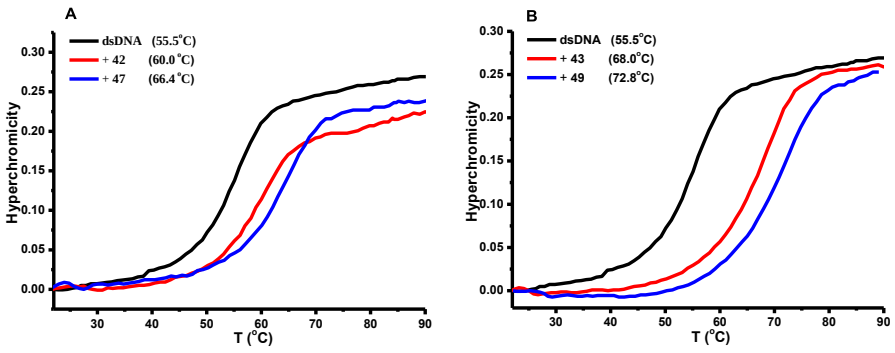

Figure 64 UV-melting curves of duplex DNA 5′-AGTGCCAAGCTTGCA-3′/3′-TCACGGTT CGAACGT-5′. Changes in absorbance upon heating as monitored at 260 nm. Conditions: 5 mM Tris-HCl, 50 mM NaCl, pH 7.4, and 2 μM of each strand in the presence of 8 μM $[Si(Phen)_2(arenediolate)]^{2+}$ (A) Complex **42** and complex **48**. (B) Complex **43** and complex **49**

CD spectroscopy was performed to further analyze the interaction of silicon complexes **48** and **51** with DNA duplex. Figure 65 shows that the addition of just one equivalent of complex **48** to duplex DNA resulted in a dramatic change of the cotton effects, which continued to be intensified with increasing complex **48** until saturation was reached at a [DNA]:[Si] ratio of around 1:5. Analogous results were observed for the 4, 5-pyrenediolate complex **51**.

A lot of metallo-intercalators, such as $[Rh(phen)_2Phi]^{3+}$ and $[Ru(bipy)_2dppz]^{2+}$, are stereoselective, and both Δ-enantiomers of the two complexes are preferred. To investigate the stereoselectivity of the silicon complexes on the DNA duplex, complex **48** was resolved with a CHIRALPAK IB HPLC column (250×4.6 mm) on an Agilent 1200 Series HPLC System by Chen Fu from Meggers Group (Figure 66). Using this method, milligram amounts of the individual enantiomers were obtained. The two enantiomers are configurationally stable at room temperature; dissolved in MeCN and stored in a glass vial at room temperature on the laboratory bench, no change in the enantiomeric ratio was observed after three days. Figures 67 and 68 show that the absolute configurations of the individual enantiomers were assigned based on their CD spectra. According to the literature, [91] the absolute stereochemistry of enantiomers of **48** can be verified, as Λ-(+)-$[Si(bpy)_3]^{4+}$ exhibited a major positive CD band at lower frequency and a negative CD band at higher frequency. The A-enantiomer of **48** showed a similar CD pattern with major negative CD bands at 256 nm and 268 nm and a positive CD band at 285 nm, so enantiomer **A** was assigned as the absolute configuration Λ. Similarly, enantiomer **B** was assigned as the absolute configuration Δ.

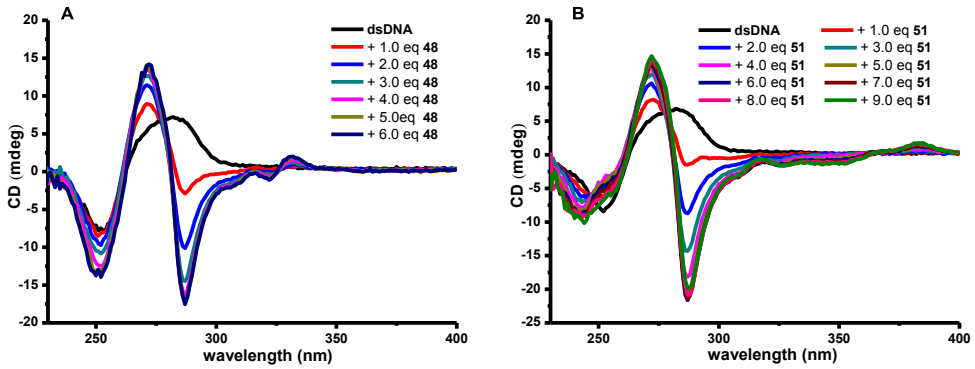

Figure 65 CD spectra of duplex DNA 5′-AGTGCCAAGCTTGCA-3′/3′-TCACGGTTCGAACGT-5′ titrated with increasing amounts of complexes. Conditions: 5 mM Tris-HCl, 50 mM NaCl, pH 7.4 and 20 μM duplex. (A) 9, 10-phenanthrenediolate **48** (0–120 μM). (B) 4, 5-pyrenediolate complex **51** (0–180 μM)

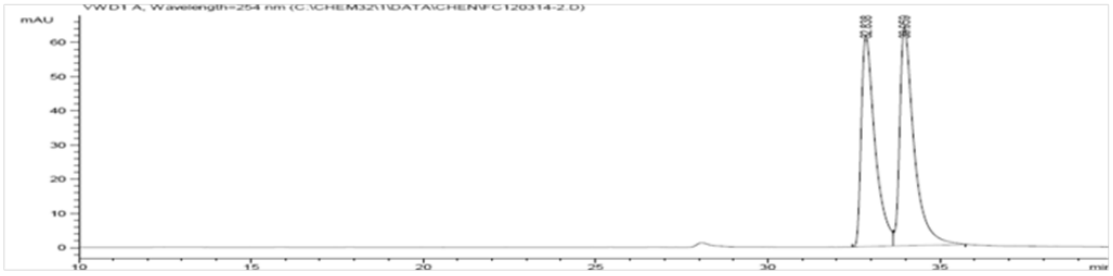

Figure 66 HPLC trace for racemic silicon complex **48** (Measurement carried out by Chen Fu from Meggers group)

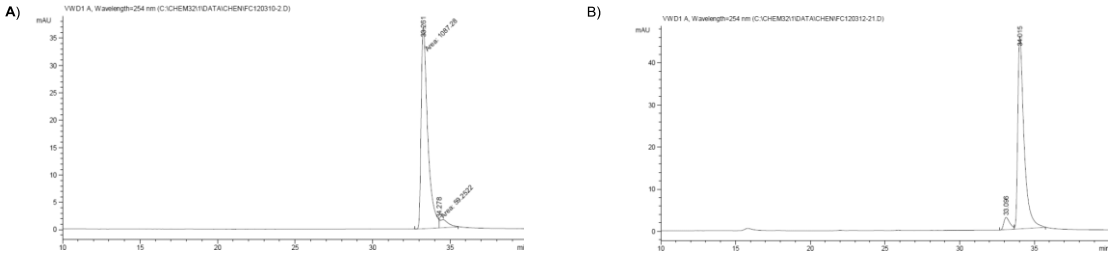

Figure 67 HPLC trace for enantiomer A of complex **48**. Integration of peak areas: 94.8:5.2 e.r.; **B**) HPLC trace for enantiomer B of complex **48**. Integration of peak areas: 5.8:94.2 e.r. (Measurement carried out by Chen Fu from Meggers Group)

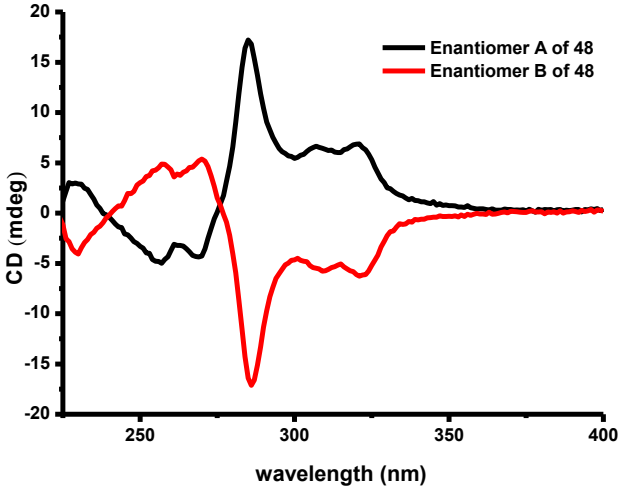

Figure 68 CD spectra of the two enantiomers of **48**. Conditions: 5 mM Tris-HCl, 50 mM NaCl, pH 7.4 and 20 μM enantiomer. Based on these CD spectra, enantiomer A is assigned the absolute configuration Λ and enantiomer B is assigned as Δ[91]

As shown in Figure 69, we noticed that the addition of both enantiomers **48** to duplex DNA resulted in a dramatic change of the cotton effects. To determine the stereoselectivity, some other measurement methods should be used.

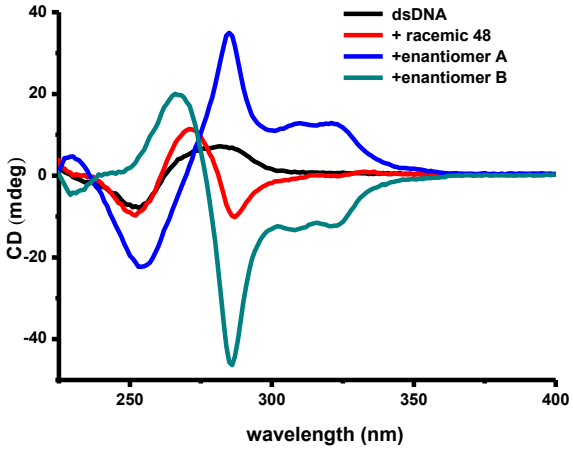

Figure 69 CD spectra of the racemic **48** and the two enantiomers of **48** in the presence of DNA. Conditions: 5 mM Tris-HCl, 50 mM NaCl, pH 7.4, 20 μM duplex and 40 μM racemic **48** or enantiomers of **48**. The CD spectra of the duplex DNA (5′-AGTGCCAAGCTTGCA-3′/3′-TCACGGTTCGAACGT-5′) alone and the sum of the CD spectra of the individual enantiomers in the presence of DNA are given for comparison

Finally, the effect of duplex DNA on the absorption spectrum of silicon complex **51** was investigated. Binding constants were measured by absorption titration of 4, 5-pyrenediolate silicon complex **51** with calf thymus DNA at room temperature, in 5 mM Tris-HCl, 20 mM NaCl, pH 7.5 and 20 μM complex, and calf thymus DNA was added from 0 to 200 μM. The dilution of silicon complex concentrations at the end of the titrations was negligible. The values of equilibrium DNA binding constants, K, were determined by the following equation, which we have discussed in the theoretical section:

$$\frac{\varepsilon_a-\varepsilon_f}{\varepsilon_b-\varepsilon_f}=\frac{b-\sqrt{b^2-\frac{2\times K_b{}^2\times 0.00003\times d}{s}}}{2\times K_b\times 0.00003} \qquad (b=1+K_b\times 0.00003+\frac{K_b\times d}{2s})$$

Figure 70 shows that the addition of calf thymus DNA to **51** produced in a concentration-dependent fashion strong hypochromicity of the π→π* absorption band at 355 nm (45% decrease), together with a modest bathochromic shift of 6 nm. Absorption titration resulted in a binding constant of (1.7 ± 0.6) ×10^6 M^{-1}.

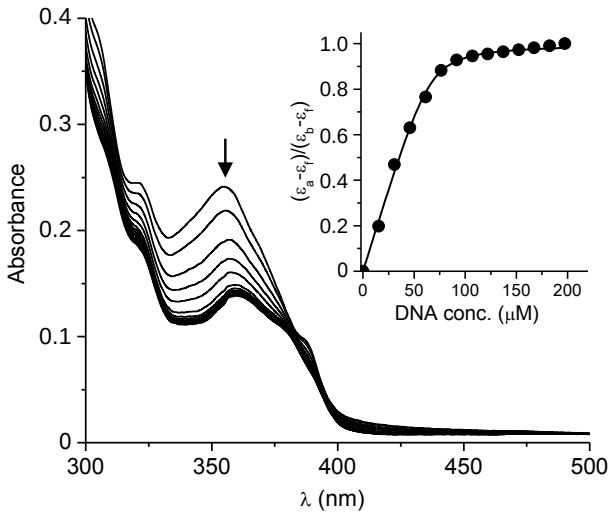

Figure 70 UV/Vis-absorption spectra of 4, 5-pyrenediolate complex **51** titrated with increasing amounts of calf thymus DNA (0-200 μM). Conditions: 5 mM Tris-HCl, 20 mM NaCl, pH 7.5 and 20 μM complex. Insert: Plot of $(\varepsilon_a-\varepsilon_f)/(\varepsilon_b-\varepsilon_f)$ *versus* increasing DNA concentration, with ε_a = extinction coefficient of the complex at a given DNA concentration, ε_b = extinction coefficient when fully bound to DNA, and ε_f = extinction coefficient of the complex in the absence of DNA. (Measurement carried out by Dr. Pijus Sasmal from Meggers Group)

Taken together, the strong thermal stabilization of duplex DNA by the silicon complexes **48** and **51**, along with the modulation of the secondary structure as observed by CD spectroscopy, and the hypochromic and bathochromic shifts of the UV-absorption of **48** (phenanthrene π→π* transition) and **51** (pyrene π→π* transition) upon DNA titration, are indicative of an intercalative binding with the extended π-systems of the 1,10-phenanthrolinediolate and 4, 5-pyrenediolate ligands inserted between neighboring base pairs.[34, 92] Furthermore, the saturation effect observed for the duplex stabilization and the change in the secondary structure at higher concentrations of **48** and **51** were consistent with the required distance between the intercalation sites of these bulky silicon complexes (neighbor exclusion principle). According to the neighbor exclusion principle, the access of another intercalator to the binding site next to the neighboring intercalation pocket is hindered.[93] Additionally, the observed tight binding of the 4, 5-pyrenediolate silicon complex **51** was comparable to high-affinity DNA metallo-intercalators. For example, for the classical metallo-intercalator $[Ru(phen)_2(dppz)]^{2+}$ (dppz = dipyrido[3,2-*a*:20,30-*c*]phenazine), binding constants in the range of 10^6-10^7 M^{-1} were reported.[42b, 94] This indicated that interaction between the previous octahedral silicon complexes with DNA duplexes was not as strong as the metallo-intercalator $[Ru(phen)_2(dppz)]^{2+}$.

3.2.2.2 Silicon complexes containing phenazinediolate

As there were ten silicon complexes containing the phenazinediolate synthesized **77**-**86** (Scheme 13), we wondered if the special ligands harboring phenazine structure of the octahedral silicon complexes would intensify the interaction with the DNA duplex. The thermal stability of the DNA duplexes in the presence of this type of silicon complexes was measured (Figure 71). The shifts in the melting temperatures (ΔT_m) of the DNA duplex were very low in the presence of four equivalents of **78**, **83**, **85** and **86**. However, the melting temperature of the DNA duplex would increase obviously in the presence of four equivalents of **77**, **79**, **80**, **81**, **82** and **84** (Table 7).

This indicated that the large π system has no strict relation to the capability of the interaction. As has been mentioned, $[Si(Phen)_2(arenediolate)]^{2+}$ (**48**-**51**) showed stronger interaction than the corresponding $[Si(bpy)_2(arenediolate)]^{2+}$ (**42**-**45**) previously. However, for phenazinediolate contained silicon complexes structure, the results were completely opposite. Some other methods were needed to fully understand the mechanism of the interaction between octahedral silicon complexes with DNA duplexes. On the other hand, complexes **78** and **79**, **83** and **84** had similar structures, and we could notice that ligand benzo[*a*]naphtho[2,3-*c*]phenazinediolate showed much stronger interaction than benzo[*a*]quinoxalino[2,3-*c*]phenazinediolate. This might be caused by hydrogen formation between the ligands and DNA bases. **79** had lower solubility than **78** in CH_3CN; the situation was similar for **83** and **84**.

Finally, we investigated the effect of duplex DNA on the absorption spectra of silicon complexes **77**, **78**, **80** and **81**. Figure 72 shows that the addition of calf thymus DNA to **51** produced in a concentration-dependent fashion strong hypochromicity of the π→π* absorption band at different bands. However, the intensity of absorption of the complexes was irregular while the concentration of the calf thymus DNA increased; this was uncommon. We inferred that the structure of calf thymus DNA might change in an uncommon way in the presence of these kinds of silicon complexes, so it was very difficult to calculate the binding constants of the complexes. On the other hand, there was an exception for complex **51**. Figure 73 shows that the addition of calf thymus DNA to **51** produced in a concentration-dependent fashion strong hypochromicity of the π→π* absorption band at 405 nm (45% decrease) together with a modest bathochromic shift of 6 nm. Absorption titration resulted in a binding constant of 2.0×10^7 M^{-1}. This complex showed a higher binding constant than the previous silicon complexes.

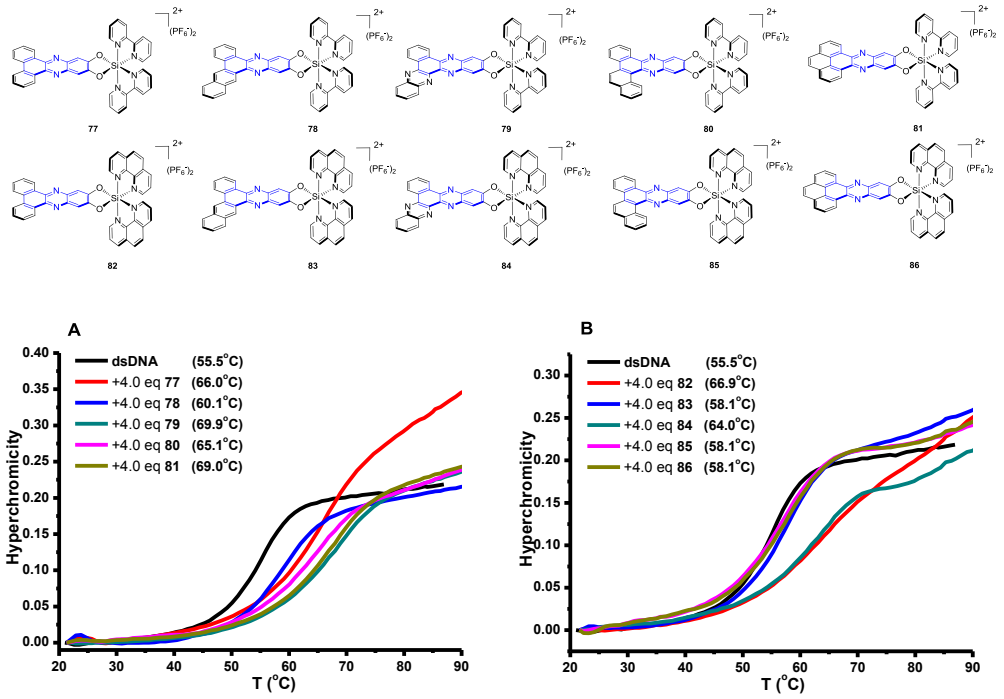

Figure 71 UV-melting curves of duplex DNA 5′-AGTGCCAAGCTTGCA-3′/3′-TCACGGTT CGAACGT-5′. Changes in absorbance upon heating as monitored at 260 nm. Conditions: 5 mM Tris-HCl, 50 mM NaCl, pH 7.4, and 2 μM of each strand in the presence of 8 μM $[Si(Phen)_2(arenediolate)]^{2+}$ (**77**-**86**)

Table 7 UV-melting temperature of 2 μM DNA duplex in Tris-HCl (5 mM, pH 7.4) with NaCl (50 mM) in the presence of or in the absence of 4.0 equiv silicon complexes

complex	T_m	ΔT_m	complex	T_m	ΔT_m
77	66.0	10.5	**82**	66.9	11.4
78	60.1	4.6	**83**	58.1	2.6
79	69.9	14.4	**84**	64.0	8.5
80	65.1	9.6	**85**	58.1	2.6
81	69.0	13.5	**86**	58.1	2.6

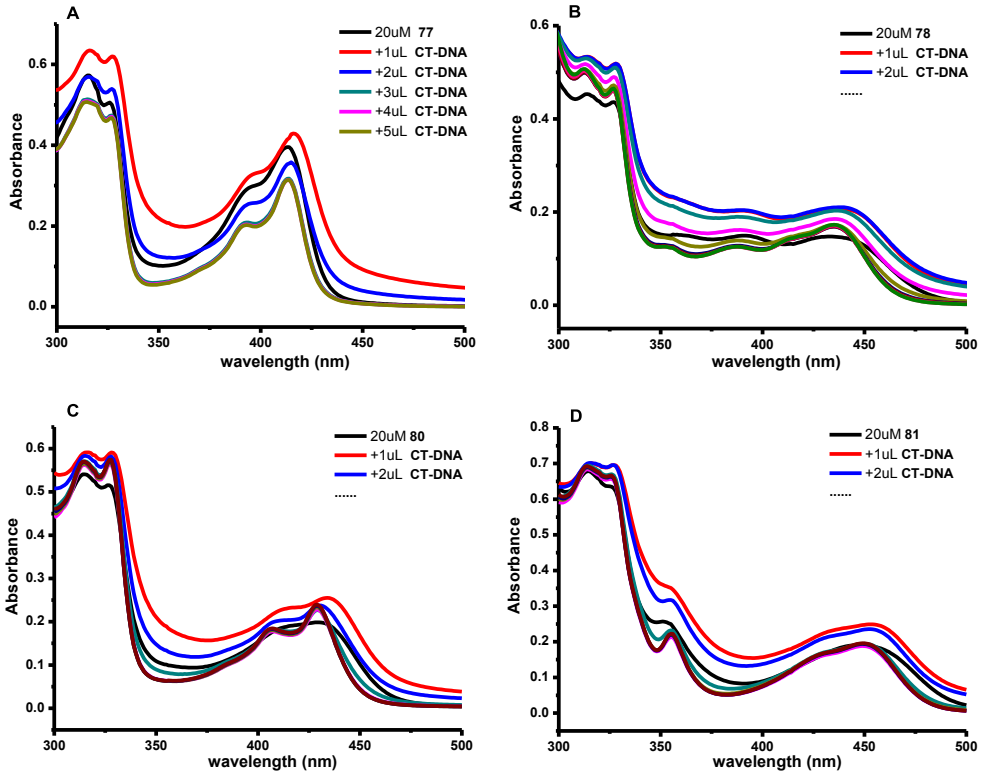

Figure 72 UV/Vis-absorption spectra of phenazinediolate complexes titrated with increasing amounts of calf thymus DNA. Conditions: 5 mM Tris-HCl, 20 mM NaCl, pH 7.5 and 20 μM complexes. (A) Complex **77**. (B) Complex **78**. (C) Complex **80**. (D) Complex **81**

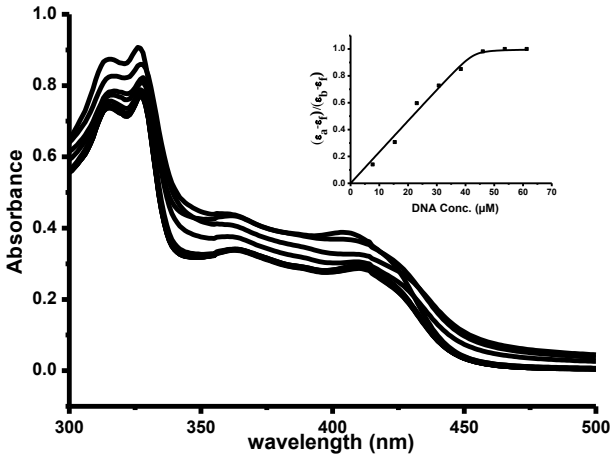

Figure 73 UV/Vis-absorption spectra of Benzo[*a*]quinoxalino[2,3-*c*]phenazinediolate complex **79** titrated with increasing amounts of calf thymus DNA (0-200 μM). Conditions: 5 mM Tris-HCl, 20 mM NaCl, pH 7.5 and 20 μM complexes. Insert: Plot of $(\varepsilon_a-\varepsilon_f)/(\varepsilon_b-\varepsilon_f)$ *versus* increasing DNA concentration, with ε_a = extinction coefficient of the complex at a given DNA concentration, ε_b = extinction coefficient when fully bound to DNA, and ε_f = coefficient of the complex in the absence of DNA

3.2.3 Silicon complexes as DNA-insertors

Metallo-insertion is another important mode. A lot of metallo-complexes have been used as DNA mismatch detectors, such as $[Rh(bpy)_2(chrysi)]Cl_3$ and $[Rh(bpy)_2(phzi)](Cl)_3$ (chrysi = 5,6-chrysene quinone diamine, dppz = dipyrido[3,2-a:29,39-c]phenazine).[49c] The complexes bind mismatched DNA sites specifically and, upon photoactivation, promote strand scission neighboring the mismatch site, which was confirmed by phosphorimagery of a 20% polyacrylamide denaturing gel. However, unlike the metallo-complexes, the silicon complexes did not cleave the DNA strands upon photoactivation. It was impossible for us to detect the mismatch site in a similar condition. For silicon complexes, only CD spectrum and UV-melting could be utilized to compare the different changes of the interaction between the complexes and matched or mismatched DNA.

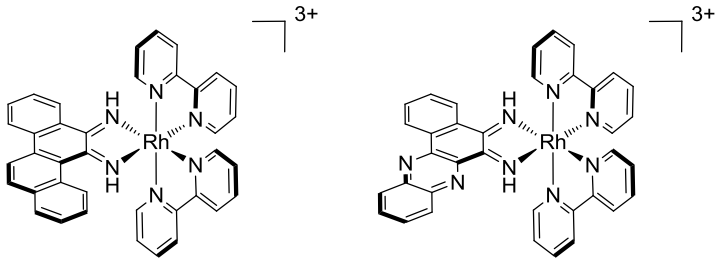

87 **88**

Scheme 14 Structure of $[Rh(bpy)_2(chrysi)]Cl_3$ (**87**) and $[Rh(bpy)_2(phzi)](Cl)_3$ (**88**)

We knew that $Rh(bpy)_2(chrysi)Cl_3$ (**87**) and $[Rh(bpy)_2(phzi)](Cl)_3$ (**88**) (Scheme 14) can target the mismatch site. According to the literature,[49c] these two rhodium complexes can be obtained easily. Two 19mer oligonucleotides (5′-GCTCGTCAT**C**GCTAGAGCA-3′/3′-CGAGCAG-TA**G**CGATCTCGT-5′ and 5′-GCTCGTCAT**C**GCTAGAGCA-3′/3′-CGAGCAGTA**C**CGATCTCGT-5′) were chosen for measurement. The first one is a completely matched duplex, the second one has one C-C mismatched base pair. As shown in Figure 74, the melting temperatures (T_m) of the matched DNA duplex would increase by 5 °C in the presence of one equivalent of **87**; however, for the mismatched DNA duplex, the ΔT_m was 9 °C,

which was higher than 5 ^{o}C. A similar situation was also observed for complex **88**. Accordingly, we also measured the shift of the melting temperature of the matched and mismatched DNA duplexes in the presence of the silicon complexes. Table 8 shows that silicon complexes **42**, **44** and **48** had a similar impact on the matched or mismatched DNA duplexes. However, these results did not give us confirmation that the octahedral silicon complexes had detected the DNA mismatched sites; so more measurement should be carried out to make the results reliable.

CD spectrum was utilized to perform the change of the DNA duplexes in the presence of complexes. Firstly, as a comparison, CD spectra of the DNA duplexes were measured as the concentration of the rhodium complexes **87** and **88** increased. For complex **87**, we could observe that the cotton effect of the matched DNA duplex at 260 nm would weaken as the concentration increased (Figure 74A). However, the situation was completely different for the C-C mismatched DNA duplexes. Figure 74B shows that the cotton effect would weaken at 260 nm as the concentration increased before the ratio of [**87**]/[mismatched DNA] reached one. After one equivalent of **87** had been added, the cotton effect would be intensified as the concentration of the complex continued to increase. This situation was not identical for complex **88**, which has been reported to be used as a DNA mismatch detector. The cotton effects of mismatched and matched DNA duplexes would both be weakened as the concentration of the complex increased, even after the ratio of [**88**]/[mismatched DNA] reached one. This might be caused by these kinds of rhodium complexes not being versatile detectors for all the C-C mismatched DNA duplexes (Figures 74C and 74D).

Table 8 UV-melting temperature of 2 μM matched and mismatched DNA duplex in Tris-HCl (5 mM, pH 7.4) with NaCl (50 mM) in the presence of or in the absence of 1.0 equiv silicon complexes

complex	Matched (^{o}C)	ΔT_m (^{o}C)	C-C mismatched (^{o}C)	ΔT_m (^{o}C)
-	61.1		50.3	
42	63	1.9	57.1	6.8
44	63	2.0	57.1	6.8
46	61.2	-	50.4	-
47	67.1	6.0	55.4	5.1
49	64.7	3.6	51.9	-
50	63.1	2.0	57.2	6.9

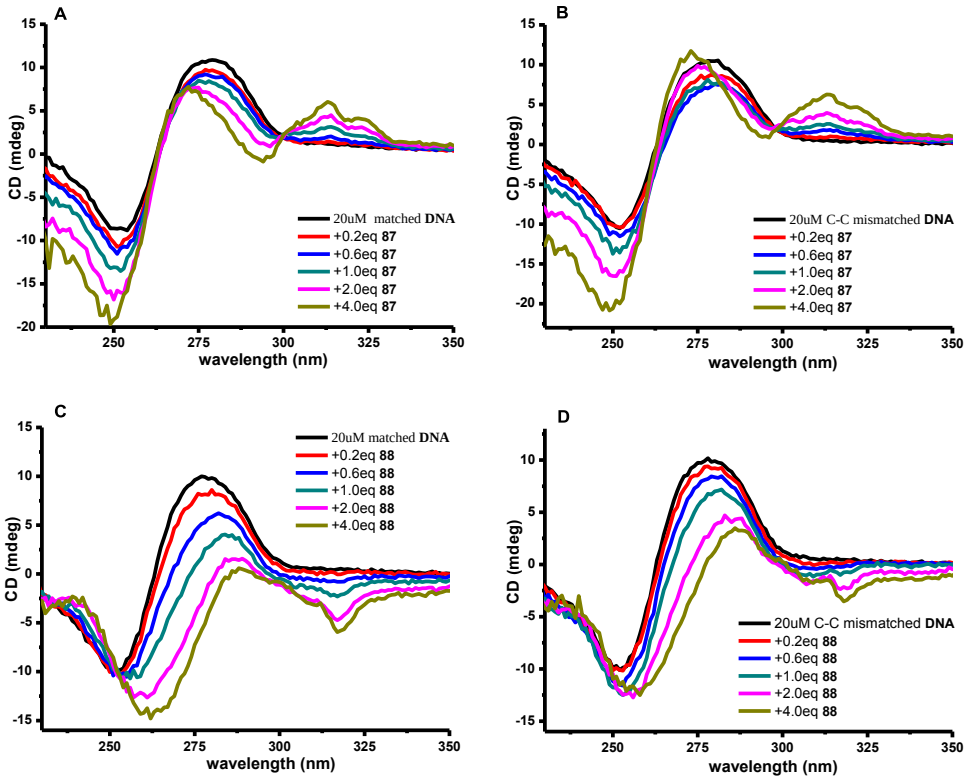

Figure 74 CD spectra of matched and C-C mismatched DNA duplexes titrated with increasing amounts of rhodium complexes. Conditions: 5 mM Tris-HCl, 50 mM NaCl, pH 7.4 and 20 μM duplex. (A) Matched DNA with complex **87** (0–80 μM). (B) C-C mismatched DNA with complex **87** (0–80 μM) (C) Matched DNA with complex **88** (0–80 μM). (D) C-C mismatched DNA with complex **88** (0–80 μM)

It was indicated that the bulky rhodium complexes might cause different changes of CD spectra of the matched and C-C mismatched DNA duplexes. Next, the change of the CD spectra of matched and mismatched DNA duplexes in the presence of silicon

complexes was investigated. As shown in Figure 75, the situation of silicon complex **44** was very similar to rhodium complex **87**; the cotton effect of the mismatched DNA duplex at 260 nm would be weakened as the concentration increased before the ratio of [**44**]/[mismatched DNA] reached one. After one equivalent of **44** had been added, the cotton effect would be intensified as the concentration of the complex continued to increase (Figure 75). It is worth noting that ligands of both complexes **44** and **87** contained similarly structured chrysene, and the change of CD spectra of matched and mismatched DNA duplexes showed a similar trend as the concentration of complex **42** increased. Accordingly, octahedral complexes might also be used as mismatched DNA detectors.

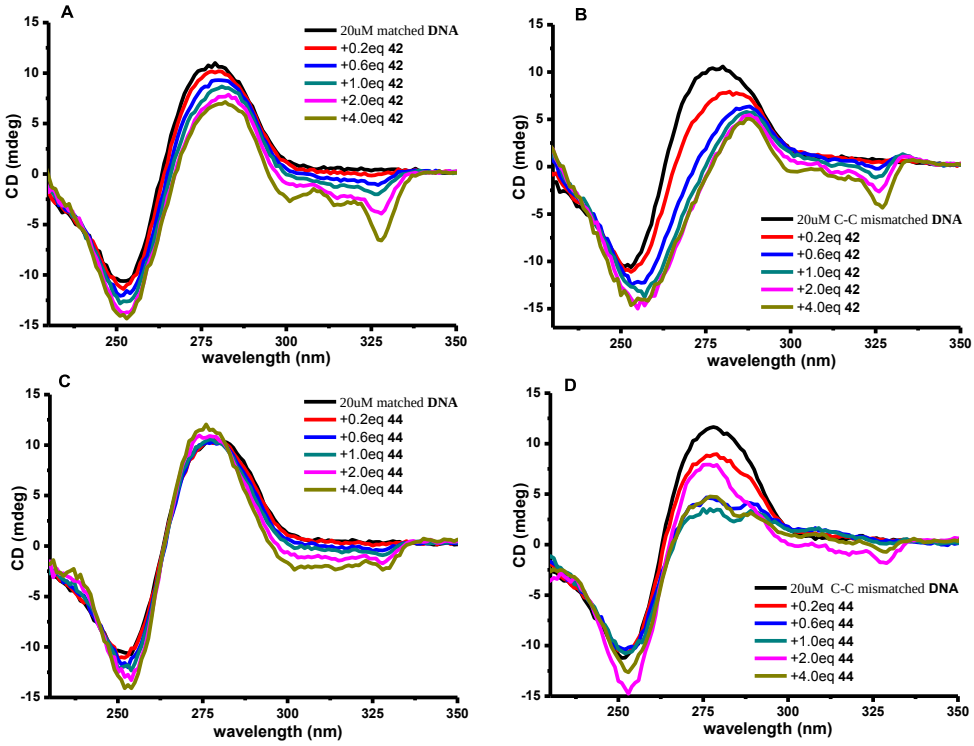

Figure 75 CD spectra of matched and C-C mismatched DNA duplexes titrated with increasing amounts of silicon complexes. Conditions: 5 mM Tris-HCl, 50 mM NaCl, pH 7.4 and 20 μM duplex. (A) Matched DNA with complex **42** (0–80 μM). (B) C-C mismatched DNA with complex **42** (0–80 μM) (C) Matched DNA with complex **44** (0–80 μM). (D) C-C mismatched DNA with Complex **44** (0–80 μM)

The interaction between other silicon complexes with mismatched DNA duplexes was also investigated. It was found that complexes **48** and **49** have a similar impact on the mismatched DNA duplexes to complex **44**. The enantiomers of **48** were also measured. Now we are striving to grow a crystal of self-complementary DNA with mismatched base-pairs in the presence of the **48**-A enantiomer and **48**-B enantiomer, respectively (Figure 76).

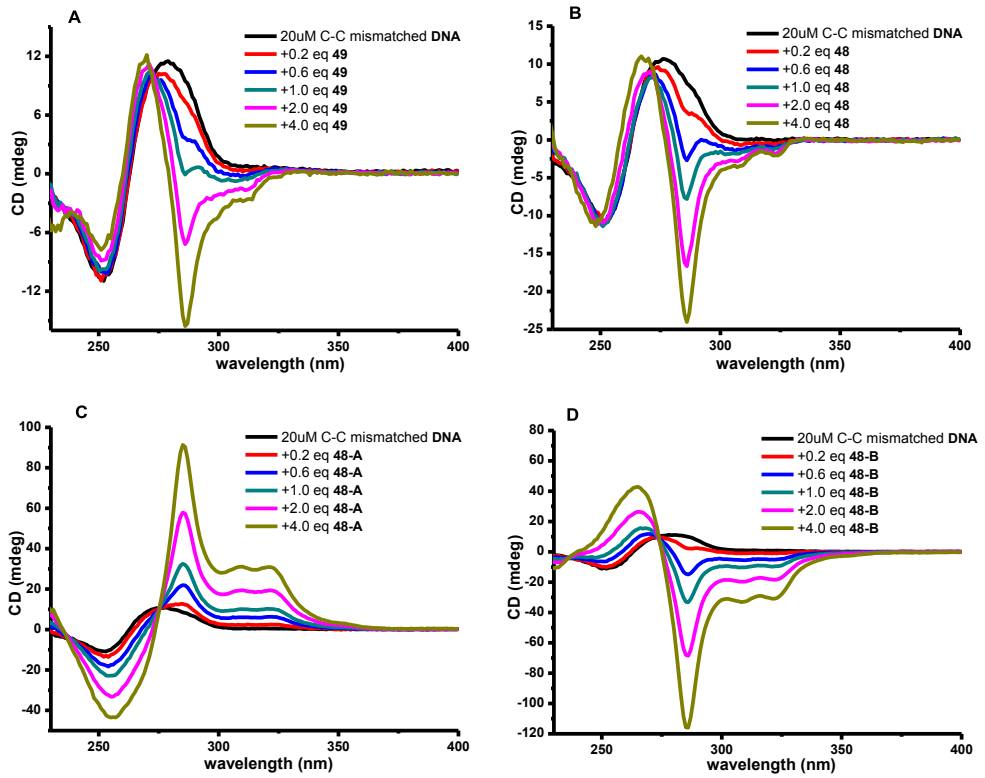

Figure 76 CD spectra of C-C mismatched DNA duplex titrated with increasing amounts of silicon complexes. Conditions: 5 mM Tris-HCl, 50 mM NaCl, pH 7.4 and 20 μM duplex. (A) C-C matched DNA with Complex **49** (0–80 μM). (B) C-C mismatched DNA with racemic complex **48** (0–80 μM) (C) C-C matched DNA with enantiomer complex **48-A** (0–80 μM). (D) C-C mismatched DNA with enantiomer complex **48-B** (0–80 μM)

In conclusion, we can infer that octahedral silicon complexes might be used as DNA mismatched base-pair detectors. However, there are not as many methods as there are for bulky rhodium complexes to confirm that the silicon complexes have really targeted the site of the mismatched base-pair. We believe that modification of

the ligand, which could induce the fluorescence signal, may help us to confirm this result.

3.2.4 Silicon complexes interaction with DNA G-quadruplex

It was very strange that several of the silicon complexes harboring phenazinediolate structure had very weak interaction with the DNA duplex, as the surface of the ligands should be strong enough to intercalate with the base pairs. As a result, we wondered whether these kinds of silicon complexes would stabilize the formation of the G-rich quadruplex.

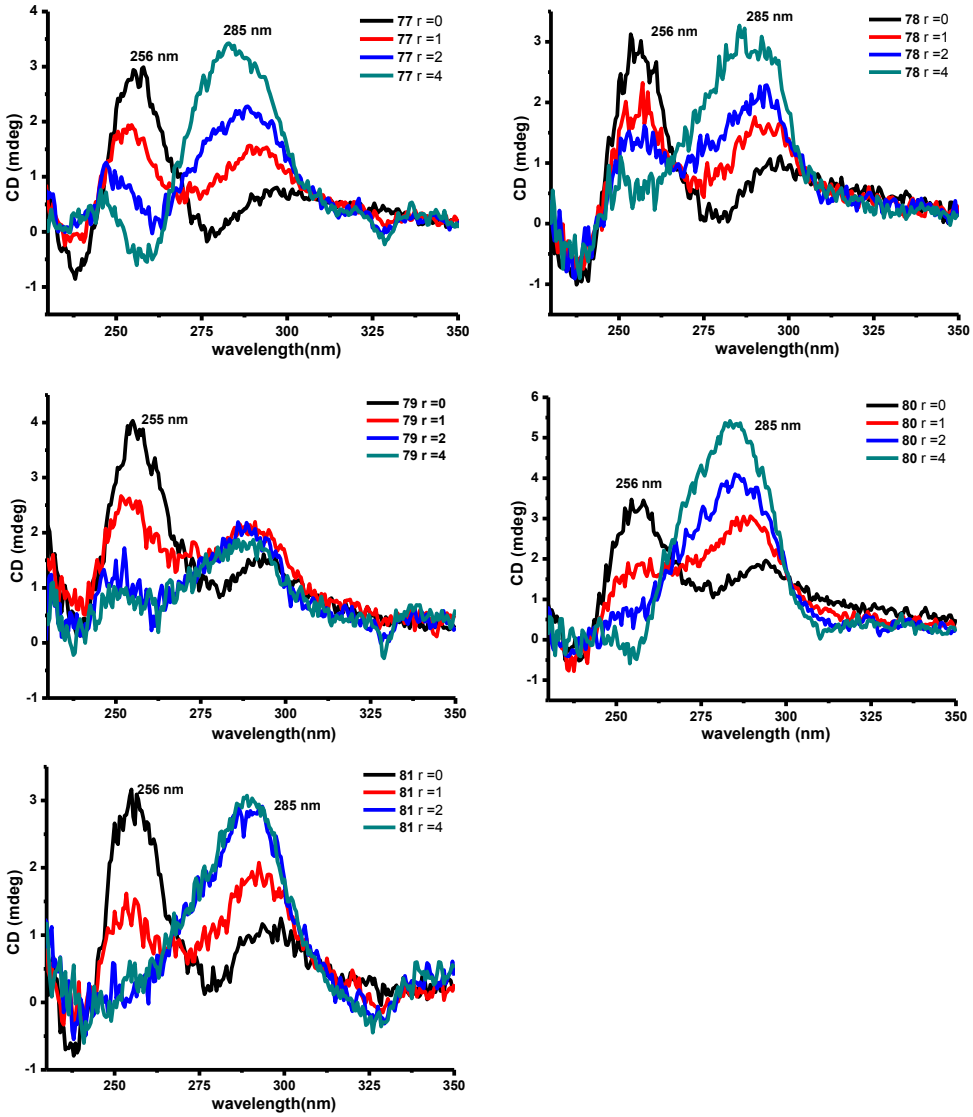

Figure 77 CD spectra of the G-quadruplex $(T_2AG_3)_4$ titrated with increasing amounts of complexes $[Si(bpy)_2(phenazinediolte)]^{2+}$. Conditions: 5 mM Tris-HCl. 12.5 μM G-quadruplex and *r* values from 0

to 4. (r = [silicon complex]/[$(T_2AG_3)_4$]). (A) Complex **77**. (B) Complex **78.** (C) Complex **79**. (D) Complex **80**. (E) Complex **81**

Figure 77 shows the CD spectra of the structures obtained by adding different concentrations of $[Si(bpy)_2(phenazinediolte)]^{2+}$ (**77**-**81**) to the human telomeric sequence Telo24 [$(T_2AG_3)_4$] in the absence of a high concentration of free univalent metal ions. For complexes **77**, **78**, **80** and **81**, as the concentration of the silicon complex increased, there was a sharp decrease in the band at 256 nm, accompanied by a sharp increase in the band at 285 nm. It was a little different for complex **79**, as the concentration of the complex increased, the band at 256 nm decreased sharply, whereas the band at 285 nm only increased slightly. As we know, the typical value of the long-wavelength CD maximum around 295 nm is the marker of the G-quadruplex formation.[50c] However, in our case, as the concentration of the silicon complexes increased, the positive peak appeared at 285 nm. A similar situation was also observed that in Zn^{2+} induced structural transition from the random coil to quadruplex of $AG_3(T_2AG_3)_3$, CD spectra had the characteristics of antiparallel G-quadruplexes, although the long-wavelength CD maximum is around 285 nm rather than the typical value of 295 nm. They explained that the difference spectrum showed an isobestic point around 280 nm, whereas a hyperchromism was observed upon G-quadruplex formation at 285 nm. Accordingly, we inferred that these silicon complexes would also induce G-quadruplex formation in the absence of the univalent metal ions.

We continued to investigate the interaction between $[Si(bpy)_2(phenazinediolte)]^{2+}$ (**82**-**86**) and G-quadruplex. Figure 78 shows that complexes $[Si(phen)_2(phenazinediolte)]^{2+}$ (**82**-**86**) might have a different impact on the quadruplex from complexes $[Si(bpy)_2(phenazinediolte)]^{2+}$(**77**-**81**). For complexes **82**, **83** and **86**, on adding increasing concentration of the silicon complex, there was a sharp increase in the band at 285 nm, accompanied by a sharp decrease in the band at 256 nm. However, the change was more complicated for the complexes **84** and **85**, and more investigation was needed to figure out the mechanism. It seemed that

complexes **82**, **83** and **86** could induce the formation of the G-quadruplex in the regard of the typical band at 294 nm.

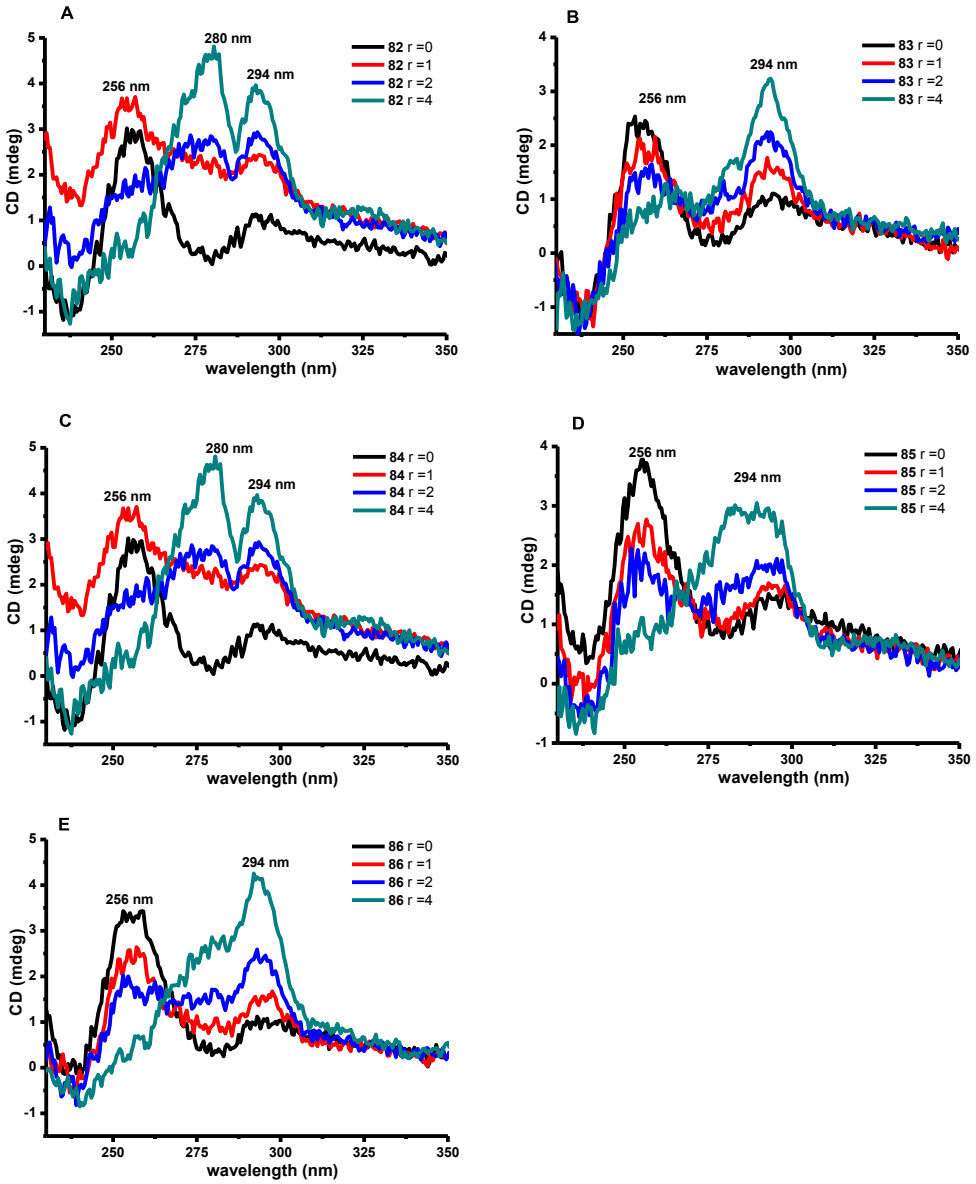

Figure 78 CD spectra of the G-quadruplex $(T_2AG_3)_4$ titrated with increasing amounts of complexes $[Si(bpy)_2(phenazinediolte)]^{2+}$. Conditions: 5 mM Tris-HCl. 12.5 μM G-quadruplex and *r* values from 0 to 4. (*r* = [silicon complex]/$[(T_2AG_3)_4]$). (A) Complex **82**. (B) Complex **83**. (C) Complex **84**. (D) Complex **85**. (E) Complex **86**

Next, we investigated the absorption spectra changes of several silicon complexes, **78**, **79**, **80** and **81**, as the concentration of G-quadruplex increased. Figure

78 shows that the addition of G-quadruplex $(T_2AG_3)_4$ to these kinds of complexes produced in a concentration-dependent fashion strong hypochromicity of the $\pi \rightarrow \pi^*$ absorption band at 435 nm for **78** (59% decrease), 405 nm for **79** (54% decrease), 430 nm for **80** (61% decrease) and **81** (46% decrease). Absorption titration resulted in a binding constant of 2.2 $\times 10^6$ M^{-1} (**78**); 2.9 $\times 10^6$ M^{-1} (**79**); 1.7 $\times 10^6$ M^{-1} (**80**); 1.2 $\times 10^6$ M^{-1} (**81**).

Thermal melting experiments were often utilized to measure the stabilization or destabilization of a duplex structure by a ligand. The same method was also used for G-quadruplex, and the absorbance was measured at 295 nm instead of 260 nm. Figure 79 shows the melting curve of G-quadruplex in the presence of **79** or **80** in 100 mM NaCl, 10 mM Tris-HCl, and 1 mM EDTA at pH 7.4. The concentration of **79** or **80** was five times greater than $(T_2AG_3)_4$. However, the ΔT_m seemed to be very low (Figure 80). These results conflicted with the binding capacity. Maybe the limitation of low-intensity signal variation of UV and CD melting curves resulted in the inaccuracy of the melting temperature. Accordingly, if we want to confirm the stabilization of the G-quadruplex in regard to the melting temperature, some other sequences or methods should be introduced to make further investigation.

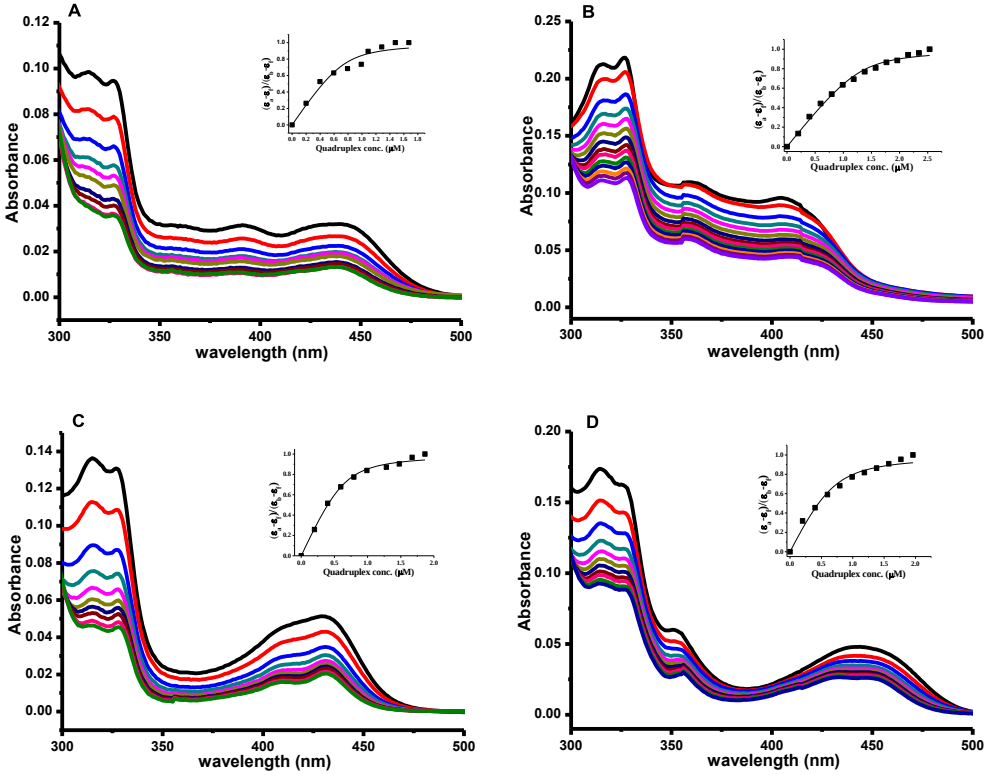

Figure 79 UV/Vis-absorption spectra of Silicon complexes titrated with increasing amounts of G-quadruplex. Conditions: 5 mM Tris-HCl, 20 mM NaCl, pH 7.5 and 20 μM complexes. (**A**) Complex **78**. (**B**) Complex **79**. (**C**) Complex **80**. (**D**) Complex **81**. Insert: Plot of $(\varepsilon_a-\varepsilon_f)/(\varepsilon_b-\varepsilon_f)$ *versus* increasing DNA concentration, with ε_a = extinction coefficient of the complex at a given DNA concentration, ε_b = extinction coefficient when fully bound to DNA, and ε_f = extinction coefficient of the complex in the absence of DNA

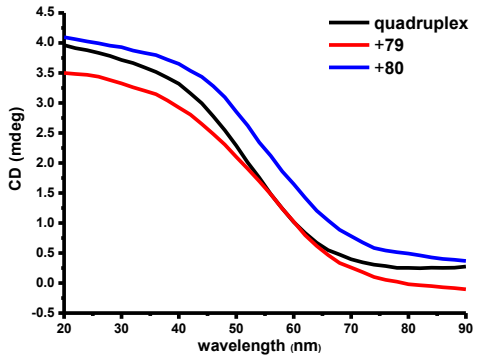

Figure 80 CD melting curves of DNA oligonucleotides $(T_2AG_3)_4$. Changes in cotton effect upon heating as monitored at 295 nm. Conditions: 10 mM Tris–HCl, 100 mM NaCl, pH 7.4, 12.5 μM DNA, and concentration ratio of complex/DNA (*r*) is 5:1

Chapter 4 Summary and Outlook

4.1 GNA as a Scaffold for Molecular Aggregates of Chromophores

In the first part of this thesis, simplified glycol nucleic acid (GNA) was used as the template for the helical assembly of covalently bound homochromophores and heterochromophores: perylene bisimide (**PBI**), phthalocyanine, and porphyrin. All three nucleotide chromophores were successfully incorporated into GNA by automated solid phase synthesis. The synthetic route of **PBI** and phthalocyanine phosphoramidite building blocks was described in detail in Chapter 3.

First, GNA as a scaffold for **PBI** homochromophores aggregation was studied (Scheme 15). The interstrand **PBI** dimers of **GNA5** and **GNA6** could stabilize the duplexes while zipper-like **PBI** trimers or tetremers of **GNA9** and **GNA10** destabilized the duplexes. Some other types of **PBI**-modified oligonucleotides were also synthesized, indicating that **PBI** could be used as an excellent artificial base surrogate. UV/Vis absorption and CD spectroscopy were used to gain insight into excitonic interaction of the **PBI**s inside the GNA duplexes.

An initial study of **PBI** as a tool for GNA-base mismatch detection was also made. Both UV/Vis-absorption spectroscopy and CD spectroscopy of **GNA13**, **GNA14**, **GNA15**, and **GNA16**, in which two **PBI** chromophores were separated by one matched **A**:**T** base pair or one mismatched **T**:**T** or **A**:**A** base pair, were measured. From these four, only **GNA14** displayed different spectrum from others.

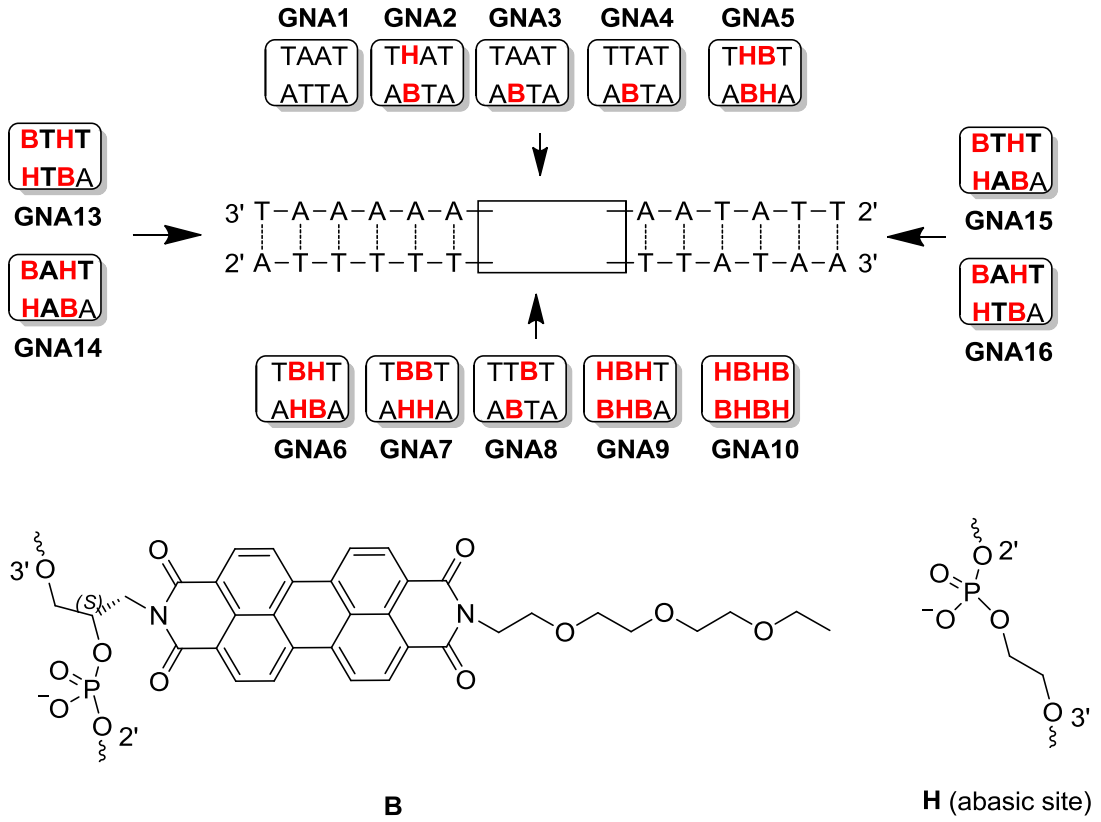

Scheme 15 Sequences of **PBI**-containing 16mer GNA duplexes together with Watson–Crick reference duplex

Second, phthalocyanine was introduced either at 3´-terminal or internal positions (Scheme 16) of GNA. Only the interstrand phthalocyanine dimers of **GNA26** and **GNA27** could stabilize the duplexes. **GNA17**, **GNA20**, **GNA21**, and **GNA22** were highly destabilized. The UV/Vis-absorption spectra of **GNA18** and **GNA19** differed from the corresponding spectra of oligonucleotides with one phthalocyanine modification. Both absorption bands shifted hypsochromically from 694 nm to 684 nm, and the relative ratios of the absorption bands at 642 nm and 694 nm were significantly changed. CD spectra were almost identical to that of the native GNA duplex, and no long-wavelength CD bands of exciton coupling (EC-CD) between the two phthalocyanine chromophores were observed.

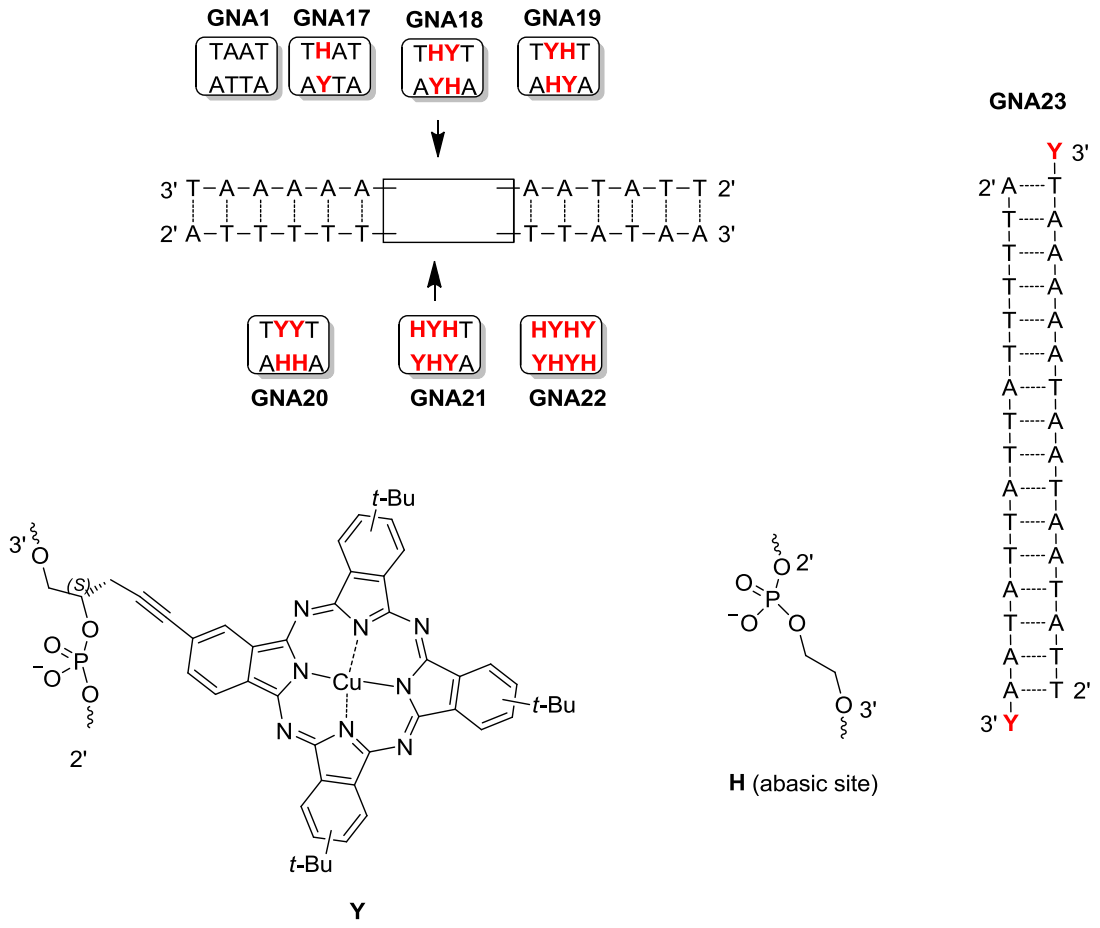

Scheme 16 Sequences of phthalocyanine-containing 16mer GNA duplexes together with Watson–Crick reference duplex

The aggregation of **GNA23** displayed that this kind of GNA-phthalocyanine conjugates have the potential to form ordered and thermally stable supramolecular GNA-based architectures, which may be applied in the field of nanotechnology.

Finally, with three different chromophores in hand, GNA as a scaffold for heterochromophores aggregation was also investigated, and these assemblies. The main work was focused on phthalocyanine-**PBI**, porphyrin-phthalocyanine, and **PBI**-porphyrin heterochromophore aggregation inside GNA duplexes. Up to four **PBI**/porphyrin, phthalocyanine/**PBI**, or phthalocyanine/porphyrin heterochromophores replaced the natural bases in the middle of the 16mer GNA duplexes in the form of an interstrand alternating sequence (Scheme 17). In the presence of zipper-like array of heterochromophores, some of them, especially

GNA28, **GNA36**, and **GNA44**, had very high thermal stability and displayed interesting UV/Vis-absorption and CD spectra.

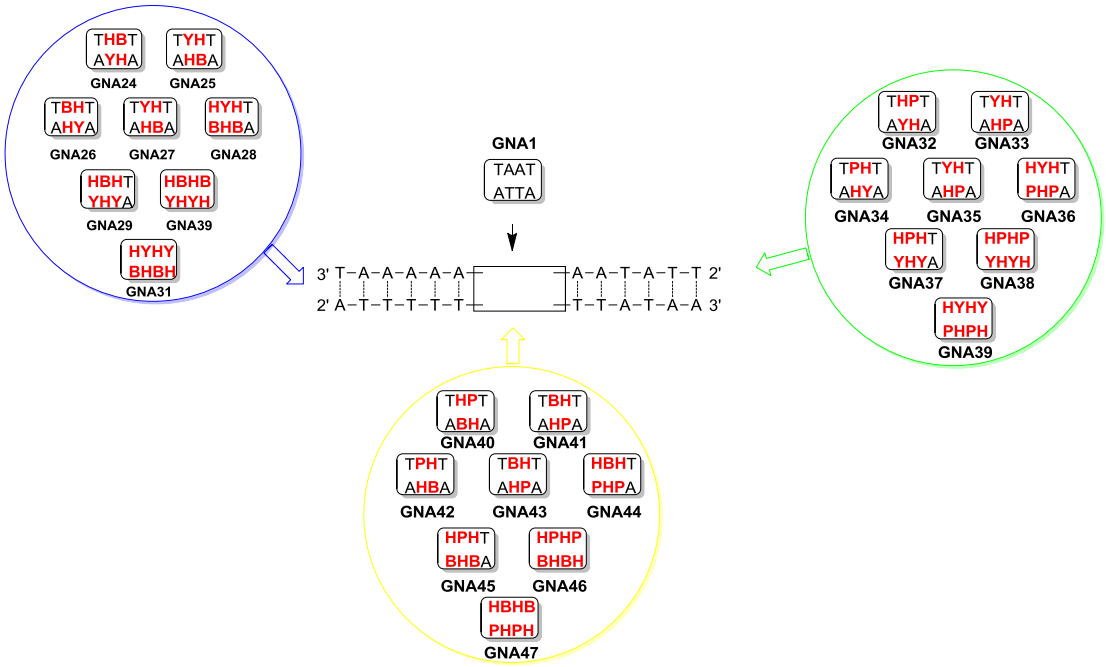

Scheme 17 Sequences of heterochromophores-containing 16mer GNA duplexes together with Watson–Crick reference duplex

Perylene bisimide, phthalocyanine, and porphyrin are important chromophores because of their excellent photophysical properties. GNA duplexes with heterchromophric modification, especially with PBI and porphyrin, shown significantly increased thermal stability. In order to better understanding their interaction in the GNA duplexes, we have been trying to grow crystal of modified GNA duplexes with different length and sequences.

4.2 Design of Octahedral Silicon Complexes as DNA binder

In this part of the thesis, the first examples of biologically active complexes based on octahedral silicon were designed, and silicon complexes with simple arenediol ligands (**42-51**) and phenazinediol ligands (**77-86**) were successfully synthesized (Scheme 18). These kinds of silicon complexes could be used to

intercalate with DNA duplexes, detect mismatched DNA base pairs, and stabilize the formation of the G-quadruplex.

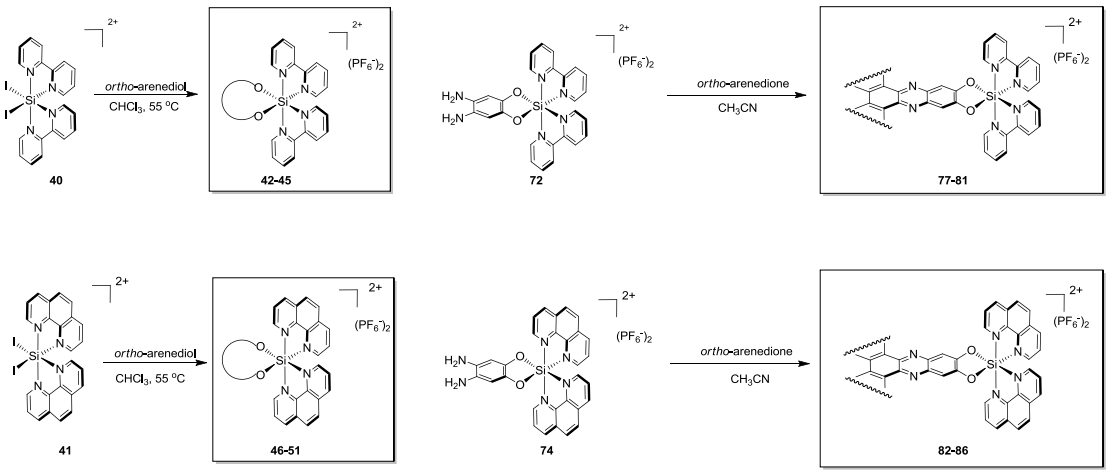

Scheme 18 Structures of octahedral silicon complexes

In a proof-of-principle study, we have shown that structural transition metals can be replaced by inert octahedral silicon. For the sole purpose of providing a structural octahedral center, the metalloid silicon may encompass several advantages over transition metals. These include: low price and unlimited availability as the second most abundant element in the Earth's crust, lack of toxicity concerns, and the absence of any interfering redox and photochemistry. Their remarkably straightforward synthesis, as well as the counterintuitive hydrolytic stability of these octahedral silicon complexes, renders them a novel class of structural templates for widespread applications in chemical biology and medicinal chemistry.

Chapter 5 Experimental part

5.1 Materials and Methods

Solvents and reagents

All reactions were carried out under nitrogen or argon atmosphere. Solvents were distilled under nitrogen from calcium hydride (CH_3CN, CH_2Cl_2 and DMF) or sodium/benzophenone (Et_2O, THF). Chlorobenzene and acetone were used as HPLC grade without further drying. All reagents were purchased from Acros, Aldrich, Alfa, Strem and Fluorochem and used without further purification. Phenanthrene-9,10-diol, bulky rhodium complexes **87** and **88** were prepared according to published procedures.[49c, 95] 1,10-Phenanthroline and 2,2'-bipyridine were sublimated before use. Column chromatography was performed with silica gel (230-400 mesh).

Nuclear magnetic resonance spectroscopy (NMR)

Bruker Advance 300 MHz (^{1}H-NMR: 300 MHz, ^{13}C-NMR: 75 MHz, ^{31}P-NMR: 121 MHz, ^{29}Si-NMR: 60 MHz)

Bruker DRX 400 MHz (^{1}H-NMR: 400 MHz, ^{13}C-NMR: 100 MHz, ^{31}P-NMR: 161 MHz, ^{29}Si-NMR: 79 MHz)

Bruker AM 500 MHz (^{1}H-NMR: 500 MHz, ^{13}C-NMR: 126 MHz, ^{31}P-NMR: 202 MHz, ^{29}Si-NMR: 99 MHz)

In the experiments, the spectroscopic NMR data are given as follows: "(MHz, deuterated solvent): δ (ppm)". The calibration of the spectrum was carried out according to the literature by Fulmer et al.[96] The characteristic signals were specified from the low field to high-field with the chemical shifts (δ in ppm). ^{1}H-NMR spectra peak multiplicities indicated as singlet (s), doublet (d), doublet of doublet (dd), doublet of doublet of doublet (ddd), triplet (t), doublet of triplet (dt), quartet (q),

multiplet (m).The coupling constant *J* indicated in hertz (Hz). And ^{1}H-NMR spectra peak also show the number of protons.

Infrared spectroscopy (IR)

The measurements were recorded on a Bruker Alpha-P FT-IR spectrometer. The absorption bands were indicated in the wave number ν (cm^{-1}). All substances were measured as film or solid. For the film, the substance was dissolved in DCM or MeCN or suspended and the solution applied to the device. After evaporation of the solvent the sample is measured.

High-performance liquid chromatography (HPLC)

Chiral HPLC chromatography was performed with an Agilent 1200 Series HPLC System. All the compounds in the thesis were detected by UV at λ = 254 nm. The flow was 0.5 mL/min or 0.9 mL/min. The injection was 1~2 μL for 2 mM solution. Y-axis range was adjusted to the 100~300 mAu. The corresponding mobile phase and the type of the columns were specified in the followed procedures.

Crystal structure analysis

Crystal X-ray measurements and the crystal structure analysis were carried out by Dr. Klaus Harms (Chemistry Department, Philipps University of Marburg) on the devices IPDS-II (Mo-Kα-irradiation, bis 2θ = 77 °, Oxford Cryosystem) or IPDS-IIT (Mo-Kα-irradiation, bis 2θ = 135 °, Oxford Cryosystem). The solution and refinement of the structures were carried with the corresponding programs. Details of crystal structures are in the Appendix.

Thermal denaturation

The melting studies were carried out in 1 cm path length quartz cells (total volume 325 μL; 200 μL sample solutions were covered by mineral oil) on a Beckman 800 UV/Vis-absorption spectrophotometer equipped with a thermo-programmer. Melting curves were monitored at 260 nm with a heating rate of 1 °C/min. Melting temperatures were calculated from the first derivatives of the heating curves. Experiments were performed in duplicate and mean values were taken.

UV/Vis-absorption spectroscopy

The absorptions of oligonucleotide solutions were measured in a quartz cuvette with a path length of 1 cm at 260 nm on Beckman 800 UV/Vis-absorption spectrophotometer. Temperature-dependent absorption spectra were obtained on Beckman 800 UV/Vis-absorption spectrophotometer equipped with a temperature controller. Spectra were obtained every 10 °C by heating from 20 to 80 °C.

Fluorescence spectroscopy

The experiments were performed in 96-well plates on a Molecular Device SpectraMax M5.

CD spectroscopy

CD measurements were performed on a JASCO J-810 spectrometer in a 1 mm path length quartz cuvette. CD spectra were recorded on a JASCO J-810 CD spectropolarimeter. The parameter which we used was the following: from 800 nm to 200 nm; data pitch (0.5 nm); band width (1 nm); response (1 second); sensitivity (standard); scanning speed (50 nm/min); accumulation (3). The concentration of the compounds in the measurements varied according to different requirements.

5.2 GNA as Scaffold for Molecular Aggregates of Chromophores

Synthesis of perylene bisimide and phthalocyanine phosphoramidites

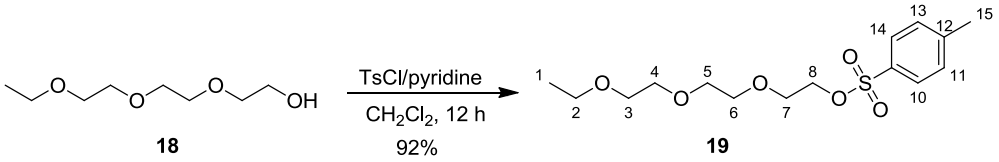

2-(2-(2-ethoxyethoxy)ethoxy)ethyl *p*-tosylate (19) It was synthesized following a modified literature procedure[97]. TsCl (11.7g, 61.6 mmol) in CH_2Cl_2 (100mL) was slowly added to an ice-cooled solution of triethylene glycol (**18**) (10 g, 56.2 mmol) and pyridine (9.1 mL, 112.4 mmol) in CH_2Cl_2 (200 mL), the mixture was allowed to stir at room temperature overnight. Then 100 mL H_2O was added to quench the reaction, the resulting mixture was extracted with CH_2Cl_2 (50 mL×3), and the combined organic layers were washed with 2*N* HCl (20 mL), brine (20 mL), dried over Na_2SO_4, filtered and concentrated *in vacuo*. The residue was purified by flash column chromatography on silica gel with 1:1 Ethyl acetate/hexane eluents to afford the product 2-(2-(2-ethoxyethoxy)ethoxy)ethyl *p*-tosylate (17.1 g, 92%). ^{1}H-NMR (300 MHz, $CDCl_3$) δ (ppm): 7.79 (t, J = 8.0 Hz, 2H, Ar-H), 7.33 (t, J = 8.0 Hz, 2H, Ar-H), 4.15 (t, J = 4.9 Hz, 2H, -CH_2-), 3.68 (t, J = 4.9 Hz, 2H, -CH_2-), 3.63-3.54 (m, 8H, -CH_2-), 3.51 (q, J = 7.0 Hz, 2H, CH_2CH_3), 2.44 (s, 3H, SO_2CH_3), 1.19 (t, J = 7.0 Hz, 3H, CH_2CH_3); ^{13}C-NMR (75 MHz, $CDCl_3$) δ (ppm): 144.7 (C-9), 133.04 (C-12), 129.76 (C_{arom}), 127.93 (C_{arom}), 70.71 (-*C*H_2-), 70.66 (-*C*H_2-), 70.48 (-*C*H_2-), 69.74 (-*C*H_2-), 69.19 (-*C*H_2-), 68.62 (-*C*H_2-), 66.65 (-*C*H_2-), 21.57 (SO_2*C*H_3), 15.09 (CH_2*C*H_3). IR (neat): ν (cm^{-1}) 2973, 2867, 1597, 1450, 1352, 1291, 1248, 1211, 1188, 1175, 1096, 1014, 918. HRMS calcd for $C_{15}H_{24}O_6S$ $(M+Na)^+$ 355.1191, found $(M+Na)^+$ 355.1184.

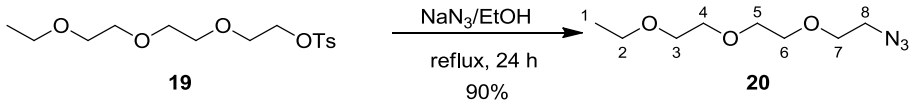

2-(2-(2-ethoxyethoxy)ethoxy)ethyl azide (**20**) A 250 mL round-bottom flask was charged with 2-(2-(2-ethoxyethoxy)ethoxy)ethyl *p*-tosylate (**19**) (10.7 g, 31.93 mmol), 140 mL dry EtOH, and sodium azide (4.2 g, 63.86 mmol) of under N_2, The mixture was stirred under reflux for 24 hours. After the solvent being evaporated, 150 mL CH_2Cl_2 was added; the organic solution was washed with H_2O, brine, then dried over Na_2SO_4, filtered and concentrated *in vacuo*. The residue was purified by flash column chromatography on silica gel with 1:1 EtOAc/hexane eluents to afford the product (5.83 g, 90%). ^{1}H-NMR (300 MHz, $CDCl_3$) δ (ppm): 3.67-3.58 (m, 8H, -CH_2-), 3.58-3.52 (m, 2 H, -CH_2-), 3.48 (q, J = 7.0 Hz, 2H, CH_2CH_3), 3.34 (t, J = 5.2 Hz, 2 H, CH_2N$_3$), 1.17 (t, J = 7.0 Hz, 3 H, CH$_2$CH_3); ^{13}C-NMR (75 MHz, $CDCl_3$) δ (ppm) 70.64 (-CH$_2$-), 70.59 (-CH$_2$-), 70.54 (-CH$_2$-), 69.90 (-CH$_2$-), 69.70 (-CH$_2$-), 66.47 (-CH$_2$-), 50.59 (CH$_2$N$_3$), 15.01 (CH$_2$$CH_3$). IR (neat): ν (cm^{-1}) 2975, 2867, 2096, 1443, 1374, 1284, 1108, 938, 844. HRMS calcd for $C_8H_{17}N_3O_3$ $(M+Na)^+$ 226.1168, found $(M+Na)^+$ 226.1160.

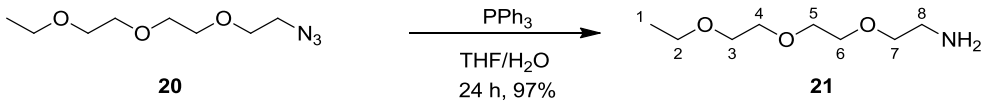

2-(2-(2-ethoxyethoxy)ethoxy)-ethanamine (**21**) A 250 mL round-bottom flask was charged with 2-(2-(2-ethoxyethoxy)ethoxy)ethyl azide (**20**) (5.0g, 24.63 mmol) and 100 mL dry THF under nitrogen. Triphenylphosphine (7.7 g, 29.56 mmol) was added to this mixture in one portion. After 2 hours, H_2O (2.2 mL, 118.22 mmol) was added, and the resulting mixture was stirred for 24 hours at room temperature. Then the THF was evaporated, and the residue was purified by flash column chromatography on silica gel with 1:10:0.01 MeOH/CH_2Cl_2/Et_3N eluents to afford the product (4.2 g. 97%). ^{1}H-NMR (300 MHz, $CDCl_3$) δ (ppm): 3.65-3.43 (m, 12H, -CH_2-), 2.82 (t, J = 5.2 Hz, 2H, CH_2NH$_2$), 1.27 (s, 2H, NH_2), 1.16 (t, J = 7.0 Hz, 3H, CH$_2$CH_3); ^{13}C-NMR

(75 MHz, $CDCl_3$) δ (ppm): 73.44 (-*C*H_2-), 70.61 (-*C*H_2-), 70.51 (-*C*H_2-), 70.22 (-*C*H_2-), 69.74 (-*C*H_2-), 66.52 (-*C*H_2-), 41.77 (*C*H_2NH_2), 15.05 (CH_2*C*H_3). IR (neat): ν (cm^{-1}) 2930, 2869, 2835, 1606, 1581, 1507, 1462, 1444, 1413, 1380, 1298, 1246, 1174, 1154, 1115, 1070, 1031, 982, 933, 902, 826. HRMS calcd for $C_8H_{19}NO_3$ $(M+H)^+$ 178.1443, found $(M+H)^+$ 178.1437.

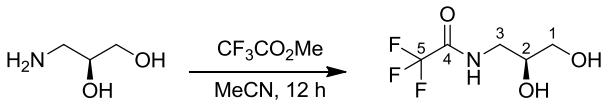

22 **23**

(*S*)-3-trifluoroacetamido-1,2-propanediol (23) To a mixture of (*S*)-3-amino-1,2-propanediol (1.82 g, 20 mmol) in acetonitrile (15 mL) was added dropwise methyl trifluoroacetate (2.5 mL, 25 mmol). The reaction was stirred for 4 hours at room temperature. The reaction mixture was evaporated and dried *in vacuo* to afford the product **23** (3.44 g, 92%). ^{1}H-NMR (300 MHz, MeOD) δ (ppm): 3.69-3.60 (m, 4H, 1-H and 3-H), 3.59-3.55 (m, 1H), 3.54-3.46 (m, 1H).

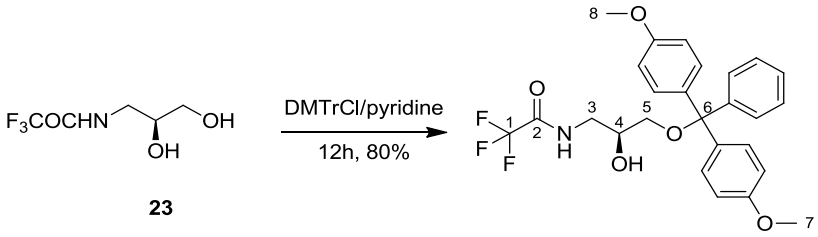

23 **24**

(*S*)-3-trifluoroacetamido-1-(4-4′-dimethoxytritriyl)-2-propanediol (24)[85] 4-4′-dimethoxytritriyl chloride (2.21 g, 6.25 mmol) was added to a solution of **23** (1.17 g, 6.25 mmol) in dry pyridine (30 mL), the mixture was stirred overnight at room temperature. The solvent was evaporated *in vacuo*. The residue was dissolved in EtOAc (50 mL), then washed with saturated $NaHCO_3$ (10 mL) and brine. The organic solvent was dried over Na_2SO_4, filtered and concentrated *in vacuo*. The pure product **24** was obtained by flash column chromatography on silica gel with 1:2:0.01 EtOAc/hexane/Et_3N eluents (2.45 g, 80%). ^{1}H-NMR (300 MHz, $CDCl_3$) δ (ppm):

8.62 (br.s, 1H, N*H*), 7.45-7.39 (m, 2H, Ar-H), 7.36-7.26 (m, 7H, Ar-H), 6.90-6.82 (m, 4H, Ar-H), 3.99-3.89 (m, 1H), 3.82 (s, 6H, OCH_3), 3.69-3.56 (m, 1H), 3.38-3.25 (m, 2H), 3.20-3.11 (m, 1H).

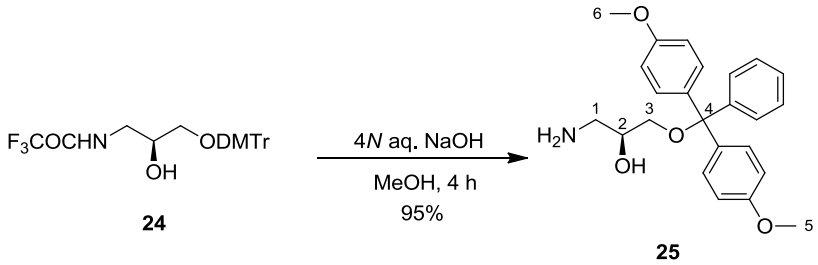

24 **25**

(*S*)-3-amino-1-(4-4′-dimethoxytritriyl)-2-propanediol (**25**)[85] Compound **24** (1.0 g, 2.04 mmol) was dissolved in 10 mL MeOH, then a 4*N* aqueous NaOH (5 mL, 20 mmol) was added. The reaction was stirred at room temperature overnight. Then the mixture was extracted with CH_2Cl_2, washed with brine, dried over Na_2SO_4, filtered and concentrated *in vacuo*. The residue was purified by flash column chromatography on silica gel with 1:10:0.01 MeOH/CH_2Cl_2/Et_3N eluents to afford the product **25** (760 mg, 95%). ^{1}H-NMR (300 MHz, $CDCl_3$) δ (ppm): 7.49-7.40 (m, 2H, Ar-H), 7.38-7.18 (m, 7H, Ar-H), 6.89-6.78 (m, 4H, Ar-H), 3.79 (s, 6H, OCH_3), 3.77-3.69 (1H, 2-H), 3.15 (d, J = 5.7 Hz, 2H, 3-H), 2.88-2.69 (m, 2H, 1-H).

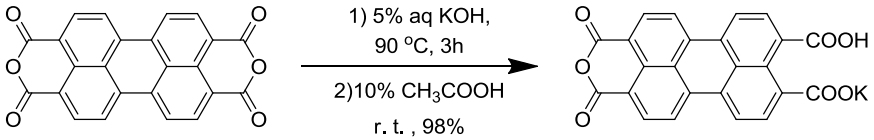

26 **27**

Perylene-3,4,9,10-tetracarboxylic acid monoanhydride monopotassium carboxylate (**27**)[98] Perylene-3,4,9,10-tetracarboxylic acid dianhydride (1.95 g, 5.0 mmol) in 5% aq. KOH (22.3 g, 20 mmol) was stirred at 90 °C for 3 h. After cooling to room temperature, 10% aq. CH_3COOH (14.0 g, 23.3 mmol) was added dropwise over half an hour. Then the mixture was stirred at 90 °C for another 1 h. The precipitate formed was filtered, washed with water and dried at 100 °C overnight to afford the bordeaux red solid product (2.2 g, 98%).

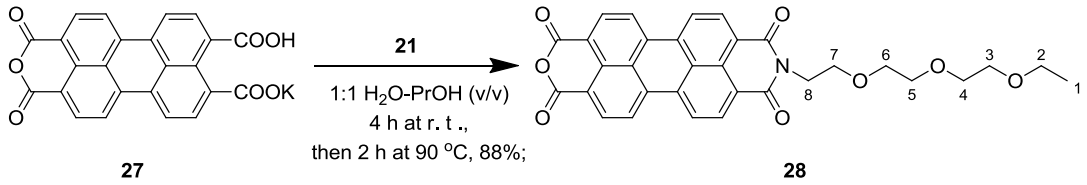

***N*-[2-(2-(2-ethoxyethoxy)ethoxy)ethyl]-3,4:9,10-tetracarboxylic-3,4-anhydride-9,10-imide** (**28**) According to the modified literature procedure[84], perylene-3,4,9,10-tetracarboxylic acid monoanhydride monopotassium (**27**) (896 mg, 2.0 mmol), 2-(2-(2-ethoxyethoxy)ethoxy)-ethanamine (**21**) (1.56 g, 8.8 mmol) in 1:1 H_2O-PrOH (v/v, 12 mL) was first stirred at room temperature for 4 h. After stirring the mixture at 90 ℃ for another 2 h, 1*N* HCl was added. The precipitate formed was filtered and washed with water. The collected solid was stirred into hot 10% aq. KOH, then the mixture was filtered to remove the unreacted **27**, and the filtrate was acidified with 1*N* HCl to precipitate the product. The final suspension was filtered, washed with water, and dried over 100 °C overnight to afford **28** (973 mg, 88%) without further purification. ^{1}H-NMR (300 MHz, $CDCl_3$ mixed with 5% CF_3COOD) δ (ppm): 8.80-8.59 (m, 8 H, Ar-H), 4.58 (t, J = 5.4 Hz, 2H, -CH_2-), 4.08 (t, J = 5.4 Hz, 2H, -CH_2-), 3.91-3.99 (m, 2H, -CH_2-), 3.77-3.87 (m, 6H, -CH_2-), 3.74 (q, J = 7.1 Hz, 2H, CH_2CH$_3$), 1.24 (t, J = 7.1 Hz, 3H, CH$_2$CH_3). IR (neat): ν (cm^{-1}) 3099, 3068, 2861, 1761, 1722, 1869, 1655, 1617, 1374, 1346, 1318, 1014, 945, 736.

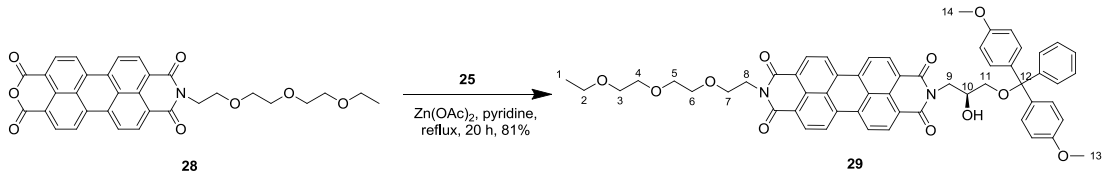

***(S)*-*N*-(3-(4,4′-Dimethoxytrityloxy)-2-hydroxypropyl)-*N*′-[2-(2-(2-ethoxyethoxy)ethoxy)-ethyl]-perylene-3,4:9,10-tetracarboxylic acid bisimide** (**29**) *N*-[2-(2-(2-ethoxyethoxy)ethoxy)ethyl]-3,4:9,10-tetracarboxylic-3,4-anhydride-9,10-imide (**28**) (1.10 g, 2.0 mmol) and $Zn(OAc)_2$ (400 mg, 2.18 mmol) were suspended in dry pyridine (80 mL) and refluxed for one hour. Then the solution of (*S*)-3-(dimethoxytrityloxy)-2-hydroxylpropanamine (**25**) (1.18 g, 3.0 mmol) in

pyridine (20 mL) was added, and the mixture was stirred under reflux for another 20 hours. The pyridine was evaporated, the resulting solid was dissolved in CH_2Cl_2, and then MeOH was added to precipitate the product. The crude product was purified by flash column chromatography on silica gel starting with 1:5 Acetone/CH_2Cl_2 eluents, then eluting with 1:4 acetone/CH_2Cl_2 to afford **29** (1.5 g, 81%). ^{1}H-NMR (400 MHz, $CDCl_3$) δ (ppm): 8.26-8.14 (m, 4H, Ar-H), 7.88-7.79 (m, 4H, Ar-H), 7.53 (d, *J* = 7.8 Hz, 2H, Ar-H), 7.40 (d, *J* = 8.8 Hz, 4H, Ar-H), 7.31 (t, *J* = 7.8 Hz, 2H, Ar-H), 7.21 (t, *J* = 7.4 Hz, 1H, Ar-H), 6.84 (d, *J* = 8.8 Hz, 4H, Ar-H), 4.63 (dd, *J* = 13.8, 9.7 Hz, 1H), 4.44-4.29 (m, 3 H), 4.22 (dd, *J* = 13.7, 3.0 Hz, 1H), 3.90-3.83 (m, 2 H), 3.78 (s, 6 H, OC*H*$_3$), 3.75 (t, *J* = 4.3 Hz, 2H), 3.65 (t, *J* = 4.3 Hz, 2H), 3.61 (t, *J* = 4.5 Hz, 2H), 3.52 (t, *J* = 4.3 Hz, 2H), 3.47 (q, *J* = 7.0 Hz, 2H), 3.42-3.29 (m, 2H), 3.21 (d, *J* = 7.0 Hz, 1H), 1.15 (t, *J* = 7.0 Hz, 3H, CH_2C*H*$_3$); ^{13}C-NMR (100 MHz, $CDCl_3$) δ (ppm): 163.40 (C_{arom}), 162.72 (C_{arom}), 158.44 (C_{arom}), 144.84 (C_{arom}), 136.00 (C_{arom}), 133.45 (C_{arom}), 133.30 (C_{arom}), 130.75 (C_{arom}), 130.53 (C_{arom}), 130.12 (C_{arom}), 129.09 (C_{arom}), 128.52 (C_{arom}), 128.40 (C_{arom}), 128.20 (C_{arom}), 127.83 (C_{arom}), 126.74 (C_{arom}), 125.12 (C_{arom}), 122.69 (C_{arom}), 122.63 (C_{arom}), 122.45 (C_{arom}), 122.35 (C_{arom}), 113.12 (C_{arom}), 86.07, 70.60, 70.57, 70.02, 69.72, 69.40, 67.80, 66.53, 65.73, 55.16, 44.02, 39.34, 15.10 (CH_2*C*H$_3$). IR (neat): ν (cm^{-1}) 3482, 2861, 1691, 1649, 1591, 1576, 1506, 1340, 1243, 1058, 1029, 807, 743. HRMS calcd for $C_{56}H_{50}N_2O_{11}$ $(M+Na)^+$ 949.3312, found $(M+Na)^+$ 949.3310.

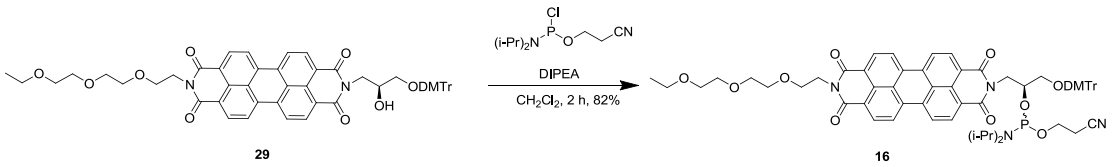

Perylene bisimide phosphoramidite (16) To a solution of **29** (500 mg, 0.54 mmol) in 20 mL anhydrous CH_2Cl_2 under nitrogen was added *N*, *N*-Diisopropylethylamine (0.56 mL, 3.24 mmol). Then *N*,*N*-diisopropylamino-*β*-cyanoethoxy chlorophosphoramidite (0.24 mL, 1.08 mmol) was added dropwise, and the solution was stirred at room temperature. Two hours later, 20 mL sat $NaHCO_3$ was added to

quench the reaction. The mixture was extracted with CH_2Cl_2, washed with brine, dried over Na_2SO_4, and concentrated *in vacuo*. The crude product was purified by flash column chromatography on silica gel with 1:0.01 EtOAc/Et_3N afforded phosphoramidite **16** (460 mg. 82%). ^{1}H-NMR (400 MHz, $CDCl_3$) δ (ppm): 8.54-8.46 (m, 4H), 8.44-8.35 (m, 4H), 7.46-7.21 (m, 6H), 7.18-7.02 (m, 3H), 6.76-6.58 (m, 4H), 4.75-4.10 (m, 5H), 3.86-3.76 (m, 2H), 3.68-3.63 (m, 6H), 3.61-3.51 (m, 6H), 3.50-3.21 (m, 8H), 3.20-2.95 (m, 2H), 2.39-2.23 (m, 2H), 1.12-1.05 (m, 3H), 1.02-0.85 (m, 12H); ^{31}P-NMR (121 MHz, $CDCl_3$) δ (ppm): 148.4, 148.2. IR (neat): ν (cm^{-1}) 2964, 2927, 2868, 1696, 1656, 1577, 1507, 1458, 1341, 1345, 1028, 809,725. HRMS calcd for $C_{65}H_{67}N_4O_{12}P$ $(M+Na)^+$ 1149.4391, found $(M+Na)^+$ 1149.4377.

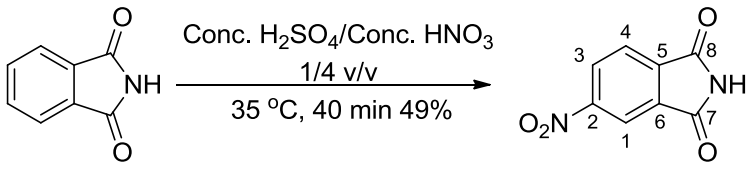

30 **31**

4-Nitrophthalimide (**31**)[99] To a mixture of *conc.* H_2SO_4 and *conc.* HNO_3 (4:1, 250 mL) was added phthalimide (40 g, 272 mmol) in portions over one hour at 15 °C. Then the temperature was raised slowly to 35 °C and the reaction was stirred for 45 min. The reaction mixture was then cooled to 0 °C and poured onto 1.4 Kg ice. The precipitate was collected by filtration and washed with cold water. The desired product was obtained by recrystallization from 700 mL EtOH (24.2 g, 49%). ^{1}H-NMR (300 MHz, $CDCl_3$) δ (ppm): 11.84 (s, 1H, N*H*), 8.60 (dd, *J* = 8.1, 2.1 Hz, 1H, 3-H), 8.43 (dd, *J* = 1.9, 0.3 Hz, 1H, 1-H), 8.H 7 (dd, *J* = 8.2, 0.4 Hz, 1H, 4-H); ^{13}C-NMR (75 MHz, $CDCl_3$) δ (ppm): 167.5 (*C*=O), 167.2 (*C*=O), 151.4 (C_{arom}), 137.3 (C_{arom}), 134.0 (C_{arom}), 129.4 (C_{arom}), 124.5 (C_{arom}), 117.7 (C_{arom}).

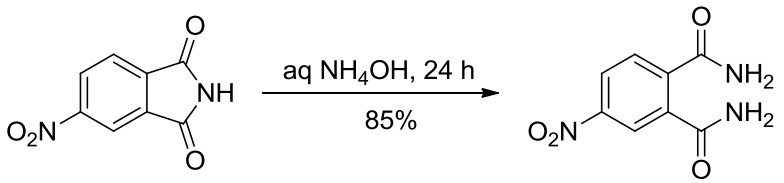

31 **32**

4-Nitrophthalamide (**32**)[99] Compound **31** (25.1 g, 130.7 mmol) dissolved in 105 mL concentrated aq. NH_4OH, the reaction solution were stirred at room temperature for 24 h. The product was collected by filtration, washed with cold water and dried as a white powder (27.3 g, 85%). ^{1}H-NMR (300 MHz, $CDCl_3$) δ (ppm): 8.37–8.24 (m, 2H, Ar-H), 8.06 (br.s, 1H, N*H*$_2$), 8.00 (br.s, 1H, N*H*$_2$), 7.70 (d, *J* = 8.3 Hz, 1H, Ar-H), 7.62 (br.s, 2H, N*H*$_2$); ^{13}C-NMR (75 MHz, $CDCl_3$) δ (ppm): 168.66 (*C*=O), 167.7 (*C*=O), 147.1 (C_{arom}), 142.6 (C_{arom}), 137.2 (C_{arom}), 129.1 (C_{arom}), 124.3 (C_{arom}), 122.4 (C_{arom}).

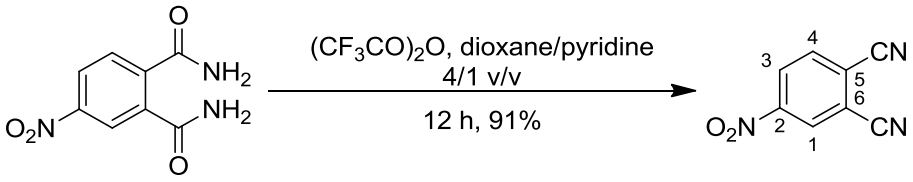

32 **33**

4-Nitrophthalonitrile (**33**)[99] 4-nitrophthalamide **32** (23 g, 110.0 mmol) was suspended in 250 mL of a 4: 1 dioxane-pyridine mixture. The suspension was cooled with an ice-bath and trifluoroacetic anhydride (39 mL, 20.1 mmol) were added dropwise. After the addition was complete, the ice-bath was removed and the reaction mixture was diluted to 2.5 times its volume with water. The mixture was then extracted with EtOAc, and the combined organic phases were washed with water, 20% HCl, water and brine, then dried over Na_2SO_4, filtered and concentrated *in vacuo*. The product was obtained as a creamy white solid without further purification (17.3 g, 91%). ^{1}H-NMR (300 MHz, $CDCl_3$) δ (ppm): 8.67 (dd, *J* = 2.3, 0.4 Hz, 1H, 1-H), 8.60 (dd, *J* = 8.5, 2.2 Hz, 1H, 3-H), 8.08 (dd, *J* = 8.5, 0.3 Hz, 1H, 4-H).

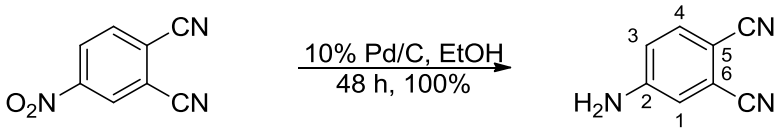

33 **34**

4-Aminophthalonitrile (**34**)[99] A suspension of **33** (5.19 g, 30.0 mmol) and 600 mg 10 wt. % Pd/C in 150 mL of 95% EtOH was stirred under H_2 for 48 hours. The palladium catalyst was removed by filtration and the solvent was evaporated. Subsequent recrystallization from MeOH afforded the product **34** (3.94 g, 92%). ^{1}H-NMR (300 MHz, MeOD) δ (ppm): 7.51 (d, J = 8.7 Hz, 1H, 4-H), 6.98 (d, J = 2.3 Hz, 1H, 1-H), 6.88 (dd, J = 8.7, 2.3 Hz, 1H, 3-H); ^{13}C-NMR (75 MHz, $CDCl_3$) δ (ppm): 154.7, 136.1, 118.8, 118.5, 118.3, 117.9, 117.4, 100.8 (*C*N).

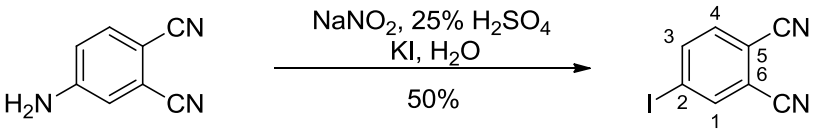

34 **35**

4-Iodophthalonitrile (**35**)[99] A suspension of **34** (3.7 g, 25.87 mmol) in 51 mL of 25% aq. H_2SO_4 was cooled to -5 ^{o}C. A solution of $NaNO_2$ (2.07 g, 30 mmol) in 6 mL water was added dropwise with stirring. After 30 min, the solution of KI (4.66 g, 28 mmol) in 30 mL water was added and the resulting black reaction mixture was allowed to warm to room temperature over 1.5 h. The mixture was extracted with EtOAc, the combined organic layers were washed with water, sat. $Na_2S_2O_3$ and brine, then dried over Na_2SO_4, filtered and concentrated *in vacuo*. The pure product **35** was obtained by flash chromatography on silica gel with 1:4 EtOAc/hexane eluents (3.73 g, 50%). ^{1}H-NMR (300 MHz, $CDCl_3$) δ (ppm): 8.16 (d, J = 1.5 Hz, 1H, 1-H), 8.11 (dd, J = 8.3, 1.7 Hz, 1H, 3-H), 7.51 (dd, J = 8.3, 0.3 Hz, 1H, 4-H).

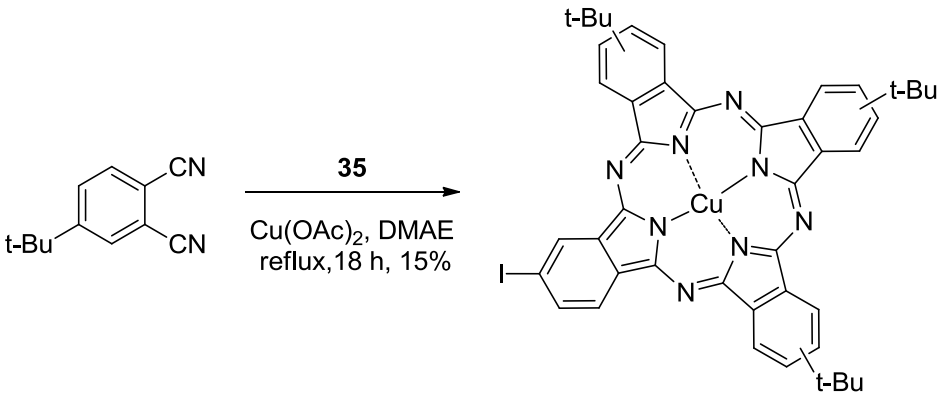

36 **37**

Tri-*tert*-butyliodophthalocyaninatocopper (**37**)[100] A mixture of 4-*tert*-butylphthalonitrile (**36**) (1 g, 5.43 mmol), 4-iodophthalonitrile (**35**) (254 mg, 1 mmol), and $Cu(AcO)_2$ (290 mg, 1.6 mmol) in DMAE (3 mL) was refluxed for 18 hours. After being cooled down to room temperature, the solvent was evaporated under reduced pressure, and the crude product was purified by flash column chromatography on silica gel to afford **37** as a blue solid (130 mg, 15%). ^{1}H-NMR (300 MHz, $CDCl_3$) δ (ppm): 10.69-7.17 (br, 12H, Ar-H), 1.57-1.46 (br, 27H, $C(CH_3)_3$)

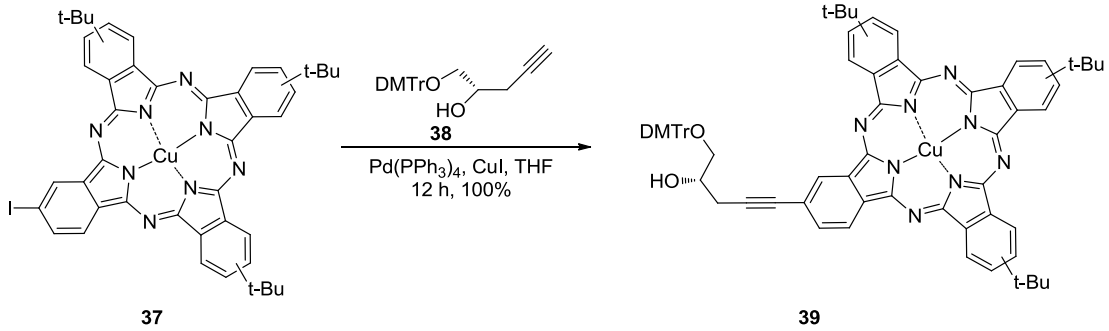

37 **39**

(*S*)-tri-*tert*-butyl-[5-(4,4'-Dimethoxytrityloxy)-3-hydroxy-1-pentynyl]phthalocyaninatocopper (**39**) A mixture of compound **37** (220 mg, 0.25 mmol) and **38** (100 mg, 0.5 mmol) in the presence of $Pd(PPh_3)_4$ (40 mg) and CuI (20 mg) in THF (20 mL) and TEA (10 mL) was degassed with N_2 for 10 min, then the reaction was stirred under reflux overnight under N_2. 50 mL H_2O was added, and then the mixture was extracted with EtOAc, washed with brine, dried over Na_2SO_4, filtered and concentrated *in*

vacuo. After the solvent was evaporated, the residue was purified by flash chromatography on silica gel to afford the product (285 mg, 100%). δ (ppm): 7.70-6.60 (m, 25H), 3.72-3.68 (m, 7H), 3.30-2.90 (m, 4H), 2.19-0.46 (m, 27H). HRMS calcd for $C_{70}H_{64}CuN_8O_4$ $(M+Na)^+$ 1166.4239, found $(M+Na)^+$ 1166.4240.

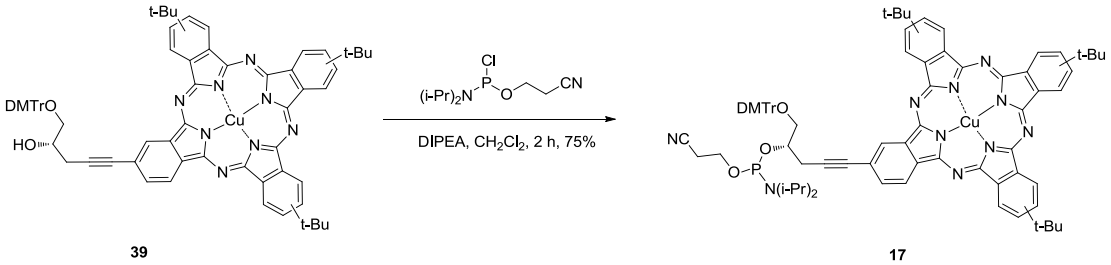

Phthalocyanine phosphoramidite (**17**) To a solution of **39** (380 mg, 0.33 mmol) in 20 mL anhydrous CH_2Cl_2 under nitrogen was added *N*, *N*-Diisopropylethylamine (0.2 mL, 1.98 mmol). Then *N*,*N*-diisopropylamino-β-cyanoethoxy chlorophosphoramidite (0.2 mL, 0.66 mmol) was added dropwise, and the solution was stirred at room temperature. Two hours later, 20 mL sat $NaHCO_3$ was added to quench the reaction. The mixture was extracted with CH_2Cl_2, washed with brine, dried over Na_2SO_4, and concentrated *in vacuo*. The crude product was purified by column chromatography on silica gel to afford the product phosphoramidite **17** (332 mg, 75%). δ (ppm): 7.70-6.60 (m, 25H), 4.14-3.89 (m, 2H), 3.87-3.43 (m, 11H), 3.22-3.04 (m, 2H), 2.43-2.30 (m, 2H), 2.05-0.64 (m, 39H); ^{31}P-NMR (121 MHz, $CDCl_3$) δ (ppm): 148.4, 148.1, 148.0. HRMS calcd for $C_{79}H_{81}CuN_{10}O_5P$ $(M+Na)^+$ 1366.5317, found $(M+Na)^+$ 1366.5319.

. GNA oligonucleotides synthesis and purification (General protocol)

The synthesis and purification of phosphoramidites was followed by repeated coevaporation with toluene to remove trace amounts of water. The phosphoramidites were left overnight under high vacuum. The phosphoramidites were dissolved using anhydrous acetonitrile or THF to a final concentration of 100 mM. Solid supports were synthesized from the dimethoxytrityl protected nucleosides as previously reported.[101]

All the oligonucleotides were prepared on an ABI 394 DNA/RNA synthesizer on a 1 micromole scale. GNA phosphoramidites (A, T and **30**) were used at a concentration of 100 mM with a standard protocol for 2-cyanoethyl phosphoramidites, except that the coupling time was extended to 3 min. After the trityl-on synthesis, the resin was incubated with conc. aq. NH_3 solution (1.5 mL) for 12 h at 55 ℃. After cooling, the entire solution was applied directly to a Sep-Pak Classic reversed-phase column (Waters, 360 mg) and washed sequentially with 3% NH_4OH (15 mL), water (10 mL), 1.5% aqueous TFA (10 mL), and finally water (10 mL). The oligo was then eluted with 20% or 30% aqueous acetonitrile for oligonucleotides containing perylene bisimide and further purified using a Waters XTerra column (MS C18, 4.6 × 50 mm, 2.5 μm) at 55 °C with aqueous TEAA and acetonitrile as the eluents. The identities of all oligonucleotides were confirmed by MALDI-TOF MS (Table 9).

The indentification of all oligonucleotides was confirmed by MALDI-TOF MS. Samples were prepared at a concentration of approximately 10 μM. One microliter of a saturated solution of trihydroxyacetophenone in 50% aqueous acetonitrile was mixed with one microliter of 100 mM ammonium tartrate and then one microliter of the GNA sample. The dried sample was then analyzed in negative mode for detection of the sample mass.

Table 9 MALDI-TOF MS data of used oligonucleotides [a]

Entry	Oligonucleotides	M_{calcd}	M_{found}
ON01	3′-TAAAAATAATAATATT-2′	3952 ($C_{120}H_{157}N_{57}O_{70}P_{14}$)	3949
ON02	2′-ATTTTTATTATTATAA-3′	3925 ($C_{120}H_{160}N_{48}O_{76}P_{14}$)	3923
ON03	3′-TAAAAATHATAATATT-2′	4074($C_{122}H_{162}N_{57}O_{74}P_{15}$)	4075
ON04	2′-ATT TTTABTATTATAA-3′	4608 ($C_{155}H_{191}N_{50}O_{87}P_{15}$)	4611
ON05	3′-TAA AAATTATAATATT-2′	4211 ($C_{128}H_{168}N_{59}O_{76}P_{15}$)	4212
ON06	3′-TAA AAATHBTAATATT-2′	4488 ($C_{149}H_{183}N_{54}O_{81}P_{15}$)	4490
ON07	2′-ATT TTTABHATTATAA-3′	4470 ($C_{149}H_{185}N_{48}O_{85}P_{15}$)	4472
ON08	3′-TAAAAATBHTAATATT-2′	4488 ($C_{149}H_{183}N_{54}O_{81}P_{15}$)	4490
ON09	2′-ATTTTTAHBATTATAA-3′	4470 ($C_{149}H_{185}N_{48}O_{85}P_{15}$)	4472
ON10	3′-TAAAAATBBTAATATT-2′	5051 ($C_{182}H_{209}N_{56}O_{88}P_{15}$)	5052
ON11	2′-ATTTTTAHHATTATAA-3′	3909 ($C_{116}H_{159}N_{46}O_{78}P_{15}$)	3911
ON12	3′-TAAAAATTBTAATATT-2′	4627 ($C_{155}H_{189}N_{56}O_{83}P_{15}$)	4630
ON13	3′-TAAAAAHBHTAATATT-2′	4351 ($C_{143}H_{177}N_{52}O_{79}P_{15}$)	4355
ON14	2′-ATTTTTBHBATTATAA-3′	4886 ($C_{176}H_{206}N_{45}O_{92}P_{15}$)	4890
ON15	3′-TAAAAAHBHBAATATT-2′	4775 ($C_{170}H_{197}N_{52}O_{84}P_{15}$)	4780
ON16	2′-ATTTTTBHBHTTATAA-3′	4739 ($C_{170}H_{201}N_{40}O_{92}P_{15}$)	4744
ON17	3′-TAAAAHBAAHBATATT-2′	4775 ($C_{170}H_{197}N_{52}O_{84}P_{15}$)	4777
ON18	2′-ATTTTBHTTBHTATAA-3′	4739 ($C_{170}H_{201}N_{40}O_{92}P_{15}$)	4744
ON19	3′-TAAAHBTAATHBTATT-2′	4757 ($C_{170}H_{199}N_{46}O_{88}P_{15}$)	4762
ON20	2′-ATTTBHATTABHATAA-3′	4756 ($C_{170}H_{199}N_{46}O_{88}P_{15}$)	4762
ON21	3′-TAAAAABTHTAATATT-2′	4489 ($C_{149}H_{183}N_{54}O_{81}P_{15}$)	4489
ON22	2′-ATTTTTHTBATTATAA-3′	4462 ($C_{149}H_{186}N_{45}O_{87}P_{15}$)	4463
ON23	3′-TAAAAABAHTAATATT-2′	4498 ($C_{149}H_{182}N_{57}O_{79}P_{15}$)	4499
ON24	2′-ATTTTTHABATTATAA-3′	4471 ($C_{149}H_{185}N_{48}O_{85}P_{15}$)	4472
ON25	2′-ATT TTT AYT ATT ATAA-3′	4826 ($C_{169}H_{205}CuN_{56}O_{80}P_{15}$)	4828
ON26	3′-TAA AAATHYTAATATT-2′	4706 ($C_{163}H_{197}CuN_{60}O_{74}P_{15}$)	4707
ON27	2′-ATT TTTAYHATTATAA-3′	4688 ($C_{163}H_{199}CuN_{54}O_{78}P_{15}$)	4689
ON28	3′-TAAAAATYHTAATATT-2′	4706 ($C_{163}H_{197}CuN_{60}O_{74}P_{15}$)	4706
ON29	2′-ATTTTTAHYATTATAA-3′	4688 ($C_{163}H_{199}CuN_{54}O_{78}P_{15}$)	4688
ON30	3′-TAAAAATYYTAATATT-2′	5485 $C_{210}H_{237}Cu_2N_{68}O_{74}P_{15}$)	
ON31	3′-TAAAAAHYHTAATATT-2′	4568 ($C_{157}H_{191}CuN_{58}O_{72}P_{15}$)	4577
ON32	2′-ATTTTTYHYATTATAA-3′	5320 ($C_{204}H_{234}Cu_2N_{57}O_{78}P_{15}$)	5332
ON33	3′-TAAAAAHYHYAATATT-2′	5209 ($C_{198}H_{225}Cu_2N_{64}O_{70}P_{15}$)	5210
ON34	2′-ATTTTTYHYHTTATAA-3′	5173 ($C_{198}H_{229}Cu_2N_{52}O_{78}P_{15}$)	5174
ON35	3′-Y TAA AAA TTA TAA TATT-2′	5115 ($C_{177}H_{213}CuN_{67}O_{80}P_{16}$)	5115
ON36	2′-ATT TTT AAT ATT ATAA Y-3′	5097 ($C_{177}H_{215}CuN_{61}O_{84}P_{16}$)	5098

Porphyrin-modified oligonucleotides (**ON37** to **ON44**) offered by Hui Zhou in our group.

Solid phase synthesis

Both native and the modified oligonucleotides were synthesized through solid phase synthesis in the ABI392 DNA/RNA Synthesizer (Figure 81). The samples were usually synthesized in a 1.0 μmol scale. The general solid phase synthesis procedure is showed in Scheme 19

Figure 81 ABI 392 Solid Phase Synthesizer

Oligonucleotide synthesis is carried out from 2′ to 3′ of a sequence on control pore glass (CPG-500) immobilized with the appropriate nucleoside through a succinate linker. Each addition is referred to as a synthetic cycle (Scheme 19) and consists of four chemical reactions. In GNA works, regular GNA phosphoramidites (dA-CE, dT-CE, dH-CE and dB-CE, 0.1 M in acetonitrile) are used for most of synthesis. Only the modified phthalocyanine phosphoramidite **17** (dP-CE) was dissolved in THF and coupling time extends to 15 min. The first step is removal of the DMTr group with a solution of 3% Dichloroacetic acid (DCA) in CH_2Cl_2, the orange-colored DMTr cation formed is washed out. The solid support-bound oligonucleotide precursor bearing a free 3'-terminal hydroxyl group is afforded. The second step is coupling, a 0.1 M solution of nucleoside phosphoramidite is activated by a 0.25 M Ethylthio-1H-tetrazole, and the mixing is brief and occurs in fluid lines of oligonucleotide synthesizer while the components are delivered to the reactors containing solid support. The activated phosphoramidite is about 20 folds excessive over the support-bound material whose 3'-hydroxy group reacts with the activated

phosphoramidite moiety to form a phosphite triester linkage. After the coupling, the unreacted residue is washed out. The third step is capping, as there is always a small percentage of the solid support-bound 3'-OH groups (0.1 to 1%) remains unreacted and needs to be prevented from further coupling in the next step; the hydroxyl group is acetylated by the capping mixture. The last step is oxidation; the tricoordinated phosphite trimester is not natural and should be treated with iodine and water in the presence of weak base to produce the tetracoordinated phosphate trimester.

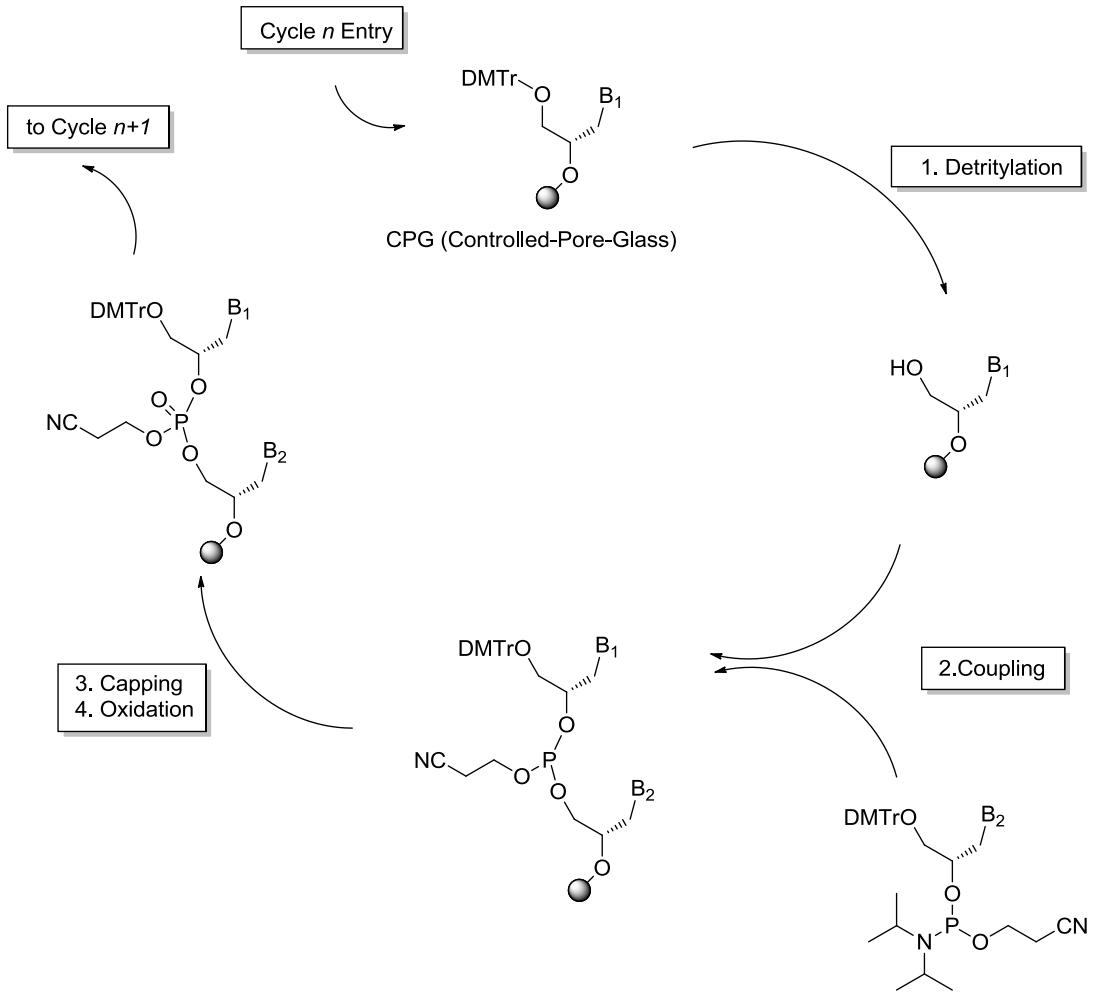

Scheme 19 Synthetic cycle for preparation of oligonucleotides by phosphoramidite method

5.3 Octahedral Silicon Complexes as DNA Binders

5.3.1 Synthesis of Octahedral Silicon Complexes

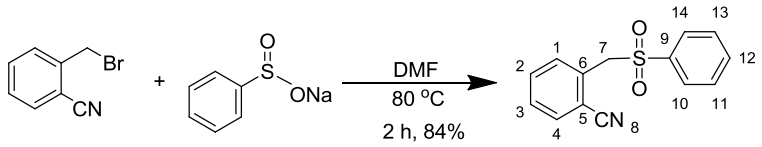

60 **61** **62**

***ortho*-(Phenylsulfonylmethyl)benzonitrile** (**62**)[90a] A 100 mL flask was charged with α-bromotolunitrile (**60**) (3.92 g, 20.0 mmol), benzenesulfinic acid sodium salt dehydrate (**61**) (4.80 g, 24.0 mmol), and DMF (30 mL). After the mixture was stirred at 80 °C for 2 hours, the reaction mixture was cooled to room temperature. The solvent was evaporated, 30 mL H_2O was added, and then the aqueous layer was extracted with EtOAc (3×20 mL). The combined organic layer was washed with brine, dried over Na_2SO_4. After evaporation of the solvent, the pure product **62** was obtained by recrystallization from EtOAc/hexane as colorless needles (4.37 g, 84%). ^{1}H-NMR (300 MHz, $CDCl_3$): δ (ppm) 7.66 (m, 5H, Ar-H), 7.50 (m, 4H, Ar-H), 4.57 (s, 2H, C*H*$_2$); ^{13}C-NMR (75 MHz, $CDCl_3$): δ (ppm) 137.57 (C_{arom}), 134.29 (C_{arom}), 132.94 (C_{arom}), 132.80 (C_{arom}), 132.22 (C_{arom}), 131.67 (C_{arom}), 129.38 (C_{arom}), 129.28 (C_{arom}), 128.72 (C_{arom}), 116.52 (C_{arom} or *C*N), 114.40 (C_{arom} or *C*N), 60.50 (*C*H$_2$).

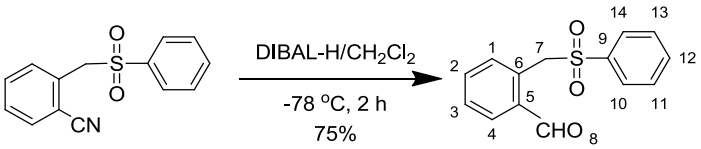

62 **63**

***ortho*-(Phenylsulfonylmethyl)benzaldehyde** (**63**)[90a] A 100 mL flask was charged with *ortho*-(phenylsulfonylmethyl)benzonitrile (**62**) (3.87 g, 15.0 mmol) and CH_2Cl_2 (45 mL), and DIBAL-H (1.0 M in hexane, 34.5 mL, 34.5 mmol) was added at -78 °C. After the mixture had been stirred at this temperature for 2 hours, aqueous NH_4Cl was

added to quench the reaction. The mixture was extracted with CH_2Cl_2, the combined organic layer was washed with 1*N* HCl and brine, then dried over Na_2SO_4, the solvent was evaporated *in vacuo*, and the residue was subjected to filtration through a thin pad (silica gel; CH_2Cl_2) and recrystallization from CH_2Cl_2/hexane gave **63** as colorless needles (2.92 g, 75%). ^{1}H-NMR (300 MHz, $CDCl_3$): δ (ppm) 9.83 (s, 1H, C*H*O), 7.72 (m, 3H, Ar-H), 7.59 (m, 3H, Ar-H), 7.45 (m, 3H, Ar-H), 5.03 (s, 2H, CH_2); ^{13}C-NMR (75 MHz, $CDCl_3$): δ (ppm) 191.95 (*C*HO), 138.27 (C_{arom}), 134.66 (C_{arom}), 134.38 (C_{arom}), 133.84 (C_{arom}), 133.77 (C_{arom}), 133.51 (C_{arom}), 129.44 (C_{arom}), 128.82 (C_{arom}), 128.66 (C_{arom}), 57.67 (*C*H_2).

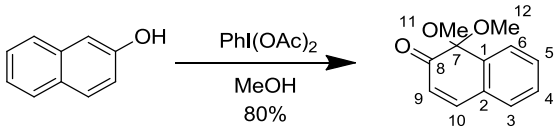

64 **65**

1,1-Dimethoxynaphthalen-2(1*H*)-one (**65**)[90b] To a solution of a 3-naphthol (**64**) (1.30 g, 9.0 mmol) in dry methanol (75 mL) at 0 ℃ under N_2 atmosphere was added phenyliodonium diacetate (6.37 g, 19.8 mmol) in two portions over 2 hours and the resulting solution was allowed to stir at room temperature for 24 hours. The reaction was then quenched with 20 mL Na_2SO_3. The solvent was evaporated and the residue was dissolved in CH_2Cl_2, The solution was washed with brine, dried over Na_2SO_4 and concentrated *in vacuo*. The crude residue was purified by flash chromatography on silica gel with 1:3 EtOAc/hexane eluents to afford the product as yellow oil (975 mg, 80%). ^{1}H-NMR (300 MHz, $CDCl_3$): δ (ppm) 7.66 (m, 1H, 10-H), 7.38 (m, 2H, Ar-H), 7.23 (m, 2H, Ar-H), 6.06 (d, J = 10.0 Hz, 1H, 9-H), 3.23 (s, 6H, OCH_3); ^{13}C-NMR (75 MHz, $CDCl_3$): δ (ppm) 195.53 (*C*=O), 144.09, 137.85, 131.54, 130.01, 129.78, 129.57, 128.17, 125.14, 95.46, 51.86 (O*C*H_3).

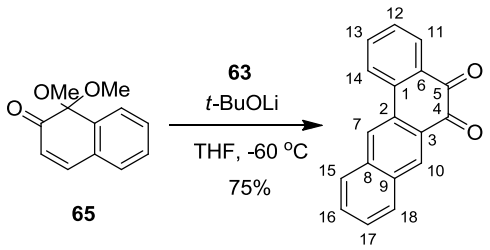

Benz[*a*]anthracene-5,6-dione (**66**)[90c] Sulfone (**63**) (1100 mg, 4.23 mmol) and quinone monoketal (**65**) (906 mg, 4.44 mmol) were dissolved in a mixture of *t*-BuOH (12 mL) and THF (30 mL), and *t*-BuOK (1420 mg, 12.69 mmol) was then added at 0 ℃. The resulting mixture was stirred at room temperature for 6 hours. Then it was diluted with H_2O (20 mL), and the mixture was extracted with EtOAc, the combined organic layer was washed with brine, dried over Na_2SO_4, and the solvent was evaporated *in vacuo* to afford a red solid. HCl (10%, 10 mL) was added to a well-stirred solution of the solid in MeOH (10 mL) at room temperature, and stirring was continued for another one hour. A red solid precipitate was collected by filtration and thoroughly washed with a mixture of MeOH and H_2O (1:10) to give the product (736 mg, 75%). ^{1}H-NMR (300 MHz, $CDCl_3$): δ (ppm) 8.72 (s, 1H, 7-H or 10-H), 8.37 (s, 1H, 7-H or 10-H), 8.18 (m, 2H, Ar-H), 7.91 (t, J = 8.8 Hz, 2H, Ar-H), 7.75 (dt, J = 11.6, 1.5 Hz, 1H, Ar-H), 7.65 (m, 1H, Ar-H), 7.55 (m, 1H, Ar-H), 7.46 (m, 1H, Ar-H); ^{13}C-NMR (75 MHz, $CDCl_3$): δ (ppm) 180.70 (*C*=O), 180.53 (*C*=O), 136.69 (C_{arom}), 136.56 (C_{arom}), 135.92 (C_{arom}), 133.59 (C_{arom}), 132.63 (C_{arom}), 131.34 (C_{arom}), 130.55 (C_{arom}), 130.41 (C_{arom}), 130.33 (C_{arom}), 130.28 (C_{arom}), 129.29 (C_{arom}), 128.73 (C_{arom}), 128.66 (C_{arom}), 128.14 (C_{arom}), 123.98 (C_{arom}), 123.93 (C_{arom}).

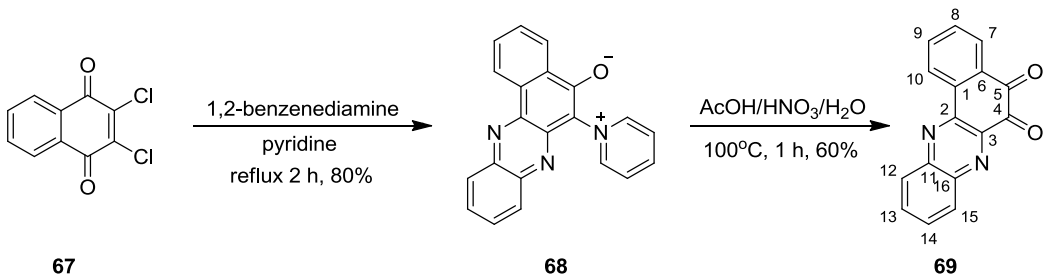

3,4-Benzo[*a*]phenazine quinine (**69**)[49c] 2,3-Dichloro-1,4- napthoquinone (**67**) (4.5 g, 20 mmol) and *o*-phenylenediamine (2.0 g, 20 mmol) were dissolved in 150 mL pyridine. The mixture was refluxed for one hour under N_2. The solution was cooled to room temperature and filtered to afford a brown red solid. Then the pure solid **68** was obtained by recrystallization from hot pyridine. To the dry red solid **68**, 20 mL CH_3COOH, 2 mL nitric acid and 1.32 mL H_2O were added. The mixture was heated at 100 ^oC. After one hour, the solution was cooled to room temperature. After filtering the cool solution, it was washed with EtOAc and Et_2O successively, and the yellow solid product was obtained (3.55 g, 60%). ^{1}H-NMR (300 MHz, $CDCl_3$): δ (ppm) 8.83 (dd, J = 8.0, 0.8 Hz, 1H), 8.28 (dd, J = 8.3, 1.1 Hz, 1H), 8.24 (dd, J = 7.8, 1.0 Hz, 1H), 8.13 (dd, J = 8.4, 1.0 Hz, 1H), 7.93-7.76 (m, 3H), 7.62 (dt, J = 7.6, 1.2 Hz, 1H). HRMS calcd for $C_{16}H_8N_2O_2Na$ $(M+Na)^+$ 283.0478, found: 283.0477.

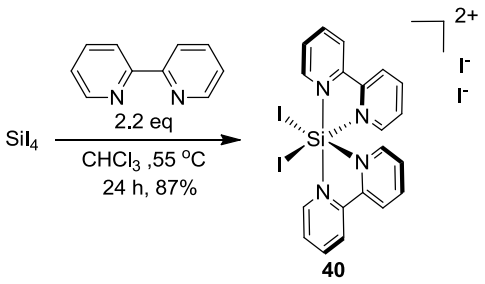

40

***cis*-Bis(2,2'-bipyridine)diiodosilicium(IV) diiodide** (**40**) This complex was synthesized by a modified literature procedure.[74a] A suspension of silicon(IV) iodide (2.03 g, 3.78 mmol) and 2,2′-bipyridine (1.30 g, 8.33 mmol) in dry $CHCl_3$ (40 mL) was purged with N_2 for 15 min and was then heated to 55 ℃ for 24 hours under N_2. The resulting brownish red suspension was cooled to room temperature and filtered to remove the solvent. The solid was washed with dry $CHCl_3$, and then it was dried *in vacuo* to afford the brownish red solid (2.79 g, 87%). The complex was used directly for the next step without further purification.

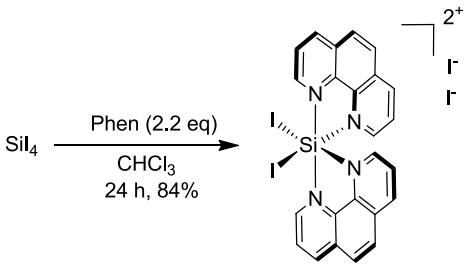

41

***cis*-Bis(1,10-phenanthroline)diiodosilicium(IV) diiodide** (**41**) This complex was synthesized by a modified literature procedure.[74b] A suspension of silicon(IV) iodide (1.83 g, 3.42 mmol) and 1,10-phenanthroline (1.35 g, 7.53 mmol) in dry $CHCl_3$ (40 mL) was purged with N_2 for 15 min and was then heated to 55 ℃ for 24 hours under N_2. The resulting brownish red suspension was cooled to room temperature and filtered to remove the solvent. The solid was washed with dry $CHCl_3$, MeOH and Et_2O successively, and then it was dried *in vacuo* to afford the brownish red solid (2.58 g, 84%). The complex was used directly for the next step without further purification.

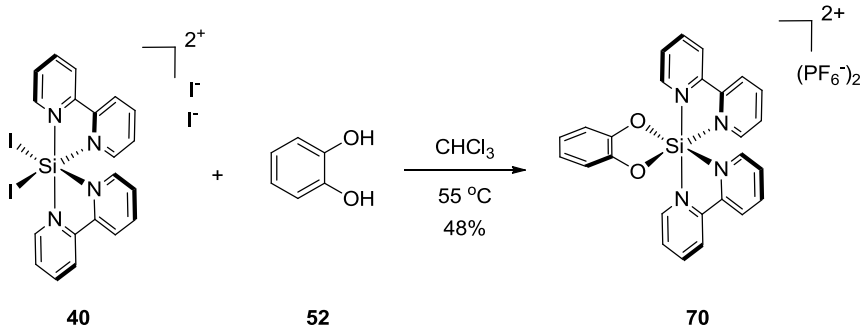

40 52 70

Bis(2,2'-bipyridine)catecholatosilicium(IV) bis(hexafluorophosphate) (**70**) A suspension of $[Si(bpy)_2I_2]I_2$ (**40**) (100 mg, 0.12 mmol) and 4 equivalents of catechol (**52**) (52 mg, 0.48 mmol) in dry $CHCl_3$ (10 mL) was purged with N_2 for 15 min and then stirred at 55 °C for 12 hours. The resulting dark-brown suspension was cooled to room temperature and the solvent was removed *in vacuo*. The crude material was subjected to silica gel chromatography with acetonitrile:water:saturated aqueous KNO_3 50:3:1. The product eluents were concentrated to dryness and the resulting

material was dissolved in minimal amounts of water. The product was precipitated by the addition of excessive solid NH_4PF_6. The precipitate was centrifuged, washed twice with water and dried under high vacuum to afford the pure diolate complex **70** as a yellow solid (42 mg, 48%). ^{1}H-NMR (300 MHz, CD_3CN): δ (ppm) 9.07 (ddd, J = 5.8; 1.4, 0.7 Hz, 2H), 8.91 (m, 2H), 8.80 (m, 4H), 8.60 (dt, J = 7.9, 1.4 Hz, 2H), 8.16 (ddd, J = 7.7, 5.9, 1.2 Hz, 2H), 7.80 (ddd, J = 7.7, 6.0, 1.3 Hz, 2H), 7.58 (ddd, J = 5.9, 1.2, 0.7 Hz, 2H), 6.78 (m, 4H); ^{13}C-NMR (75 MHz, CD_3CN): δ (ppm) 148.63, 148.35, 148.02, 146.91, 146.16, 144.86, 144.13, 131.88, 131.36, 126.16, 125.92, 123.02, 114.66. IR (neat): ν (cm^{-1}) 2934, 1674, 1592, 1482, 1454, 1443, 1387, 1335, 1283, 1242, 1179, 1140, 1104, 994, 979, 952, 927, 909, 838, 747, 730, 695, 675, 613, 588, 557, 534, 521, 502, 470, 455, 422, 410, 394, 384. HRMS calcd for $C_{26}H_{20}F_6N_4O_2PSi$ $(M\text{-}PF_6)^+$ 593.0992, found: 593.0982.

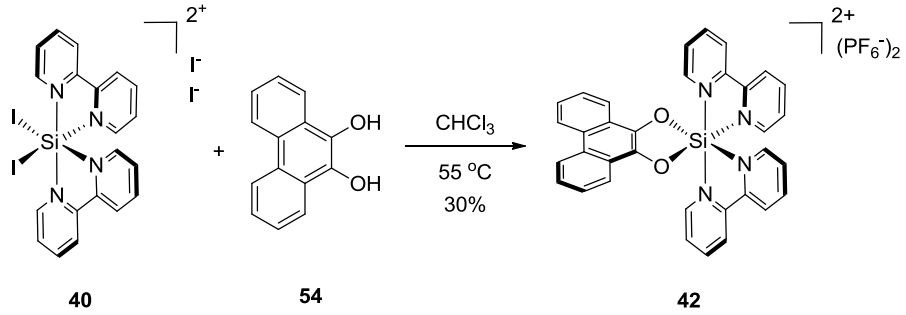

40 54 42

Bis(2,2'-bipyridine)-(9,10-phenanthrenediolato)silicium(IV) bis(hexafluorophosphate) (**42**) A suspension of $[Si(bpy)_2I_2]I_2$ (**40**) (160 mg, 0.19 mmol) and 4 equivalents of phenanthrene-9,10-diol (**54**) (160 mg, 1.76 mmol) in dry $CHCl_3$ (30 mL) was purged with N_2 for 15 min and then stirred at 55 °C for 12 hours. The resulting dark-brown suspension was cooled to room temperature and the solvent was removed *in vacuo*. The crude material was subjected to silica gel chromatography with acetonitrile:water:saturated aqueous KNO_3 50:3:1. The product eluents were concentrated to dryness and the resulting material was dissolved in minimal amounts of water. The product was precipitated by the addition of excessive solid NH_4PF_6. The precipitate was centrifuged, washed twice with water and dried under high vacuum to

afford the pure diolate complex **42** as a yellow solid (48 mg, 30%). ^{1}H-NMR (300 MHz, CD_3CN): δ (ppm) 9.06 (m, 2H), 8.93 (dd, J = 14.6; 8.0 Hz, 4H), 8.71 (m, 6H), 8.05 (ddd, J = 7.7, 5.9, 1.2 Hz, 2H), 7.87 (m, 4H), 7.73 (m, 2H), 7.59 (m, 4H); ^{13}C-NMR (75 MHz, CD_3CN): δ (ppm) 147.42, 147.11, 146.65, 144.96, 143.70, 142.81, 135.74, 130.64, 130.03, 126.69, 126.53, 124.77, 124.69, 124.62, 123.79, 122.88, 120.19. IR (neat): ν (cm^{-1}) 1627, 1617, 1507, 1454, 1366, 1344, 1323, 1172, 1057, 1045, 1029, 945, 875, 839, 780, 769, 758, 736, 726, 686, 672, 646, 582, 557, 546, 515, 499, 483, 460, 427. HRMS calcd for $C_{34}H_{24}F_6N_4O_2PSi$ $(M\text{-}PF_6)^+$ 693.1305, found: 693.1288.

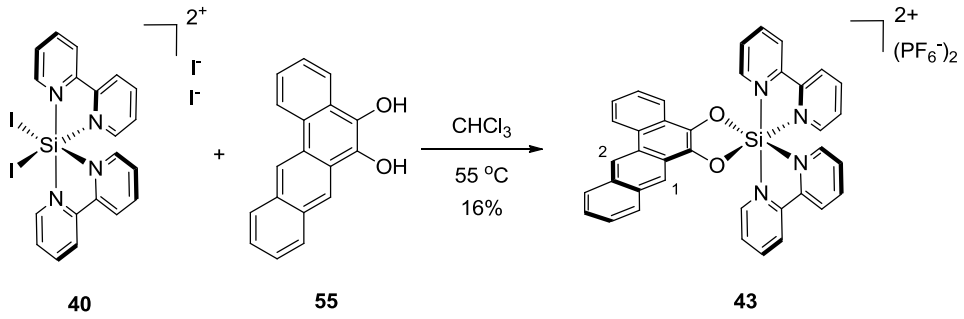

40 **55** **43**

Bis(2,2'-bipyridine)-(5,6-tetraphenediolato)silicium(IV) bis(hexafluorophosphate) (**43**) A suspension of $[Si(bpy)_2I_2]I_2$ (**40**) (300 mg, 0.35 mmol) and 4 equivalents of tetraphene-5,6-diol (**55**) (360 mg, 1.42 mmol) in dry $CHCl_3$ (40 mL) was purged with N_2 for 15 min and then stirred at 55 °C for 12 hours. The resulting dark-brown suspension was cooled to room temperature and the solvent was removed *in vacuo*. The crude material was subjected to silica gel chromatography with acetonitrile:water:saturated aqueous KNO_3 50:3:1. The product eluents were concentrated to dryness and the resulting material was dissolved in minimal amounts of water. The product was precipitated by the addition of excessive solid NH_4PF_6. The precipitate was centrifuged, washed twice with water and dried under high vacuum to afford the pure diolate complex **43** as a yellow solid (50 mg, 16%). ^{1}H-NMR (300 MHz, CD_3CN): δ (ppm) 9.30 (s, 1H, 1-H or 2-H), 9.09 (m, 2H), 8.93 (m, 5H), 8.71 (m, 4H), 8.31 (s, 1H, 1-H or 2-H), 8.18 (m, 1H), 8.03 (m, 3H), 7.91 (m, 2H), 7.82 (m, 1H), 7.76 (m, 2H), 7.60 (m, 4H); ^{13}C-NMR (75 MHz, CD_3CN): δ (ppm) 147.53, 147.12,

147.07, 146.70, 146.65, 144.99, 143.74, 143.71, 142.85, 135.36, 135.21, 131.56, 130.68, 130.64, 130.48, 130.08, 128.34, 127.34, 127.08, 126.96, 126.23, 126.10, 125.14, 125.12, 124.78, 124.65, 123.12, 122.95, 122.31, 120.34, 117.96. IR (neat): ν (cm^{-1}) 1674, 1621, 1592, 1482, 1454, 1443, 1387, 1336, 1283, 1242, 1179, 1140, 1104, 1073, 1043, 994, 979, 953, 928, 910, 838, 748, 731, 695, 675, 613, 588, 558, 534, 521, 502, 470, 455, 422, 410, 394, 384. HRMS calcd for $C_{38}H_{26}F_6N_4O_2PSi$ $(M\text{-}PF_6)^+$ 741.1305, found: 741.1440.

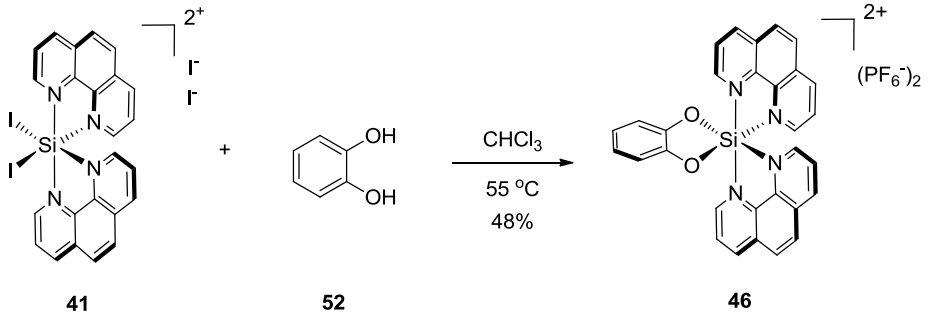

41 52 46

Bis(1,10-phenanthroline)catecholatosilicium(IV) bis(hexafluorophosphate) (**46**) A suspension of $[Si(phen)_2I_2]I_2$ (**41**) (358 mg, 0.4 mmol) and 4 equivalents of catechol (**52**) (176 mg, 1.6 mmol) in dry $CHCl_3$ (20 mL) was purged with N_2 for 15 min and then stirred at 55 °C for 12 hours. The resulting dark-brown suspension was cooled to room temperature and the solvent was removed *in vacuo*. The crude material was subjected to silica gel chromatography with acetonitrile:water:saturated aqueous KNO_3 50:3:1. The product eluents were concentrated to dryness and the resulting material was dissolved in minimal amounts of water. The product was precipitated by the addition of excess solid NH_4PF_6. The precipitate was centrifuged, washed twice with water and dried under high vacuum to afford the pure diolate complexes **46** (150 mg, 48%). ^{1}H-NMR (300 MHz, CD_3CN): δ (ppm) 9.46 (dd, J = 5.4, 1.1 Hz, 2H), 9.38 (dd, J = 8.3, 1.1 Hz, 2H), 9.09 (dd, J = 8.3, 1.0 Hz, 2H), 8.60 (d, J = 9.1 Hz, 2H), 8.51 (d, J = 9.1 Hz, 2H), 8.49 (dd, J = 8.3, 5.5 Hz, 2H), 7.92 (dd, J = 8.3, 5.5 Hz, 2H), 7.73 (dd, J = 5.5, 1.0 Hz, 2H), 6.81 (m, 4H); ^{13}C-NMR (75 MHz, CD_3CN): δ (ppm) 149.5, 147.5, 147.3, 147.0, 146.4, 135.8, 134.8, 131.4, 131.0, 129.7, 129.6, 129.3, 128.9,

123.0, 114.6. IR (neat): ν (cm^{-1}) 3075, 1629, 1585, 1528, 1482, 1437, 1335, 1244, 1154, 1115, 1019, 884, 826, 759, 738, 714, 666, 620, 582, 554, 521, 484, 456, 416. HRMS calcd for $C_{30}H_{20}F_6N_4O_2PSi$ $(M\text{-}PF_6)^+$ 641.1003, found: 641.0978.

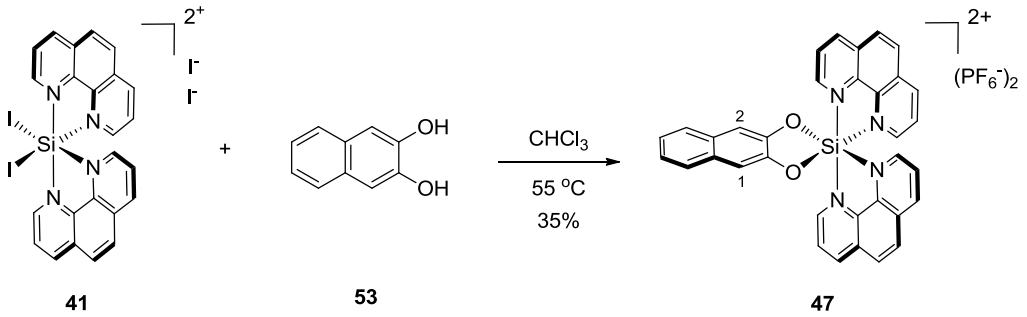

41 53 47

Bis(1,10-phenanthroline)-(2,3-naphthalenediolato)silicium(IV) bis(hexafluorophosphate) (**47**) A suspension of $[Si(phen)_2I_2]I_2$ (**41**) (358 mg, 0.4 mmol) and 4 equivalents of naphthalene-2,3-diol (**53**) (256 mg, 1.6 mmol) in dry $CHCl_3$ (20 mL) was purged with N_2 for 15 min and then stirred at 55 °C for 12 hours. The resulting dark-brown suspension was cooled to room temperature and the solvent was removed *in vacuo*. The crude material was subjected to silica gel chromatography with acetonitrile:water:saturated aqueous KNO_3 50:3:1. The product eluents were concentrated to dryness and the resulting material was dissolved in minimal amounts of water. The product was precipitated by the addition of excess solid NH_4PF_6. The precipitate was centrifuged, washed twice with water and dried under high vacuum to afford the pure diolate complex **47** (117 mg, 35%). ^{1}H-NMR (300 MHz, CD_3CN): δ (ppm) 9.51 (dd, J = 5.4, 1.0 Hz, 2H), 9.37 (dd, J = 8.4, 1.0 Hz, 2H), 9.11 (dd, J = 8.3, 0.8 Hz, 2H), 8.61 (d, J = 9.1 Hz, 2H), 8.52 (d, J = 9.1 Hz, 2H), 8.45 (dd, J = 8.3, 5.4 Hz, 2H), 7.94 (dd, J = 8.3, 5.6 Hz, 2H), 7.75 (dd, J = 5.5, 0.8 Hz, 2H), 7.66 (m, 2H), 7.30 (m, 2H), 7.15 (s, 2H, 1-H and 2-H);.^{13}C-NMR (75 MHz, CD_3CN): δ (ppm) 149.6, 147.6, 147.5, 147.1, 146.5, 135.8, 134.9, 131.6, 131.4, 131.1, 129.8, 129.8, 129.4, 128.9, 127.7, 125.3, 109.9; IR (neat): ν (cm^{-1}) 1625, 1586, 1530, 1464, 1436, 1323, 1249, 1221, 1161, 880, 833, 757, 741, 715, 667, 621, 579, 556, 520, 508, 486, 463, 411, 385. HRMS calcd for $C_{34}H_{22}F_6N_4O_2PSi$ $(M\text{-}PF_6)^+$ 691.1159, found: 691.1143.

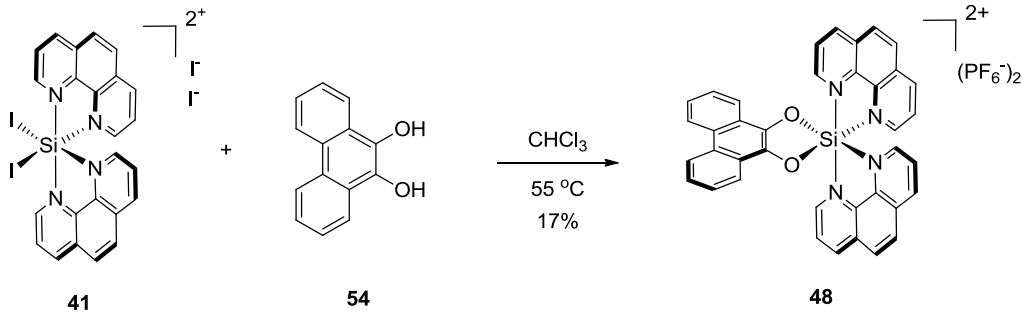

41 54 48

Bis(1,10-phenanthroline)-(9,10-phenanthrenediolato)silicium(IV) bis(hexafluoro phosphate) (**48**) A suspension of $[Si(phen)_2I_2]I_2$ (**41**) (352 mg, 0.4 mmol) and 4 equivalents of phenanthrene-9,10-diol (**54**) (332 mg, 1.6 mmol) in dry $CHCl_3$ (20 mL) was purged with N_2 for 15 min and then stirred at 55 ^oC for 12 hours. The resulting dark-brown suspension was cooled to room temperature and the solvent was removed *in vacuo*. The crude material was subjected to silica gel chromatography with acetonitrile:water:saturated aqueous KNO_3 50:3:1. The product eluents were concentrated to dryness and the resulting material was dissolved in minimal amounts of water. The product was precipitated by the addition of excess solid NH_4PF_6. The precipitate was centrifuged, washed twice with water and dried under high vacuum to afford the pure diolate complex **48** as a brown-red solid (60 mg, 17%). ^{1}H-NMR (300 MHz, CD_3CN): δ (ppm) 9.41(dd, J = 5.4, 1.2 Hz, 2H), 9.31 (dd, J = 8.4, 1.2 Hz, 2H), 9.13 (dd, J = 8.3, 1.1 Hz, 2H), 8.70 (m, 2H), 8.59 (d, J = 9.2 Hz, 2H), 8.53 (d, J = 9.2 Hz, 2H), 8.35 (dd, J = 8.3, 5.4 Hz, 2H), 7.98 (dd, J = 8.3, 5.6 Hz, 2H), 7.82 (dd, J = 5.6, 1.1 Hz, 2H), 7.80 (m, 2H), 7.53 (m, 4H); ^{13}C-NMR (75 MHz, CD_3CN): δ (ppm) 149.9, 147.6, 146.8, 146.3, 137.4, 135.9, 134.8, 131.4, 131.1, 129.7, 129.7, 129.3, 128.9, 128.0, 127.8, 125.9, 125.2, 124.1, 121.6. IR (neat): ν (cm^{-1}) 3112, 1626, 1586, 1530, 1436, 1367, 1341, 1115, 1054, 1030, 886, 833, 802, 757, 738, 715, 686, 669, 650, 581, 556, 546, 523, 508, 483, 468, 443, 414, 394, 382. HRMS calcd for $C_{38}H_{24}F_6N_4O_2PSi$ $(M\text{-}PF_6)^+$ 741.1316, found: 741.1285.

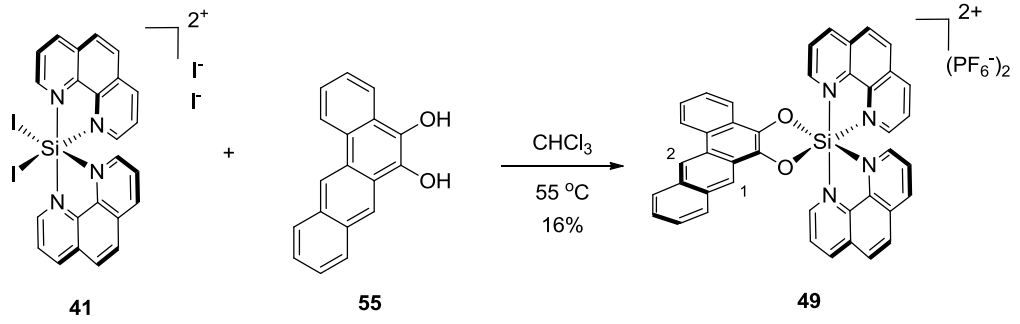

41 55 49

Bis(1,10-phenanthroline)-(5,6-tetraphenediolato)silicium(IV) bis(hexafluorophos phate) (**49**) suspension of $[Si(phen)_2I_2]I_2$ (**41**) (352 mg, 0.4 mmol) and 4 equivalents of tetraphene-5,6-diol (**55**) (416 mg, 1.6 mmol) in dry $CHCl_3$ (20 mL) was purged with N_2 for 15 min and then stirred at 55 °C for 12 hours. The resulting dark-brown suspension was cooled to room temperature and the solvent was removed *in vacuo*. The crude material was subjected to silica gel chromatography with acetonitrile:water:saturated aqueous KNO_3 50:3:1. The product eluents were concentrated to dryness and the resulting material was dissolved in minimal amounts of water. The product was precipitated by the addition of excess solid NH_4PF_6. The precipitate was centrifuged, washed twice with water and dried under high vacuum to afford the pure diolate complex **49** as a brown-red solid (60 mg, 16%). ^{1}H-NMR (300 MHz, CD_3CN): δ (ppm) 9.45 (ddd, J = 10.5, 5.4, 1.0 Hz, 2H), 9.31 (dd, J = 3.3, 0.9 Hz, 2H), 9.26 (s, 1H, 1-H or 2-H), 9.14 (m, 2H), 8.34 (m, 1H), 8.56 (m, 4H), 8.37 (dd, J = 8.5, 5.3 Hz, 1H), 8.31 (dd, J = 8.4, 5.4 Hz, 1H), 8.28 (s, 1H, 1-H or 2-H), 8.12 (dd, J = 6.2, 3.4 Hz, 1H), 8.00 (m, 2H), 7.89 (m, 3H), 7.78 (m, 1H), 7.56 (m, 2H), 7.50 (m, 2H); ^{13}C-NMR (75 MHz, CD_3CN): δ (ppm) 145.00, 147.70, 146.80, 146.77, 146.31, 146.29, 136.97, 136.81, 135.87, 134.85, 134.84, 132.85, 131.73, 131.38, 131.36, 131.10, 129.74, 129.72, 129.65, 129.62, 129.28, 128.98, 128.94, 128.66, 128.36, 128.24, 127.74, 127.50, 127.45, 126.37, 126.17, 123.56, 124.40, 121.71, 119.28. IR (neat): ν (cm^{-1}) 1627, 1586, 1530, 1437, 1361, 1337, 1361, 1337, 1153, 1117, 1099, 1048, 885, 837, 760, 717, 606, 596, 575, 557, 524, 508, 485, 471, 444, 418. HRMS calcd for $C_{42}H_{26}F_6N_4O_2PSi$ $(M\text{-}PF_6)^+$ 791.1461, found: 791.1444.

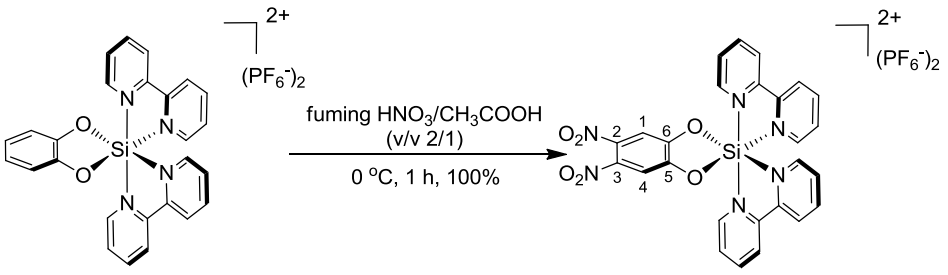

70 71

Bis(2,2'-bipyridine)-(4,5-dinitro-1,2-benzenediolato)silicium(IV) bis(hexafluorophosphate) (**71**) To complex **70** (74 mg, 0.1 mmol), CH_3COOH (0.5 mL, 8.7 mmol) was added, and then the mixture was cooled in ice bath. The fuming nitric acid (1 mL, 21.1 mmol) was added slowly. After finishing the addition, the mixture was stirred at room temperature. One hour later, the mixture was poured on ice, 10*N* a.q KOH (about 3 mL) was added to adjust the pH to 5-6, and the product was precipitated by the addition of excessive solid NH_4PF_6. The precipitate was centrifuged, washed twice with water and dried under high vacuum to afford the pure complex **71** (82 mg, 100%). ^{1}H-NMR (300 MHz, CD_3CN): δ (ppm) 9.06-8.92 (m, 4H, Ar-H), 8.92-8.78 (m, 4H, Ar-H), 8.70-8.65 (m, 2H, Ar-H), 8.26-8.16 (m, 2H, Ar-H), 7.89-7.80 (m, 2H, Ar-H). 7.65-7.58 (m, 2H, Ar-H), 7.33 (s, 2H, H-1 and H-4); ^{13}C-NMR (75 MHz, CD_3CN): δ (ppm) 150.91, 149.18, 148.75, 148.57, 146.53, 144.91, 144.04, 138.84, 132.49, 131.59, 126.51, 126.14, 111.51. HRMS calcd for $C_{26}H_{18}F_6N_6O_6PSi$ $(M\text{-}PF_6)^+$ 683.0693, found: 683.0681.

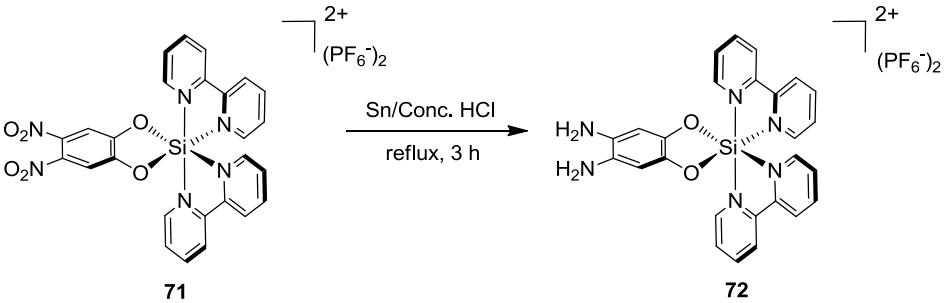

71 72

Bis(2,2'-bipyridine)-(4,5-diamino-1,2-benzenediolato)silicium(IV) bis(hexafluorophosphate) (**72**) Complex **71** (200 mg, 0.04 mmol) was dissolved in conc. HCl (2

mL), and then tin (147 mg, 1.25 mmol) was added. The mixture was stirred at reflux. After 3 hours, the mixture was cooled to room temperature, then the solution was poured on ice, and 10*N* a.q KOH (about 1.2 mL) was added to adjust the pH to 5-6. The product was precipitated by the addition of excessive solid NH_4PF_6. The precipitate was centrifuged, washed twice with water and dried under high vacuum to afford the crude product **72**. The product was very unstable under air and decomposed very quickly even when kept at –20 ^oC. So it should be used directly for the next step.

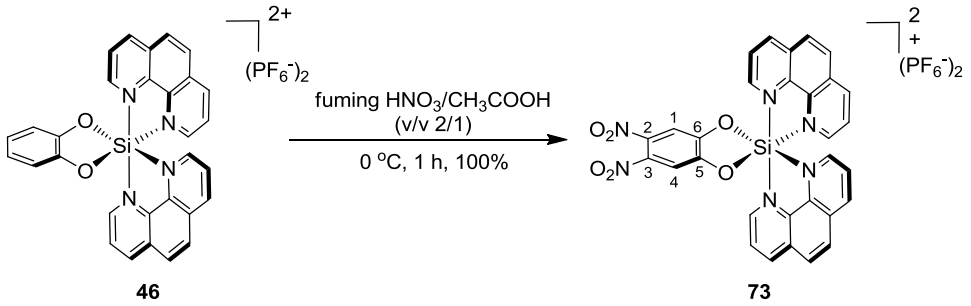

46 **73**

Bis(1,10-phenanthroline)-(4,5-dinitro-1,2-benzenediolato)silicium(IV) bis(hexafluorophosphate) (**73**) To complex **46** (802 mg, 1.02 mmol), CH_3COOH (5 mL, 87 mmol) was added, and then the mixture was cooled in ice bath. The fuming nitric acid (10 mL, 211 mmol) was added slowly. After finishing the addition, the mixture was stirred at room temperature. One hour later, the mixture was poured on ice, 10*N* a.q KOH (about 30 mL) was added to adjust the pH to 5-6, the product was precipitated by the addition of excessive solid NH_4PF_6. The precipitate was centrifuged, washed twice with water and dried under high vacuum to afford the pure complex **73** (893 mg, 100%). ^{1}H-NMR (300 MHz, CD_3CN): δ (ppm) 9.46-9.43 (m, 2H, Ar-H), 9.42 (s, 2H, Ar-H), 9.14 (dd, J = 8.3, 0.9 Hz, 2H, Ar-H), 8.67-8.48 (m, 6H, Ar-H), 7.95 (dd, J = 8.3, 5.7 Hz, 2H, Ar-H), 7.79-7.73 (m, 2H, Ar-H), 7.35 (s, 2H, H-1 and H-4); ^{13}C-NMR (75 MHz, CD_3CN): δ (ppm) 151.32, 149.97, 148.01, 147.58, 147.12, 138.87, 135.64, 134.65, 131.55, 131.07, 130.07, 129.86, 129.51, 129.06, 111.44. HRMS calcd for $C_{30}H_{18}F_6N_6O_6PSi$ $(M\text{-}PF_6)^+$ 731.0693, found: 731.0681.

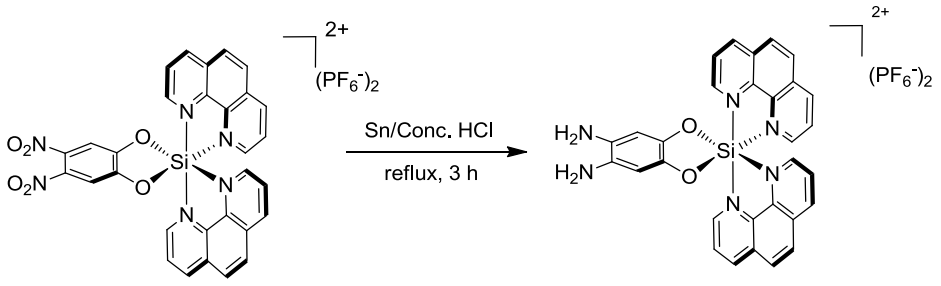

Bis(1,10-phenanthroline)-(4,5-diamino-1,2-benzenediolato)silicium(IV) bis(hexafluorophosphate) (**74**) Complex **73** (1300 mg, 1.49) was dissolved in conc. HCl (2 mL), and then tin (860 mg, 7.12 mmol) was added. The mixture was stirred at reflux. After 3 hours, the mixture was cooled to room temperature, then the solution was poured on ice, and 10*N* a.q KOH (about 1.2 mL) was added to adjust the pH to 5-6. The product was precipitated by the addition of excessive solid NH_4PF_6. The precipitate was centrifuged, washed twice with water and dried under high vacuum to afford the crude product **74**. The product was very unstable under air and decomposed very quickly even when kept at -20 ^oC. So it should be used directly for the next step.

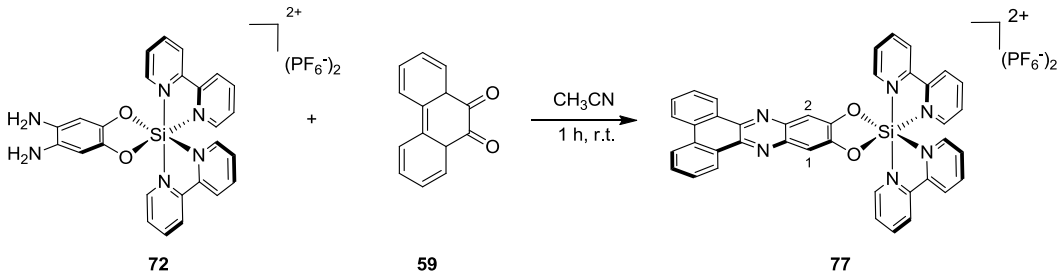

Bis(2,2'-bipyridine)-(11,12-dibenzo[*a*,*c*]phenazinediolato)silicium(IV) bis(hexafluorophosphate) (**77**) Crude complex **72** (100 mg, 0.13 mmol) was dissolved in CH_3CN (15 mL), then 4 equivalents of phenanthrene-9,10-dione (**59**) (108 mg, 0.52 mmol) was added. The mixture was stirred at room temperature. After one hour, the solvent was evaporated *in vacuo*. The crude material was subjected to silica gel chromatography with acetonitrile:water:saturated aqueous KNO_3 50:3:1, and the product eluents were concentrated to dryness and the resulting material was dissolved in minimal amounts of water. The product was precipitated by the addition of

excessive solid NH_4PF_6. The precipitate was centrifuged, washed twice with water and dried under high vacuum to afford the pure phenazinediolate complex **77** as a yellow solid (37 mg, about 20% in two steps). ^{1}H-NMR (300 MHz, CD_3CN): δ (ppm) 9.33 (dd, J = 7.7, 1.1 Hz, 2H), 9.26-9.20 (m, 2H), 8.97 (d, 2H), 8.88 (d, J = 8.1 Hz, 2H), 8.79 (dt, J = 7.9, 1.4 Hz, 2H), 8.66 (dt, J = 7.9, 1.3 Hz, 2H), 8.28 (dd, J = 7.8, 1.1 Hz, 2H), 8.20-8.21 (m, 2H), 8.10-8.01 (m, 4H), 7.91-7.83 (m, 2H), 7.69 (d, J = 5.9 Hz, 2H), 7.54 (s, 2H, 1-H and 2-H); ^{13}C-NMR (75 MHz, CD_3CN): δ (ppm) 151.42, 148.94, 148.47, 148.43, 146.43, 144.95, 144.32, 141.67, 140.95, 132.39, 132.30, 131.55, 131.29, 130.87, 129.01, 126.38, 126.14, 126.10, 124.26, 110.29. HRMS calcd for $C_{40}H_{26}F_6N_6O_2PSi$ $(M\text{-}PF_6)^+$ 795.1523, found: 791.1505.

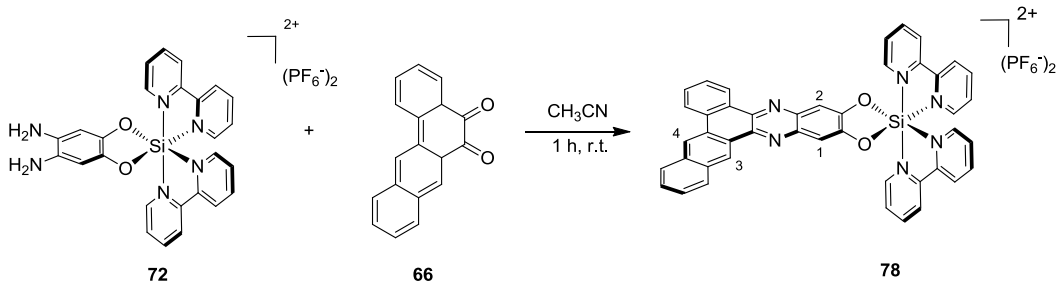

72 66 78

Bis(2,2'-bipyridine)-(2,3-benzo[*a*]naphtho[2,3-*c*]phenazinediolato)silicium(IV) bis(hexafluorophosphate) (**78**) Crude complex **72** (100 mg, 0.13 mmol) was dissolved in CH_3CN (15 mL), then 4 equivalents of tetraphene-5,6-dione (**66**) (134 mg, 0.52 mmol) was added. The mixture was stirred at room temperature. After one hour, the solvent was evaporated *in vacuo*. The crude material was subjected to silica gel chromatography with acetonitrile:water:saturated aqueous KNO_3 50:3:1, and the product eluents were concentrated to dryness and the resulting material was dissolved in minimal amounts of water. The product was precipitated by the addition of excessive solid NH_4PF_6. The precipitate was centrifuged, washed twice with water and dried under high vacuum to afford the pure phenazinediolate complex **78** as a yellow solid (38 mg, about 20% in two steps). ^{1}H-NMR (300 MHz, CD_3CN): δ (ppm) 9.73 (s, 1H, 3-H or 4-H), 9.26-9.13 (m, 4H), 8.98 (d, J = 8.1 Hz, 2H), 8.91 (d, J = 8.1 Hz, 2H), 8.85-8.75 (m, 3H), 8.72-8.62 (m, 2H), 8.25-8.12 (m, 4H), 7.92-7.60 (m, 8H),

7.53 (s, 1H, 1-H or 2-H), 7.50 (s, 1H, 1-H or 2-H). HRMS calcd for $C_{44}H_{28}F_{12}N_6O_2P_2SiNa$ $(M+Na)^+$ 1013.1219, found: 1213.1222.

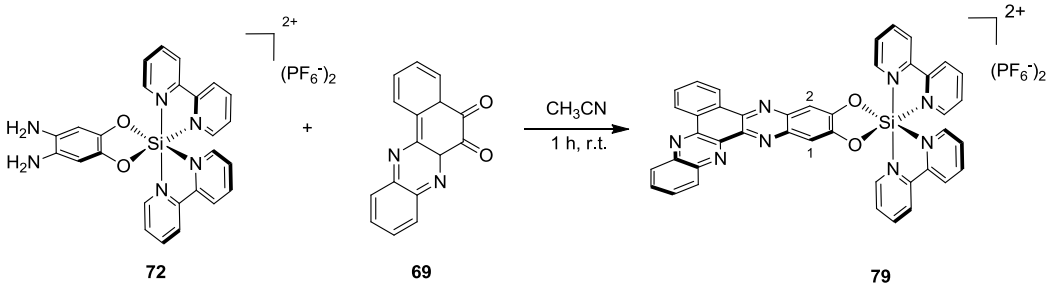

72 69 79

Bis(2,2'-bipyridine)-(2,3-benzo[*a*]quinoxalino[2,3-*c*]phenazinediolato)silicium(IV) bis(hexafluorophosphate) (**79**) Crude complex **72** (100 mg, 0.13 mmol) was dissolved in CH_3CN (15 mL), then 4 equivalents of benzo[a]phenazine-5,6-dione (**69**) (135 mg, 0.52 mmol) was added. The mixture was stirred at room temperature. After one hour, the solvent was evaporated *in vacuo*. The crude material was subjected to silica gel chromatography with acetonitrile:water:saturated aqueous KNO_3 50:3:1, and the product eluents were concentrated to dryness and the resulting material was dissolved in minimal amounts of water. The product was precipitated by the addition of excessive solid NH_4PF_6. The precipitate was centrifuged, washed twice with water and dried under high vacuum to afford the pure phenazinediolate complex **79** as a yellow solid (37 mg, about 20% in two steps). ^{1}H-NMR (300 MHz, CD_3CN): δ (ppm) 9.29-9.20 (m, 2H), 9.18-9.13 (m, 1H), 9.08-8.88 (m, 4H), 8.87-8.76 (m, 2H), 8.74-8.62 (m, 2H), 8.40-8.30 (m, 2H), 8.28-8.10 (m, 3H), 8.05-7.84 (m, 6H), 7.8-7.67 (m, 2H), 7.61 (s, 1H, 1-H or 2-H), 7.53 (s, 1H, 1-H or 2-H); ^{29}Si-NMR (79.5 MHz, CD_3CN): δ (ppm) -107.9. HRMS calcd for $C_{42}H_{26}F_6N_8O_2PSi$ $(M-PF_6)^+$ 847.1584, found: 847.1565.

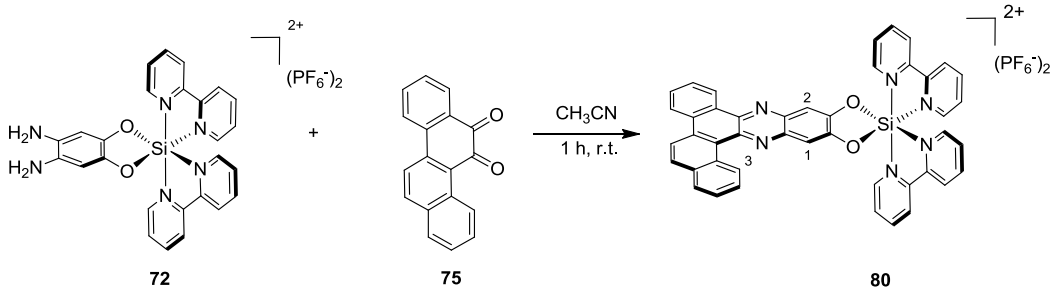

72 75 80

Bis(2,2'-bipyridine)-(13,14-benzo[*a*]naphtho[2,1-*c*]phenazinediolato)silicium(IV) bis(hexafluorophosphate) (**80**) Crude complex **72** (100 mg, 0.13 mmol) was dissolved in CH_3CN (15 mL), then 4 equivalents of chrysene-5,6-dione (**75**) (134 mg, 0.52 mmol) was added. The mixture was stirred at room temperature. After one hour, the solvent was evaporated *in vacuo*. The crude material was subjected to silica gel chromatography with acetonitrile:water:saturated aqueous KNO_3 50:3:1, and the product eluents were concentrated to dryness and the resulting material was dissolved in minimal amounts of water. The product was precipitated by the addition of excessive solid NH_4PF_6. The precipitate was centrifuged, washed twice with water and dried under high vacuum to afford the pure phenazinediolate complex **80** as a yellow solid (30 mg, about 20% in two steps). ^{1}H-NMR (300 MHz, CD_3CN): δ (ppm) 11.1 (d, J = 9.3 Hz, 2H, 3-H), 9.36 (dd, J = 7.9, 1.3 Hz, 2H), 9.28-9.20 (m, 2H), 9.02-8.94 (m, 2H), 8.94-8.87 (m, 2H), 8.86-8.75 (m, 2H), 8.73-8.63 (m, 2H), 8.30-8.06 (m, 4H), 7.95-7.76 (m, 5H), 7.75-7.64 (m, 4H), 7.56 (s, 1H, 1-H or 2-H); ^{13}C-NMR (75 MHz, CD_3CN): δ (ppm) 151.68, 151.51, 148.97, 148.48, 148.46, 148.43, 146.42, 144.94, 144.32, 143.23, 141.19, 140.70, 140.05, 134.84, 132.80, 132.60, 132.59, 132.32, 132.18, 131.59, 131.56, 131.21, 130.92, 129.61, 129.06, 128.75, 127.49, 126.39, 126.11, 125.49, 125.04, 122.23, 110.20, 110.0; ^{29}Si-NMR (79.5 MHz, CD_3CN): δ (ppm) -109.3. HRMS calcd for $C_{44}H_{28}F_6N_6O_2PSi$ $(M\text{-}PF_6)^+$ 845.1679, found: 845.1659.

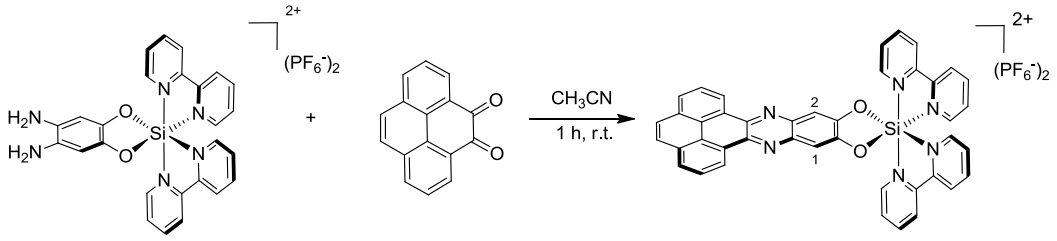

72 76 81

Bis(2,2'-bipyridine)-(11,12-phenanthro[4,5-*abc*]phenazinediolato)silicium(IV) bis (hexafluorophosphate) (**81**) Crude complex **72** (100 mg, 0.13 mmol) was dissolved in CH_3CN (15 mL), then 4 equivalents of pyrene-4,5-dione (**76**) (134 mg, 0.52 mmol) was added. The mixture was stirred at room temperature. After one hour, the solvent was evaporated *in vacuo*. The crude material was subjected to silica gel chromatography with acetonitrile:water:saturated aqueous KNO_3 50:3:1, and the product eluents were concentrated to dryness and the resulting material was dissolved in minimal amounts of water. The product was precipitated by the addition of excessive solid NH_4PF_6. The precipitate was centrifuged, washed twice with water and dried under high vacuum to afford the pure phenazinediolate complex **81** as a yellow solid (33 mg, about 20% in two steps). ^{1}H-NMR (300 MHz, CD_3CN): δ (ppm) 9.33 (dd, J = 7.7, 1.1 Hz, 2H), 9.26-9.21 (m, 2H), 8.07 (d, J = 8.1 Hz, 2H), 8.88 (d, J = 8.1 Hz, 2H), 8.79 (dt, J = 7.9. 1.4 Hz, 2H), 8.66 (dt, J = 7.9, 1.3 Hz, 2H), 8.28 (dd, J = 7.8, 1.1 Hz, 2H), 8.20-8.13 (m, 2H), 8.10-8.01 (m, 4H), 7.91-7.84 (m, 2H), 7.71-7.66 (m, 2H), 7.54 (s, 2H, 1-H and 2-H); ^{13}C-NMR (75 MHz, CD_3CN): 151.51, 148.96, 148.45, 148.44, 146.45, 144.95, 144.34, 141.90, 141.66, 132.42, 132.30, 131.54, 130.56, 129.53, 128.24, 127.93, 126.40, 126.25, 126.10, 123.76, 110.39. HRMS calcd for $C_{42}H_{26}F_6N_6O_2PSi$ $(M\text{-}PF_6)^+$ 819.1523, found: 819.1523.

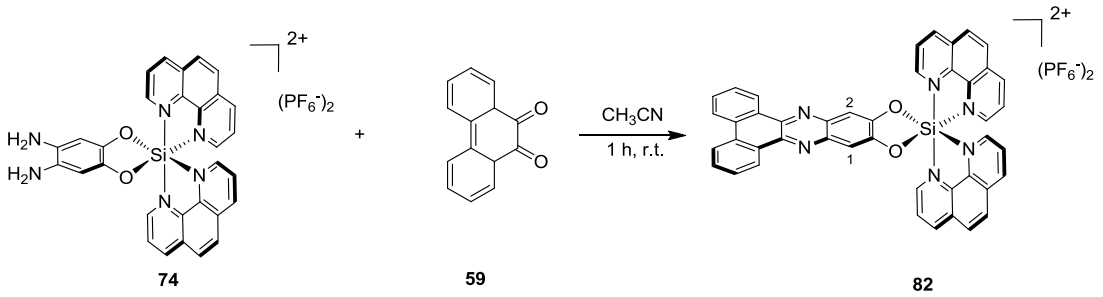

74 59 82

Bis(1,10-phenanthroline)-(11,12-dibenzo[*a,c*]phenazinediolato)silicium(IV) bis (hexafluorophosphate) (**82**) Crude complex **74** (82 mg, 0.11 mmol) was dissolved in CH_3CN (15 mL), then 4 equivalents of phenanthrene-9,10-dione (**59**) (92 mg, 0.44 mmol) was added. The mixture was stirred at room temperature. After one hour, the solvent was evaporated *in vacuo*. The crude material was subjected to silica gel chromatography with acetonitrile:water:saturated aqueous KNO_3 50:3:1, and the product eluents were concentrated to dryness and the resulting material was dissolved in minimal amounts of water. The product was precipitated by the addition of excessive solid NH_4PF_6. The precipitate was centrifuged, washed twice with water and dried under high vacuum to afford the pure phenazinediolate complex **82** as a yellow solid (30 mg, about 20% in two steps). ^{1}H-NMR (300 MHz, CD_3CN): δ (ppm) 9.61 (d, J = 9.6 Hz, 2H), 9.40 (d, J = 9.4 Hz, 2H), 9.24-9.13 (m, 4H), 8.71-8.65 (d, 2H), 8.62-8.52 (m, 4H), 8.47 (dd, J = 8.3, 5.5 Hz, 2H), 7.98 (dd, J = 8.3, 5.7 Hz, 2H), 7.88-7.70 (m, 6H), 7.53 (s, 2H , 1-H and 2-H); ^{13}C-NMR (75 MHz, CD_3CN): δ (ppm) 151.87, 149.74, 147.85, 147.32, 146.83, 141.76, 140.93, 135.76, 134.96, 132.39, 131.50, 131.32, 131.09, 130.86, 129.95, 129.82, 129.42, 129.03, 129.01, 126.13, 124.26, 110.24. HRMS calcd for $C_{44}H_{26}F_6N_6O_2PSi$ $(M\text{-}PF_6)^+$ 843.1513, found: 843.1523.

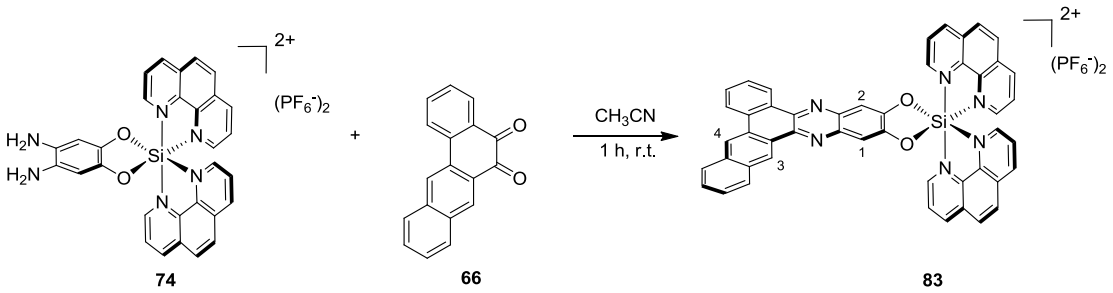

Bis(1,10-phenanthroline)-(2,3-benzo[*a*]naphtho[2,3-*c*]phenazinediolato)silicium(IV) bis(hexafluorophosphate) (**83**) Crude complex **74** (82 mg, 0.11 mmol) was dissolved in CH_3CN (15 mL), then 4 equivalents of tetraphene-5,6-dione (**66**) (113 mg, 0.44 mmol) was added. The mixture was stirred at room temperature. After one hour, the solvent was evaporated *in vacuo*. The crude material was subjected to silica gel chromatography with acetonitrile:water:saturated aqueous KNO_3 50:3:1, and the product eluents were concentrated to dryness and the resulting material was dissolved in minimal amounts of water. The product was precipitated by the addition of excessive solid NH_4PF_6. The precipitate was centrifuged, washed twice with water and dried under high vacuum to afford the pure phenazinediolate complex **83** as a yellow solid (30 mg, about 20% in two steps). ^{1}H-NMR (300 MHz, CD_3CN): δ (ppm) 9.73 (s, 1H, 3-H or 4-H), 9.65-9.60 (m, 2H), 9.43-9.37 (m, 2H), 9.23-9.12 (m, 4H), 8.85-8.78 (m, 1H), 8.68-8.53 (m, 4H), 8.52-8.44 (m, 2H), 8.25-8.16 (m, 2H), 8.03-7.94 (m, 2H), 7.87-7.63 (m, 6H), 7.55 (s, 1H, 1-H or 2-H), 7.52 (s, 1H, 1-H or 2-H). HRMS calcd for $C_{48}H_{28}F_6N_6O_2PSi$ $(M\text{-}PF_6)^+$ 893.1679, found: 893.1727.

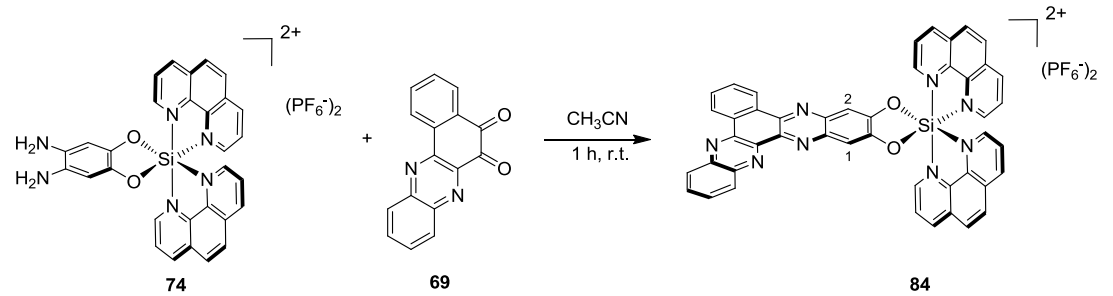

Bis(1,10-phenanthroline)-(2,3-benzo[*a*]quinoxalino[2,3-*c*]phenazinediolato)siliciu m(IV) bis(hexafluorophosphate) (**84**) Crude complex **74** (82 mg, 0.11 mmol) was

dissolved in CH_3CN (15 mL), then 4 equivalents of benzo[a]phenazine-5,6-dione (**69**) (114 mg, 0.44 mmol) was added. The mixture was stirred at room temperature. After one hour, the solvent was evaporated *in vacuo*. The crude material was subjected to silica gel chromatography with acetonitrile:water:saturated aqueous KNO_3 50:3:1, and the product eluents were concentrated to dryness and the resulting material was dissolved in minimal amounts of water. The product was precipitated by the addition of excessive solid NH_4PF_6. The precipitate was centrifuged, washed twice with water and dried under high vacuum to afford the pure phenazinediolate complex **84** as a yellow solid (26 mg, about 20% in two steps). ^{1}H-NMR (300 MHz, CD_3CN): δ (ppm) 9.76-9.70 (m, 1H), 9.67 (d, J = 5.3 Hz, 1H), 9.30 (d, J = 8.3 Hz, 1H), 9.26-9.00 (m, 4H), 8.97 (d, J = 8.1 Hz, 1H), 8.67 (br, 1H), 8.54-8.14 (m, 7H), 8.00 (dd, J = 8.4, 5.8 Hz, 1H), 7.96-7.62 (m, 8H), 7.52 (s, 1H, 1-H or 2-H). HRMS calcd for $C_{46}H_{26}F_6N_8O_2PSi$ $(M\text{-}PF_6)^+$ 895.1584, found: 895.1573.

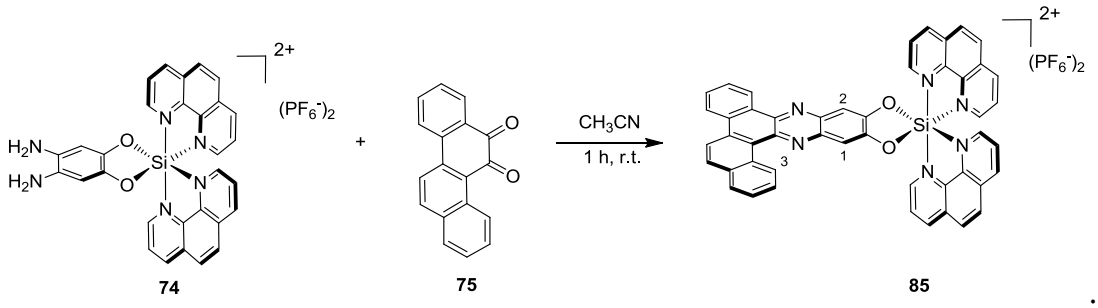

74 75 85

Bis(1,10-phenanthroline)-(13,14-benzo[*a*]naphtho[2,1-*c*]phenazinediolato)siliciu m(IV) bis(hexafluorophosphate) (**85**) Crude complex **74** (82 mg, 0.11 mmol) was dissolved in CH_3CN (15 mL), then 4 equivalents of chrysene-5,6-dione (**75**) (113 mg, 0.44 mmol) was added. The mixture was stirred at room temperature. After one hour, the solvent was evaporated *in vacuo*. The crude material was subjected to silica gel chromatography with acetonitrile:water:saturated aqueous KNO_3 50:3:1, and the product eluents were concentrated to dryness and the resulting material was dissolved in minimal amounts of water. The product was precipitated by the addition of excessive solid NH_4PF_6. The precipitate was centrifuged, washed twice with water

and dried under high vacuum to afford the pure phenazinediolate complex **85** as a yellow solid (28 mg, about 20% in two steps). ^{1}H-NMR (300 MHz, CD_3CN): δ (ppm) 11.1 (d, J = 8.3 Hz, 1H, 3-H), 9.64 (dd, J = 5.5, 1.1 Hz, 2H), 9.44-9.32 (m, 3H), 9.20-9.14 (m, 2H), 8.88-8.78 (m, 2H), 8.68-8.53 (m, 4H), 8.52-8.45 (m, 2H), 8.26 (d, J = 9.1 Hz, 1H), 8.10 (d, J = 7.9, 1.5 Hz, 1H), 7.99 (ddd, J = 8.3, 5.5, 0.8 Hz, 2H), 7.93-7.76 (m, 5H), 7.74 (s, 1H, 1-H or 2-H), 7.72-7.65 (m, 1H), 7.58 (s, 1H, 1-H or 2-H). HRMS calcd for $C_{48}H_{28}F_6N_6O_2PSi$ $(M\text{-}PF_6)^+$ 893.1679, found: 893.1664.

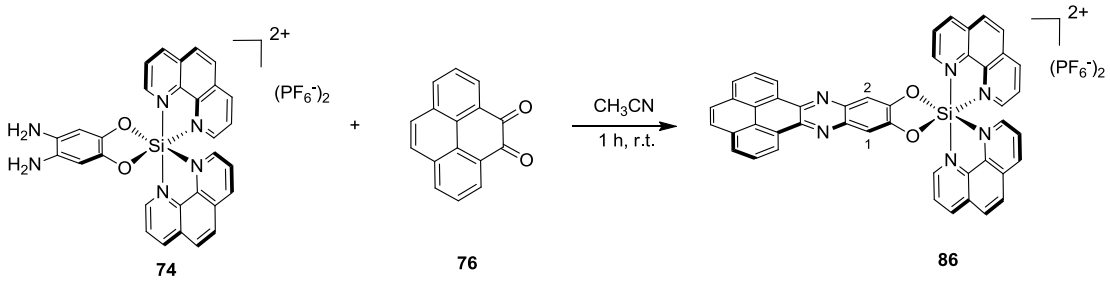

Bis(1,10-phenanthroline)-(11,12-phenanthro[4,5-*abc*]phenazinediolato)silicium(IV) bis(hexafluorophosphate) (**86**) Crude complex **74** (82 mg, 0.11 mmol) was dissolved in CH_3CN (15 mL), then 4 equivalents of pyrene-4,5-dione (**76**) (102 mg, 0.44 mmol) was added. The mixture was stirred at room temperature. After one hour, the solvent was evaporated *in vacuo*. The crude material was subjected to silica gel chromatography with acetonitrile:water:saturated aqueous KNO_3 50:3:1, and the product eluents were concentrated to dryness and the resulting material was dissolved in minimal amounts of water. The product was precipitated by the addition of excessive solid NH_4PF_6. The precipitate was centrifuged, washed twice with water and dried under high vacuum to afford the pure phenazinediolate complex **86** as a yellow solid (26 mg, about 20% in two steps). ^{1}H-NMR (300 MHz, CD_3CN): δ (ppm) 9.64 (dd, J = 5.5, 1.1 Hz, 2H), 9.47-9.36 (m, 4H), 9.16 (dd, J = 8.3, 1.1 Hz, 2H), 8.67-8.53 (m, 4H), 8.48 (dd, J = 8.3, 5.5 Hz, 2H), 8.36 (d, J = 7.9 Hz, 2H), 8.18-8.08 (m, 4H), 7.99 (dd, J = 8.3, 5.5 Hz, 2H), 7.84 (d, J = 5.3 Hz, 2H), 7.59 (s, 2H, 1-H and 2-H). HRMS calcd for $C_{46}H_{26}F_6N_6O_2PSi$ $(M\text{-}PF_6)^+$ 867.1523, found: 867.1531.

According to exact procedure in the literature,[49c] bulky rhodium complexes **87** and **88** have been obtained.

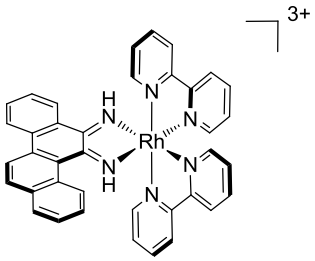

87

[Rh(bpy)$_2$(chrysi)](PF$_6$)$_3$ (**87**) ^{1}H-NMR (300 MHz, CD_3CN): δ (ppm) 9.78 (d, J = 8.9 Hz, 1H), 8.68-8.54 (m, 5H), 8.44-8.20 (m, 8H), 8.09 (d, J = 8.9 Hz, 1H), 7.96-7.86 (m, 2H), 7.84-7.74 (m, 2H), 7.73-7.67 (m, 1H), 7.67-7.44 (m, 5H), 7.42-7.32 (m, 1H).

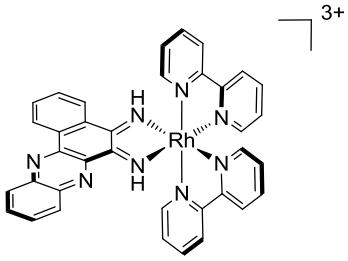

88

[Rh(bpy)$_2$(phzi)](PF$_6$)$_3$ (**88**) ^{1}H-NMR (300 MHz, CD_3CN): δ (ppm) 8.56-8.42 (m, 5H), 8.34 (d, J = 7.7 Hz, 1H), 8.18 (d, J = 5.3 Hz, 1H), 8.10-7.98 (m, 3H), 7.96-7.84 (m, 2H), 7.76 (d, J = 8.5 Hz, 1H), 7.64 (d, J = 7.7 Hz, 1H), 7.60-7.10 (m, 10H).

5.3.2 Evaluation of Hydrolytic Stabilities of Octahedral Silicon Complexes

The hydrolytic stability of the complexes **42**, **46** and **47**, were evaluated by ^{1}H-NMR in different mixed solvent. No signs of decomposition were observed after 3 days at room temperature. The spectrums and conditions are in detail (Figure 82-87).

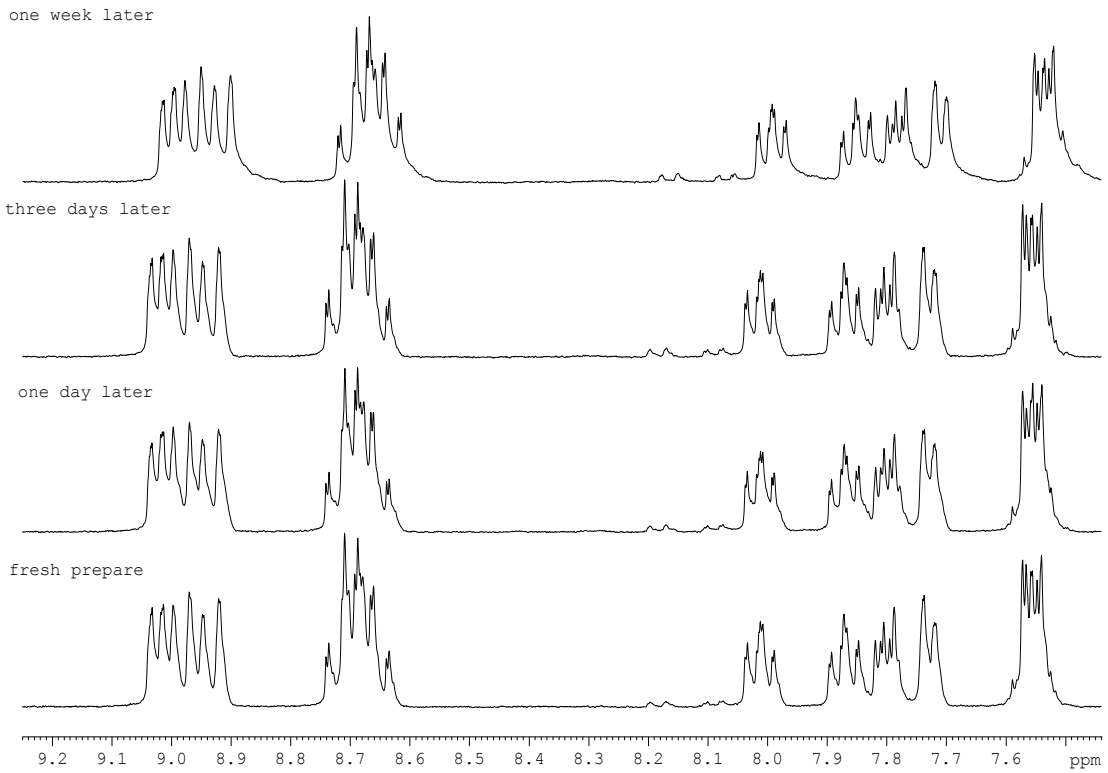

Figure 82 Hydrolytic stability of complex **42** at room temperature in CD_3CN/D_2O 5:1

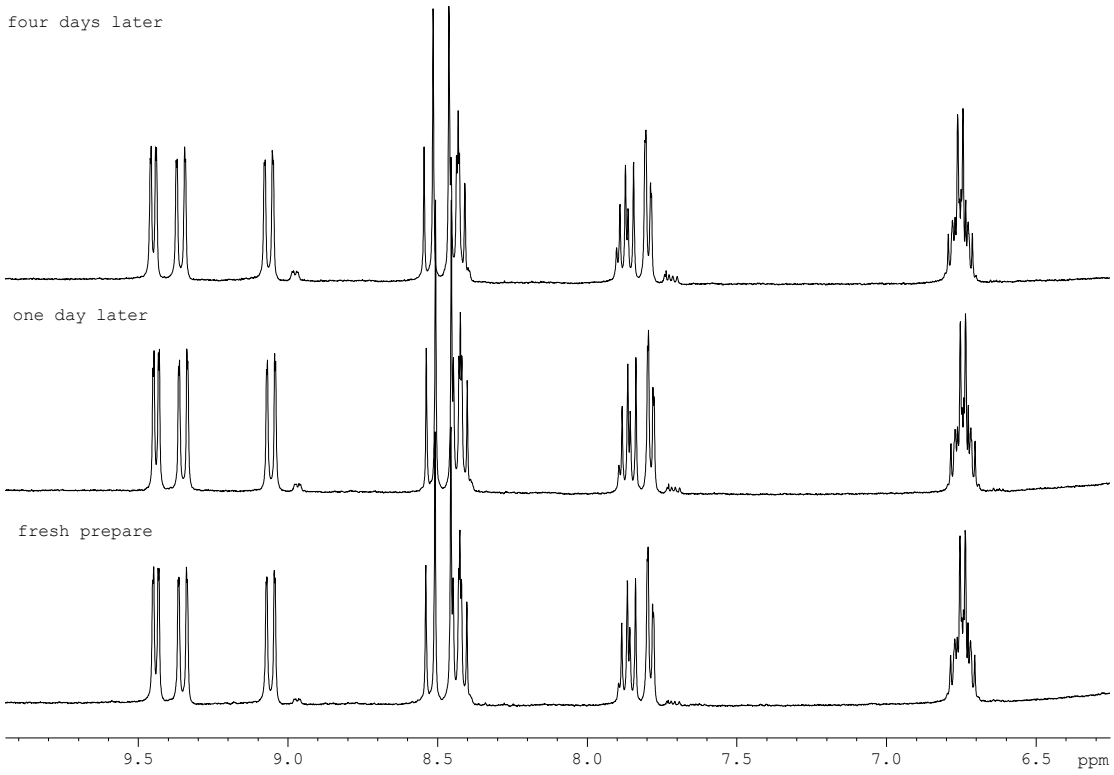

Figure 83 Hydrolytic stability of complex **46** at room temperature in CD_3CN/D_2O 5:1

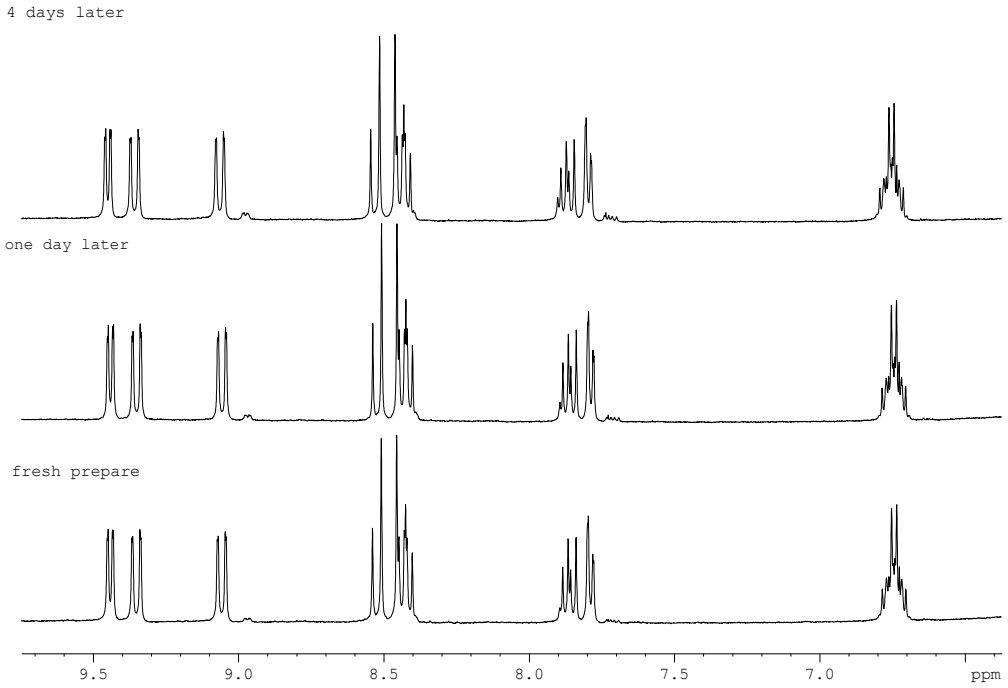

Figure 84 Hydrolytic stability of complex **46** at room temperature in 1:1 DMSO/buffer (10 mM sodium phosphate, 20 mM NaCl, pH 7.0)

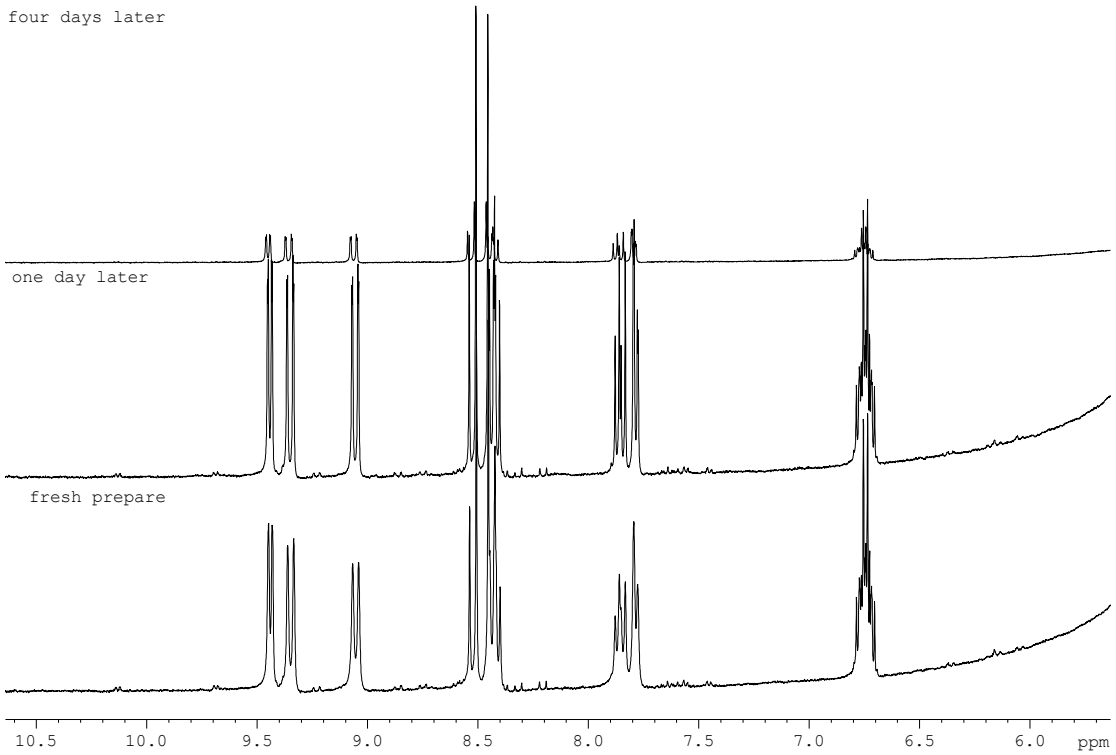

Figure 85 Hydrolytic stability of complex **46** at room temperature in in 1:1 DMSO/D_2O with 5 mM β-mercaptoethanol

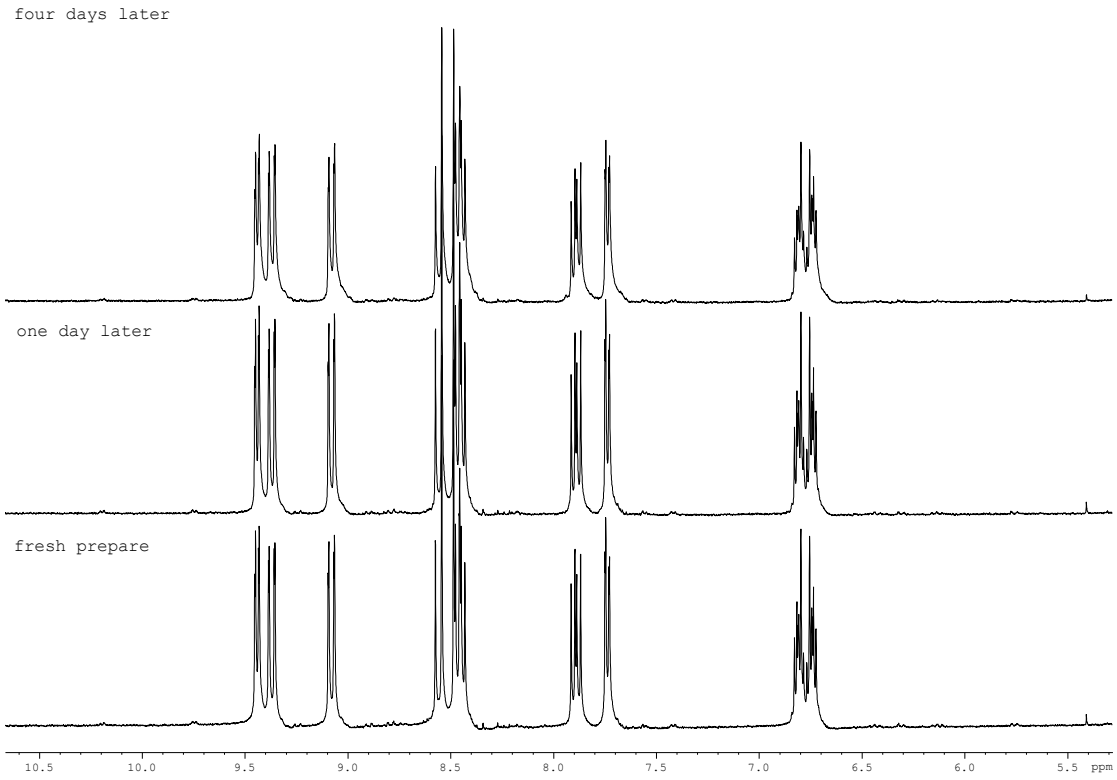

Figure 86 Hydrolytic stability of complex **46** at 40 ^{o}C in CD_3CN/D_2O 1:1

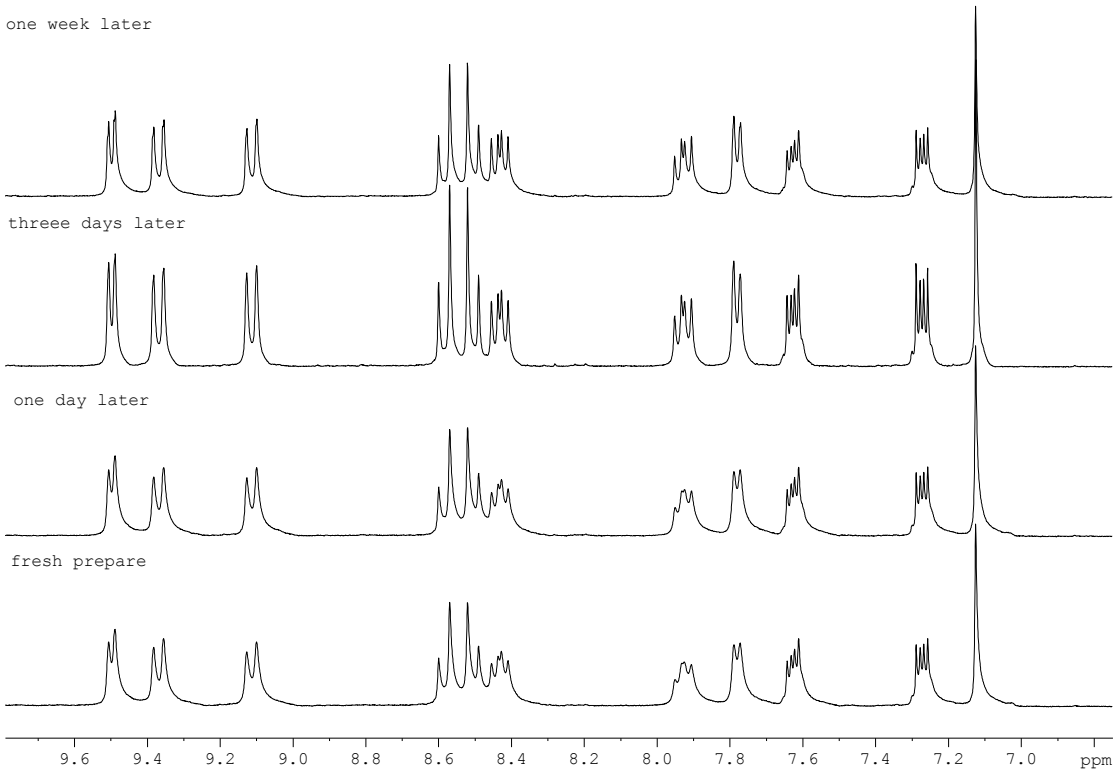

Figure 87 Hydrolytic stability of complex **47** at room temperature in CD_3CN/D_2O 5:1

Chapter 6 References

6.1 Literature

[1] a) *About supramolecular assemblies of pi-conjugated systems,* F. J. M. Hoeben, P. Jonkheijm, E. W. Meijer, A. P. H. J. Schenning, *Chem. Rev.* **2005**, *105*, 1491-1546; b) *Self-Assembly Strategies for Integrating Light Harvesting and Charge Separation in Artificial Photosynthetic Systems,* M. R. Wasielewski, *Acc. Chem. Res.* **2009**, *42*, 1910-1921.

[2] *Macromolecular multi-chromophoric scaffolding,* E. Schwartz, S. Le Gac, J. J. L. M. Cornelissen, R. J. M. Nolte, A. E. Rowan, *Chem. Soc. Rev.* **2010**, *39*, 1576-1599.

[3] a) *Singlet Exciton Fission for Solar Cell Applications Energy Aspects of Interchromophore Coupling,* E. C. Greyson, B. R. Stepp, X. D. Chen, A. F. Schwerin, I. Paci, M. B. Smith, A. Akdag, J. C. Johnson, A. J. Nozik, J. Michl, M. A. Ratner, *J. Phys. Chem. B* **2010**, *114*, 14223-14232; b) *Increased light harvesting in dye-sensitized solar cells with energy relay dyes,* B. E. Hardin, E. T. Hoke, P. B. Armstrong, J. H. Yum, P. Comte, T. Torres, J. M. J. Frechet, M. K. Nazeeruddin, M. Gratzel, M. D. McGehee, *Nat. Photonics* **2009**, *3*, 406-411.

[4] *Dipolar interactions and hydrogen bonding in supramolecular aggregates: understanding cooperative phenomena for 1st hyperpolarizability,* A. Datta, S. K. Pati, *Chem. Soc. Rev.* **2006**, *35*, 1305-1323.

[5] *Self-assembled pi-stacks of functional dyes in solution: structural and thermodynamic features,* Z. J. Chen, A. Lohr, C. R. Saha-Moller, F. Wurthner, *Chem. Soc. Rev.* **2009**, *38*, 564-584.

[6] *From supramolecular chemistry towards constitutional dynamic chemistry and adaptive chemistry,* J. M. Lehn, *Chem. Soc. Rev.* **2007**, *36*, 151-160.

[7] *Supramolecular DNA assembly,* C. K. McLaughlin, G. D. Hamblin, H. F. Sleiman, *Chem. Soc. Rev.* **2011**, *40*, 5647-5656.

[8] *DNA-Multichromophore Systems,* Y. N. Teo, E. T. Kool, *Chem. Rev.* **2012**, *112*, 4221-4245.

[9] a) *Porphyrins conjugated to DNA as CD reporters of the salt-induced B to Z-DNA transition,* M. Balaz, B. C. Li, J. D. Steinkruger, G. A. Ellestad, K. Nakanishi, N. Berova, *Org. Biomol. Chem.* **2006**, *4*, 1865-1867; b) *Porphyrin-DNA conjugates: porphyrin induced adenine-guanine homoduplex stabilization and interduplex assemblies,* M. Balaz, G. Sargsyan, *Org. Biomol. Chem.* **2012**; c) *Perylene-3,4 : 9,10-tetracarboxylic acid bisimide dye as an artificial DNA base surrogate,* C. Wagner, H. A. Wagenknecht, *Org. Lett.* **2006**, *8*, 4191-4194.

[10] *Anthracene-DNA conjugates as building blocks of designed DNA structures constructed by photochemical reactions,* M. Mukae, T. Ihara, M. Tabara, A. Jyo, *Org. Biomol. Chem.* **2009**, *7*, 1349-1354.

[11] *Hydrophobic Dimerization and Thermal Dissociation of Perylenediimide-Linked DNA Hairpins,* M. Hariharan, Y. Zheng, H. Long, T. A. Zeidan, G. C. Schatz, J. Vura-Weis, M. R. Wasielewski, X. B. Zuo, D. M. Tiede, F. D. Lewis, *J. Am. Chem. Soc.* **2009**, *131*, 5920-5929.

[12] *Hydrophobic Self-Assembly of a Perylenediimide-Linked DNA Dumbbell into Supramolecular Polymers*, P. P. Neelakandan, Z. Z. Pan, M. Hariharan, Y. Zheng, H. Weissman, B. Rybtchinski, F. D. Lewis, *J. Am. Chem. Soc.* **2010**, *132*, 15808-15813.

[13] *Assembly of DNA Triangles Mediated by Perylene Bisimide Caps*, H. A. Wagenknecht, F. Menacher, V. Stepanenko, F. Wurthner, *Chem.--Eur. J.* **2011**, *17*, 6683-6688.

[14] *DNA conformational switches as sensitive electronic sensors of analytes*, R. P. Fahlman, D. Sen, *J. Am. Chem. Soc.* **2002**, *124*, 4610-4616.

[15] *Role of Environmental Factors on the Structure and Spectroscopic Response of 5 '-DNA-Porphyrin Conjugates Caused by Changes in the Porphyrin-Porphyrin Interactions*, A. Mammmana, G. Pescitelli, T. Asakawa, S. Jockusch, A. G. Petrovic, R. R. Monaco, R. Purrello, N. J. Turro, K. Nakanishi, G. A. Ellestad, M. Balaz, N. Berova, *Chem.--Eur. J.* **2009**, *15*, 11853-11866.

[16] a) *Replacing the nucleohases in DNA with designer molecules*, E. T. Kool, *Acc. Chem. Res.* **2002**, *35*, 936-943; b) *C-nucleosides derived from simple aromatic hydrocarbons*, N. C. Chaudhuri, R. X. F. Ren, E. T. Kool, *Synlett* **1997**, 341-347.

[17] *Fluorescent hydrophobic zippers inside duplex DNA: Interstrand stacking of perylene-3,4 : 9,10-tetracarboxylic acid bisimides as artificial DNA base dyes*, D. Baumstark, H. A. Wagenknecht, *Chem.--Eur. J.* **2008**, *14*, 6640-6645.

[18] a) *Duplex Stabilization and Energy Transfer in Zipper Porphyrin-DNA*, T. Nguyen, A. Brewer, E. Stulz, *Angew. Chem. Int. Ed.* **2009**, *48*, 1974-1977; b) *Interstrand communication between 2 '-N-(pyren-1-yl)methyl-2 '-amino-LNA monomers in nucleic acid duplexes: directional control and signalling of full complementarity*, P. J. Hrdlicka, B. R. Babu, M. D. Sorensen, J. Wengel, *Chem. Commun.* **2004**, 1478-1479; c) *Functionalized LNA (locked nucleic acid): high-affinity hybridization of oligonucleotides containing N-acylated and N-alkylated 2 '-amino-LNA monomers*, M. D. Sorensen, M. Petersen, J. Wengel, *Chem. Commun.* **2003**, 2130-2131; d) *Base-Modified DNA Labeled by [Ru(bpy)(3)](2+) and [Os(bpy)(3)](2+) Complexes: Construction by Polymerase Incorporation of Modified Nucleoside Triphosphates, Electrochemical and Luminescent Properties, and Applications*, M. Vrabel, P. Horakova, H. Pivonkova, L. Kalachova, H. Cernocka, H. Cahova, R. Pohl, P. Sebest, L. Havran, M. Hocek, M. Fojta, *Chem.--Eur. J.* **2009**, *15*, 1144-1154; e) *DNA-directed synthesis of aniline and 4-aminobiphenyl, oligomers: Programmed transfer of sequence information to a conjoined polymer nanowire*, B. Datta, G. B. Schuster, *J. Am. Chem. Soc.* **2008**, *130*, 2965-2973; f) *Pyrene-zipper array assembled via RNA duplex formation*, M. Nakamura, Y. Murakami, K. Sasa, H. Hayashi, K. Yamana, *J. Am. Chem. Soc.* **2008**, *130*, 6904-+; g) *Porphyrin-DNA: A supramolecular scaffold for functional molecules on the nanometre scale*, I. Bouamaied, L. A. Fendt, D. Haussinger, M. Wiesner, S. Thoni, N. Amiot, E. Stulz, *Nucleosides Nucleotides & Nucleic Acids* **2007**, *26*, 1533-1538; h) *DNA as a supramolecular scaffold for the helical arrangement of a stack of 1-ethynylpyrene chromophores*, J. Barbaric, H. A. Wagenknecht, *Org. Biomol. Chem.* **2006**, *4*, 2088-2090.

[19] *DNA as supramolecular scaffold for porphyrin arrays on the nanometer scale*, L. A. Fendt, I. Bouamaied, S. Thoni, N. Amiot, E. Stulz, *J. Am. Chem. Soc.* **2007**, *129*, 15319-15329.

[20] a) *An extremely stable and orthogonal DNA base pair with a simplified three-carbon backbone*, L. L. Zhang, E. Meggers, *J. Am. Chem. Soc.* **2005**, *127*, 74-75; b) *A simple glycol*

nucleic acid, L. L. Zhang, A. Peritz, E. Meggers, *J. Am. Chem. Soc.* **2005**, *127*, 4174-4175; c) *Synthesis and Properties of the Simplified Nucleic Acid Glycol Nucleic Acid*, E. Meggers, L. Zhang, *Acc. Chem. Res.* **2010**, *43*, 1092-1102.

[21] *Duplex formation of the simplified nucleic acid GNA*, M. Schlegel, A. Peritz, K. Kittigowittana, L. Zhang, E. Meggers, *ChemBioChem* **2007**, *25*, 927-932.

[22] a) *Synthesis of glycol nucleic acids*, L. L. Zhang, A. E. Peritz, P. J. Carroll, E. Meggers, *Synthesis* **2006**, 645-653; b) *Improved Phosphoramidite Building Blocks for the Synthesis of the Simplified Nucleic Acid GNA*, M. K. Schlegel, E. Meggers, *J. Org. Chem.* **2009**, *74*, 4615-4618.

[23] a) *A purine-like nickel(II) base pair for DNA*, C. Switzer, S. Sinha, P. H. Kim, B. D. Heuberger, *Angew. Chem. Int. Ed.* **2005**, *44*, 1529-1532; b) *Efficient incorporation of a copper hydroxypyridone base pair in DNA*, K. Tanaka, A. Tengeiji, T. Kato, N. Toyama, M. Shiro, M. Shionoya, *J. Am. Chem. Soc.* **2002**, *124*, 12494-12498; c) *Metal-mediated base pairing within the simplified nucleic acid GNA*, M. K. Schlegel, L. L. Zhang, N. Pagano, E. Meggers, *Org. Biomol. Chem.* **2009**, *7*, 476-482.

[24] *Duplex structure of a minimal nucleic acid*, M. K. Schlegel, L. O. Essen, E. Meggers, *J. Am. Chem. Soc.* **2008**, *130*, 8158-+.

[25] a) *GLYCOL NUCLEIC ACIDS AS DUPLEX SCAFFOLD FOR THE DESIGN OF SELF-ASSEMBLED AND SELF-ORGANIZED ARCHITECTURES*, H. Zhou, *Thesis* **2012**; b) *Pyrene acetylide nucleotides in GNA: probing duplex formation and sensing of copper(II) ions*, H. Zhou, X. Y. Ma, J. P. Wang, L. L. Zhang, *Org. Biomol. Chem.* **2009**, *7*, 2297-2302.

[26] *Incorporation of porphyrin acetylides into duplexes of the simplified nucleic acid GNA*, L. L. Zhang, H. Zhou, A. T. Johnson, O. Wiest, *Org. Biomol. Chem.* **2011**, *9*, 2840-2849.

[27] *On protein synthesis*, F. H. Crick, *Symp. Soc. Exp. Biol.* **1958**, *12*, 138-163.

[28] *Small Molecule DNA And RNA Binders From Synthesis To Nucleic Acid Complexes*, M. Demeunynck, C. Bailly, W. D. Wilson, **2002**.

[29] *Chelating agents and metal chelates*, F. P. J. Dwyer, D. P. Mellor, *Academic Press, New York* **1964**.

[30] *Metallointercalation Reagents - 2-Hydroxyethanethiolato(2,2',2''-Terpyridine)-Platinum(Ii) Monocation Binds Strongly to DNA by Intercalation*, K. W. Jennette, S. J. Lippard, Vassilia.Ga, W. R. Bauer, *Proc. Natl. Acad. Sci. U. S. A.* **1974**, *71*, 3839-3843.

[31] *Metal Ions in Biological Systems*, B. Nordén, P. Lincoln, B. Akerman, E. Tuite, *Marcel Dekker, New York, NY* **1996**, *33*, 177.

[32] *Probing Nucleic-Acids with Transition-Metal Complexes*, A. M. Pyle, J. K. Barton, *Prog. Inorg. Chem.* **1990**, *38*, 413-475.

[33] *Structure, Recognition, and Processing of Cisplatin-DNA Adducts*, E. R. Jamieson, S. J. Lippard, *Chem. Rev.* **1999**, *99*, 2467-2498.

[34] *Metallo-intercalators and metallo-insertors*, B. M. Zeglis, V. C. Pierre, J. K. Barton, *Chem. Commun.* **2007**, 4565-4579.

[35] *Binding of Platinum(Ii) Intercalation Reagents to Deoxyribonucleic-Acid - Dependence on Base-Pair Composition, Nature of the Intercalator, and Ionic-Strength*, M. Howegrant, S. J. Lippard, *Biochemistry* **1979**, *18*, 5762-5769.

[36] *Molecular-Structure of a Double Helical DNA Fragment Intercalator Complex between Deoxy Cpg and a Terpyridine Platinum Compound,* A. H. J. Wang, J. Nathans, G. Vandermarel, J. H. Vanboom, A. Rich, *Nature* **1978**, *276*, 471-474.

[37] a) *The DNA and RNA specificity of eilatin Ru(II) complexes as compared to eilatin and ethidium bromide,* N. W. Luedtke, J. S. Hwang, E. Nava, D. Gut, M. Kol, Y. Tor, *Nucleic Acids Res.* **2003**, *31*, 5732-5740; b) *Photo-reduction of polyazaaromatic Ru(II) complexes by biomolecules and possible applications,* B. Elias, A. Kirsch-De Mesmaeker, *Coord. Chem. Rev.* **2006**, *250*, 1627-1641.

[38] *Ru(phen)(2)dppz(2+) luminescence: Dependence on DNA sequences and groove-binding agents,* R. E. Holmlin, E. D. A. Stemp, J. K. Barton, *Inorg. Chem.* **1998**, *37*, 29-34.

[39] *Dipyridophenazine complexes of cobalt(III) and nickel(II): DNA-Binding and photocleavage studies,* S. Arounaguiri, B. G. Maiya, *Inorg. Chem.* **1996**, *35*, 4267-4270.

[40] *A New Class of DNA Metallobinders Showing Spectator Ligand Size-Selectivity - Binding of Ligand-Bridged Bimetallic Complexes of Ru(Ii) to Calf Thymus DNA,* D. L. Carlson, D. H. Huchital, E. J. Mantilla, R. D. Sheardy, W. R. Murphy, *J. Am. Chem. Soc.* **1993**, *115*, 6424-6425.

[41] *Recognition and reaction of metallointercalators with DNA,* K. E. Erkkila, D. T. Odom, J. K. Barton, *Chem. Rev.* **1999**, *99*, 2777-2795.

[42] a) *Novel Dipyridophenazine Complexes of Ruthenium(Ii) - Exploring Luminescent Reporters of DNA,* R. M. Hartshorn, J. K. Barton, *J. Am. Chem. Soc.* **1992**, *114*, 5919-5925; b) *Molecular Light Switch for DNA - Ru(Bpy)2(Dppz)2+,* A. E. Friedman, J. C. Chambron, J. P. Sauvage, N. J. Turro, J. K. Barton, *J. Am. Chem. Soc.* **1990**, *112*, 4960-4962; c) *Characterization of Dipyridophenazine Complexes of Ruthenium(Ii) - the Light Switch Effect as a Function of Nucleic-Acid Sequence and Conformation,* Y. Jenkins, A. E. Friedman, N. J. Turro, J. K. Barton, *Biochemistry* **1992**, *31*, 10809-10816; d) *Photophysical evidence that Delta- and Lambda-[Ru(phen)(2)(dppz)](2+) intercalate DNA from the minor groove,* E. Tuite, P. Lincoln, B. Norden, *J. Am. Chem. Soc.* **1997**, *119*, 239-240; e) *DNA-Binding of Delta-[Ru(Phen)2dppz]2+ and Lambda-[Ru(Phen)2dppz]2+,* C. Hiort, P. Lincoln, B. Norden, *J. Am. Chem. Soc.* **1993**, *115*, 3448-3454.

[43] *H-1-Nmr Studies of Tris(Phenanthroline) Metal-Complexes Bound to Oligonucleotides - Structural Characterizations Via Selective Paramagnetic Relaxation,* J. P. Rehmann, J. K. Barton, *Biochemistry* **1990**, *29*, 1710-1717.

[44] *Crystal structures of Lambda- Ru(phen)(2)dppz (2+) with oligonucleotides containing TA/TA and AT/AT steps show two intercalation modes,* H. Niyazi, J. P. Hall, K. O'Sullivan, G. Winter, T. Sorensen, J. M. Kelly, C. J. Cardin, *Nature Chemistry* **2012**, *4*, 621-628.

[45] *Targeted Chemical Nucleases,* D. S. Sigman, T. W. Bruice, A. Mazumder, C. L. Sutton, *Acc. Chem. Res.* **1993**, *26*, 98-104.

[46] a) *Enantiomeric Selectivity in Binding Tris(Phenanthroline)Zinc(Ii) to DNA,* J. K. Barton, J. J. Dannenberg, A. L. Raphael, *J. Am. Chem. Soc.* **1982**, *104*, 4967-4969; b) *Tris(Phenanthroline)Ruthenium(Ii) - Stereoselectivity in Binding to DNA,* J. K. Barton, A. T. Danishefsky, J. M. Goldberg, *J. Am. Chem. Soc.* **1984**, *106*, 2172-2176; c) *Photophysics of Ruthenium Complexes Bound to Double Helical DNA,* C. V. Kumar, J. K. Barton, N. J. Turro, *J. Am. Chem. Soc.* **1985**, *107*, 5518-5523; d) *Binding Modes and Base Specificity of*

Tris(Phenanthroline)Ruthenium(Ii) Enantiomers with Nucleic-Acids - Tuning the Stereoselectivity, J. K. Barton, J. M. Goldberg, C. V. Kumar, N. J. Turro, *J. Am. Chem. Soc.* **1986**, *108*, 2081-2088; e) *Site-Specific Cleavage of Left-Handed DNA in Pbr322 by Lambda-Tris(Diphenylphenanthroline)Cobalt(Iii)*, J. K. Barton, A. L. Raphael, *Proc. Natl. Acad. Sci. U. S. A.* **1985**, *82*, 6460-6464.

[47] *Chiral Probes for the Handedness of DNA Helices - Enantiomers of Tris(4,7-Diphenylphenanthroline)Ruthenium(Ii)*, J. K. Barton, L. A. Basile, A. Danishefsky, A. Alexandrescu, *Proceedings of the National Academy of Sciences of the United States of America-Biological Sciences* **1984**, *81*, 1961-1965.

[48] *Chiral Probe for a-Form Helices of DNA and Rna - Tris(Tetramethylphenanthroline)Ruthenium(Ii)*, H. Y. Mei, J. K. Barton, *J. Am. Chem. Soc.* **1986**, *108*, 7414-7416.

[49] a) *Recognition of DNA base mismatches by a rhodium intercalator*, B. A. Jackson, J. K. Barton, *J. Am. Chem. Soc.* **1997**, *119*, 12986-12987; b) *A versatile mismatch recognition agent: Specific cleavage of a plasmid DNA at a single base mispair*, B. A. Jackson, V. Y. Alekseyev, J. K. Barton, *Biochemistry* **1999**, *38*, 4655-4662; c) *DNA base mismatch detection with bulky rhodium intercalators: synthesis and applications*, B. M. Zeglis, J. K. Barton, *Nat. Protoc.* **2007**, *2*, 357-371.

[50] a) *Four-stranded nucleic acids: structure, function and targeting of G-quadruplexes*, J. L. Huppert, *Chem. Soc. Rev.* **2008**, *37*, 1375-1384; b) *G-quadruplex DNA structures - Variations on a theme*, T. Simonsson, *Biol. Chem.* **2001**, *382*, 621-628; c) *Methods for investigating G-quadruplex DNA/ligand interactions*, P. Murat, Y. Singh, E. Defrancq, *Chem. Soc. Rev.* **2011**, *40*, 5293-5307.

[51] *Crystal structure of parallel quadruplexes from human telomeric DNA*, G. N. Parkinson, M. P. H. Lee, S. Neidle, *Nature* **2002**, *417*, 876-880.

[52] *Quantitative visualization of DNA G-quadruplex structures in human cells*, G. Biffi, D. Tannahill, J. McCafferty, S. Balasubramanian, *Nature Chemistry* **2013**.

[53] *Targeting G-quadruplexes in gene promoters: a novel anticancer strategy?*, S. Balasubramanian, L. H. Hurley, S. Neidle, *Nat. Rev. Drug Discovery* **2011**, *10*, 261-275.

[54] *Erosion of the telomeric single-strand overhang at replicative senescence*, S. A. Stewart, I. Ben-Porath, V. J. Carey, B. F. O'Connor, W. C. Hahn, R. A. Weinberg, *Nat. Genet.* **2003**, *33*, 492-496.

[55] *Telomerase: a potential therapeutic target for cancer*, T. M. Fletcher, *Expert Opinion on Therapeutic Targets* **2005**, *9*, 457-469.

[56] a) *Inhibition of Telomerase by G-Quartet DNA Structures*, A. M. Zahler, J. R. Williamson, T. R. Cech, D. M. Prescott, *Nature* **1991**, *350*, 718-720; b) *Long G tails at both ends of human chromosomes suggest a C strand degradation mechanism for telomere shortening*, V. L. Makarov, Y. Hirose, J. P. Langmore, *Cell* **1997**, *88*, 657-666; c) *Telomeres and telomerase as targets for anticancer drug development*, K. A. Olaussen, K. Dubrana, J. Dornont, J. P. Spano, L. Sabatier, J. C. Soria, *Crit. Rev. Oncol./Hematol* **2006**, *57*, 191-214.

[57] *Structure of a G-quadruplex-ligand complex*, S. M. Haider, G. N. Parkinson, S. Neidle, *J. Mol. Biol.* **2003**, *326*, 117-125.

[58] *Selective interactions of cationic porphyrins with G-quadruplex structures*, H. Y. Han, D. R. Langley, A. Rangan, L. H. Hurley, *J. Am. Chem. Soc.* **2001**, *123*, 8902-8913.

[59] a) *Telomestatin, a potent telomerase inhibitor that interacts quite specifically with the human telomeric intramolecular G-quadruplex*, M. Y. Kim, H. Vankayalapati, S. Kazuo, K. Wierzba, L. H. Hurley, *J. Am. Chem. Soc.* **2002**, *124*, 2098-2099; b) *Stabilization of G-quadruplex DNA by highly selective ligands via click chemistry*, A. D. Moorhouse, A. M. Santos, M. Gunaratnam, M. Moore, S. Neidle, J. E. Moses, *J. Am. Chem. Soc.* **2006**, *128*, 15972-15973.

[60] *Structural and thermodynamic studies of the interaction of distamycin a with the parallel quadruplex structure [d(TGGGGT)](4)*, L. Martino, A. Virno, B. Pagano, A. Virgilio, S. Di Micco, A. Galeone, C. Giancola, G. Bifulco, L. Mayol, A. Randazzo, *J. Am. Chem. Soc.* **2007**, *129*, 16048-16056.

[61] *Interaction of Metal Complexes with G-Quadruplex DNA*, S. N. Georgiades, N. H. Abd Karim, K. Suntharalingam, R. Vilar, *Angew. Chem. Int. Ed.* **2010**, *49*, 4020-4034.

[62] *Ligand-driven G-quadruplex conformational switching by using an unusual mode of interaction*, R. Rodriguez, G. D. Pantos, D. P. N. Goncalves, J. K. M. Sanders, S. Balasubramanian, *Angew. Chem. Int. Ed.* **2007**, *46*, 5405-5407.

[63] *iFRET: an improved fluorescence system for DNA-melting analysis*, W. M. Howell, M. Jobs, A. J. Brookes, *Genome Res.* **2002**, *12*, 1401-1407.

[64] *Telomerase inhibitors based on quadruplex ligands selected by a fluorescence assay*, J. L. Mergny, L. Lacroix, M. P. Teulade-Fichou, C. Hounsou, L. Guittat, M. Hoarau, P. B. Arimondo, J. P. Vigneron, J. M. Lehn, J. F. Riou, T. Garestier, C. Helene, *Proc. Natl. Acad. Sci. U. S. A.* **2001**, *98*, 3062-3067.

[65] *H-1-Nmr of Rh(Nh3)(4)Phi(3+) Bound to D(Tggcca)(2) - Classical Intercalation by a Nonclassical Octahedral Metallointercalator*, J. G. Collins, T. P. Shields, J. K. Barton, *J. Am. Chem. Soc.* **1994**, *116*, 9840-9846.

[66] *NMR-based model of a telomerase-inhibiting compound bound to G-quadruplex DNA*, O. Y. Fedoroff, M. Salazar, H. Y. Han, V. V. Chemeris, S. M. Kerwin, L. H. Hurley, *Biochemistry* **1998**, *37*, 12367-12374.

[67] *Crystal structure of Delta-[Ru(bpy)(2)dppz](2+) bound to mismatched DNA reveals side-by-side metalloinsertion and intercalation*, H. Song, J. T. Kaiser, J. K. Barton, *Nature Chemistry* **2012**, *4*, 615-620.

[68] *Advances in the analysis of isothermal titration calorimetry data for ligand-DNA interactions*, N. J. Buurma, I. Haq, *Methods* **2007**, *42*, 162-172.

[69] *REACTIVITY OF PENTACOORDINATE AND HEXACOORDINATE SILICON-COMPOUNDS AND THEIR ROLE AS REACTION INTERMEDIATES*, C. Chuit, R. J. P. Corriu, C. Reye, J. C. Young, *Chem. Rev.* **1993**, *93*, 1371-1448.

[70] *Organofluorosilicates in Organic-Synthesis .12. Preparation of Organopentafluorosilicates and Their Cleavage Reactions by Halogens and N-Bromosuccinimide - Synthetic and Mechanistic Aspects*, K. Tamao, J. Yoshida, H. Yamamoto, T. Kakui, H. Matsumoto, M. Takahashi, A. Kurita, M. Murata, M. Kumada, *Organometallics* **1982**, *1*, 355-368.

[71] *Addition-Compounds of Methylhalogenosilanes and Pyridine at Low-Temperatures*, K. Hensen, R. Busch, *Zeitschrift Fur Naturforschung Section B-a Journal of Chemical Sciences* **1982**, *37*, 1174-1177.

[72] *Acceptor Properties of Silicon(4) . Class (B) or Soft Acid Behaviour by Silicon Tetrachloride and Silicon Tetrabromide,* I. R. Beattie, G. A. Ozin, *J. Chem. SOC. (A)* **1969**, 2267-2269.

[73] a) *Reaktionen der Siliciumtetrahalogenide mit 2,2'-Dipyridyl und mit 1,10-Phenanthrolin,* U. Wannagat, K. Hensen, P. Petesch, F. Vielberg, *Monatsh. Chem.* **1967**, *98*, 1415-1422; b) *Einige Neuere Ergebnisse Und Probleme Aus Der Chemie Der Silicum-Organischen Verbindungen,* U. Wannagat, *Angew. Chem. Int. Ed.* **1957**, *69*, 516-516.

[74] a) *Beiträge zur Chemie der Halogensilan-Addukte, X. Bis(2,2'-bipyridin)-Komplexe des Siliciums Direktsynthese, Struktur und Eigenschaften,* D. Kummer, K.-E. Gaißer, T. Seshadri, *Chem. Ber.* **1977**, *110*, 1950-1962; b) *Beiträge zur Chemie der Halogensilan-Addukte, XI. Bis(1,10-phenanthrolin)-Komplexe des Siliciums. Darstellung, Struktur und Eigenschaften,* D. Kummer, T. Seshadri, *Chem. Ber.* **1977**, *110*, 2355-2367.

[75] *Beiträge zur Chemie der Halogensilan- Addukte. V. [Si bipy3]Br4, ein neuer ionischer Tris-2,2-Bipyridin-Komplex des Siliciums,* D. Kummer, H. Köster, *anorg. allg. chem.* **1973**, *402*, 297-304.

[76] a) *Electrochemical and spectral properties of hexacoordinate polypyridyl silicon complexes,* B. Suthar, A. Aldongarov, I. S. Irgibaeva, M. Moazzen, B. T. Donovan-Merkert, J. W. Merkert, T. A. Schmedake, *Polyhedron* **2012**, *31*, 754-758; b) *Beiträge zur Chemie der Halogensilan-Addukte. XIV. Neutralligand-Komplexe des Siliciums mit sechs N-Donoratomen,* D. Kummer, K. E. Gaisser, J. Seifert, R. Wagner, *anorg. allg. chem.* **1979**, *459*, 145-156.

[77] *Silicon(4) Compounds Containing 1,3-Diketo Ligands,* R. M. Pike, R. R. Luongo, *J. Am. Chem. Soc.* **1966**, *88*, 2972-&.

[78] *Silicon and Organosilicon Derivatives of Acetylacetone,* R. West, *J. Am. Chem. Soc.* **1958**, *80*, 3246-3249.

[79] *The E. coli Siderophores Enterobactin and Salmochelin Form Six-Coordinate Silicon Complexes at Physiological pH,* T. Schmiederer, S. Rausch, M. Valdebenito, Y. Mantri, E. Mosker, T. Baramov, K. Stelmaszyk, P. Schmieder, D. Butz, S. I. Muller, K. Schneider, M. H. Baik, K. Hantke, R. D. Sussmuth, *Angew. Chem. Int. Ed.* **2011**, *50*, 4230-4233.

[80] a) *Electrontransfer through DNA and metal-containing DNA,* T. Carell, C. Behrens, J. Gierlich, *Org. Biomol. Chem.* **2003**, *1*, 2221-2228; b) *Spatially-Interactive Biomolecular Networks Organized by Nucleic Acid Nanostructures,* J. L. Fu, M. H. Liu, Y. Liu, H. Yan, *Acc. Chem. Res.* **2012**, *45*, 1215-1226; c) *Functionalized DNA Nanostructures,* O. I. Wilner, I. Willner, *Chem. Rev.* **2012**, *112*, 2528-2556.

[81] *Exploring biologically relevant chemical space with metal complexes,* E. Meggers, *Curr. Opin. Chem. Biol.* **2007**, *11*, 287-292.

[82] a) *Targeting proteins with metal complexes,* E. Meggers, *Chem. Commun.* **2009**, 1001-1010; b) *Supramolecular interactions between functional metal complexes and proteins,* C. L. Davies, E. L. Dux, A. K. Duhme-Klair, *Dalton Trans.* **2009**, 10141-10154.

[83] a) *Comparison of phosphorus and silicon: Hypervalency, stereochemistry, and reactivity,* R. R. Holmes, *Chem. Rev.* **1996**, *96*, 927-950; b) *Novel neutral hexacoordinate benzamidinatosilicon(IV) complexes with SiN3OF2, SiN3OCl2, SiN3OBr2, SiN5O and SiN3O3 skeletons,* K. Junold, C. Burschka, R. Bertermann, R. Tacke, *Dalton Trans.* **2011**, *40*, 9844-9857; c) *Hexacoordinate Silacyclobutane Dichelate Complexes: Structure, Properties, and Ligand Crossover,* S. Yakubovich, B. Gostevskii, I. Kalikhman, M. Botoshansky, L. E.

Gusel'nikov, V. A. Pestunovich, D. Kost, *Organometallics* **2011**, *30*, 405-413; d) *Neutral Lewis Base Adducts of Silicon Tetraazide*, P. Portius, A. C. Filippou, G. Schnakenburg, M. Davis, K. D. Wehrstedt, *Angew. Chem. Int. Ed.* **2010**, *49*, 8013-8016; e) *Neutral Penta- and Hexacoordinate Silicon(IV) Complexes Containing Two Bidentate Ligands Derived from the alpha-Amino Acids (S)-Alanine, (S)-Phenylalanine, and (S)-tert-Leucine*, S. Cota, M. Beyer, R. Bertermann, C. Burschka, K. Gotz, M. Kaupp, R. Tacke, *Chem.--Eur. J.* **2010**, *16*, 6582-6589; f) *Synthesis and Structural Characterization of Neutral Hexacoordinate Silicon(IV) Complexes with SiO2N4 Skeletons*, S. Metz, C. Burschka, R. Tacke, *Chemistry-an Asian Journal* **2009**, *4*, 581-586; g) *Synthesis and structural characterization of neutral higher-coordinate silicon(IV) complexes with tridentate dianionic chelate ligands*, O. Seiler, C. Burschka, S. Metz, M. Penka, R. Tacke, *Chem.--Eur. J.* **2005**, *11*, 7379-7386; h) *Neutral hexacoordinate silicon tris-chelates: Structure and stereodynamics*, I. Kalikhman, V. Kingston, O. Girshberg, D. Kost, *Organometallics* **2001**, *20*, 4713-4720; i) *Synthesis and characterization of new cationic hexacoordinate silanes*, B. K. Kim, S. B. Choi, S. D. Kloos, P. Boudjouk, *Inorg. Chem.* **2000**, *39*, 728-731; j) *Silicon-29 NMR evidence of a transient hexavalent silicon complex in the diatom Navicula pelliculosa*, S. D. Kinrade, A. M. E. Gillson, C. T. G. Knight, *Journal of the Chemical Society-Dalton Transactions* **2002**, 307-309.

[84] *Synthesis and properties of long and branched alkyl chain substituted perylenetetracarboxylic monoanhydride monoimides*, Y. Nagao, T. Naito, Y. Abe, T. Misono, *Dyes Pigm.* **1996**, *32*, 71-83.

[85] *Amide group assisted 3 '-dephosphorylation of oligonucleotides synthesized on universal A-supports*, A. V. Azhayev, M. L. Antopolsky, *Tetrahedron* **2001**, *57*, 4977-4986.

[86] N. Berova, K. Nakanishi, R. W. Woody, *Circular Dichroism: Principles and Applications, Vol. p337*, Wiley-VCH, New York, **2000**.

[87] *Duplex and hairpin dimer structures for perylene diimide-oligonucleotide conjugates*, Y. Zheng, H. Long, G. C. Schatz, F. D. Lewis, *Chem Commun (Camb)* **2005**, 4795-4797.

[88] *Perylene bisimide dyes as versatile building blocks for functional supramolecular architectures*, F. Wurthner, *Chem. Commun.* **2004**, 1564-1579.

[89] *J-Aggregates: From Serendipitous Discovery to Supramolecular Engineering of Functional Dye Materials*, F. Würthner, T. E. Kaiser, C. R. Saha-Möller, *Angew. Chem. Int. Ed.* **2011**, *50*, 3376-3410.

[90] a) *Sulfoximine version of double elimination protocol for synthesis of chiral acetylenic cyclophanes*, A. Orita, D. An, T. Nakano, J. Yaruva, N. C. Ma, J. Otera, *Chem.--Eur. J.* **2002**, *8*, 2005-2010; b) *A rapid access to hydroxylated benz[a]anthraquinones: Hypervalent iodine oxidation of beta-naphthols*, D. Mal, H. N. Roy, N. K. Hazra, S. Adhikari, *Tetrahedron* **1997**, *53*, 2177-2184; c) *Regiospecific synthesis of benzo[b]fluorenones via ring contraction by benzil-benzilic acid rearrangement of benz[a]anthracene-5,6-diones*, A. Patra, S. K. Ghorai, S. R. De, D. Mal, *Synthesis* **2006**, 2556-2562.

[91] a) *Stereochemistry of six-coordinated silicon complexes. 2. Optical resolution of [Si(.alpha.-diimine)3]4+ (.alpha.-diimine = 2,2'-bipyridine, 1,10-phenanthroline)*, Y. Ohmori, M. Namba, Y. Kuroda, M. Kojima, Y. Yoshikawa, *Inorg. Chem.* **1992**, *31*, 2299-2300; b)

Stereochemistry of six-coordinate octahedral silicon(IV) complexes containing 2,2 '-bipyridine, H. L. Liu, Y. Ohmori, M. Kojima, Y. Yoshikawa, *J. Coord. Chem.* **1998**, *44*, 257-268.

[92] *On Demonstrating DNA Intercalation,* E. C. Long, J. K. Barton, *Acc. Chem. Res.* **1990**, *23*, 271-273.

[93] *Molecular Mechanical Simulations on Double Intercalation of 9-Amino Acridine into D(Cgcgcgc).D(Gcgcgcg) - Analysis of the Physical Basis for the Neighbor-Exclusion Principle,* S. N. Rao, P. A. Kollman, *Proc. Natl. Acad. Sci. U. S. A.* **1987**, *84*, 5735-5739.

[94] a) *Interaction of Delta-[Ru(Phen)(2)Dppz](2+) and Lambda-[Ru(Phen)(2)Dppz](2+) with DNA - a Calorimetric and Equilibrium Binding Study,* I. Haq, P. Lincoln, D. C. Suh, B. Norden, B. Z. Chowdhry, J. B. Chaires, *J. Am. Chem. Soc.* **1995**, *117*, 4788-4796; b) *Synthesis and DNA-binding properties of [Ru(NH3)(4)dppz](2+),* R. B. Nair, E. S. Teng, S. L. Kirkland, C. J. Murphy, *Inorg. Chem.* **1998**, *37*, 139-141.

[95] *Reaction of phenanthrene-9,10-dione with phenanthrene-9,10-diol: Synthesis and characterization of the first ortho-quinhydrone derivative,* F. Calderazzo, C. Forte, F. Marchetti, G. Pampaloni, L. Pieretti, *Helv. Chim. Acta* **2004**, *87*, 781-789.

[96] *NMR Chemical Shifts of Trace Impurities: Common Laboratory Solvents, Organics, and Gases in Deuterated Solvents Relevant to the Organometallic Chemist,* G. R. Fulmer, A. J. M. Miller, N. H. Sherden, H. E. Gottlieb, A. Nudelman, B. M. Stoltz, J. E. Bercaw, K. I. Goldberg, *Organometallics* **2010**, *29*, 2176-2179.

[97] *A convenient synthetic route to polyether-tagged cyclam ligands and their nickel derivatives,* F. Bellouard, F. Chuburu, J. J. Yaouanc, H. Handel, Y. Le Mest, *Eur. J. Org. Chem.* **1999**, 3257-3261.

[98] *Untersuchungen zur protonierung von perylen-3, 4, 9, 10-tetracarbonsaurealkalisalzen,* T. Helmat, *Dyes Pigm.* **1983**, *4*, 171-177.

[99] *An application of the stille coupling for the preparation of arylated phthalonitriles and phthalocyanines,* H. Grennberg, V. Aranyos, A. M. Castano, *Acta Chem. Scand.* **1999**, *53*, 714-720.

[100] *Metallophthalocyanines: Versatile electron-donating building blocks for fullerene dyads,* D. M. Guldi, I. Zilbermann, A. Gouloumis, P. Vazquez, T. Torres, *J. Phys. Chem. B* **2004**, *108*, 18485-18494.

[101] *An Improved Procedure for Derivatization of Controlled-Pore Glass-Beads for Solid-Phase Oligonucleotide Synthesis,* M. J. Damha, P. A. Giannaris, S. V. Zabarylo, *Nucleic Acids Res.* **1990**, *18*, 3813-3821.

6.2 List of synthesized compounds

N°	Corresponding Compound	N°	Corresponding Compound
1	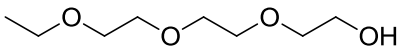 **18**	2	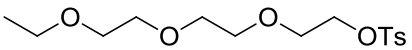 **19**
3	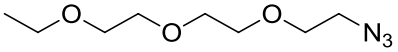 **20**	4	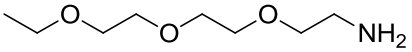 **21**
5	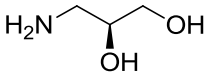 **22**	6	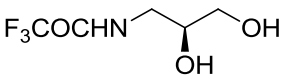 **23**
7	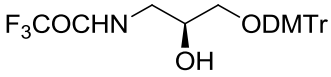 **24**	8	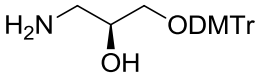 **25**
9	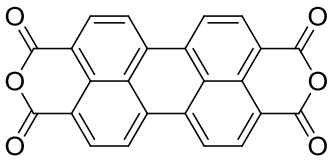 **26**	10	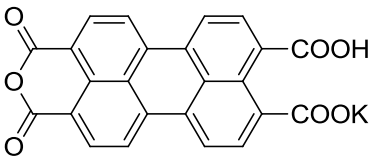 **27**
11	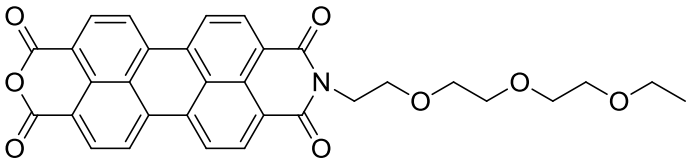 **28**		
12	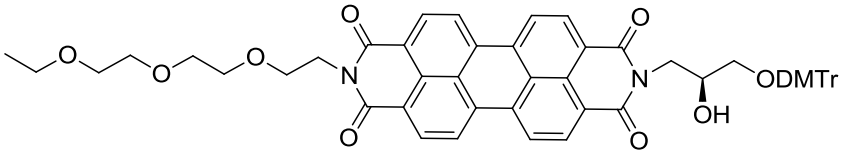 **29**		
13	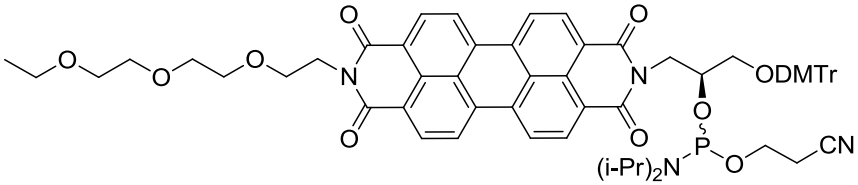 **16**		

N°	Corresponding Compound	N°	Corresponding Compound
14	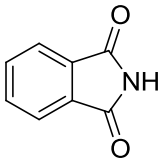 **30**	15	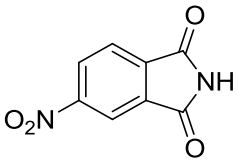 **31**
16	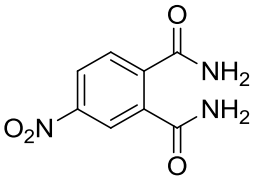 **32**	17	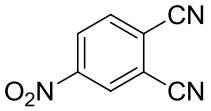 **33**
18	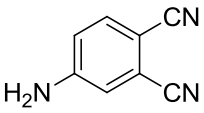 **34**	19	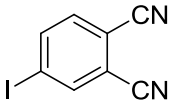 **35**
20	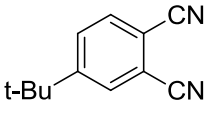 **36**	21	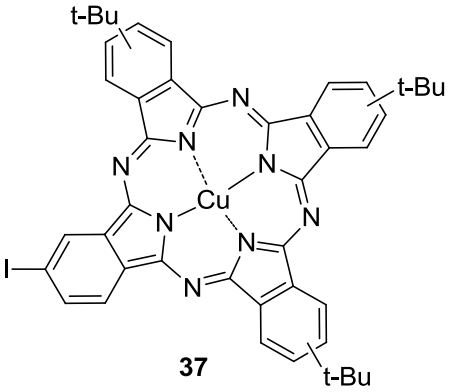 **37**
22	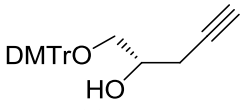 **38**	23	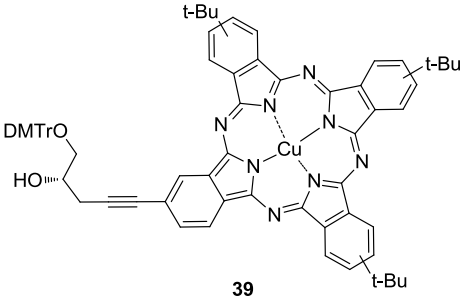 **39**
24	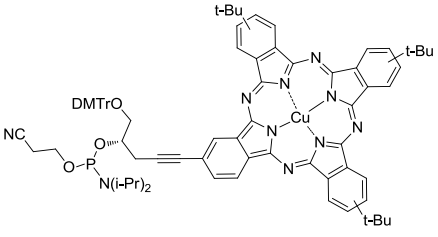 **17**		

N°	Corresponding Compound	N°	Corresponding Compound
25	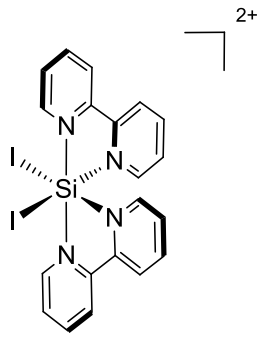 **40**	26	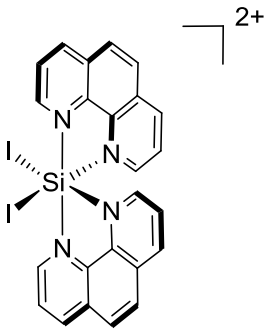 **41**
27	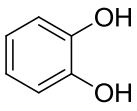 **52**	28	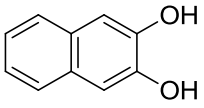 **53**
29	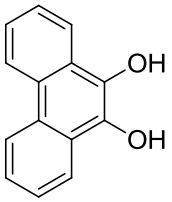 **54**	30	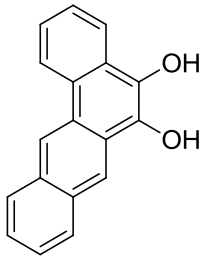 **55**
31	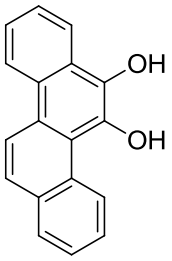 **56**	32	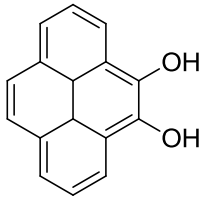 **57**
33	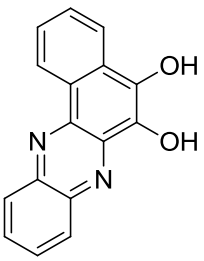 **58**	34	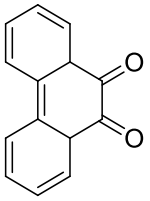 **59**

N°	Corresponding Compound	N°	Corresponding Compound
35	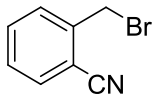 **60**	36	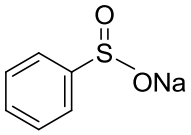 **61**
37	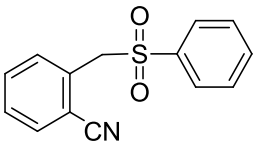 **62**	38	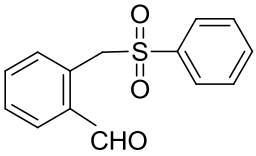 **63**
39	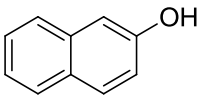 **64**	40	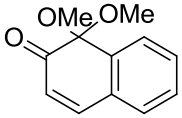 **65**
41	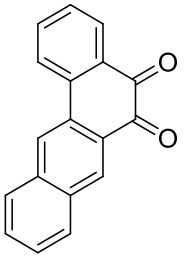 **66**	42	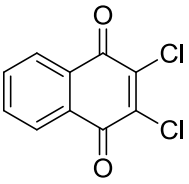 **67**
43	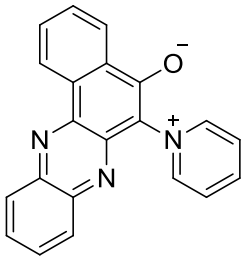 **68**	44	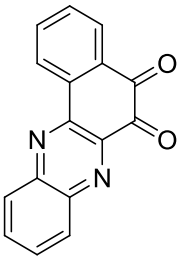 **69**

N°	Corresponding Compound	N°	Corresponding Compound
45	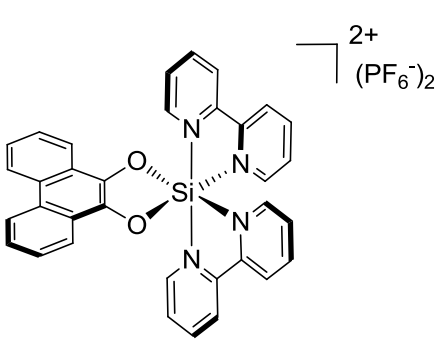 **42**	46	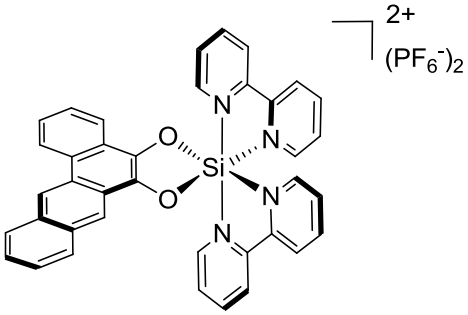 **43**
47	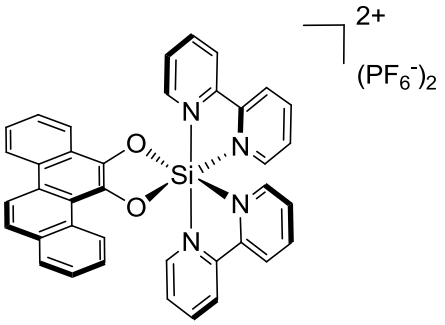 **44**	48	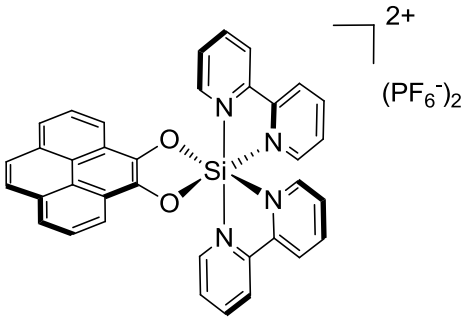 **45**
49	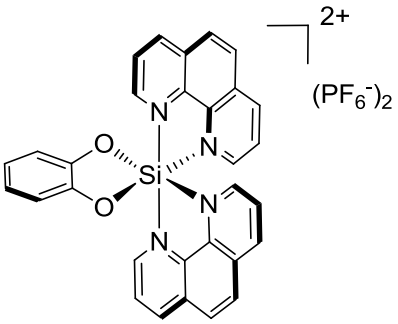 **46**	50	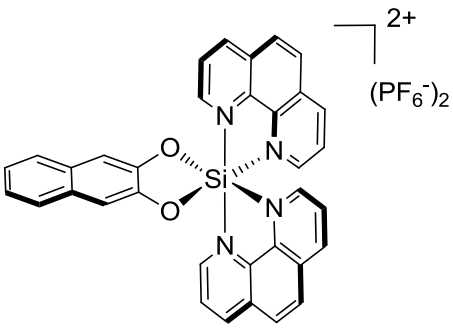 **47**
51	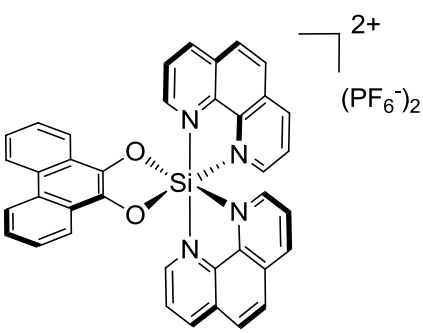 **48**	52	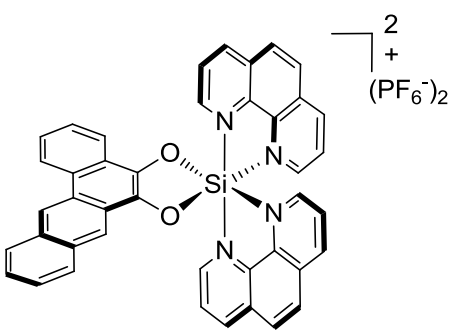 **49**

N°	Corresponding Compound	N°	Corresponding Compound
53	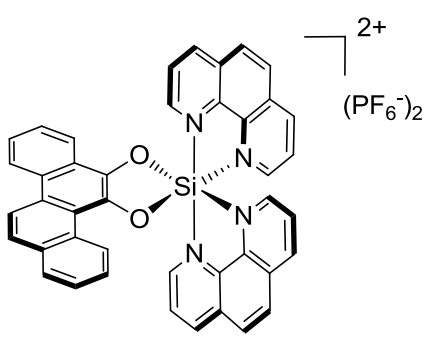 **50**	54	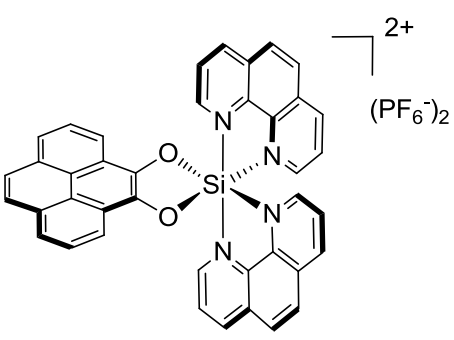 **51**
55	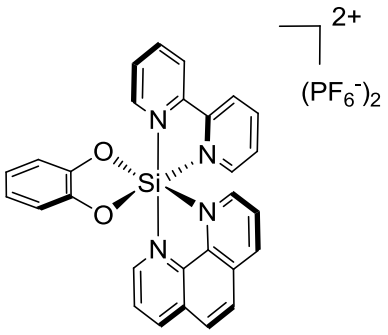 **70**	56	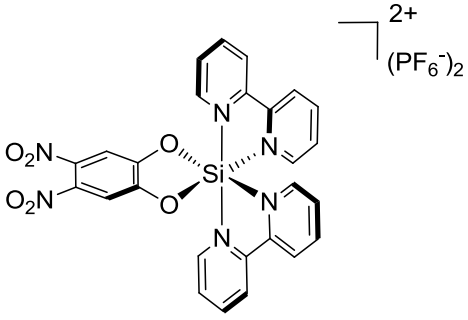 **71**
57	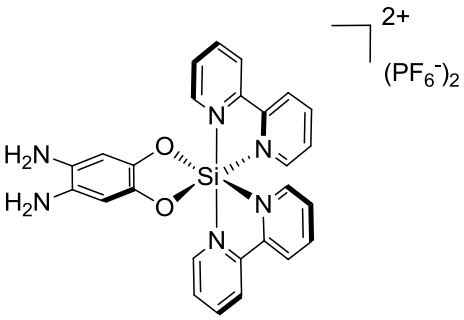 **72**	58	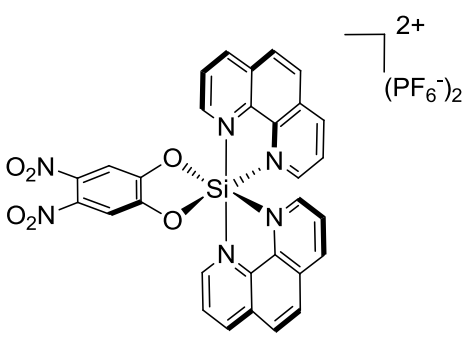 **73**
59	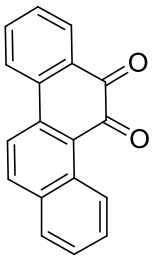 **75**	60	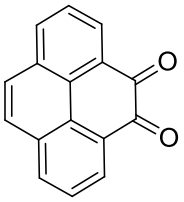 **76**

N°	Corresponding Compound	N°	Corresponding Compound
61	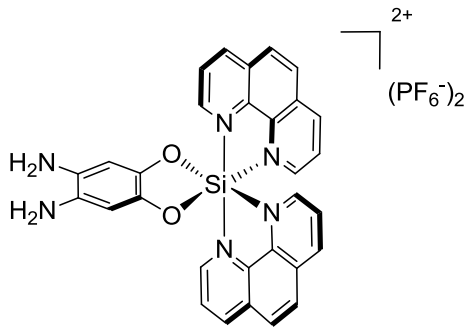 **74**	62	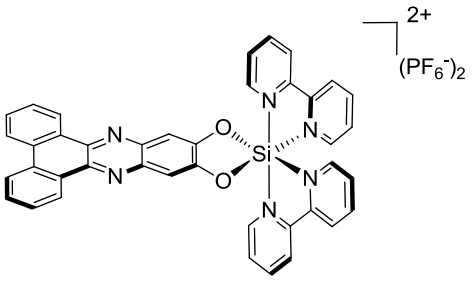 **77**
63	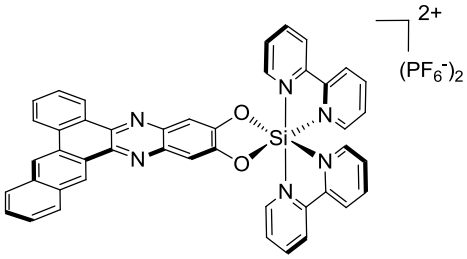 **78**	64	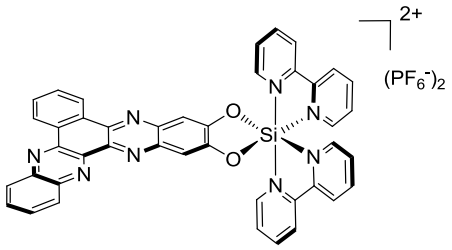 **79**
65	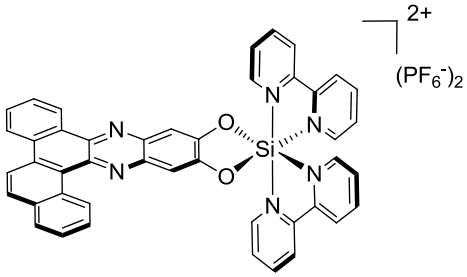 **80**	66	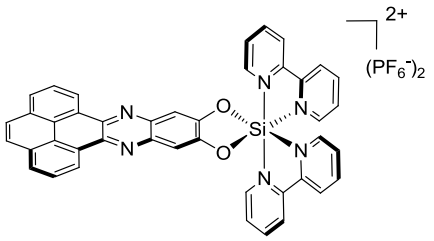 **81**
67	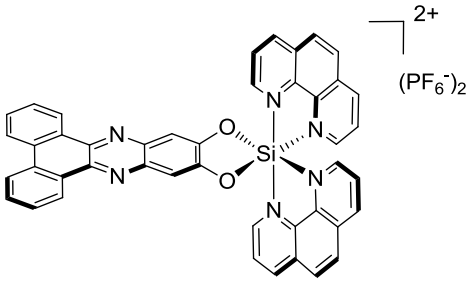 **82**	68	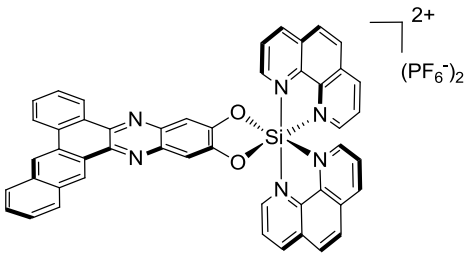 **83**

N°	Corresponding Compound	N°	Corresponding Compound
69	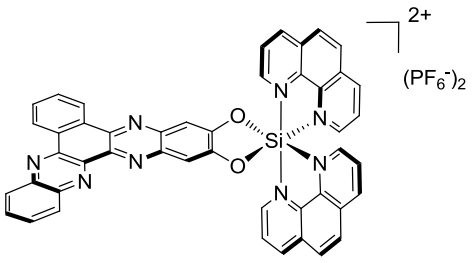 **84**	70	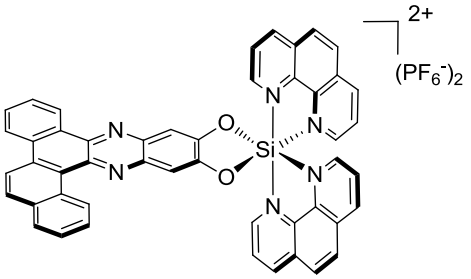 **85**
71	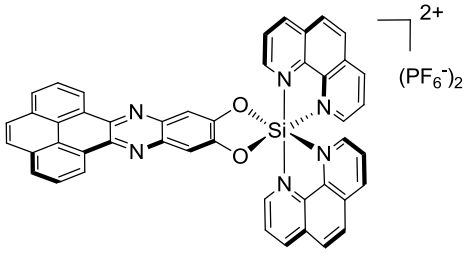 **86**	72	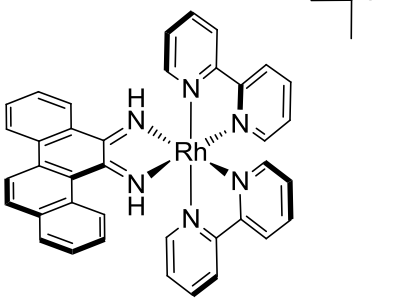 **87**
73	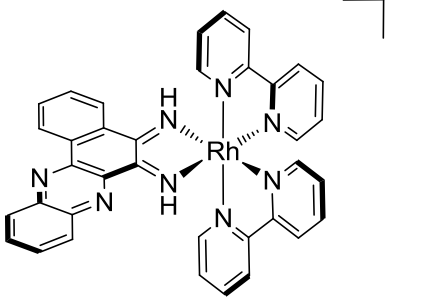 **88**		

6.3 Abbreviations and Symbols

A	adenosine
ACN	acetonitrile
AcOH	acetic acid
aq	aqueous
Ar	aromatic
bipy	2,2 ´-bipyridine
bp	base pair
br	broad
C	cytosine
Calcd	calculated
CD	circular dichroism
$CDCl_3$	deuterated chloroform
conc	concentrated
chrysi	5,6-chrysene quinone diimine
CPG	controlled porous glass
d	doublet
dA	2′-deoxyadenpsine
dc	2′-deoxycytosine
DCA	Dichloroacetic acid
DCE	1,2-dichloroethane
DCM	dichloromethane
DDQ	2,3-dichloro-5,6-dicyanobenzoquinone
dG	2′-deoxyguanosine
DIP	4,7-diphenyl-1,10-phenanthroline
DIPEA	*N*,*N*-Diisopropylethylamine
DMAP	4-dimethylaminopyridine
DMEA	*N*,*N*′-Dimethyl-1,2-ethanediamine

DMF	*N*,*N*-dimethylformamide
DMTr	4,4′-dimethoxytrityl
DMSO	dimethyl sulfoxide
DNA	deoxyribonucleic acid
dppz	dipyrido[3,2-a:2',3'-c]phenazine
DSSC	dye sensitised solar cell
EC-CD	exciton coupling
EDTA	ethylenediaminetetraacetate acid
en	ethanediamine
eq	equivalent
ESI	electrospray ionization
EtOH	ethanol
FRET	Fluorescence resonance energy transfer
G	guanosine
GNA	glycol nucleic acid
GQ	guanosine quadruplex
h	hour(s)
HAT	1,4,5,8,12-hexaazaphenylene
HET	2-hydroxyethanethiolate
HPLC	high performance liquid chromatography
HRMS	high resolution mass spectrometry
IR	infra-red spectroscopy
ITC	isothermal titration calorimetry
L	liters
LNA	locked nucleic acid
LRMS	low resolution mass spectrometry
m	multiplet
M	mol/L
MALDI	matrix assisted laser desorption ionization

MeOH	methanol
min	minute
mL	milliliters
MLCT	metal-to-ligand charge transfer
mmol	millimole
MMR	complex mismatch repair
NBS	*N*-bromosuccinimide
NMR	nuclear magnetic resonance
ON	oligodeoxynucleotide
PAGE	poluacryamide gel electrophoresis
PBI	perylene bisimide
Ph	phenyl
Phi	9,10-phenanthrenequinone diimine
Phen	1,10-phenantroline
PHETA	1,10-phenanthrolino[5,6-*b*]1,4,5,8,12-hexaazaphenylene
phzi	benzo[a]phenazine-5,6-quinone diimine
PIPER	*N*,*N*′-bis-(2-(dimethylamino)ethyl)-3,4,9,10-perylenetetracarboxylic acid diimide
ppm	parts per million
R_f	retention factor

6.4 Appendix

Crystal structure data:

The 9,10-phenanthrenediolate complex **42** was crystallized from a MeCN solution layered with Et_2O.

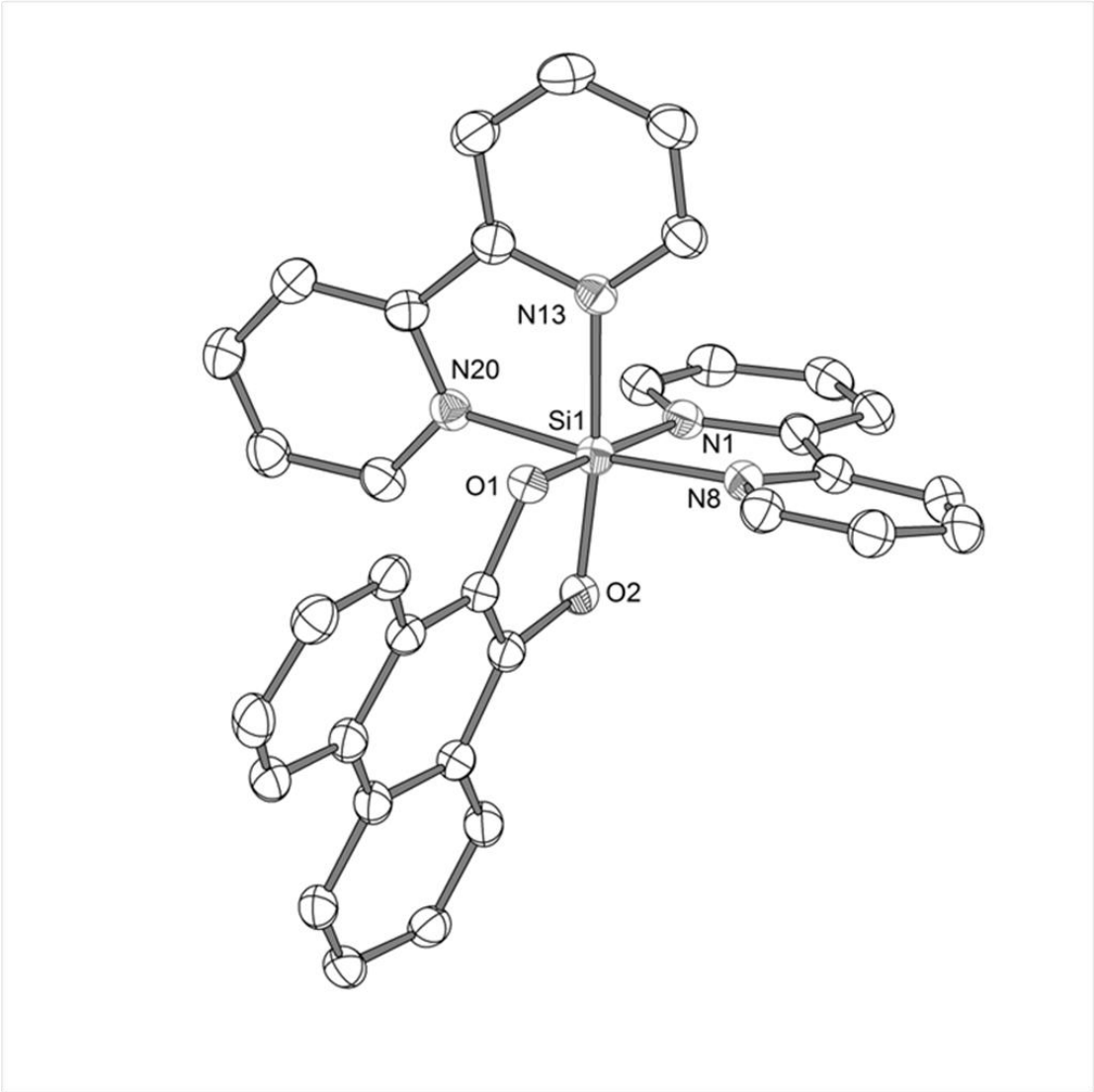

Figure 88 Crystal structure of silicon complex **42**. ORTEP representation with 50% thermal ellipsoids. Two hexafluorophosphate counterions and three acetonitrile solvent molecules are omitted for clarity.

Dr. Klaus Harms

Chemistry Department
University of Marburg

Crystal data and structure refinement for.**42**

Crystal data	
Identification code	**42**
Habitus, colour	block, red
Crystal size	$0.21 \times 0.20 \times 0.13$ mm^3
Crystal system	Monoclinic
Space group	P 2_1/n
Z	4
Unit cell dimensions	a = 10.2585(4) Å b = 26.0773(14) Å c = 13.2293(5) Å α= 90°. β= 111.273(3)° γ= 90°
Volume	3297.9(3) Å^3
Cell determination	12151 peaks with Theta 1.6 to 27.1 °.
Empirical formula	C_{34} H_{24} F_{12} N_4 O_2 P_2 Si
Formula weight	838.6
Density (calculated)	1.689 Mg/m^3
Absorption coefficient	0.279 mm^{-1}
F(000)	1696
Data collection:	
Diffractometer type	STOE IPDS 2
Wavelength	0.71073 Å
Temperature	100(2) K
Theta range for data collection	1.56 to 26.75 °.
Index ranges	-12<=h<=12, -32<=k<=32, -16<=l<=16
Data collection software	STOE X-AREA
Cell refinement software	STOE X-AREA
Data reduction software	STOE X-RED
Solution and refinement:	
Reflections collected	28836
Independent reflections	6969 [R(int) = 0.0689]
Completeness to theta = 26.75 °	99.50%
Observed reflections	3913[I>2sigma(I)]
Reflections used for refinement	6969
Absorption correction	Integration
Max. and min. transmission	0.9698 and 0.9410
Largest diff. peak and hole	0.272 and -0.259 e.Å^{-3}

Solution	Direct methods
Refinement	Full-matrix least-squares on F^2
Treatment of hydrogen atoms	Calculated positions, riding model
Programs used	SIR-2008 SHELXL-97 (Sheldrick, 2008) DIAMOND 3.2h STOE XAREA software
Data / restraints / parameters	6969 / 0 / 496
Goodness-of-fit on F2	0.755
R index (all data)	$wR_2 = 0.0696$
R index conventional [I>2sigma(I)]	$R_1 = 0.0334$

Crystal Structure of Silicon Complex 48

The 9,10-phenanthrenediolate complex **48** was crystallized from a MeCN solution layered with Et_2O.

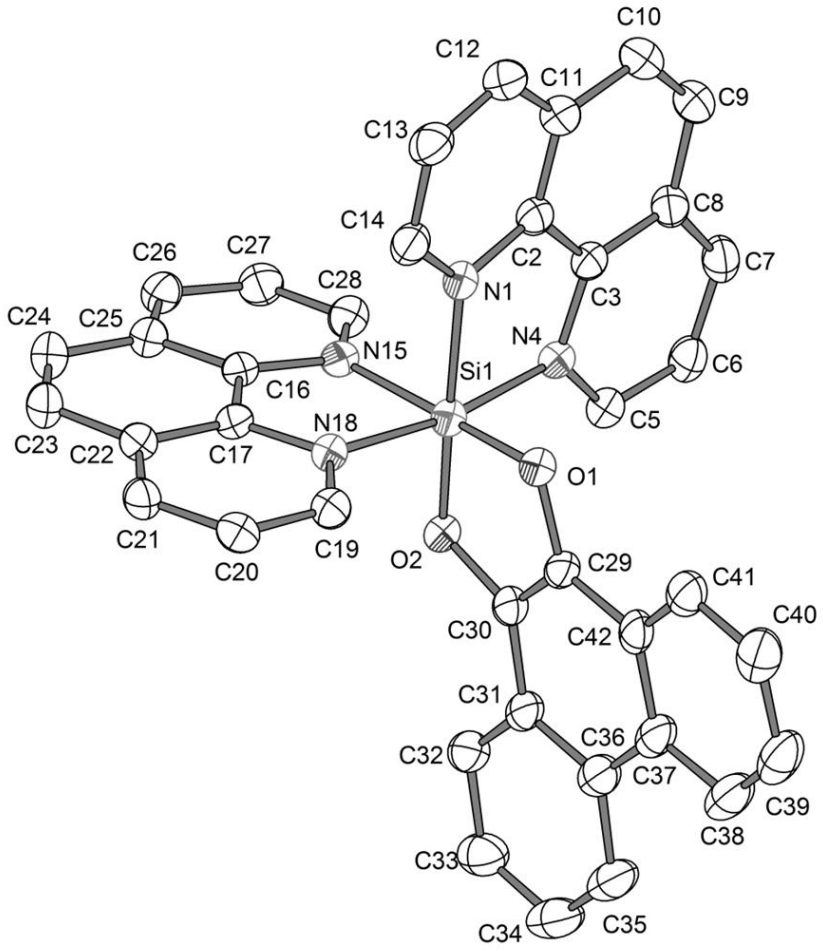

Figure 89 Crystal structure of silicon complex **48**. ORTEP representation with 50% thermal ellipsoids. Two hexafluorophosphate counterions and three acetonitrile solvent molecules are omitted for clarity

Dr. Klaus Harms
Chemistry Department
University of Marburg

Crystal data and structure refinement for **48**.

Crystal data	
Identification code	**48**
Habitus, colour	block, red
Crystal size	0.38 × 0.20 × 0.09 mm^3
Crystal system	Monoclinic
Space group	P 2_1/c
Z	4
Unit cell dimensions	a = 10.9077(5) Å
	b = 28.9688(9) Å
	c = 14.5670(6) Å
	α= 90°
	β=109.451(3)°
	γ = 90°
Volume	4340.2(3) $Å^3$
Cell determination	16075 peaks with Theta 1.4 to 27.0 °.
Empirical formula	C_{44} H_{33} F_{12} N_7 O_2 P_2 Si
Formula weight	1009.8
Density (calculated)	1.545 Mg/m^3
Absorption coefficient	0.228 mm^{-1}
F(000)	2056
Data collection:	
Diffractometer type	STOE IPDS 2
Wavelength	0.71073 Å
Temperature	100(2) K
Theta range for data collection	1.41 to 25.25 °.
Index ranges	-13<=h<=13, -32<=k<=34, -17<=l<=17
Data collection software	STOE X-AREA
Cell refinement software	STOE X-AREA
Data reduction software	STOE X-RED
Solution and refinement:	
Reflections collected	24134
Independent reflections	7731 [R(int) = 0.0326]
Completeness to theta = 25.25 °	98.70%
Observed reflections	4516[I>2sigma(I)]
Reflections used for refinement	7731
Absorption correction	Integration
Max. and min. transmission	0.9831 and 0.9376

Largest diff. peak and hole	0.393 and -0.282 e.Å^{-3}
Solution	Direct methods
Refinement	Full-matrix least-squares on F^2
Treatment of hydrogen atoms	Calculated positions, constr. ref.
Programs used	SIR 2011 SHELXL-97 (Sheldrick, 1997) DIAMOND 3.2h STOE IPDS2 software
Data / restraints / parameters	7731 / 15 / 616
Goodness-of-fit on F2	0.823
R index (all data)	wR2 = 0.0955
R index conventional [I>2sigma(I)]	R1 = 0.0415

Curriculum Vitae

Name :Yonggang Xiang
Address
Lab 4226, FB Chemie, Hans-Meerwein-Straße, D-35032
Marburg, Hessen, Germany
(49) 06421-28/25681
ygxiang@gmail.com

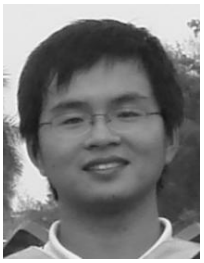

Academic Qualifications

2009-present	Doctoral degree in Organic Chemistry, Philipps-Universität Marburg. Under the supervision of Prof. Lilu Zhang and Prof. Eric Meggers.
2005-2009	Master degree in Organic Chemistry, Xiamen University, China. Under the supervision of Prof. Peiqiang Huang and Prof. Xiao Zheng.
2001-2005	Bachelor degree in Applied Chemistry, Huazhong Agricultural University, China.

Research Experience

Research Work in Xiamen University

- The synergistic action of $BF_3 \cdot OEt_2$ and SmI_2 allowed a series of intermolecular cross-couplings of readily available *N*-acyl *N*, *O*-acetals with α, β-unsaturated compounds to be performed in high yields, and application of stereoselective synthesis of pyrrolizidine alkaloid (+)-xenovenine. This part of work has been published in the Chemical Communication.

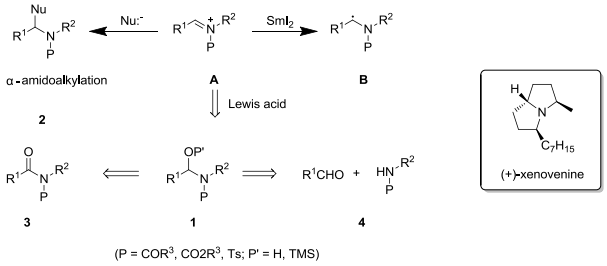

- In corporation with colleagues, we have accomplished a series of asymmetric syntheses of the sex pheromones of pine sawflies with three chiral centers starting from simple and easily available one chiral center compound (*S*)-malic acid. 12 of them were synthesized by me.

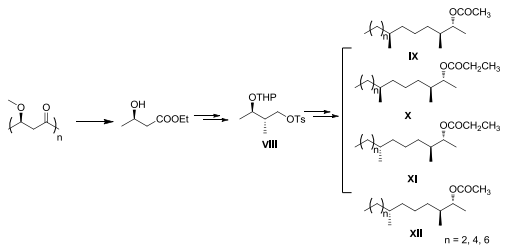

Research Work in Marburg University

- Incorporation of modified chromophores (such as porphyrin, phthalocyanine, perylene bisimide) into duplexes of the simplified nucleic acid GNA and exploration of the interaction between the chromophores inside the GNA.

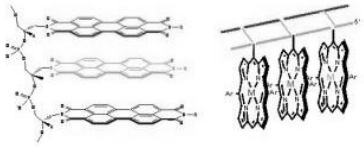

- First examples of hydrolytically stable octahedral silicon complexes with biological activity. This part of work has been published in Chemical Communication as **Front Cover**.

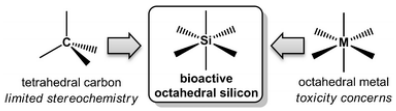

Publication

"One-pot cross-coupling of *N*-acyl *N*, *O*-acetals with α, β-unsaturated compounds." **Xiang, Y. G.**; Wang, X. W.; Zheng, X.; Ruan, Y. P.; Huang, P. Q. *Chem. Commun.* **2009**, 7045-7047.

"SmI_2-Mediated Radical Cross-Couplings of alpha-Hydroxylated Aza- hemiacetals and *N*, *S*-Acetals with α, β-Unsaturated Compounds: Asymmetric Synthesis of (+)-Hyacinthacine A(2), (-)-Uniflorine A, and (+)-7-epi-Casuarine." Liu, X. K.; Qiu, S.; **Xiang, Y. G.**; Ruan, Y. P.; Zheng, X.; Huang, P. Q. *J. Org. Chem.* **2011**, *76*, 4952-4963.

"Asymmetric Syntheses of the Sex Pheromones of Pine Sawflies, Their Homologs and Stereoisomers**"** Zheng, J. F.; Zhang, Z.; Lan, H. Q.; Yang, R. F.; Peng, Q. L.; Xiao, Z. H.; Tuo, S. C.; Hu, K. Z.; **Xiang, Y. G.**; Wei, Z.; Huang, P. Q. *Helvetica Chimica Acta*. 2012, 1799-1808.

"Hydrolytically stable octahedral silicon complexes as bioactive scaffolds: application to the design of DNA intercalators." **Xiang, Y. G.**; Fu, C.; Breiding, T.; Sasmal, P. K.; Liu, H. D.; Shen, Q.; Harms, K.; Zhang, L. L.; Meggers, E. *Chem. Commun.* **2012**, *48*, 7131-7133 (**Front Cover**).

References:

Professor Zhang
Chemistry Department
Hans-Meerwein-Straße,D-35032 Marburg
zhangl@staff.uni-marburg.de

Professor Meggers
Chemistry Department
Hans-Meerwein-Straße, D-35032 Marburg
meggers@chemie.uni-marburg.de